UNIVERSITY OF CALIFORNIA,
IRVINE

Aβ-degrading proteases in the pathogenesis of late-onset Alzheimer disease

DISSERTATION

submitted in partial satisfaction of the requirements
for the degree of

DOCTOR OF PHILOSOPHY

in Biological Sciences

by

Caitlin N. Suire

Dissertation Committee:
Professor Frank LaFerla, Chair
Assistant Professor Mathew Blurton-Jones
Associate Professor Masashi Kitazawa

2020

DEDICATION

To

friends and family,

those that served as loving support

to fuel my fire

For the correct analogy for the mind is not a vessel that needs filling,
but wood that needs igniting
— no more —
and then it motivates one towards originality and instills the desire for truth.
Plutarch
the essay "On Listening"

and kept me laughing

How does a farmer count his cows?
With a cowculator!

TABLE OF CONTENTS

LIST OF FIGURES

LIST OF TABLES

LIST OF ABBREVIATIONS

Aβ	Amyloid β-protein
AβDP	Aβ-degrading protease
ACH	Amyloid cascade hypothesis
AD	Alzheimer disease
AICD	Amyloid precursor protein intracellular domain
AP	Avidin-agarose precipitation
A/P	Anteroposterior
ApoE	Apolipoprotein E
APOE	Apolipoprotein E gene
APP	Amyloid precursor protein
APP	Amyloid precursor protein gene
BACE1	β-site APP-cleaving enzyme 1
BBB	Blood-brain barrier
BSA	Bovine serum albumin
CatB	Cathepsin B
CatD	Cathepsin D
CHI	Closed-head impact
COL1A1	Alpha-1 type 1 collagen gene
CTD	C-terminal domain
CTF	C-terminal fragment
CTL	Control
CTSD	Cathepsin D gene
DEA	Diethylamine
DMSO	Diimethyl sulfoxide
DS	Down Syndrome
D/V	Dorsoventral
ECE	Endothelin-converting enzyme

ECM	Extracellular matrix
ELISA	Enzyme-linked immunosorbent assay
EOAD	Early-onset Alzheimer disease
FAβB	Fluorescein-Aβ(1-40)-Lys-biotin
FBDD	Fragment-based drug discovery
FBG	Fluoresceinated, biotinylated glucagon
FP	Fluorescence polarization
GALC	Galactosylceramidase gene
GAPDH	Anti-glyceraldehyde-3-phosphate dehydrogenase
GuITC	Guanidinium isothiocyanate
HET	Heterozygous
HRP	Horseradish peroxidase
HTRF	Homogenous time-resolved fluorescence
HTS	High-throughput screening
I.C.V.	Intracerebroventricularly
IDE	Insulin-degrading enzyme
IHC	Immunohistochemistry
k_{cat},	Turnover number
K_M	Michaelis-Menten constant
KI	Knock-in
KO	Knock-out
LOAD	Late-onset Alzheimer disease
LPS	Lipopolysaccharide
MALDI-TOF	Matrix-assisted laser desorption/ionization-time-of-flight
MBP	Metal-binding pharmacophore
MCI	Mild cognitive impairment
M/L	Mediolateral
MMP	Matrix-metalloproteinase
mP	Millipolarization units
MS	Mass spectrometry

MSD	Meso Scale diagnostics
NEP	Neprilysin
NFT	Neurofibrillary tangle
NTD	N-terminal domain
P3	Alpha/gamma-secretase-derived fragment of APP
PBS	Phosphate-buffered saline
PepA	Pepstatin A
PreP	Presequence protease
PS1	Presenilin-1 protein
PS2	Presenilin-2 protein
PSEN1	*Presenilin-1* gene
PSEN2	*Presenilin-2* gene
RFU	Relative fluorescence units
sAPP	Secreted amyloid precursor protein
SEC	Size-exclusion chromatography
SNP	Single-nucleotide polymorphism
SubV	Substrate V
T2DM	Type-2 diabetes mellitus
TBI	Traumatic brain injury
TBS	Tris-buffered saline
TBST	Tris-buffered saline supplemented with Triton X-100
Thio-S	Thioflavin S
tPA	Tissue-type plasminogen activator
Tryp	Trypsin
WT	Wild-type

ACKNOWLEDGEMENTS

I sincerely thank my doctoral thesis advisor and mentor, Dr. Frank LaFerla and Dr. Malcolm Leissring, whose combined efforts and support throughout the years have made this work possible. In particular I thank them for providing opportunities to expand my research into fields I have been interested in but have not had the opportunity to work with, such as drug discovery. I also want to express my gratitude for the encouragement to participate in extracurricular activities and careers within both academia and industry.

I am incredibly grateful to my advancement and dissertation committee members, Dr. Brian Cummings, Dr. Kim Green, Dr. Masashi Kitazawa, and Dr. Mathew Blurton-Jones, as well as Dr. David Baglietto-Vargas, for fostering my scientific growth, taking time to serve as mentors, and talk through experimental design and data.

I wholeheartedly thank the graduate students and professors within the University of California, Irvine that have served as pillars, providing emotional and intellectual support throughout this journey. I would also like to thank Beall Applied Innovation; my time working with the patent office has allowed me to broaden my scientific and professional knowledge.

The studies described herein were supported by grants from the National Institutes of Health (GM115617; AG052718), the American Health Assistance Foundation, the Alzheimer's Association, Coins for Alzheimer's Research Trust Fund, American Diabetes Association (7-11-CD-13), and the UCI Applied Innovation Technology Development Innovation Fund (to M.A.L.).

To all friends, family, and passersby: I appreciate all the love and encouragement over the years.

Thank you.

VITA

Caitlin N. Suire

EDUCATION

Doctor of Philosophy in Neurobiology and Behavior (2020)
University of California, Irvine, CA.

Bachelor of Science with Honors in Biology of Mind (2015)
Wake Forest University, Winston-Salem, NC.

RESEARCH EXPERIENCE

Department of Neurobiology and Behavior (2016-2020)
University of California, Irvine, CA.

National Institute on Aging (2015-2016)
National Institutes of Health, Baltimore, MD.

Department of Biology (2013-2015)
Wake Forest University, Winston-Salem, NC.

Department of Psychology (2013-2015)
Wake Forest University, Winston-Salem, NC.

AWARDS

AGS Graduate Student International Travel Award (2019)

Fine Science Tools Graduate Travel Award (2018)

John Haycock Travel Award (2018)

School of Biological Sciences Dean's Graduate Fellowship (2016)

CERTIFICATES

Science Communication Skills for STEM Scientists, *UC Irvine* (2020)

Basics of Medical Writing, *UC Irvine* (2020)

Micro-MBA, *UC San Diego Rady School of Management* (2020)

Business Concepts for STEM Scientists, *UC Irvine* (2019)

Mentoring in Excellence, *UC Irvine* (2018)

Science Policy Program, *AAAS* (2018)

Scientific Writing and Publishing, *Nature Masterclass* (2017)

Business of Science, *SciPhD* (2017)

Effective Communication for Scientists, *UC Irvine* (2017)

PUBLICATIONS

1. **Suire CN** & Leissring MA. Role of Lysosomal Aβ protein in Alzheimer disease. Journal of Experimental Neurology, In preparation: To be submitted January 2021.
2. **Suire CN** & Leissring MA. Early increases in amyloid β-protein as a trigger for sporadic Alzheimer disease. Journal of Alzheimer's disease, In preparation: To be submitted December 2020.
3. Adamek RN*, **Suire CN*,** Brizuela MK, Leissring MA, & Cohen SM. Isosteres of hydroxypyridinethione as inhibitors of human insulin-degrading enzyme. ChemMedChem, Submitted November 2020.
4. **Suire CN**, Brizuela MK, & Leissring MA. Quantitative, high-throughput assays for proteolytic degradation of amylin. Methods and Protocols, 2020 3(4):81.
5. **Suire CN**, Abdul-Hay SO, Sahara T, Kang D, Brizuela MK, Saftig P, Dickson DW, Rosenberry TL, & Leissring MA. Cathepsin D regulates cerebral Aβ42/40 ratios via differential degradation of Aβ42 and Aβ40. Alzheimer's Research & Therapy, 2020 12 (1).
6. Hamilton KA, Wang Y, Raefsky SM, Berkowitz S, Spangler R, **Suire CN**, Camamndola S, Lipsky RH, Mattson MP. Mice lacking the transcriptional regulator Bhlhe40 have enhanced neuronal excitability and impaired hippocampal synaptic plasticity. PLoS ONE, 2018 13(5).
7. **Suire CN**, Lane SR & Leissring MA. Development and characterization of quantitative high-throughput-compatible assays for proteolytic degradation of glucagon. SLAS Discovery, 2018 23 (10):1060-1069.
8. **Suire CN**, Nainar SJ, Fazio M, Kreutzer AG, Paymozd-Yazdi T, Topper CL, Thompson CR & Leissring MA. Peptidic inhibitors of insulin-degrading enzyme suitable for dermatological applications discovered via phage display. PLoS ONE, 2018 13(2).
9. **Suire CN**, Eitan E, Shaffer NC, Tian Q, Studenski S, Mattson MP, Kapoginnis D. Walking speed decline in older adults is associated with elevated pro-BDNF in plasma extracellular vesicles. Experimental Gerontology, 2017 98: 209-216.
10. Eitan E*, Tosti V*, **Suire CN*,** Cava E, Berkowitz S, Bertozzi B, Raefsky SM, Veronese N, Spangler R, Spelta F, Mustapic M, Kapogiannis D, Mattson MP, Fontana L. In a randomized Trial in prostate cancer patients, dietary protein restriction modifies markers of leptin and insulin signaling in plasma extracellular vesicles. Aging Cell, 2017 16(6): 1430-1433.
11. Eitan E, **Suire CN**, Zhang S, and Mattson MP. Impact of lysosome status on extracellular vesicle content and release. Ageing Res Rev, Dec 2016 (32):65-74.
12. Eitan E, Hutchison ER, Marosi K, Comotto J, Mustapic M, Nigam SM, **Suire CN**, Maharana C, Jicha GA, Liu D, Machairaki V, Witwer KW, Kapogiannis D, Mattson MP. Extracellular vesicles propagate Aβ-mediated neurodegenerative bioenergic and Ca2+-handling deficits. Npj Aging and Mech Dis, 2016 (2):1-11.

PRESENTATIONS

Poster Presentations

1. **Suire CN**, Abdul-Hay SO, Lane SR, Leissring MA. Regulation of cerebral Aβ42/40 ratios by differential, aggregation-independent processing of Aβ42 versus Aβ40 by cathepsin D. AD/PD. March 2019
2. **Suire CN**, Abdul-Hay SO, Lane SR, Leissring MA. Regulation of cerebral Aβ42/40 ratios by differential, aggregation-independent processing of Aβ42 versus Aβ40 by cathepsin D. Emerging Scientist Symposium UCI. February 2019
3. **Suire CN**, Abdul-Hay SO, Lane SR, Leissring MA. Regulation of amyloidogenesis by cathepsin D in murine models of Alzheimer disease. Society for Neuroscience. November 2018
4. **Suire CN**, Lane SR, Leissring MA. Development and characterization of quantitative high-throughput-compatible assays for proteolytic degradation of glucagon. Southern California Biomedical Sciences Graduate Student Symposium, October 2018
5. **Suire CN**, Eitan E, Hutchison ER, Mattson MP. Neuroblastoma extracellular vesicles alter reactive glial response to promote tumor growth. National Institutes of Health Post-baccalaureate Poster Session May 2016 Top presenter award
6. **Suire CN**, Eitan E, Hutchison ER, Mattson MP. Neuroblastoma extracellular vesicles alter reactive glial response to promote tumor growth. National Institute on Aging Poster Session May 2016 Top presenter award
7. **Suire CN**, Eitan E, Mustapic M, Kapogiannis D, Mattson MP. The response of blood-derived extracellular vesicles to caloric restriction and intermittent fasting in overweight women. National Institute on Aging Summer Poster Session August 2015

Oral Presentations

- **Suire CN**, Leissring MA. Investigation of amyloid-β proteases and their role in the development of Alzheimer disease. Neuroblitz. December 2019
- **Suire CN**, Leissring MA. Investigation of amyloid-β proteases and their role in the development of Alzheimer disease. Neuroblitz. December 2018
- **Suire CN**, Leissring MA. The role of risk factors in the etiology of sporadic Alzheimer's disease investigated in a novel mouse model. Neuroblitz. May 2018
- **Suire CN**, Abdul-Hay SO, Lane SR, Leissring MA. Taking out the Trash: Importance of protein clearance in Alzheimer's disease. AGS Research Symposium April 2018
- **Suire CN**, Abdul-Hay SO, Lane SR, Leissring MA. Regulation of amyloidogenesis by cathepsin D in murine models of Alzheimer disease. International Conference on Learning and Memory. April 2018
- **Suire CN**, Leissring MA. The search for inhibitors of insulin-degrading enzyme. Neuroblitz. Spring 2017

ABSTRACT OF THE DISSERTATION

Aβ-degrading proteases in the pathogenesis of
late-onset Alzheimer disease

by

Caitlin N. Suire

Doctor of Philosophy in Biological Sciences

University of California, Irvine, 2020

Dean Frank LaFerla, Chair

Alzheimer disease (AD) is a devastating neurodegenerative disorder, affecting almost 6 million people in the United States alone, characterized by abnormal accumulation of an aggregation-prone, variable-length peptide known as the amyloid-β protein (Aβ). Considerable progress has been made elucidating the molecular pathogenesis of rare forms of early-onset AD (EOAD) attributable to autosomal-dominant mutations, which in all cases have been found to affect the *production* of Aβ either by elevating the levels of all forms of Aβ or by increasing the relative proportion of longer, more amyloidogenic species (e.g., Aβ42) to shorter, less aggregation-prone species (e.g., Aβ40). Nevertheless, these familial forms of the disease account for <2% of all AD diagnoses, and the precise mechanistic cause(s) of the remaining >98% of late-onset AD (LOAD) cases remains poorly understood, apart from the identification of certain genetic and environmental factors affecting AD risk. This proposal explores the overall hypothesis that LOAD can be triggered by defective *clearance* of Aβ by one or more Aβ-degrading proteases (AβDPs). More specifically, we investigate the hypothesis that a transient increase in Aβ early in life can serve as a common pathogenic mechanism for LOAD risk factors. We demonstrate that a severe traumatic brain injury in novel model of LOAD,

which lacks the genetic mutations associated with EOAD, can trigger an acute rise in Aβ as well as accumulation of Aβ fibrils by 1-day post-injury. Additionally, we identify cathepsin D (CatD), a lysosomal protease, as a novel AβDP, demonstrating that it is the most important in vivo regulator of intracellular, insoluble Aβ yet identified. Intriguingly, we discovered that CatD degrades Aβ42 and Aβ40 with markedly different kinetics, resulting in increases to the Aβ42/40 ratio resembling those produced by EOAD-linked mutations. Finally, we detail the successful development of high-throughput assays to measure the proteolytic degradation of different substrates for insulin-degrading enzyme (IDE). We use these assays, in combination with other methods, to discover novel peptidic and zinc-targeting inhibitors of IDE, which can serve as novel pharmacological tools to help elucidate the role of IDE in the pathogenesis of LOAD.

CHAPTER 1

INTRODUCTION

1.1 Rationale and Aims

Alzheimer disease (AD) is a devastating and presently incurable neurodegenerative disorder that affects millions of individuals worldwide and exacts an enormous economic and interpersonal burden on society (1). Histopathologically, AD is characterized by abnormal accumulation of neurotoxic peptides known as amyloid β-protein (Aβ), which accumulate in extracellular deposits known as "plaques," as well as hyperphosphorylated forms of the microtubule-associated protein, tau, which form intraneuronal aggregates known as neurofibrillary "tangles" (NFTs) (2). Much has been learned about the molecular pathogenesis of AD from the study of rare, very aggressive, inherited forms of the disease, known as early-onset AD (EOAD), but the cause(s) of the vast majority of AD cases, known as late-onset AD (LOAD), remains unknown. Moreover, despite heroic efforts within academia and the pharmaceutical industry to develop therapeutics, these efforts have so far failed to generate successful disease-modifying treatments (3, 4). Thus, there remains a great need to identify the cause(s) of LOAD so that interventions can be developed that slow or halt the development of this devastating disease of brain and mind.

To date, most research within the AD field has been focused on the mechanisms by which Aβ is produced from the amyloid precursor protein (APP). This is in part because the mutations that cause EOAD have been shown to affect Aβ production universally, and also because the proteases that cleave Aβ from APP have been regarded as attractive therapeutic targets (5). However, Aβ levels are determined not only by its production but also by its elimination—via proteolytic degradation and other clearance mechanisms—and research on the catabolic fate of Aβ

holds great promise both for elucidating the molecular pathogenesis of LOAD and also potentially for developing effective treatments (6, 7). This thesis is focused on elucidating the role of Aβ-degrading proteases (AβDPs), including the prominent proteases cathepsin D (CatD) and insulin-degrading enzyme (IDE), in the pathogenesis of LOAD. AβDPs are potent regulators of Aβ accumulation and are likely to be centrally involved in the altered proteostasis that occurs in aging and in neurodegenerative diseases. AβDPs also constitute important research tools for understanding different aspects of AD pathogenesis, in particular because they are located in different cellular and subcellular compartments and, as such, regulate distinct pools of Aβ that may be differentially relevant to downstream pathological sequelae (8, 9). Dysfunction of certain AβDPs has also been implicated in other diseases, some of which alter risk for AD, by virtue of their action on different peptide substrates (10, 11). Despite numerous disease-relevant aspects of AβDPs, to date only a subset has been identified and, for known AβDPs, substantially more study is needed to fully understand their role in AD pathogenesis and potentially therapeutic value. Finally, for some key AβDPs, such as IDE in particular, we currently lack the pharmacological tools needed to fully elucidate their role(s) in Aβ proteostasis and AD pathogenesis.

The overall focus of this thesis is on elucidating the role of AβDPs in the pathogenesis of AD, particularly LOAD. The work presented herein covers many different aspects of AβDPs, in the form of three Aims:

Aim 1: To test the hypothesis that the emergence of LOAD late in life can be triggered by transient increases in Aβ early in life and, further, that this represents a common molecular mechanism linking different known risk factors for AD, such as traumatic brain injury (TBI). This hypothesis is tested a novel mouse model of LOAD.

Aim 2: To characterize a candidate AβDP that is genetically linked to LOAD, CatD, specifically its ability to degrade different-length Aβ species (Aβ40 and Aβ42) *in vitro* and its impact on Aβ proteostasis *in vivo* relative to other, major AβDPs.

Aim 3: To develop novel substrate-specific pharmacological inhibitors of IDE for probing the involvement of different substrates in LOAD pathogenesis. To this end, we develop novel high-throughput-compatible assays for different IDE substrates and use them to screen compound libraries and develop potent pharmacological inhibitors of IDE.

1.2 Background

AD was described for the first time by the German psychiatrist Alois Alzheimer in 1906 (12). In that report, Dr. Alzheimer described the clinicopathological examination of a woman, Auguste Deter, who presented severe symptoms of dementia at the early age of 51 years (13). AD is characterized clinically by the appearance of gradual and progressive memory loss and cognitive impairment. Although Auguste Deter was in her early 50s, most AD cases appear in individuals 65 and older, with increased incidence in subsequent decades (14). From a public health perspective, AD imposes a severe financial and social burden, currently ranked as the 6th leading cause of death, with a current global estimated annual cost of ~$600 billion that is projected to grow to $1.1 trillion by 2030 (14). Alzheimer's Disease International estimates that AD affects ~35 million people worldwide today, a figure that is expected to quadruple in the next 30 years, with one new case appearing every 33 seconds (15-17).

Thought to be the most common form of dementia, AD is studied across the world in efforts to understand its causes, identify biomarkers, and discover new methods of treatment. However, all science is limited by the tools and technology that we use to explore it, and while there have

been many advances in recent years, faithfully modeling complex diseases such as AD remains a challenging goal. AD is incredibly complicated: the proteins and proteases involved are often implicated in other diseases, making them difficult to study in isolation. Current animal models are ideal for the study of genetic mutations responsible for EOAD, but create several confounds when used in the investigation of environmental and external components of AD. These components are vital to the understanding of LOAD, which accounts for >98% of AD diagnoses and is influenced by an array of factors including age, genetics, diet, and injury (18, 19). Dementia is most commonly known for the behavioral and cognitive changes, such as memory loss, aggression, and depression, that do not occur until later stages of the disease (Fig. 1.1) (20), but there is a prolonged pre-symptomatic period in AD patients during which distinct AD pathological changes take place (Fig. 1.2).

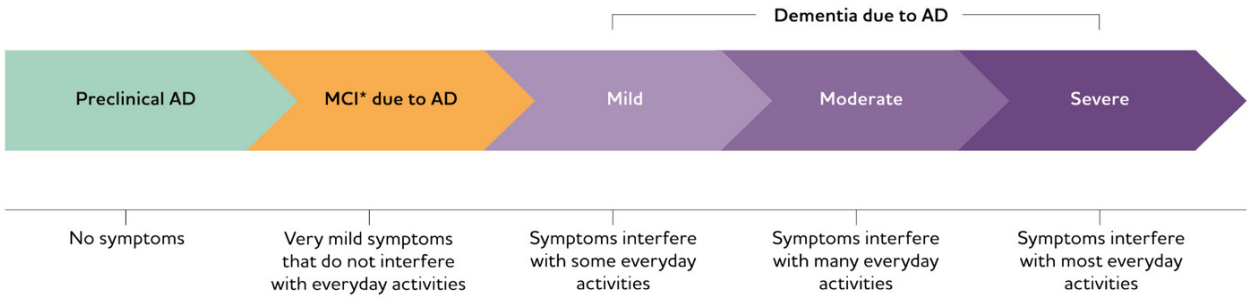

Figure 1.1. Alzheimer disease continuum. Cartoon illustrating the approximate times that different neuropsychological symptoms occur over the course of dementia. Reprinted from 2020 Alzheimer's disease facts and figures with permission from John Wiley and Sons (20).

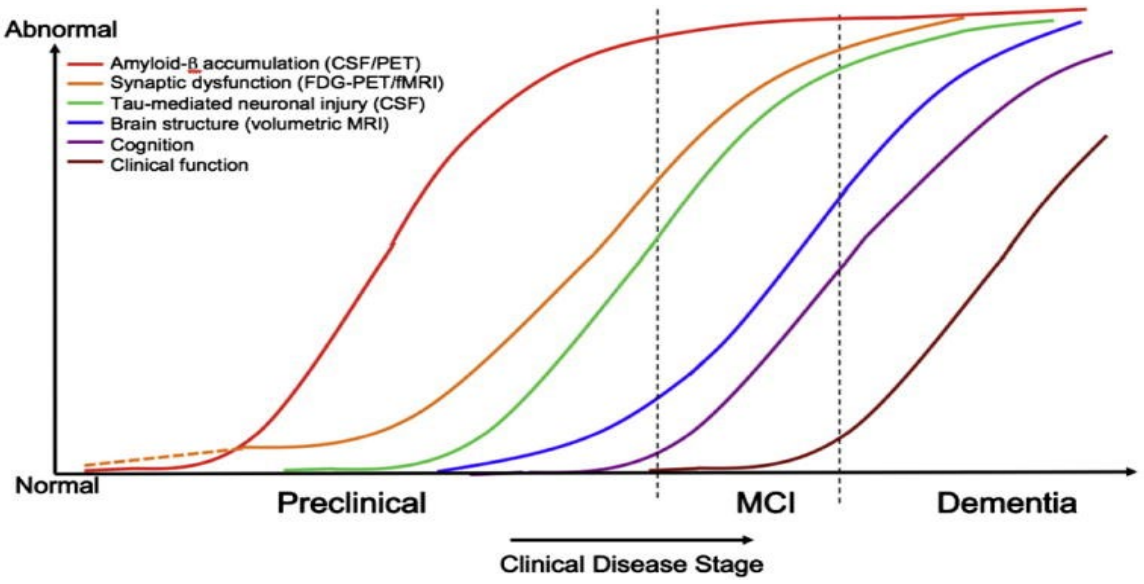

Figure 1.2. Progression of AD pathology. Cartoon illustrating the approximate times that different pathological changes occur over the course of dementia. Reprinted from Sperling et al., 2011 *Alzheimer Dement* with permission from John Wiley and Sons (21).

The brains of AD patients are characterized by the presence of two principal histopathological hallmarks, which accumulate to abnormally high levels, progressively and irreversibly during the course of the disease. The first defining hallmark is extracellular deposits of Aβ, often referred to as "plaques" (Fig. 1.3) (22, 23). Amyloid plaques come in two major forms: neuritic and diffuse. Neuritic or "dense-core" plaques are infrequent in normal aging and are thus believed to be pathognomonic for AD, while diffuse plaques, which are less dense accumulations of Aβ, appear even in cognitively normal aged individuals. The second major histopathological feature is the accumulation of intraneuronal deposits, sometimes referred to as "neurofibrillary tangles" (NFTs), that are composed of hyperphosphorylated forms of the microtubule-associated protein, tau (Fig. 1.3) (22, 23). NFTs are a common feature in several other forms of dementia (e.g., frontotemporal dementia), suggesting that they play a necessary causal role in the development of dementia, perhaps mediating the extensive neuronal loss that

characterizes many neurodegenerative diseases (22, 23). Other well-known features of AD include: synapse loss, the best correlate to cognitive changes; inflammation, typified by the presence of activated microglia surrounding neuritic plaques; and mitochondrial and lysosomal dysfunction, often thought to be among the earliest signs of neuronal malfunction (24).

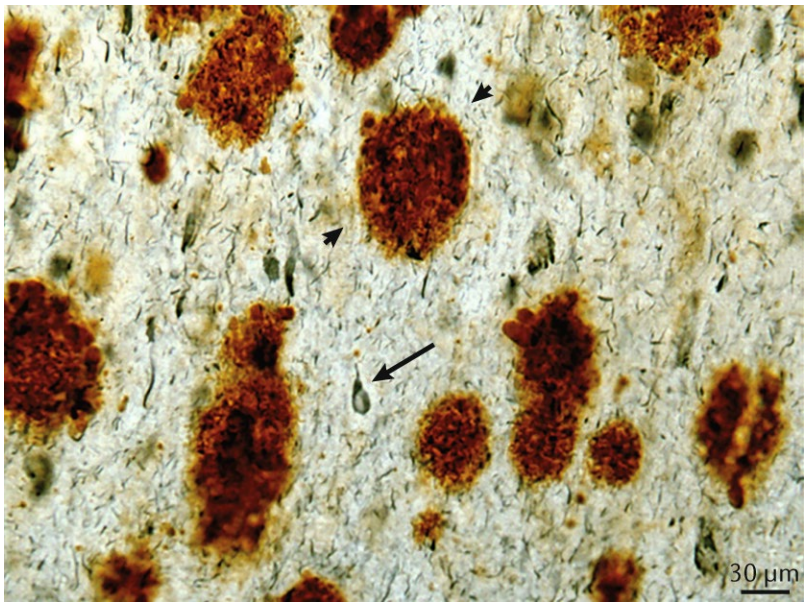

Figure 1.3. AD pathology in the human brain. Example of the histopathological hallmarks of AD. Aβ plaques (brown staining; arrowheads) and NFTs (PHF1 antibody; blue staining; arrow) in the frontal cortex of a 46-year-old person with Down syndrome and end-stage AD. Reprinted from Lott and Head, 2019 *Nat Rev Neurol* with permission from Springer Nature (22).

A widely accepted theory about the molecular pathogenesis of AD is known as the amyloid cascade hypothesis (ACH) (25, 26), which postulates that abnormal accumulation of Aβ is the trigger for all other pathological sequelae, including tangle formation, synapse loss, and eventual neuronal cell death (Fig. 1.4). Widespread acceptance of the ACH is primarily attributable to the discovery of several hundred autosomal-dominant mutations in 3 different genes that cause EOAD with high penetrance and invariably disrupt Aβ proteostasis in one way or another (reviewed in detail below) (26, 27). While the ACH remains the leading hypothesis about AD pathogenesis,

others, such as the mitochondrial dysfunction hypothesis or the oxidative stress hypothesis (Fig. 1.5) still enjoy substantial support (28).

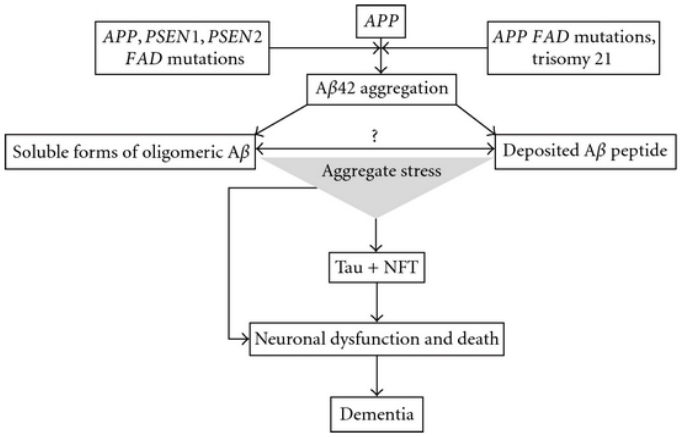

Figure 1.4. The amyloid cascade hypothesis (ACH). Overview of the basic tenets of the ACH. Note that Aβ accumulation is the most upstream event, triggering all other symptoms and hallmarks of AD. Reprinted via Open Access from Reitz, 2012 *Int J Alzheimer's Dis* (25).

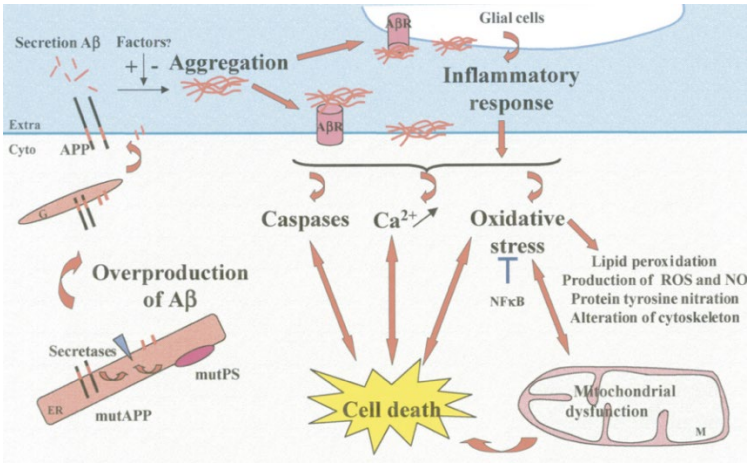

Figure 1.5. Alternative hypotheses for the etiology of AD. Alternative hypotheses besides the ACH include the inflammation hypothesis, oxidative stress hypothesis, and the mitochondrial dysfunction hypothesis. Reprinted from Drouet et al., 2000 *Cell Mol Life Sci* with permission from Springer Nature (28).

Despite the widespread acceptance of the ACH, the role of Aβ as the *proximal* cause of various aspects of AD pathology remains somewhat problematic. For instance, the brains of many

cognitively normal aged adults have been found to contain abundant Aβ plaques (29), and human studies have shown that overall Aβ levels do not correlate with cognitive function in AD patients or those with mild cognitive impairment (MCI: a stage at which there are some cognitive deficits but not to the extent of AD) (30). These inconsistencies suggest that there are many additional factors that can trigger or worsen the effects of Aβ or, alternatively, that Aβ may serve a role in the initiation of AD-type pathology but is not the primary factor contributing to cognitive symptoms emerging at later stages.

AD cases can be broadly divided into two groups: early-onset and late-onset, also commonly known as familial and sporadic AD. EOAD is highly heritable, represents only a tiny minority of all AD cases (<2%), and occurs in patients younger than 65 years of age, in some cases as early as the 40s (17). LOAD, on the other hand, the most common form of AD, is typically found in individuals 65 years of age or older and does not have a clear-cut genetic basis like EOAD; instead, risk for LOAD appears to be influenced by numerous factors, both environmental and genetic. Although the triggering factors for the two types of AD are drastically different, the pathology—accumulation of Aβ and hyperphosphorylated tau, synapse and neuronal loss, etc.—looks very similar in both forms of the disease. Given that the vast majority of AD cases are late onset, identifying the triggers and contributing risk factors that lead to LOAD is critical for preventative efforts and discovery of new therapeutics.

1.3 Molecular pathogenesis of AD

From a historical perspective, the elucidation of the molecular pathogenesis of AD in general, and the detailed molecular mechanisms of Aβ production in particular, is a complex story derived from an interconnected series of advances in the areas of human molecular genetics and

basic molecular biology. This section aims to provide a roughly historical account of these two principal lines of evidence, describing the key discoveries that made the ACH a dominant paradigm in the AD field.

Historically, one of the most helpful clues about the specific molecular pathogenesis of AD came from the investigation of individuals with Down syndrome (DS), a genetic disease caused by triplication of Chromosome 21 (trisomy 21) that produces mild to moderate intellectual disability and physical growth delays. Notably, AD-type pathology is found in the vast majority of DS patients over the age of 40 (Fig. 1.6) (22), and it is estimated that these individuals have over a 90% risk of developing dementia in their lifetime (31).

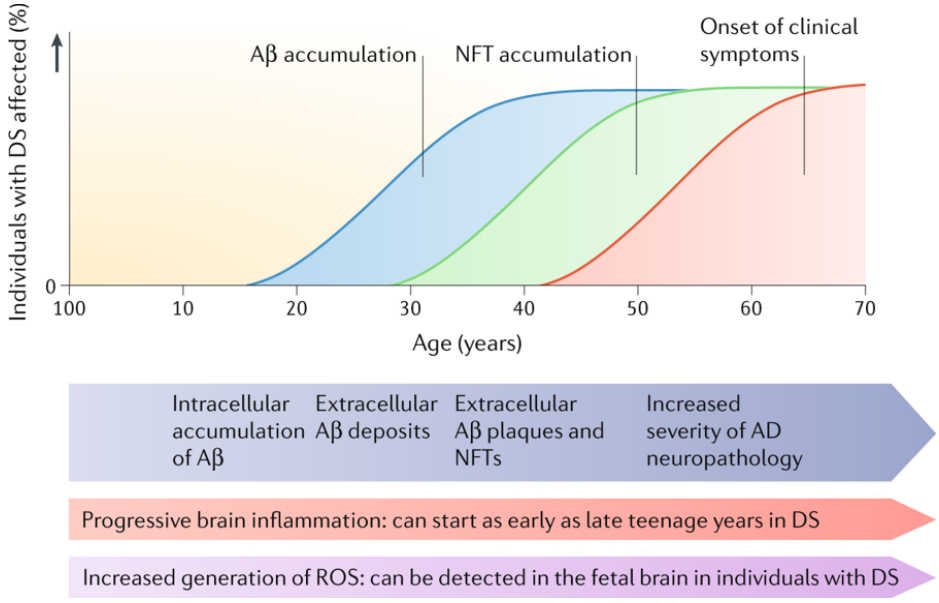

Figure 1.6. Progression of AD-type pathology in DS patients. Cartoon illustrating the average time course for the development of various features of AD in DS patients. All of these features appear earlier in DS than is typical in LOAD. Reprinted from Lott and Head, 2019 *Nat Rev Neurol* with permission from Springer Nature (22).

The fact that an extra copy of Chr. 21 leads to the development of AD-type pathology meant little until coupled with several other key advances. First, George Glenner purified amyloid plaques from amyloid patients, and succeeded in sequencing the Aβ peptide (32). Second, this same team showed that the amyloid plaques in DS patients are also comprised of Aβ (33). Finally, using the Aβ peptide sequence to generate redundant DNA primers, the amyloid precursor protein (APP) gene (*APP*) was cloned and sequenced and found to be located on Chr. 21 (34). Together, these observations made a strong case that Aβ plays a causal role in the pathogenesis of AD, since a mere 50% increase in Aβ production—in this case due to 3 copies of the *APP* gene instead of 2, as happens in DS—is sufficient to trigger the full spectrum of AD-type pathology with extremely high penetrance.

The cloning of APP initiated an "amyloid cascade" of its own, in the form of a series of discoveries about the fundamental biology of Aβ production. It was evident from the amino acid sequence that APP is a Type I integral membrane protein (Fig. 1.7), with a large ectodomain facing the extracellular space or lumen of the endoplasmic reticulum (34). The Aβ sequence itself is positioned on the extracellular/lumenal side, adjacent to the plasma membrane, with the C-terminus partially embedded within the latter, followed by a short cytoplasmic domain, the APP intracellular domain (AICD). Three principal splice isoforms were discovered varying lengths, with 695, 751 or 770 amino acids in length (35). Although the 695-amino acid variant is the most common isoform within neurons (36), it is interesting to note that the two longer variants both contain a Kunitz protease inhibitor domain that potently inhibits serine proteases (35). Notably, a second protease inhibitor domain, present in all isoforms of APP was later identified (37) that potently inhibits matrix-metalloproteinases (MMPs).

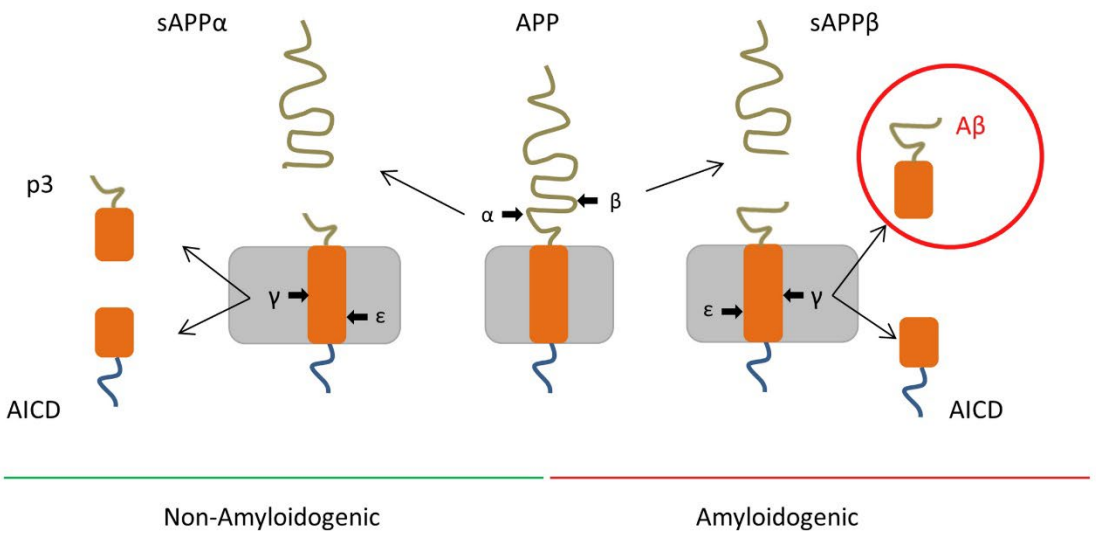

Figure 1.7. APP processing. Cartoon demonstrating the complexities of APP processing. In the non-amyloidogenic pathway (left side), the transmembrane protein APP is sequentially cleaved by α- and γ-secretases, producing three fragments: a secreted ectodomain (sAPPα), the P3 fragment (amino acid 37-43), and the APP intracellular domain (AICD). In the amyloidogenic pathway (right side), APP is sequentially cleaved by β- and γ-secretases, producing a slightly smaller secreted ectodomain (sAPPβ), Aβ (which can range in length, from Aβ37 to Aβ43), and the AICD. The different cleavage products have all been shown to have various physiological functions; for example, sAPPα protects against cell death (17, 25, 38) Reprinted from Cacace et al., 2016 *Alzheimer Dement* with permission from John Wiley and Sons (17).

1.3.1 APP processing and the production of Aβ and P3 peptides

APP processing is divided into mutually exclusive non-amyloidogenic and amyloidogenic pathways. In the former, full length APP is first processed by any one of a group of proteases collectively known as α-secretases, which cut inside the Aβ sequence within APP, thereby precluding Aβ formation (17, 39). The action of α-secretases results in the liberation and ultimate secretion of the large ectodomain of APP, referred to as sAPPα (Fig. 1.7). An estimated 90% of all APP is processed via the non-amyloidogenic pathway (40). In the amyloidogenic pathway, by contrast, full-length APP is initially cleaved by a protease called β-secretase, thereby liberating a slightly smaller secreted ectodomain (sAPPβ) and simultaneously producing the N-terminus of Aβ (Fig. 1.7). After cleavage by α- or β-secretase, the C-terminal fragments (CTFs) of APP remains

remain membrane bound until further proteolytic processing (Fig. 1.7). β-secretase activity is mediated by a single membrane-bound, aspartyl protease, known as β-site APP-cleaving enzyme 1 (BACE1) (41, 42).

The next step in APP processing is cleavage of the membrane-bound CTFs by yet another protease known as γ-secretase. Interestingly, γ-secretase cleaves APP within the highly hydrophobic plasma membrane, an unusual site for hydrolysis to occur (since hydrolysis, by definition, requires an H_2O molecule). Another notable feature of γ-secretase activity is that it does not cleave at a single site; instead, γ-secretase can cleave at any of 6-7 different sites within the CTFs of APP. For the amyloidogenic pathway, this results in the generation of Aβ peptides (Fig. 1.7) of various lengths, ranging from 37 to 43 amino acids, with certain Aβ variants, such as Aβ40, being more common than others. This point is critical, because longer Aβ species are more likely to aggregate (43). For the non-amyloidogenic pathway, the action of γ-secretase results in the generation of a different set of heterogeneous peptides in the place of Aβ (Fig. 1.7). Known as P3 fragments, these peptides share the C-terminal heterogeneity of Aβ (i.e., corresponding to C-terminal fragments from Aβ37 to Aβ43), but in this case are 17-amino acids shorter, because α-secretase cuts APP 17 amino acids inside the Aβ region. Notably, P3 fragments are more hydrophobic than Aβ peptides because a comparatively greater proportion of their sequence is embedded within the plasma membrane, yet they are less prone to aggregation. Moreover, it is worth emphasizing that APP processing yields approximately 10 times more P3 peptides than Aβ peptides. In the final stage of APP processing, the same proteolytic complex that mediates γ-secretase cleavage cleaves the remaining C-terminal fragment of APP once more at yet another site (the ε-site), thereby liberating the AICD (Fig. 1.7).

1.3.2 Discovery of *APP* mutations

The cloning of the *APP* gene represented a major breakthrough not only for the elucidation of the detailed molecular mechanisms of Aβ production, but also for the human molecular genetics of EOAD, albeit reached by a somewhat circuitous route. By 1987, families of EOAD patients had been identified that exhibited a clear autosomal-dominant pattern of transmission of the disease, and with the discovery of the *APP* gene, the race was on to identify mutations within APP in those cases. Ironically, the first *APP* mutations were discovered not in those EOAD cases, but in patients with an entirely separate but related disease called hereditary cerebral hemorrhage with angiopathy, Dutch type (HCHWA-D). In this rare bleeding disorder, blood vessels in the brain are lined with the same Aβ peptide that accumulates extracellularly in plaques in AD (44). Sequencing of the *APP* gene in these families led to the discovery of a mutation (APP E693Q) located within the Aβ sequence (45, 46). Encouraged by this seminal discovery, multiple mutations in *APP* linked to EOAD cases were discovered soon thereafter and reported in rapid succession (47-49).

The discovery of A*PP* mutations definitively linked to EOAD cases both confirmed and extended the ACH. Mechanistically, it was soon discovered that these mutations affected Aβ in several discrete ways (Fig. 1.8). Some mutations, located near the β-secretase cleavage site (e.g., the Swedish mutation), lead to increases in β-secretase activity and therefore increased the production of all Aβ peptides (50). This discovery reinforced the prior conclusion that overproduction of Aβ was critical for AD. Mutations in other regions of the Aβ sequence act by different mechanisms: rather than increasing Aβ production, many located within the central region of Aβ accelerate aggregation of the peptide (51), while others in this region decrease α-secretase processing (52). Yet other mutations located near the C-terminus of Aβ were found to affect γ-secretase activity in specific ways (53). As of today, more than 52 pathogenic A*PP*

mutations have been discovered, all located within the Aβ region of APP, along with duplications of the *APP* region of Chr. 21, that are causally linked to EOAD (Fig. 1.8). Intriguingly, other mutations have been identified that are actually protective against LOAD. As might be predicted, these mutations decrease the production of Aβ (54, 55).

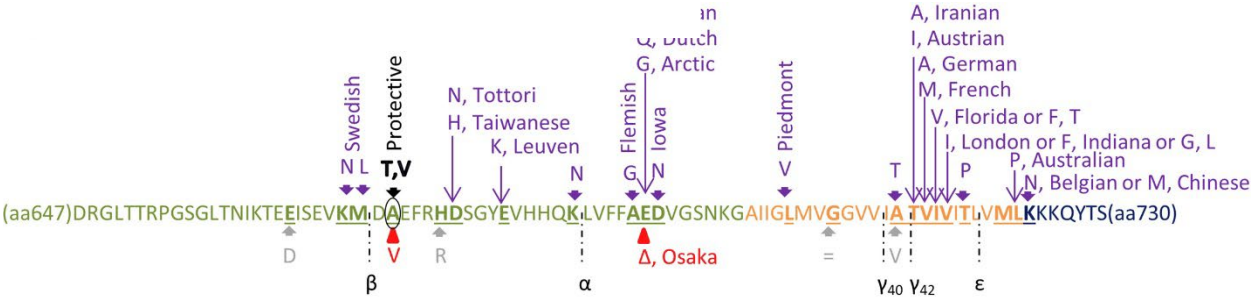

Figure 1.8. Mutations in *APP*. The Aβ region of the human APP protein illustrating the various missense mutations discovered to date. Portions of the extracellular domain (green), the transmembrane domain (orange) and the intracellular domain (dark blue) are shown. Known pathogenic mutations are depicted in purple. In red are two recessive pathogenic mutations, grey are non-pathogenic. Deltas (**Δ**) denote a deletion . Reprinted from Cacace et al., 2016 *Alzheimer Dement* with permission from John Wiley and Sons (17).

1.3.3 Discovery of presenilin mutations and elucidation of the γ-secretase complex

In 1995, Peter St. George-Hyslop and colleagues reported on the discovery of mutations linked to EOAD cases that were within an entirely new gene, dubbed "*presenilin*" (*PSEN1*) to reflect the fact that the mutations caused presenile dementia (56). Soon thereafter, a second *presenilin* gene was identified, later dubbed *presenilin-2* (*PSEN2*) that also harbored EOAD-linked mutations (57). Initially, the function of the presenilin proteins (PS1, PS2), which are multi-pass, integral membrane proteins with both the N- and C-termini located on the cytoplasmic side (see Fig. 1.9), was unknown. An early clue as to their relationship to Aβ production, however, was provided by Steve Younkin and colleagues, who reported that PS1 missense mutations result in

increases in the proportion of longer forms of Aβ, such as Aβ42, that are produced by cultured cells (53).

Michael Wolfe, Dennis Selkoe and colleagues hypothesized that presenilins might represent aspartyl proteases mediating γ-secretase cleavage, based on the unusual presence of aspartyl residues within two (normally hydrophobic) transmembrane-spanning domains. Confirming their hypothesis, mutation of these residues led to an abrogation of γ-secretase-mediated cleavage of APP, together with accumulation of APP CTFs (58). These results, together with numerous other lines of evidence, confirmed that presenilins do indeed make up the active site of what is now referred to as the γ-secretase complex, which is comprised of at least 4 proteins, either PS1 or PS2, plus nicastrin, presenilin enhancer 2, and anterior pharynx defective 1 (59).

To date, several hundred mutations have been identified within *PSEN1*, together with at least 31 within *PSEN2* (Fig. 1.9) (17). The age of onset for patients with mutations in these genes vary by the type of mutation and the affected gene, but all typically cause onset before the age of 65 (17). In terms of the mechanistic effects on Aβ, all of these pathogenic mutations have been shown to increase the proportion of longer, more amyloidogenic Aβ species, such as Aβ42, relative to shorter, less aggregation-prone species, such as Aβ40 (52, 60), confirming the initial observations by Younkin and colleagues (53). It is worth emphasizing that *presenilin* mutations are not pathogenic because they increase the overall production of Aβ, but specifically because they increase the Aβ42/40 ratio (61). Indeed, some presenilin mutations actually lower overall Aβ production (62). Hence, the Aβ42/40 ratio has emerged as one of the most critical mechanistic determinants of AD pathogenesis. Thus far, however, perturbations to this key parameter have only been observed in EOAD cases.

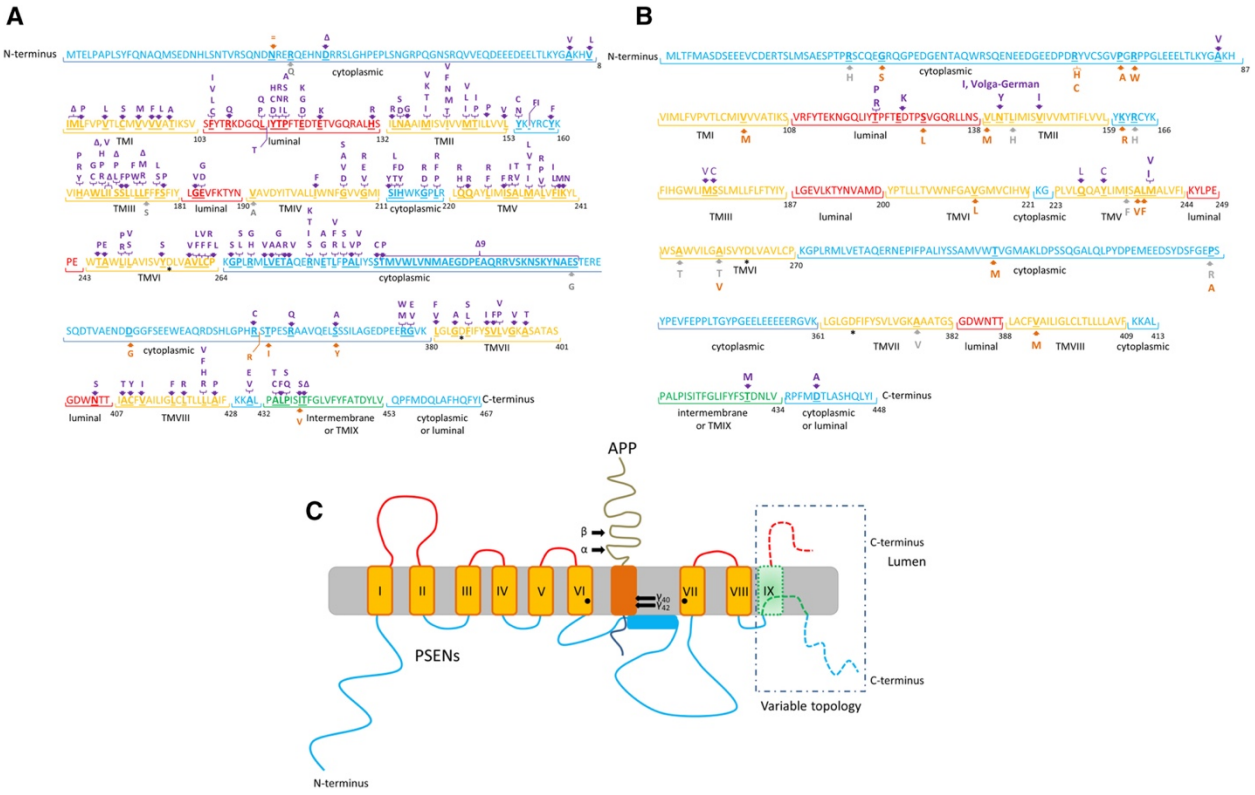

Figure 1.9. Presenilin mutations. ***A,B,*** EOAD-linked, pathogenic mutations (purple) discovered as of 2016 in *PSEN1* (***A***) and *PSEN2* (***B***)**.** ***C***, Proposed structure of presenilin proteins. Cytoplasmic domains are shown in blue, transmembrane domains in yellow, luminal domains in red, a controversial intermembrane/transmembrane domain in green. Reprinted from Cacace et al., 2016 *Alzheimer Dement* with permission from John Wiley and Sons (17).

1.3.4 Other genetic risk factors for AD

As the preceding section makes evident, EOAD is known to be caused by hundreds of different mutations located in 3 different genes, all involved in Aβ production. Is there any genetic contribution to LOAD? Despite several decades of intensive genetic research, relatively few genetic factors have been shown to contribute to LOAD risk. By far the strongest risk factor for AD so far identified is attributable to variations in the *apolipoprotein E* (ApoE) gene (*APOE*), which encodes a protein involved in cholesterol metabolism (63). Notably, the link between ApoE and AD was made in 1993 (64, 65), prior to the discovery of APP and the presenilin proteins.

Three different alleles of the *APOE* gene are present in the human population, referred to as ε2, ε3, and ε4. The different alleles have drastically different effects on AD risk. A single copy of the *APOEε4* allele increases AD risk 3-fold, while two copies increase risk 12-fold, leading to severe pathology and behavioral deficits very early in life, oftentimes around the age of 60 (66). *APOEε2*, by contrast, decreases AD risk and contributes to later age of onset (66). Unlike the autosomal-dominant mutations in *APP*, *PSEN1*, and *PSEN2*, the presence of one or more copies of the *APOEε4* allele is neither necessary nor sufficient to lead to AD (67). Although APOE's primary function involves transportation of cholesterol to glial cells, extensive work in the literature has shown that it plays a role in the clearance and aggregation of Aβ (63, 68). These lines of evidence would seem to bolster the ACH, but ApoE has more recently been implicated in the development of tau-related diseases such as frontotemporal lobe dementia (63, 69), suggesting it may play Aβ-independent roles in the pathogenesis of AD.

In addition to *APP*, *PSEN1*, *PSEN2*, and *APOE*, a growing number of genetic variants in other genes have been identified, albeit playing significantly smaller roles in LOAD risk than *APOE*. One example is *triggering receptor expressed on myeloid cells 2*, a gene that encodes a transmembrane glycoprotein involved in chronic inflammation and immune response (63, 68). Another well-studied gene is *sortilin related receptor L*, which encodes a cargo protein and regulates the direction of APP recycling and is reduced in the AD brain (66, 68, 70). Yet another interesting gene is *clusterin*, also known as apolipoprotein J, which provides a variety of functions, serving as a stress-activated regulator of cell-cell interactions, apoptosis, and lipid transport (66, 71). Many more genes beyond these are being investigated, primarily for their role in LOAD, each affecting a different aspect of AD development, as is summarized in Figure 1.10.

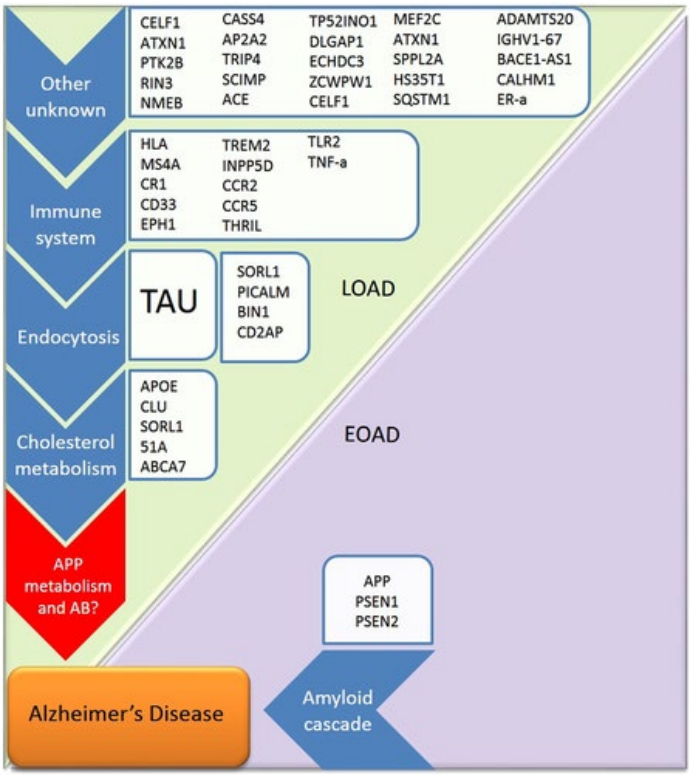

Figure 1.10. Genetic risk factors for AD. The figure shows a categorization of various genetic risk factors in AD, separated by their impact on EOAD vs. LOAD, as well as by general physiological function. Reprinted from Rezazadeh et al., 2019 *J Cell Physiol* with permission from John Wiley and Sons (63).

1.3.5 Non-genetic risk factors for AD

Risk for AD—and LOAD in particular—is not determined solely by genetics. This conclusion is confirmed by a recent, well powered twin study, which revealed that, although concordance for AD is predictably higher in monozygotic twins than in dizygotic twins (males 45% vs. 19%; females 61% vs. 41%), AD is far from being determined exclusively by genetics (68). As this section discusses, numerous factors, such as aging, vascular issues, or previous injury can drastically influence the onset, progression, and severity of AD.

Aging

In marked contrast to early-onset forms of AD, which are attributable to pathogenic mutations, LOAD emerges in the context of aging. In fact, aging is by far the most critical non-

genetic risk factor influencing the development of LOAD, with incidence of AD rising from 10% in the 70s to as high as 50% in individuals >80 years old (72). Thus, in order to fully understand the etiology of LOAD, aging itself needs to be taken into consideration, together with environmental factors that can influence it.

Aging results in a host of changes of many different kinds, ranging from the molecular to the cognitive. Even normal, healthy aging is associated with some degree of decreased working memory and short-term recall, as well as slower information processing (29). Numerous neurological changes are associated with normal aging, as well. For example, decreases in dendritic branching and loss of synaptic function and density are considered critical alterations in the aging brain, leading to issues with long-term potentiation—a proposed mechanism for memory formation—thus affecting learning (29). An accumulation of damaged DNA, perturbed cellular membranes, misfolded proteins, and oxidative stress can occur through acquired mutations, and defects in proteostasis and/or modified neurotransmitter signaling can lead to cell death (73-75). Problematically, many normal consequences of aging overlap with early signs of neurodegenerative disease pathology, including the development of extracellular Aβ deposits, the buildup of proteins within lysosomes, and accumulation of NFTs (29). Thus, many signs of a true underlying disease are matters of degree, rather than being clear-cut distinctions. Complicating things further, although a "healthy ager" may not have age-related cognitive defects, older individuals often have other health problems, some of which are known risk factors for AD, such as diabetes, heart disease/vascular issues, and obesity, which have been shown to affect numerous brain factors including inflammation and Aβ processing (76-82). These risk factors can influence, in isolation or in combination, whether or not a person switches from normal aging to "unhealthy aging" or the disease state.

Risk factors can help explain some aspects of both unhealthy aging and LOAD but can be difficult to target therapeutically or preventively. For instance, diet, exercise, and lifestyle can be manipulated both to delay the onset and treat certain symptoms of AD (19, 78, 79, 83), but can be difficult to implement and therefore is subject to low rates of compliance by patients and caretakers.

Brain injury

The rise in popularity of many high-impact sports has made brain injuries increasingly common in younger people, with an estimated 1.7 million Americans visiting the emergency room for a traumatic brain injury (TBI) every year (84). This is likely a severe underestimation of actual TBI incidents, as many people assume that only head injuries resulting in loss of consciousness require medical attention. These brain injuries, in conjunction with those acquired in older age due to a fall, a stroke, etc., can lead to drastic changes in Aβ, tau, and inflammation. There is contradictory evidence, however, about precisely how and to what extent such insults affect aging and the severity or onset of AD. In a variety of AD animal models, TBI has been shown to increase Aβ plaques, tau hyperphosphorylation, inflammation, and occasionally result in cognitive changes, leading to the conclusion that a TBI may accelerate the onset of AD (85-88). Research has confirmed that similar short-term pathological consequences of TBI occur in humans, but there is limited data showing a correlation between TBI and AD, with either no association found (89), or only a correlation in men (summarized in 84). Difficulty in analyzing this association arises due to the wide variance in the types and severity of traumas that can occur, with severe injuries likely playing a larger impact in older individuals (90) and multiple mild injuries potentially creating an additive effect that is difficult to quantify (85, 91).

One well-established short-term consequence of TBI is the acute activation of astrocytes and microglia, the immune cells of the brain, due to inflammation. Inflammation is caused by a variety of factors including TBI, ischemia, as well as injection of lipopolysaccharide (LPS), a constituent of bacterial membranes (88, 92, 93). The recruitment and activation of microglia is a particularly important component of AD, being a potentially protective response in the short-term, because microglia are typically co-localized with neuritic plaques and will release AβDPs such as CatD (see *Aspartyl AβDPs*: page 29) in response to inflammation (94-96). However, injury and disease states can also contribute to chronic inflammation, lasting months to years after injury. Rather than being protective, prolonged inflammatory responses can lead to Aβ accumulation, neuronal death, and disruption of the blood-brain barrier (BBB) (88, 97). These factors can initiate a positive-feedback loop wherein chronic inflammation activates immune cells, leading to a release of pro-inflammatory cytokines, which can stimulate γ-secretase activity and promote toxic Aβ42 production (98), making anti-inflammatory treatments a prime target for new therapeutics.

1.3.6. Aβ proteostasis: Aβ clearance and AβDPs

The ACH proposes that abnormal accumulation of Aβ is an invariant, causal feature of all AD cases, but it is critical to recognize that Aβ accumulation can occur in multiple ways besides those triggered by mutations in APP or presenilins (Fig. 1.11). Like all biogenic molecules in the body, Aβ levels are determined by the relative rates of its *production* versus its *elimination*. (Fig. 1.11). Thus, whereas many EOAD-linked genetic mutations lead to *increased production* of Aβ (total Aβ or specifically Aβ42), it is reasonable to hypothesize that *reduced elimination* of Aβ—generally and/or specifically by AβDPs—may represent the operative pathogenic mechanism in LOAD. Of special significance to this thesis, selective impairments in the degradation of Aβ42 relative to Aβ40 could also theoretically alter the Aβ42/40 ratio, which is known to be the most

critical parameter in the pathogenesis of EOAD. Given that there is no overproduction of Aβ in LOAD, but there is nevertheless an accumulation of Aβ, this is a reasonable inference. Moreover, it is worth emphasizing that aging, oxidative damage, and other deleterious environmental factors tend to *decrease* the functioning of proteases and other catabolic processes, not increase them, adding weight to the idea that defective clearance of Aβ, rather than increased production, may be a more relevant pathogenic mechanism in LOAD (99).

Until relatively recently, the idea that reduced clearance of Aβ was occurring in LOAD remained purely hypothetical, but there is some direct evidence supporting this basic idea. Mawuenyega and colleagues used metabolic labeling to conduct real-time measurements of Aβ42 and Aβ40 production and clearance rates in the central nervous system of live LOAD patients and cognitively normal controls. Their data showed that the production of these two peptides was similar in all patients, but the clearance of both Aβ42 and Aβ40 was significantly lower in LOAD patients. When comparing production and clearance, they found a 30% impairment in the clearance of Aβ in LOAD patients (100).

Aβ clearance is mediated by a large number of processes, including active and passive transport across the BBB, cell-mediated uptake, and proteolytic degradation by AβDPs (101, 102). Even though multiple clearance mechanisms are operative, it remains the case that all Aβ molecules are eventually broken down by proteases, whether extracellularly, inside cells, or outside the BBB, with the sole exception of highly aggregated Aβ molecules present in plaques.

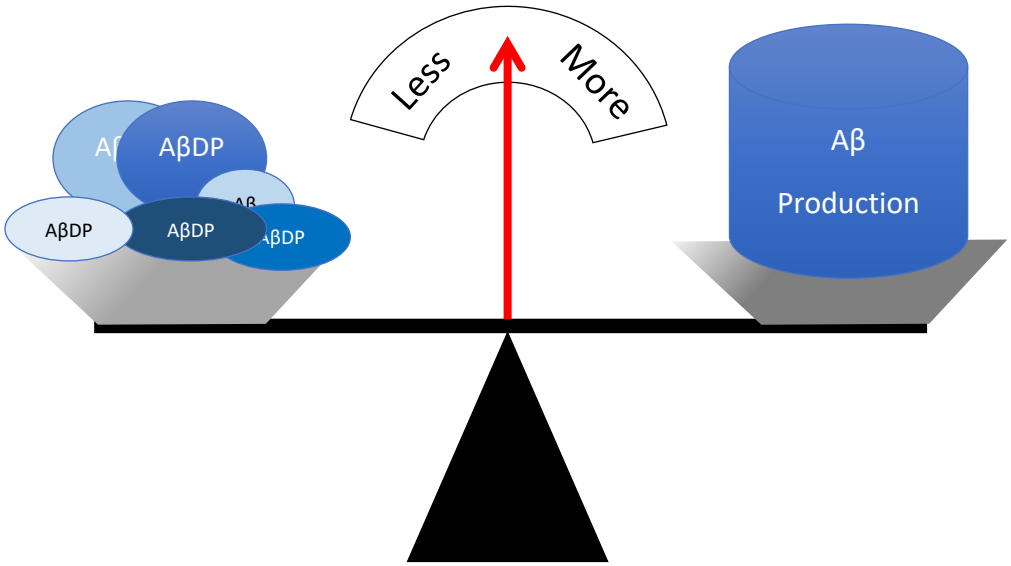

Figure 1.11. Aβ proteostasis. Cartoon illustrating the idea that Aβ proteostasis is determined by the balance between Aβ production (by secretases) and Aβ clearance (by AβDPs and other mechanisms (not shown)). Reprinted from Saido and Leissring, 2012 *Cold Spring Harb Perspect Med* with permission from Cold Harbor Laboratory Press (6).

Characteristics of AβDPs

There are number of very interesting aspects of AβDPs that deserve highlighting. First, there is a large, diverse, and growing collection of AβDPs, each with unique properties. AβDPs are thought to work in concert to eliminate Aβ, albeit not to the extent that one AβDP can fully compensate for the malfunction of another (103). Second, they operate at capacity, making many of them rate-limiting determinants of steady-state Aβ levels (99). Genetic deletion of several AβDPs causes increased Aβ in gene-dosage-dependent manner and conversely, overexpression of various AβDPs in AD transgenic mice results in reduced Aβ pathology and, in some cases, improved cognitive performance (104-113). Third, AβDPs can operate in different subcellular compartments, and thereby can both define and regulate different pools or Aβ (Table 1.1) (9). The distinct subcellular localizations of different AβDPs may help explain why Aβ and plaque levels do not correlate well with cognitive decline: certain pools of Aβ appear to be more important than

others due to differential toxicity, timing of the appearance of dysfunction, and other factors (114). Fourth, AβDPs vary in terms of their ability to degrade Aβ in different aggregation states (e.g., Aβ monomers, oligomers, protofibrils, etc.) (Fig. 1.12), meaning the loss of some AβDPs can only affect ongoing aggregation of Aβ by lowering the concentration of Aβ monomers, while others can help break down Aβ aggregates after they are formed.

Table 1.1. Subcellular location of known AβDPs. Figure shows a list of well-established AβDPs categorized by protease class and by subcellular location (9). CatB, cathepsin B; CatD, cathepsin D; ECE, endothelin-converting enzyme; IDE, insulin-degrading enzyme; MMP, matrix metalloproteinase; NEP, neprilysin; PreP, presequence protease;. Reprinted via Open Access from Leissring and Turner, 2013 *Alzheimers Res Ther*.

		Location					
Protease	**Class**	**Extracellular**	**ER/Golgi**	**Lysosomes**	**Cytosol**	**Mitochondria**	**Peroxisomes**
NEP	Metallo	+	+				
ECE-1	Metallo	+	+				
ECE-2	Metallo	+	+				
MMP-2	Metallo	+	+				
MMP-9	Metallo	+	+				
IDE	Metallo	+			+	+	+
PreP	Metallo					+	
Plasmin	Serine	+					
CatB	Cysteine	+		+			
CatD	Aspartyl			+	+		

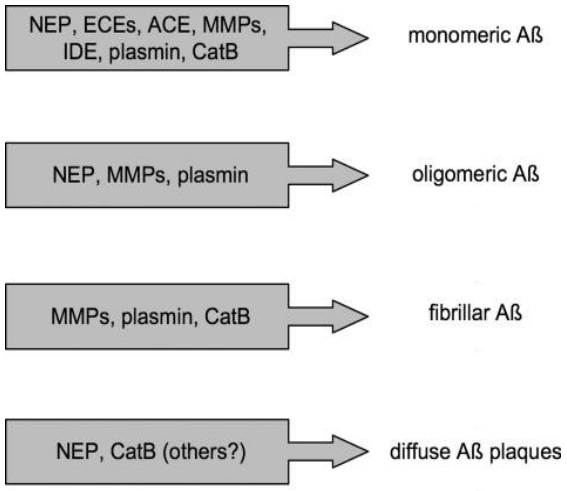

Figure 1.12. Different AβDPs degrade different aggregation states of Aβ. Note that the majority of AβDPs can degrade monomeric Aβ, but only a subset can degrade plaques (8). Reprinted via Open Access from Leissring, 2008 *J Biol Chem*.

Examples of known AβDPs

There are a wide variety of AβDPs, comprising members of several different protease classes, including metallo-, serine, cysteine, and aspartyl proteases. This section summarizes what is known about several well-characterized AβDPs.

Zinc-metalloproteases

The majority of AβDPs are zinc-metalloproteases, which can be further divided into vasopeptidases, inverzincins, and matrix-metalloproteinases (MMPs). Vasopeptidases are the most well researched of zinc metalloproteases and include many well-established AβDPs such as neprilysin (NEP) and endothelin-converting enzymes-1 and -2 (ECE1/2). These proteases are named for their ability to hydrolyze vasoactive peptides, and a particularly interesting feature is that their active site faces the extracellular space allowing the degradation of secreted Aβ. NEP, perhaps the most extensively studied AβDP, can degrade monomeric and oligomeric Aβ, as well as diffuse plaques (Fig. 1.12). Although playing an integral role in Aβ proteostasis, NEP is also involved in inflammation, cell migration and proliferation, and most critically, blood pressure

regulation. In the brain, NEP is expressed predominantly in neurons, and genetic deletion of NEP in mice results in roughly a doubling of cerebral Aβ42 levels relative to WT controls (6, 74, 103, 115). Conversely, transgenic overexpression of NEP in APP transgenic mice completely prevented Aβ plaque formation in APP transgenic mice (10). It is of special relevance to note that, whereas Aβ plaque formation is completely abrogated in the latter NEP/APP double transgenic line, these mice nevertheless still express Aβ oligomers at the same levels as APP transgenic line and, moreover, cognitive deficits are not improved by NEP overexpression (116). These results highlight the fact that different forms and/or pools of Aβ may be differentially important for AD pathology. In terms of human studies, NEP levels and activity have been found to be elevated and positively correlated to Braak stage in the AD human brain, but interestingly negatively correlated with age (112). This decrease in NEP with age is recapitulated in the 5xFAD mutant APP/PS1 transgenic mouse line with significant decreases in NEP expression at 6 and 18 months (117).

Several known AβDPs belong to a second family of zinc metalloproteases, sometimes referred to as "inverzincins" because they feature a zinc-binding motif (HxxEH) that is inverted with respect to that within most zinc-metalloproteases (HExxH) (118). The primary protease in this family is insulin-degrading enzyme (IDE), a ubiquitously expressed soluble protease that is present in the cytosol and various other subcellular compartments, but that also is exported into the extracellular space (119). IDE is the most abundant AβDP in soluble brain extracts (120), as well as in the conditioned medium of numerous cultured cells (121, 122), including primary neurons (123). This clam-shell shaped enzyme can only degrade monomeric Aβ (51) and—like all other AβDPs—is also is known to degrade several other substrates, including important physiological peptide hormones such as insulin (124) and glucagon (125). From a human molecular genetic perspective, there was considerable interest in IDE because of strong linkage of

the Chr. 10 region containing the *IDE* gene to LOAD (126, 127). Nevertheless, as is the case for most candidate LOAD risk factors, including all known AβDPs, no definitive evidence has emerged for missense or other functional mutations and LOAD to date. Due to its ability to hydrolyze both insulin and Aβ, IDE has been considered an attractive therapeutic target for both type 2 diabetes and AD (128). However, these goals are in conflict: for diabetes, the therapeutic goal would be to decrease IDE activity, whereas for AD the goal would be to increase it. Until recently, available methods for manipulating IDE were all or nothing, affecting all IDE substrates equivalently. Remarkably, however, by virtue of its unusual structure, pharmacological modulators of IDE can be substrate selective, showing different potencies against different substrates (129). Maianti and colleagues recently developed a novel substrate-selective inhibitor of IDE that potently blocks insulin degradation while leaving the hydrolysis of other IDE substrates unaffected (130). Such substrate-selective IDE modulators are attractive for therapeutic applications, most certainly, but they are equally important as pharmacological tools for disentangling the effect of IDE on different substrates. Developing additional IDE modulators selective for other substrates is a major goal pursued in this thesis (see Chapter 4, page 131).

MMPs such as MMP-2 and MMP-9 are of special interest because they have been shown to degrade both monomeric and fibrillar forms of Aβ (131). Although genetic deletion of MMPs in mice produces only minimal effects on endogenous mouse Aβ levels (132), MMPs may nevertheless be important in a pathological context: MMPs exist as proenzymes that can become activated in certain circumstances, such as in the presence of β-pleated sheet-containing proteins such as Aβ (133). There are a large number of proteases in the MMP superfamily, but only a few have been implicated as AβDPs, with the primary focus has been on MMP-2 and MMP-9 (131,

134, 135). With increasing interest in the role of inflammation in AD, MMPs may start to receive more attention, as they are well known to be expressed in astrocytes (132, 136).

Serine AβDPs

There are several serine proteases tied to Aβ proteostasis, of which plasmin is the most widely studied (137). The plasmin cascade is initiated by the action of urokinase-type plasminogen activator and tissue-type plasminogen activator (tPA), which convert plasminogen to active plasmin. Although all of these components are located within the brain, they are localized in different cell types with tPA primarily in neurons and microglia, while plasminogen is chiefly present in neurons (138). Plasmin plays roles in long-term potentiation and cognition and can degrade both monomeric and fibrillar forms of Aβ (8, 73). Plasmin is located in the extracellular space and has been found to have reduced activity in both the serum and brain of AD patients (73). Interesting work by Tucker and colleagues found that, though plasmin very efficiently clears Aβ, in a non-pathological environment the deletion of plasmin had no effect on Aβ steady-state levels (139). In contrast, when a pharmacological inhibitor of plasminogen activator inhibitor 1 (i.e., essentially an activator of plasmin) is orally delivered to APP transgenic mice, there is a significant decrease in both plasma and brain Aβ levels. Additionally, this inhibitor rescued cognitive deficits and restored long-term potentiation deficits (138). It is of interest to note that sAPP containing a Kunitz protease inhibitor domain is a potent inhibitor of plasmin (140).

Cysteine AβDPs

Of the cysteine proteases, cathepsin B (CatB), a lysosomal protease, has been definitively demonstrated to be involved in Aβ proteostasis (141). Originally thought to be an alternative β-secretase, CatB is now thought to serve a role in the control of endolysosomal APP processing, as it degrades APP C-terminal fragments as well as Aβ peptides (73). Notably, CatB has dipeptidyl

carboxypeptidase activity, which allows to progressively convert Aβ42 into Aβ40 and successively smaller species (141). CatB is one of the few AβDPs capable of cleaving both fibrils and oligomers, and is active both intracellularly, within the endolysosomal system, and extracellularly, when secreted from microglia (73, 141). Contradictorily, although CatB has been also shown to reduce Aβ levels and is thought to be protective, inhibition of CatB has also been shown to improve memory deficits and reduce Aβ levels (73).

Aspartyl AβDPs

As discussed above, the proteases responsible for Aβ production (BACE1 and the presenilin/ γsecretase- complex) are both aspartyl proteases. Several known and candidate AβDPs are also aspartyl proteases, which makes sense given that Aβ is produced in acidic compartments. One of the more interesting discoveries is that BACE2, the closest homolog of BACE1, is an avid AβDP with a catalytic efficiency exceeded only by IDE (142). BACE2 is also known to have as α–secretase-like, so called "θ-secretase" activity wherein it cleaves APP within the Aβ region, thus shuttling APP processing into the non-amyloidogenic pathway (143). Thus, BACE2 has two separate Aβ-lowering mechanisms—intriguingly, precisely the opposite function of its closest homolog BACE1, which is essential for Aβ production.

Cathepsin D (CatD) is a lysosomal aspartyl protease, within the same family as BACE1 and BACE2. Very little is known about CatD's precise role in Aβ proteostasis, beyond the fact that it cleaves Aβ40 at the same sites as BACE2 (144, 145), and that haploinsufficiency has no effect on extracellular plaque burden in APP transgenic mice (146). Intriguingly, CatD was originally a candidate for both the β- and γ-secretase (147-149), which may explain why its role in Aβ catabolism was ignored. There is a large literature dating back decades that implicates CatD dysfunction as playing a role in AD. For instance, high levels of CatD immunoreactivity were

found in senile plaques, but not in age-matched brains from control patients or in the brains of patients with different neurodegenerative disease (150). Furthermore, elevated expression was also found in degenerating neurons, and when tested, the proteases were found to be highly enzymatically active (150). Data from a separate cohort of AD patients showed increased CatD levels in portions of the neocortex responsible for cognition, with no changes in the levels of lysosomal markers (151). These and other observations likely contributed to the idea that inhibiting CatD might be warranted in AD. In terms of human molecular genetics, there is a coding, missense single-nucleotide polymorphism (SNP) in CatD (rs17571) that some groups, but not others, have linked to both early- and late-onset AD (152). More research is needed to elucidate the role of CatD, its therapeutic potential, and its potential pathogenic role in LOAD.

1.4 Mouse models of AD

The development of transgenic rodent models has been one of the most significant technological advances in science, allowing genetic manipulations that occur in a variety of human diseases to be placed in animals. However, successfully recapitulating all of the complexities of different disease states remains highly challenging, particularly with diseases like AD that have a variety of genetic and environmental components and also depend critically on aging. For the sake of brevity, this review will focus on only a few of the most widely used AD mouse models.

Progress in the development of suitable models of Aβ plaque formation was initially slow, until the generation of transgenic mice that overexpress APP containing EOAD-linked mutations. Numerous mouse models containing EOAD have been created and although there are at least 52 pathogenic *APP* mutations, 215 *PSEN1* mutations, and 31 *PSEN2* mutations (17) (Fig. 1.7 and 1.8), only 9 familial mutations have been incorporated into mouse models (Fig. 1.13) (153).

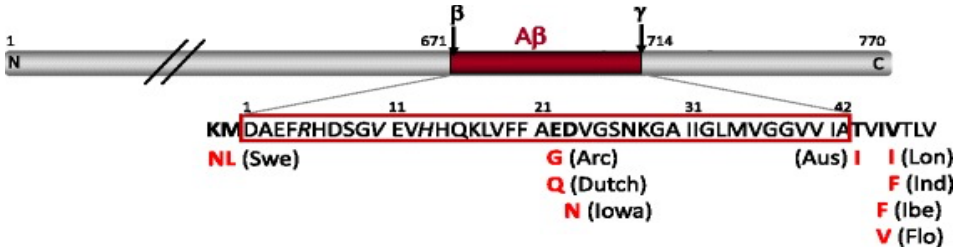

Figure 1.13. EOAD-linked mutations used in mouse models. Despite the identification of a vast number of EOAD-linked mutations, only 9 have been used to make mouse models (153). Reprinted via Open Access from Jankowsky and Zheng, 2017 *Mol Neurodegener.*

Some of the most regularly used mouse models include Tg2576, 5xFAD, and 3xTgAD. Unfortunately, no single mouse model can fully recapitulate AD. These popular models display large variations in pathology (e.g., the 3xTg-AD line models tauopathy as well as amyloidogenesis), severity, and behavioral consequences. These and most other AD mouse models have intrinsic limitations, such as a lack of significant neuronal cell death and the presence of Aβ-dependent memory defects (something not evident in humans). Most, but not all mouse models also fall short because murine Aβ (and tau) are present, which can interfere with the aggregation of human Aβ (154) (and human tau 155). Necessarily, by virtue of the presence of EOAD-linked mutations, which either increase total Aβ or the Aβ42/40 ratio, these models—at best—represent models of EOAD, but not LOAD. Another major disadvantage of almost all AD mouse models derives from the fact that they require very high levels of overexpression of APP to obtain Aβ plaques within a reasonable time frame. Thus, these models express super-physiological levels, not only of Aβ, but also of full-length APP and its many fragments, each of which has multiple known (and certainly many other unknown) functions (see Fig. 1.7).

Tg2576 line

The Tg2576 is one of the first successful transgenic mouse models developed (156). This line overexpresses human APP containing the "Swedish" double mutation (K670N/M671L) (Fig.

1.13) leading to a 5-fold increase in APP and Aβ production. The amyloid deposition is age-dependent and results in the development of large, dense, thioflavin S-positive plaques similar to those seen in AD beginning at approximately 11-13 months of age (157). However, the plaques are composed primarily of Aβ40 (158), which is interesting given that Aβ40 and Aβ42 are elevated proportionally, rather than one form over the other, keeping the ratio of Aβ42/40 the same (Elder et al. 2010). Although these mice have some impairments in short-term memory (159), these mice lack the profound cognitive impairments characterizing AD, even at old age (160). Additionally, unlike the case in AD, these cognitive problems either precede or coincide with Aβ plaques, (24) and, instead, are most closely correlated with soluble Aβ oligomers (161). Importantly, there is no documented neuronal loss or changes in synaptic density in the Tg2576 line (24). Little is known about modifications in AβDPs in this mouse line, but work by Leal and colleagues suggests that IDE serves a protective role in AD-type pathology in Tg2576 mice by increasing IDE levels in response to Aβ accumulation (162).

5xFAD line

One of the few AD mouse models to feature neuronal cell death, the 5xFAD mouse line (163) derives its name from the fact that it features 5 different EOAD-linked mutations: 3 APP mutations (Swedish K670N/M671L, Florida I716V, and London V7a7I) and 2 PS1 mutations (M146L and L286V) (12). Individually, each mutation is sufficient for Aβ accumulation but not neuronal death (160). Interestingly, the neuronal loss occurs in cortical layer 5, with 25-40% of pyramidal neurons dying between 9 and 12 months of age (12, 153). Although there is no hippocampal cell loss (12), there are impairments in long-term potentiation in the hippocampus at 6 months of age (161). 5xFAD mice develop rapid amyloid pathology beginning at 2 months of age (153), with memory deficits following at 3 months (164), and hippocampal specific

impairments around 6 months of age (161). A particularly interesting aspect of the 5xFAD line is that it recapitulates the deficits in neprilysin that are seen in AD patients (161); meanwhile CatD levels, which are normally increased in AD patients, are significantly decreased (165).

3xTg-AD

To develop a mouse line that models both amyloidogenesis and tauopathy, LaFerla and colleagues generated the 3xTgAD mouse line (166). This line was generated by co-injecting transgenes expressing APP with the Swedish mutation and tau with the P301L mutation into fertilized embryos from mice homozygous for the *PSEN1* M146V knock-in mutation (12). These mice develop increased Aβ levels, along with intracellular and extracellular Aβ accumulation, at 6 months of age, and neurofibrillary tangles at 12 months (12). This is paired with increases in inflammatory markers (12). Though this mouse line has no decrease in synapse number or density in the hippocampus (CA1) (12), there are data showing age-specific synaptic dysfunction and long-term potentiation deficits (24, 160, 167). Memory deficits and cognitive impairments are reported to start between 3 and 6 months of age (24, 164). In contrast to the previously mentioned models, the 3xTgAD mice show decreases in neprilysin, cathepsin D, and IDE (although IDE was not found to be altered by Stargardt et al., 2013) (168-171).

While each mouse model brings unique features that are useful to elucidating the various molecular and cognitive changes that occur in EOAD, there are many things to take into consideration for general extrapolations, particularly when using these mice investigating LOAD. APP overexpression leads to drastically increased levels of sAPP and Aβ, as well as all other cleavage products of APP processing, which does not occur in LOAD. Additionally, APP is almost always expressed via a heterologous promoter and so does not mimic the normal spatial and temporal expression patterns of endogenous APP, or the responsiveness of APP to various insults

(59, 153, 172). Moreover, because most AD mouse models develop plaques inexorably, often at an early age, it precludes the investigation of the triggers for AD such as aging, the most significant risk factor for LOAD. Nevertheless, designing an animal model of LOAD is challenging given that the exact cause(s) of LOAD are unknown.

1.4.1 Mouse models of LOAD

Although the development of animal models for disease states is a difficult task, a large number of genetically modified and unmodified animals have been used as AD models, ranging from monkeys (173) to beagles (174, 175) to guinea pigs (176). These models each offer a different set of benefits such as the longer life spans of monkeys and dogs, the identical Aβ peptide sequence present in guinea pigs (176), and conserved age-related memory loss in several models (29, 174, 177). Despite these benefits, it is often difficult to study AD in these animals as the expanded lifetime makes them very expensive to maintain, more difficult to control the numerous variables that can be important in the development of LOAD, and the use of more complex behavioral tasks make them harder to train.

It might be thought that an ideal mouse model for LOAD would invariably develop all aspects of AD-type pathology, including neuritic plaques, tangles, and microglial activation, and feature cognitive decline occurring only late in life. However, such a model would in fact be very limiting, because it would be impossible to investigate factors responsible for triggering AD pathology that would otherwise not develop. Moreover, mouse models that overexpress APP and/or develop Aβ pathology every early, like the 5xFAD line, make it impossible to investigate how aging contributes to AD pathogenesis. A new mouse model has been developed by the LaFerla laboratory, called the hAβ-KI mouse, which was generated in an attempt to better model LOAD in mice and offers new opportunities to explore the impact of risk factors and their interaction with

aging without the commonly used genetic mutations. The hAβ-KI line was generated by using homologous recombination to "knock in" one exon of the endogenous murine *APP* gene with a humanized version (full description of the model can be found in Chapter 2, Introduction, page 54). Because this dissertation investigates hypothetical mechanisms by which LOAD is triggered, we use the hAβ-KI line for these studies.

1.5 Conclusion

The study of AD, and LOAD in particular, is complex and made all the more difficult by the extended duration of disease, its late onset, and the multiplicity of disease pathways involved. The overarching goal of the work presented in this dissertation is to provide greater insight into the molecular mechanisms underlying LOAD, with specific emphasis on AβDPs. In Aim 1, we inhibit AβDPs as a means to manipulate Aβ levels and thereby test a specific mechanistic hypothesis about the etiology of LOAD. In Aim 2, we describe the identification and detailed characterization of a major new AβDP, CatD. Finally, in Aim 3, we develop novel pharmacological tools needed elucidate the role of IDE, a major AβDP, in the pathogenesis of LOAD.

1.6 References

1. Lane CA, Hardy J, Schott JM. Alzheimer's disease. Eur J Neurol. 2018;25(1):59-70.

2. Perl DP. Neuropathology of Alzheimer's disease. Mt Sinai J Med. 2010;77(1):32-42.

3. Hardy J, Selkoe DJ. The amyloid hypothesis of Alzheimer's disease: progress and problems on the road to therapeutics. Science. 2002;297(5580):353-6.

4. Huang YaM, L. Alzheimer mechanisms and therapeutic strategies. Cell. 2012;148(5):1204-22.

5. Barao S, Moechars D, Lichtenthaler SF, De Strooper B. BACE1 Physiological Functions May Limit Its Use as Therapeutic Target for Alzheimer's Disease. Trends Neurosci. 2016;39(3):158-69.

6. Saido T, Leissring MA. Proteolytic degradation of amyloid beta-protein. Cold Spring Harb Perspect Med. 2012;2(6):a006379.

7. Selkoe DJ. Clearing the brain's amyloid cobwebs. Neuron. 2001;32(2):177-80.

8. Leissring MA. The AbetaCs of Abeta-cleaving proteases. J Biol Chem. 2008;283(44):29645-9.

9. Leissring MA, Turner AJ. Regulation of distinct pools of amyloid beta-protein by multiple cellular proteases. Alzheimers Res Ther. 2013;5(4):37.

10. Leissring MA, Farris W, Chang AY, Walsh DM, Wu X, Sun X, et al. Enhanced proteolysis of beta-amyloid in APP transgenic mice prevents plaque formation, secondary pathology, and premature death. Neuron. 2003;40(6):1087-93.

11. Nalivaeva NN, Belyaev ND, Zhuravin IA, Turner AJ. The Alzheimer's amyloid-degrading peptidase, neprilysin: can we control it? Int J Alzheimers Dis. 2012;2012:383796.

12. Puzzo D, Gulisano W, Palmeri A, Arancio O. Rodent models for Alzheimer's disease drug discovery. Expert Opin Drug Discov. 2015;10(7):703-11.

13. Graeber MB, Kosel S, Egensperger R, Banati RB, Muller U, Bise K, et al. Rediscovery of the case described by Alois Alzheimer in 1911: historical, histological and molecular genetic analysis. Neurogenetics. 1997;1(1):73-80.

14. 2014 Alzheimer's disease facts and figures. Alzheimer's & dementia : the journal of the Alzheimer's Association. 2014;10(2):e47-92.

15. 2012 Alzheimer's disease facts and figures. Alzheimer's & dementia : the journal of the Alzheimer's Association. 2012;8(2):131-68.

16. Hebert LE, Scherr PA, Bienias JL, Bennett DA, Evans DA. Alzheimer disease in the US population: prevalence estimates using the 2000 census. Archives of neurology. 2003;60(8):1119-22.

17. Cacace R, Sleegers K, Van Broeckhoven C. Molecular genetics of early-onset Alzheimer's disease revisited. Alzheimers Dement. 2016;12(6):733-48.

18. Honig LS, Tang MX, Albert S, Costa R, Luchsinger J, Manly J, et al. Stroke and the risk of Alzheimer disease. Arch Neurol. 2003;60(12):1707-12.

19. Hu N, Yu JT, Tan L, Wang YL, Sun L, Tan L. Nutrition and the risk of Alzheimer's disease. Biomed Res Int. 2013;2013:524820.

20. 2020 Alzheimer's disease facts and figures. Alzheimer's & Dementia. 2020;16(3):391-460.

21. Sperling RA, Aisen PS, Beckett LA, Bennett DA, Craft S, Fagan AM, et al. Toward defining the preclinical stages of Alzheimer's disease: recommendations from the National Institute on Aging-Alzheimer's Association workgroups on diagnostic guidelines for Alzheimer's disease. Alzheimers Dement. 2011;7(3):280-92.

22. Lott IT, Head E. Dementia in Down syndrome: unique insights for Alzheimer disease research. Nat Rev Neurol. 2019;15(3):135-47.

23. Roberson ED, Scearce-Levie K, Palop JJ, Yan F, Cheng IH, Wu T, et al. Reducing endogenous tau ameliorates amyloid beta-induced deficits in an Alzheimer's disease mouse model. Science. 2007;316(5825):750-4.

24. Ameen-Ali KE, Wharton SB, Simpson JE, Heath PR, Sharp P, Berwick J. Review: Neuropathology and behavioural features of transgenic murine models of Alzheimer's disease. Neuropathol Appl Neurobiol. 2017;43(7):553-70.

25. Reitz C. Alzheimer's disease and the amyloid cascade hypothesis: a critical review. Int J Alzheimers Dis. 2012;2012:369808.

26. Selkoe DJ, Hardy J. The amyloid hypothesis of Alzheimer's disease at 25 years. EMBO Mol Med. 2016;8(6):595-608.

27. Scheuner D, Eckman C, Jensen M, Song X, Citron M, Suzuki N, et al. Secreted amyloid beta-protein similar to that in the senile plaques of Alzheimer's disease is increased in vivo by the presenilin 1 and 2 and APP mutations linked to familial Alzheimer's disease. Nat Med. 1996;2(8):864-70.

28. Drouet B, Pincon-Raymond M, Chambaz J, Pillot T. Molecular basis of Alzheimer's disease. Cell Mol Life Sci. 2000;57(5):705-15.

29. Yankner BA, Lu T, Loerch P. The aging brain. Annu Rev Pathol. 2008;3:41-66.

30. Terry RD, Masliah E, Salmon DP, Butters N, DeTeresa R, Hill R, et al. Physical basis of cognitive alterations in Alzheimer's disease: synapse loss is the major correlate of cognitive impairment. Ann Neurol. 1991;30(4):572-80.

31. Strydom A, Coppus A, Blesa R, Danek A, Fortea J, Hardy J, et al. Alzheimer's disease in Down syndrome: An overlooked population for prevention trials. Alzheimers Dement (N Y). 2018;4:703-13.

32. Glenner GG, Wong CW. Alzheimer's disease: initial report of the purification and characterization of a novel cerebrovascular amyloid protein. Biochem Biophys Res Commun. 1984;120(3):885-90.

33. Glenner GG, Wong CW. Alzheimer's disease and Down's syndrome: sharing of a unique cerebrovascular amyloid fibril protein. Biochem Biophys Res Commun. 1984;122(3):1131-5.

34. Kang J, Lemaire HG, Unterbeck A, Salbaum JM, Masters CL, Grzeschik KH, et al. The precursor of Alzheimer's disease amyloid A4 protein resembles a cell-surface receptor. Nature. 1987;325(6106):733-6.

35. Sandbrink R, Masters CL, Beyreuther K. APP gene family. Alternative splicing generates functionally related isoforms. Ann N Y Acad Sci. 1996;777:281-7.

36. O'Brien RJ, Wong PC. Amyloid precursor protein processing and Alzheimer's disease. Annu Rev Neurosci. 2011;34:185-204.

37. Higashi S, Miyazaki K. Identification of a region of beta-amyloid precursor protein essential for its gelatinase A inhibitory activity. J Biol Chem. 2003;278(16):14020-8.

38. Gralle M, Botelho MG, Wouters FS. Neuroprotective secreted amyloid precursor protein acts by disrupting amyloid precursor protein dimers. J Biol Chem. 2009;284(22):15016-25.

39. De Strooper B, Vassar R, Golde T. The secretases: enzymes with therapeutic potential in Alzheimer disease. Nat Rev Neurol. 2010;6(2):99-107.

40. Selkoe DJ, Yamazaki T, Citron M, Podlisny MB, Koo EH, Teplow DB, et al. The role of APP processing and trafficking pathways in the formation of amyloid beta-protein. Ann N Y Acad Sci. 1996;777:57-64.

41. Kandalepas PC, Vassar R. Identification and biology of beta-secretase. J Neurochem. 2012;120 Suppl 1:55-61.

42. Vassar R, Bennett BD, Babu-Khan S, Kahn S, Mendiaz EA, Denis P, et al. Beta-secretase cleavage of Alzheimer's amyloid precursor protein by the transmembrane aspartic protease BACE. Science. 1999;286(5440):735-41.

43. Pike CJ, Burdick D, Walencewicz AJ, Glabe CG, Cotman CW. Neurodegeneration induced by beta-amyloid peptides in vitro: the role of peptide assembly state. J Neurosci. 1993;13(4):1676-87.

44. van Duinen CM, Feldmann CT. [Minor symptoms in family practice; pityriasis versicolor]. Ned Tijdschr Geneeskd. 1990;134(7):331-3.

45. Van Broeckhoven C, Haan J, Bakker E, Hardy JA, Van Hul W, Wehnert A, et al. Amyloid beta protein precursor gene and hereditary cerebral hemorrhage with amyloidosis (Dutch). Science. 1990;248(4959):1120-2.

46. Levy E, Carman MD, Fernandez-Madrid IJ, Power MD, Lieberburg I, van Duinen SG, et al. Mutation of the Alzheimer's disease amyloid gene in hereditary cerebral hemorrhage, Dutch type. Science. 1990;248(4959):1124-6.

47. Goate A, Chartier-Harlin MC, Mullan M, Brown J, Crawford F, Fidani L, et al. Segregation of a missense mutation in the amyloid precursor protein gene with familial Alzheimer's disease. Nature. 1991;349(6311):704-6.

48. Chartier-Harlin MC, Crawford F, Houlden H, Warren A, Hughes D, Fidani L, et al. Early-onset Alzheimer's disease caused by mutations at codon 717 of the beta-amyloid precursor protein gene. Nature. 1991;353(6347):844-6.

49. Murrell J, Farlow M, Ghetti B, Benson MD. A mutation in the amyloid precursor protein associated with hereditary Alzheimer's disease. Science. 1991;254(5028):97-9.

50. Cai XD, Golde TE, Younkin SG. Release of excess amyloid beta protein from a mutant amyloid beta protein precursor. Science. 1993;259(5094):514-6.

51. Betts V, Leissring MA, Dolios G, Wang R, Selkoe DJ, Walsh DM. Aggregation and catabolism of disease-associated intra-Abeta mutations: reduced proteolysis of AbetaA21G by neprilysin. Neurobiol Dis. 2008;31(3):442-50.

52. Dimitrov M, Alattia JR, Lemmin T, Lehal R, Fligier A, Houacine J, et al. Alzheimer's disease mutations in APP but not gamma-secretase modulators affect epsilon-cleavage-dependent AICD production. Nat Commun. 2013;4:2246.

53. Suzuki N, Cheung TT, Cai XD, Odaka A, Otvos L, Jr., Eckman C, et al. An increased percentage of long amyloid beta protein secreted by familial amyloid beta protein precursor (beta APP717) mutants. Science. 1994;264(5163):1336-40.

54. Jonsson T, Atwal JK, Steinberg S, Snaedal J, Jonsson PV, Bjornsson S, et al. A mutation in APP protects against Alzheimer's disease and age-related cognitive decline. Nature. 2012;488(7409):96-9.

55. Di Fede G, Catania M, Morbin M, Rossi G, Suardi S, Mazzoleni G, et al. A recessive mutation in the APP gene with dominant-negative effect on amyloidogenesis. Science. 2009;323(5920):1473-7.

56. Sherrington R, Rogaev EI, Liang Y, Rogaeva EA, Levesque G, Ikeda M, et al. Cloning of a gene bearing missense mutations in early-onset familial Alzheimer's disease. Nature. 1995;375(6534):754-60.

57. Rogaev EI, Sherrington R, Rogaeva EA, Levesque G, Ikeda M, Liang Y, et al. Familial Alzheimer's disease in kindreds with missense mutations in a gene on chromosome 1 related to the Alzheimer's disease type 3 gene. Nature. 1995;376(6543):775-8.

58. Wolfe MS, Xia W, Ostaszewski BL, Diehl TS, Kimberly WT, Selkoe DJ. Two transmembrane aspartates in presenilin-1 required for presenilin endoproteolysis and gamma-secretase activity. Nature. 1999;398(6727):513-7.

59. Kitazawa M, Medeiros R, Laferla FM. Transgenic mouse models of Alzheimer disease: developing a better model as a tool for therapeutic interventions. Curr Pharm Des. 2012;18(8):1131-47.

60. Borchelt DR, Thinakaran G, Eckman CB, Lee MK, Davenport F, Ratovitsky T, et al. Familial Alzheimer's disease-linked presenilin 1 variants elevate Abeta1-42/1-40 ratio in vitro and in vivo. Neuron. 1996;17(5):1005-13.

61. Li N, Liu K, Qiu Y, Ren Z, Dai R, Deng Y, et al. Effect of Presenilin Mutations on APP Cleavage; Insights into the Pathogenesis of FAD. Front Aging Neurosci. 2016;8:51.

62. Saito T, Suemoto T, Brouwers N, Sleegers K, Funamoto S, Mihira N, et al. Potent amyloidogenicity and pathogenicity of Abeta43. Nat Neurosci. 2011;14(8):1023-32.

63. Rezazadeh M, Hosseinzadeh H, Moradi M, Salek Esfahani B, Talebian S, Parvin S, et al. Genetic discoveries and advances in late-onset Alzheimer's disease. J Cell Physiol. 2019.

64. Corder EH, Saunders AM, Strittmatter WJ, Schmechel DE, Gaskell PC, Small GW, et al. Gene dose of apolipoprotein E type 4 allele and the risk of Alzheimer's disease in late onset families. Science. 1993;261(5123):921-3.

65. Cosentino S, Scarmeas N, Helzner E, Glymour MM, Brandt J, Albert M, et al. APOE epsilon 4 allele predicts faster cognitive decline in mild Alzheimer disease. Neurology. 2008;70(19 Pt 2):1842-9.

66. Karch CM, Goate AM. Alzheimer's disease risk genes and mechanisms of disease pathogenesis. Biol Psychiatry. 2015;77(1):43-51.

67. Yamazaki Y, Painter MM, Bu G, Kanekiyo T. Apolipoprotein E as a Therapeutic Target in Alzheimer's Disease: A Review of Basic Research and Clinical Evidence. CNS Drugs. 2016;30(9):773-89.

68. Nicolas G, Charbonnier C, Campion D. From Common to Rare Variants: The Genetic Component of Alzheimer Disease. Hum Hered. 2016;81(3):129-41.

69. Small SA, Duff K. Linking Abeta and tau in late-onset Alzheimer's disease: a dual pathway hypothesis. Neuron. 2008;60(4):534-42.

70. Rogaeva E, Meng Y, Lee JH, Gu Y, Kawarai T, Zou F, et al. The neuronal sortilin-related receptor SORL1 is genetically associated with Alzheimer disease. Nat Genet. 2007;39(2):168-77.

71. Rezazadeh M, Hosseinzadeh H, Moradi M, Salek Esfahani B, Talebian S, Parvin S, et al. Genetic discoveries and advances in late-onset Alzheimer's disease. J Cell Physiol. 2019;234(10):16873-84.

72. Alzheimer's A. 2012 Alzheimer's disease facts and figures. Alzheimers Dement. 2012;8(2):131-68.

73. Nalivaeva NN, Beckett C, Belyaev ND, Turner AJ. Are amyloid-degrading enzymes viable therapeutic targets in Alzheimer's disease? J Neurochem. 2012;120 Suppl 1:167-85.

74. Turner AJ, Fisk L, Nalivaeva NN. Targeting amyloid-degrading enzymes as therapeutic strategies in neurodegeneration. Ann N Y Acad Sci. 2004;1035:1-20.

75. Wyss-Coray T. Ageing, neurodegeneration and brain rejuvenation. Nature. 2016;539(7628):180-6.

76. de Bruijn RF, Ikram MA. Cardiovascular risk factors and future risk of Alzheimer's disease. BMC Med. 2014;12:130.

77. de la Torre JC. How do heart disease and stroke become risk factors for Alzheimer's disease? Neurol Res. 2006;28(6):637-44.

78. Imtiaz B, Tolppanen AM, Kivipelto M, Soininen H. Future directions in Alzheimer's disease from risk factors to prevention. Biochem Pharmacol. 2014;88(4):661-70.

79. Kilian J, Kitazawa M. The emerging risk of exposure to air pollution on cognitive decline and Alzheimer's disease - Evidence from epidemiological and animal studies. Biomed J. 2018;41(3):141-62.

80. Purnell C, Gao S, Callahan CM, Hendrie HC. Cardiovascular risk factors and incident Alzheimer disease: a systematic review of the literature. Alzheimer Dis Assoc Disord. 2009;23(1):1-10.

81. Sahathevan R, Brodtmann A, Donnan GA. Dementia, stroke, and vascular risk factors; a review. Int J Stroke. 2012;7(1):61-73.

82. Verdile G, Keane KN, Cruzat VF, Medic S, Sabale M, Rowles J, et al. Inflammation and Oxidative Stress: The Molecular Connectivity between Insulin Resistance, Obesity, and Alzheimer's Disease. Mediators Inflamm. 2015;2015:105828.

83. Xu W, Tan L, Wang HF, Jiang T, Tan MS, Tan L, et al. Meta-analysis of modifiable risk factors for Alzheimer's disease. J Neurol Neurosurg Psychiatry. 2015;86(12):1299-306.

84. Plassman BL, Grafman J. Traumatic brain injury and late-life dementia. Handb Clin Neurol. 2015;128:711-22.

85. Winston CN, Noel A, Neustadtl A, Parsadanian M, Barton DJ, Chellappa D, et al. Dendritic Spine Loss and Chronic White Matter Inflammation in a Mouse Model of Highly Repetitive Head Trauma. Am J Pathol. 2016;186(3):552-67.

86. Villapol S, Loane DJ, Burns MP. Sexual dimorphism in the inflammatory response to traumatic brain injury. Glia. 2017;65(9):1423-38.

87. Kay AD, Petzold A, Kerr M, Keir G, Thompson E, Nicoll JA. Alterations in cerebrospinal fluid apolipoprotein E and amyloid beta-protein after traumatic brain injury. J Neurotrauma. 2003;20(10):943-52.

88. Glushakova OY, Johnson D, Hayes RL. Delayed increases in microvascular pathology after experimental traumatic brain injury are associated with prolonged inflammation, blood-brain barrier disruption, and progressive white matter damage. J Neurotrauma. 2014;31(13):1180-93.

89. Dams-O'Connor K, Gibbons LE, Bowen JD, McCurry SM, Larson EB, Crane PK. Risk for late-life re-injury, dementia and death among individuals with traumatic brain injury: a population-based study. J Neurol Neurosurg Psychiatry. 2013;84(2):177-82.

90. Johnson VE, Stewart W. Age at injury influences dementia risk after TBI. Nature Reviews. 2015;11:128-30.

91. Edwards G, 3rd, Moreno-Gonzalez I, Soto C. Amyloid-beta and tau pathology following repetitive mild traumatic brain injury. Biochem Biophys Res Commun. 2017;483(4):1137-42.

92. Pluta R, Furmaga-Jablonska W, Maciejewski R, Ulamek-Koziol M, Jablonski M. Brain ischemia activates beta- and gamma-secretase cleavage of amyloid precursor protein: significance in sporadic Alzheimer's disease. Mol Neurobiol. 2013;47(1):425-34.

93. Wendeln AC, Degenhardt K, Kaurani L, Gertig M, Ulas T, Jain G, et al. Innate immune memory in the brain shapes neurological disease hallmarks. Nature. 2018;556(7701):332-8.

94. Lowry JR, Klegeris A. Emerging roles of microglial cathepsins in neurodegenerative disease. Brain Res Bull. 2018;139:144-56.

95. Sheng JG, Bora SH, Xu G, Borchelt DR, Price DL, Koliatsos VE. Lipopolysaccharide-induced-neuroinflammation increases intracellular accumulation of amyloid precursor protein and amyloid beta peptide in APPswe transgenic mice. Neurobiol Dis. 2003;14(1):133-45.

96. Nakanishi H. Neuronal and microglial cathepsins in aging and age-related diseases. Ageing Res Rev. 2003;2(4):367-81.

97. Qin L, Wu X, Block ML, Liu Y, Breese GR, Hong JS, et al. Systemic LPS causes chronic neuroinflammation and progressive neurodegeneration. Glia. 2007;55(5):453-62.

98. Breunig JJ, Guillot-Sestier MV, Town T. Brain injury, neuroinflammation and Alzheimer's disease. Front Aging Neurosci. 2013;5:26.

99. Leissring MA. Proteolytic degradation of the amyloid beta-protein: the forgotten side of Alzheimer's disease. Curr Alzheimer Res. 2006;3(5):431-5.

100. Mawuenyega KG, Sigurdson W, Ovod V, Munsell L, Kasten T, Morris JC, et al. Decreased clearance of CNS beta-amyloid in Alzheimer's disease. Science. 2010;330(6012):1774.

101. Kline A. Apolipoprotein E, amyloid-ss clearance and therapeutic opportunities in Alzheimer's disease. Alzheimers Res Ther. 2012;4(4):32.

102. Leissring MA. Abeta-Degrading Proteases: Therapeutic Potential in Alzheimer Disease. CNS Drugs. 2016;30(8):667-75.

103. Eckman EA, Adams SK, Troendle FJ, Stodola BA, Kahn MA, Fauq AH, et al. Regulation of steady-state beta-amyloid levels in the brain by neprilysin and endothelin-converting enzyme but not angiotensin-converting enzyme. J Biol Chem. 2006;281(41):30471-8.

104. Spencer B, Marr RA, Rockenstein E, Crews L, Adame A, Potkar R, et al. Long-term neprilysin gene transfer is associated with reduced levels of intracellular Abeta and behavioral improvement in APP transgenic mice. BMC Neurosci. 2008;9:109.

105. Marr RA, Rockenstein E, Mukherjee A, Kindy MS, Hersh LB, Gage FH, et al. Neprilysin gene transfer reduces human amyloid pathology in transgenic mice. J Neurosci. 2003;23(6):1992-6.

106. Iwata N, Tsubuki S, Takaki Y, Shirotani K, Lu B, Gerard NP, et al. Metabolic regulation of brain Abeta by neprilysin. Science. 2001;292(5521):1550-2.

107. Farris W, Schutz SG, Cirrito JR, Shankar GM, Sun X, George A, et al. Loss of neprilysin function promotes amyloid plaque formation and causes cerebral amyloid angiopathy. Am J Pathol. 2007;171(1):241-51.

108. Farris W, Mansourian S, Leissring MA, Eckman EA, Bertram L, Eckman CB, et al. Partial loss-of-function mutations in insulin-degrading enzyme that induce diabetes also impair degradation of amyloid beta-protein. Am J Pathol. 2004;164(4):1425-34.

109. Farris W, Mansourian S, Chang Y, Lindsley L, Eckman EA, Frosch MP, et al. Insulin-degrading enzyme regulates the levels of insulin, amyloid beta-protein, and the beta-amyloid precursor protein intracellular domain in vivo. Proc Natl Acad Sci U S A. 2003;100(7):4162-7.

110. Wang DS, Dickson DW, Malter JS. beta-Amyloid degradation and Alzheimer's disease. J Biomed Biotechnol. 2006;2006(3):58406.

111. Miners JS, Barua N, Kehoe PG, Gill S, Love S. Abeta-degrading enzymes: potential for treatment of Alzheimer disease. J Neuropathol Exp Neurol. 2011;70(11):944-59.

112. Miners JS, Baig S, Tayler H, Kehoe PG, Love S. Neprilysin and insulin-degrading enzyme levels are increased in Alzheimer disease in relation to disease severity. J Neuropathol Exp Neurol. 2009;68(8):902-14.

113. Madani R, Poirier R, Wolfer DP, Welzl H, Groscurth P, Lipp HP, et al. Lack of neprilysin suffices to generate murine amyloid-like deposits in the brain and behavioral deficit in vivo. J Neurosci Res. 2006;84(8):1871-8.

114. LaFerla FM, Green KN, Oddo S. Intracellular amyloid-beta in Alzheimer's disease. Nat Rev Neurosci. 2007;8(7):499-509.

115. Holma KM, Melartin TK, Holma IA, Paunio T, Isometsa ET. Family history of psychiatric disorders and the outcome of psychiatric patients with DSM-IV major depressive disorder. J Affect Disord. 2011;131(1-3):251-9.

116. Meilandt WJ, Cisse M, Ho K, Wu T, Esposito LA, Scearce-Levie K, et al. Neprilysin overexpression inhibits plaque formation but fails to reduce pathogenic Abeta oligomers and associated cognitive deficits in human amyloid precursor protein transgenic mice. J Neurosci. 2009;29(7):1977-86.

117. Devi L, Ohno M. Mechanisms that lessen benefits of beta-secretase reduction in a mouse model of Alzheimer's disease. Transl Psychiatry. 2013;3:e284.

118. Becker AB, Roth RA. An unusual active site identified in a family of zinc metalloendopeptidases. Proc Natl Acad Sci U S A. 1992;89(9):3835-9.

119. Zhao J, Li L, Leissring MA. Insulin-degrading enzyme is exported via an unconventional protein secretion pathway. Mol Neurodegener. 2009;4:4.

120. McDermott JR, Gibson AM. Degradation of Alzheimer's beta-amyloid protein by human and rat brain peptidases: involvement of insulin-degrading enzyme. Neurochem Res. 1997;22(1):49-56.

121. Chesneau V, Vekrellis K, Rosner MR, Selkoe DJ. Purified recombinant insulin-degrading enzyme degrades amyloid beta-protein but does not promote its oligomerization. Biochem J. 2000;351 Pt 2:509-16.

122. Qiu WQ, Walsh DM, Ye Z, Vekrellis K, Zhang J, Podlisny MB, et al. Insulin-degrading enzyme regulates extracellular levels of amyloid beta-protein by degradation. J Biol Chem. 1998;273(49):32730-8.

123. Newman MM, Feminella JW, Liles MR. Purification of genomic DNA extracted from environmental sources for use in a polymerase chain reaction. Cold Spring Harb Protoc. 2010;2010(2):pdb prot5383.

124. Suire CN, Nainar S, Fazio M, Kreutzer AG, Paymozd-Yazdi T, Topper CL, et al. Peptidic inhibitors of insulin-degrading enzyme with potential for dermatological applications discovered via phage display. PLoS One. 2018;13(2):e0193101.

125. Suire CN, Lane S, Leissring MA. Development and Characterization of Quantitative, High-Throughput-Compatible Assays for Proteolytic Degradation of Glucagon. SLAS Discov. 2018;23(10):1060-9.

126. Bertram L, Blacker D, Mullin K, Keeney D, Jones J, Basu S, et al. Evidence for genetic linkage of Alzheimer's disease to chromosome 10q. Science. 2000;290(5500):2302-3.

127. Myers A, Holmans P, Marshall H, Kwon J, Meyer D, Ramic D, et al. Susceptibility locus for Alzheimer's disease on chromosome 10. Science. 2000;290(5500):2304-5.

128. Maianti JP, McFedries A, Foda ZH, Kleiner RE, Du XQ, Leissring MA, et al. Anti-Diabetic Activity of Insulin-Degrading Enzyme Inhibitors Mediated by Multiple Hormones. Nature. 2014;511:94-8.

129. Abdul-Hay SO, Lane AL, Caulfield TR, Claussin C, Bertrand J, Masson A, et al. Optimization of peptide hydroxamate inhibitors of insulin-degrading enzyme reveals marked substrate-selectivity. J Med Chem. 2013;56(6):2246-55.

130. Maianti JP, Tan GA, Vetere A, Welsh AJ, Wagner BK, Seeliger MA, et al. Substrate-Selective Inhibitors that Reprogram the Activity of Insulin-Degrading Enzyme. Nat Chem Biol. 2019;15:565-74.

131. Yan P, Hu X, Song H, Yin K, Bateman RJ, Cirrito JR, et al. Matrix metalloproteinase-9 degrades amyloid-beta fibrils in vitro and compact plaques in situ. J Biol Chem. 2006;281(34):24566-74.

132. Yin KJ, Cirrito JR, Yan P, Hu X, Xiao Q, Pan X, et al. Matrix metalloproteinases expressed by astrocytes mediate extracellular amyloid-beta peptide catabolism. J Neurosci. 2006;26(43):10939-48.

133. Miners JS, Baig S, Palmer J, Palmer LE, Patrick PG, Love S. Clearance of Aß from the Brain in Alzheimer’s Disease: Aß-degrading Enzymes in Alzheimer’s Disease. Brain Pathol. 2008;18(2).

134. Liao MC, Van Nostrand WE. Degradation of soluble and fibrillar amyloid beta-protein by matrix metalloproteinase (MT1-MMP) in vitro. Biochemistry. 2010;49(6):1127-36.

135. Roher AE, Kasunic TC, Woods AS, Cotter RJ, Ball MJ, Fridman R. Proteolysis of A beta peptide from Alzheimer disease brain by gelatinase A. Biochem Biophys Res Commun. 1994;205(3):1755-61.

136. Nirzhor SSR, Khan RI, Neelotpol S. The Biology of Glial Cells and Their Complex Roles in Alzheimer's Disease: New Opportunities in Therapy. Biomolecules. 2018;8(3).

137. Van Nostrand WE, Davis J, Previti ML, Xu F. Clearance of amyloid-beta protein deposits in transgenic mice following focal cerebral ischemia. Neurodegener Dis. 2012;10(1-4):108-11.

138. Jacobsen JS, Comery TA, Martone RL, Elokdah H, Crandall DL, Oganesian A, et al. Enhanced clearance of Abeta in brain by sustaining the plasmin proteolysis cascade. Proc Natl Acad Sci U S A. 2008;105(25):8754-9.

139. Tucker HM, Simpson J, Kihiko-Ehmann M, Younkin LH, McGillis JP, Younkin SG, et al. Plasmin deficiency does not alter endogenous murine amyloid beta levels in mice. Neurosci Lett. 2004;368(3):285-9.

140. Van Nostrand WE, Schmaier AH, Neiditch BR, Siegel RS, Raschke WC, Sisodia SS, et al. Expression, purification, and characterization of the Kunitz-type proteinase inhibitor domain of the amyloid beta-protein precursor-like protein-2. Biochim Biophys Acta. 1994;1209(2):165-70.

141. Mueller-Steiner S, Zhou Y, Arai H, Roberson ED, Sun B, Chen J, et al. Antiamyloidogenic and neuroprotective functions of cathepsin B: implications for Alzheimer's disease. Neuron. 2006;51(6):703-14.

142. Abdul-Hay SO, Sahara T, McBride M, Kang D, Leissring MA. Identification of BACE2 as an avid ss-amyloid-degrading protease. Mol Neurodegener. 2012;7:46.

143. Sun X, He G, Song W. BACE2, as a novel APP theta-secretase, is not responsible for the pathogenesis of Alzheimer's disease in Down syndrome. FASEB J. 2006;20(9):1369-76.

144. McDermott JR, Gibson AM. Degradation of Alzheimer's beta-amyloid protein by human cathepsin D. Neuroreport. 1996;7(13):2163-6.

145. Hamazaki H. A beta-amyloid peptide variant related with familial Alzheimer's disease and hereditary cerebral hemorrhage with amyloidosis is poorly eliminated by cathepsin D. FEBS Lett. 1996;397(2-3):313-5.

146. Cheng S, Wani WY, Hottman DA, Jeong A, Cao D, LeBlanc KJ, et al. Haplodeficiency of Cathepsin D does not affect cerebral amyloidosis and autophagy in APP/PS1 transgenic mice. J Neurochem. 2017;142(2):297-304.

147. Evin G, Cappai R, Li QX, Culvenor JG, Small DH, Beyreuther K, et al. Candidate gamma-secretases in the generation of the carboxyl terminus of the Alzheimer's disease beta A4 amyloid: possible involvement of cathepsin D. Biochemistry. 1995;34(43):14185-92.

148. Higaki J, Catalano R, Guzzetta AW, Quon D, Nave JF, Tarnus C, et al. Processing of beta-amyloid precursor protein by cathepsin D. J Biol Chem. 1996;271(50):31885-93.

149. Thompson A, Grueninger-Leitch F, Huber G, Malherbe P. Expression and characterization of human beta-secretase candidates metalloendopeptidase MP78 and cathepsin D in beta APP-overexpressing cells. Brain Res Mol Brain Res. 1997;48(2):206-14.

150. Cataldo AM, Nixon RA. Enzymatically active lysosomal proteases are associated with amyloid deposits in Alzheimer brain. Proc Natl Acad Sci U S A. 1990;87(10):3861-5.

151. Chai YL, Chong JR, Weng J, Howlett D, Halsey A, Lee JH, et al. Lysosomal cathepsin D is upregulated in Alzheimer's disease neocortex and may be a marker for neurofibrillary degeneration. Brain Pathol. 2019;29(1):63-74.

152. Vidoni C, Follo C, Savino M, Melone MA, Isidoro C. The Role of Cathepsin D in the Pathogenesis of Human Neurodegenerative Disorders. Med Res Rev. 2016;36(5):845-70.

153. Jankowsky JL, Zheng H. Practical considerations for choosing a mouse model of Alzheimer's disease. Mol Neurodegener. 2017;12(1):89.

154. Kim J, Onstead L, Randle S, Price R, Smithson L, Zwizinski C, et al. Abeta40 inhibits amyloid deposition in vivo. J Neurosci. 2007;27(3):627-33.

155. Ando K, Leroy K, Heraud C, Yilmaz Z, Authelet M, Suain V, et al. Accelerated human mutant tau aggregation by knocking out murine tau in a transgenic mouse model. Am J Pathol. 2011;178(2):803-16.

156. Hsiao K, Chapman P, Nilsen S, Eckman C, Harigaya Y, Younkin S, et al. Correlative memory deficits, Abeta elevation, and amyloid plaques in transgenic mice. Science. 1996;274(5284):99-102.

157. Kawarabayashi T, Younkin LH, Saido TC, Shoji M, Ashe KH, Younkin SG. Age-dependent changes in brain, CSF, and plasma amyloid (beta) protein in the Tg2576 transgenic mouse model of Alzheimer's disease. J Neurosci. 2001;21(2):372-81.

158. Saito T, Saido TC. Neuroinflammation in mouse models of Alzheimer's disease. Clin Exp Neuroimmunol. 2018;9(4):211-8.

159. Kotilinek LA, Bacskai B, Westerman M, Kawarabayashi T, Younkin L, Hyman BT, et al. Reversible memory loss in a mouse transgenic model of Alzheimer's disease. J Neurosci. 2002;22(15):6331-5.

160. Elder GA, Gama Sosa MA, De Gasperi R. Transgenic mouse models of Alzheimer's disease. Mt Sinai J Med. 2010;77(1):69-81.

161. Ohno M. Alzheimer's therapy targeting the beta-secretase enzyme BACE1: Benefits and potential limitations from the perspective of animal model studies. Brain Res Bull. 2016;126(Pt 2):183-98.

162. Leal MC, Dorfman VB, Gamba AF, Frangione B, Wisniewski T, Castano EM, et al. Plaque-associated overexpression of insulin-degrading enzyme in the cerebral cortex of aged transgenic tg2576 mice with Alzheimer pathology. J Neuropathol Exp Neurol. 2006;65(10):976-87.

163. Jawhar S, Trawicka A, Jenneckens C, Bayer TA, Wirths O. Motor deficits, neuron loss, and reduced anxiety coinciding with axonal degeneration and intraneuronal Abeta aggregation in the 5XFAD mouse model of Alzheimer's disease. Neurobiol Aging. 2012;33(1):196 e29-40.

164. Webster SJ, Bachstetter AD, Nelson PT, Schmitt FA, Van Eldik LJ. Using mice to model Alzheimer's dementia: an overview of the clinical disease and the preclinical behavioral changes in 10 mouse models. Front Genet. 2014;5:88.

165. Avrahami L, Farfara D, Shaham-Kol M, Vassar R, Frenkel D, Eldar-Finkelman H. Inhibition of glycogen synthase kinase-3 ameliorates beta-amyloid pathology and restores lysosomal acidification and mammalian target of rapamycin activity in the Alzheimer disease mouse model: in vivo and in vitro studies. J Biol Chem. 2013;288(2):1295-306.

166. Oddo S, Caccamo A, Shepherd JD, Murphy MP, Golde TE, Kayed R, et al. Triple-transgenic model of Alzheimer's disease with plaques and tangles: intracellular Abeta and synaptic dysfunction. Neuron. 2003;39(3):409-21.

167. Martini AC, Forner S, Trujillo-Estrada L, Baglietto-Vargas D, LaFerla FM. Past to Future: What Animal Models Have Taught Us About Alzheimer's Disease. J Alzheimers Dis. 2018;64(s1):S365-S78.

168. Stargardt A, Gillis J, Kamphuis W, Wiemhoefer A, Kooijman L, Raspe M, et al. Reduced amyloid-beta degradation in early Alzheimer's disease but not in the APPswePS1dE9 and 3xTg-AD mouse models. Aging Cell. 2013;12(3):499-507.

169. Billings LM, Green KN, McGaugh JL, LaFerla FM. Learning decreases A beta*56 and tau pathology and ameliorates behavioral decline in 3xTg-AD mice. J Neurosci. 2007;27(4):751-61.

170. Hirata-Fukae C, Li HF, Hoe HS, Gray AJ, Minami SS, Hamada K, et al. Females exhibit more extensive amyloid, but not tau, pathology in an Alzheimer transgenic model. Brain Res. 2008;1216:92-103.

171. Zhang ZH, Wu QY, Zheng R, Chen C, Chen Y, Liu Q, et al. Selenomethionine Mitigates Cognitive Decline by Targeting Both Tau Hyperphosphorylation and Autophagic Clearance in an Alzheimer's Disease Mouse Model. J Neurosci. 2017;37(9):2449-62.

172. Sasaguri H, Nilsson P, Hashimoto S, Nagata K, Saito T, De Strooper B, et al. APP mouse models for Alzheimer's disease preclinical studies. EMBO J. 2017;36(17):2473-87.

173. Lourenco MV, Clarke JR, Frozza RL, Bomfim TR, Forny-Germano L, Batista AF, et al. TNF-alpha mediates PKR-dependent memory impairment and brain IRS-1 inhibition induced by Alzheimer's beta-amyloid oligomers in mice and monkeys. Cell Metab. 2013;18(6):831-43.

174. Cummings BJ, Su JH, Cotman CW, White R, Russell MJ. Beta-amyloid accumulation in aged canine brain: a model of early plaque formation in Alzheimer's disease. Neurobiol Aging. 1993;14(6):547-60.

175. Head E. A canine model of human aging and Alzheimer's disease. Biochim Biophys Acta. 2013;1832(9):1384-9.

176. Sharman MJ, Moussavi Nik SH, Chen MM, Ong D, Wijaya L, Laws SM, et al. The Guinea Pig as a Model for Sporadic Alzheimer's Disease (AD): The Impact of Cholesterol Intake on Expression of AD-Related Genes. PLoS One. 2013;8(6):e66235.

177. Lai ZC, Moss MB, Killiany RJ, Rosene DL, Herndon JG. Executive system dysfunction in the aged monkey: spatial and object reversal learning. Neurobiol Aging. 1995;16(6):947-54.

CHAPTER 2

AIM 1

2.1 Background

Historically, research on the molecular pathogenesis of Alzheimer disease (AD) has been focused primarily on two aspects of amyloid β-protein (Aβ) proteostasis: its production and its aggregation (1). The emphasis on these two topics was justified based on human molecular genetic findings showing that AD-linked mutations in *APP*, *PSEN1*, and *PSEN2* affect both of these factors (2). Moreover, these discoveries provided substantial support for the amyloid cascade hypothesis (ACH), which proposes that excessive Aβ accumulation plays an invariant, causal role in AD pathogenesis, being the most upstream event triggering all other aspects of AD (3-5). Although the mechanisms of Aβ production and aggregation are critical for understanding the pathogenesis of all AD cases, as well as for developing potential therapies, what was left unanswered was the question of what causes the vast majority of late-onset AD (LOAD) cases that do not involve mutations affecting these aspects of Aβ homeostasis. Beginning in the mid- to late-1990s, it became clear that Aβ production and aggregation are not the sole factors regulating Aβ proteostasis. Rather, Aβ levels are determined by the balance between Aβ production and clearance, the latter of which can occur through activity by Aβ-degrading proteases (AβDPs) and other catabolic pathways (6, 7). This more holistic view of Aβ proteostasis immediately suggests an alternative mechanism for the etiology of LOAD: decreased clearance of Aβ. Although Aβ can be cleared from the brain in several ways (e.g., via active or passive transport across the blood-brain barrier (BBB)), it is speculated that a primary method of Aβ removal is through AβDPs (8). Consequently, dysfunction of AβDPs could be operative in many—possibly even most—cases of LOAD. This idea is supported by the literature in a variety of ways. For instance, direct

quantification of the rates of Aβ production and degradation in living LOAD patients, obtained by monitoring the incorporation of labeled amino acids into Aβ in real time, showed that Aβ clearance, rather than overproduction, is occurring in LOAD (9). Furthermore, ApoE, the most important genetic risk factor for LOAD, has been shown to regulate Aβ degradation in microglia (10) and astrocytes (11) as well as to mediate the trafficking of extracellular Aβ into the lysosome of neurons (12). Levels of neprilysin, a major AβDP, have been found to be decreased in both AD brains and cognitively normal control aged brains, with a significant negative correlation between neprilysin and insoluble Aβ levels in both groups (14, 15). Importantly, these decreases have been found in brain regions particularly important in AD such as the hippocampus (15). Likewise, cathepsin D (CatD), a lysosomal AβDP that is highly abundant in microglia, has decreased activity in AD brains (16, 17). On the other hand, two other AβDPs, matrix-metalloproteinase-2 and -9 (MMP-2, MMP-9) have been shown to be upregulated after traumatic brain injury (TBI), an AD risk factor, and are associated with early inflammation (18-22). MMP-9 in particular has been shown to be elevated as early as three hours after a TBI; in MMP-9 KO mice, researchers have found less disruption of the BBB, decreased motor behavioral deficits, and smaller brain lesion volume (18-22). Similarly, yet another pair of AβDPs, endothelin-converting enzymes-1 and -2 (ECE-1,ECE-2) have also been found to be upregulated following injuries such as a TBI or stroke (23). Taken together, these reports show that individual AβDPs respond differently to known AD risk factors, but several show reduced activity, which is expected if dysfunction of AβDPs plays a causal role in LOAD pathogenesis. Nevertheless, the more general hypothesis that Aβ clearance is impaired in LOAD is bolstered by the observation of deficiencies in the degradation of CSF Aβ in LOAD patients (9) as well as of age-associated alterations in AβDP levels in AD patients (14, 24).

In what follows, we present experimental findings produced from two projects that explore whether risk factors for LOAD can, in the absence of mutations that cause early-onset AD (EOAD), affect Aβ accumulation, potentially via modulation of AβDP activity. We first investigated the acute effects of TBI on Aβ in the absence of *APP* mutations (Aim 1A), followed by a long-term project on how an early, transient increase in Aβ, induced by pharmacological inhibition of AβDPs, interacts with aging in a novel model of LOAD (Aim 1B).

2.2 Aims and rationale

Aim 1A: Effects of TBI on cerebral Aβ levels in a novel mouse model of LOAD

Rationale & Hypothesis: It is hypothesized that transient increases in Aβ represent a common mechanism linking different AD risk factors, including TBI, transient ischemic stroke, and potentially other acute brain trauma. Mechanistically, we hypothesize that trauma-induced increases in Aβ may arise as a result of defects in AβDPs, and that these increases in Aβ occur irrespective of the presence of EOAD-linked mutations, such that they could be operative in LOAD. Regardless of the precise mechanism involved, if our hypothesis is confirmed, it follows that blocking Aβ production immediately after one of these acute risk factors could serve a protective role against the development of AD-type pathology later in life. This Aim focuses exclusively on TBI.

Aim 1B: Is a transient increase in Aβ early in life, triggered by inhibiting AβDPs, sufficient to trigger AD-type pathology later in life in a mouse model of LOAD?

Rationale & Hypothesis: It is hypothesized that a transient increase in Aβ early in life is sufficient to trigger AD pathogenesis later in life, in the absence of AD-linked mutations or overproduction

of Aβ. We hypothesize that transient increases in Aβ represent a common mechanism linking different AD risk factors, such as traumatic brain injury (TBI).

2.3 Unpublished work:

Transient increases in Aβ as a potential trigger for the pathogenesis of LOAD

2.3.1 Abstract

Current research investigating the etiology of Alzheimer disease (AD) has focused primarily on the molecular pathogenesis of rare forms of early-onset AD (EOAD) attributable to autosomal-dominant mutations, which in all cases have been found to affect the *production* of an aggregation-prone peptide known as the amyloid β-protein (Aβ). The causes of late-onset AD (LOAD), on the other hand, remain poorly understood, apart from the identification of certain genetic and environmental factors affecting AD risk. This proposal explores the overall hypothesis that LOAD can be triggered by transient increases in Aβ occurring early in life, as the result of various known risk-factors for AD. In this project, we use a novel mouse model for LOAD, known as the hAβ-KI line, in which gene targeting was used to convert the Aβ region of the amyloid precursor protein gene (*APP*) from the murine form to the more amyloidogenic human form of Aβ. The resulting mice faithfully model the biological milieu present in LOAD, allowing us to examine how the brain responds to various insults in the absence of genetic mutations in *APP* or other genes linked to early-onset AD (EOAD). We successfully demonstrate that a closed-head TBI triggers an acute increase in Aβ, including the formation of fibrillar deposits of Aβ by 3 days after injury, while also triggering activation and migration of glial cells. These results closely resemble what occurs following TBI in humans, and therefore validate the hAβ-KI line as a useful model of LOAD. These findings are consistent with the hypothesis that acute increases in Aβ

arising early in life might represent a common molecular mechanism among TBI and other AD risk factors for triggering the full spectrum of AD pathology later in life, in the context of an aging brain.

2.3.2 Introduction

The effort to elucidate the etiology of LOAD is complicated by the fact that there are a multitude of environmental risk factors that, unhelpfully, are likely to interact in complex ways both with one another and with the greatest known risk factor—aging. As posited by the amyloid cascade hypothesis (ACH), perturbed Aβ proteostasis is a critical pathological process in AD, representing the most upstream event that subsequently triggers a cascade of pathological sequelae, including inflammation, tau hyperphosphorylation and, ultimately, neuronal cell death. Given that Aβ deposits are present in cognitively normal aged individuals, some Aβ deposition is clearly not inherently toxic. Hence, there must be some trigger or critical threshold, involving Aβ, that converts a person from the disease-free state to LOAD.

We hypothesize that transient increases in Aβ, induced by any of a variety of insults, represents the common Aβ-dependent molecular mechanism that triggers LOAD. As Aβ concentrations rise, its rate of aggregation increases. Thus, mechanistically, we propose that transient rises in Aβ levels trigger Aβ aggregation once they exceed a certain critical threshold concentration (Fig. 2.1). Once irreversible aggregates of Aβ are formed, they can "seed" the formation of larger aggregates, as is well established (25, 26). Thus, transient rises in Aβ occurring early in life, even if they are modest in amount, could result in pathological accumulation of Aβ later in life as aggregation of the "seeds" continues over the span of decades (Fig. 2.1).

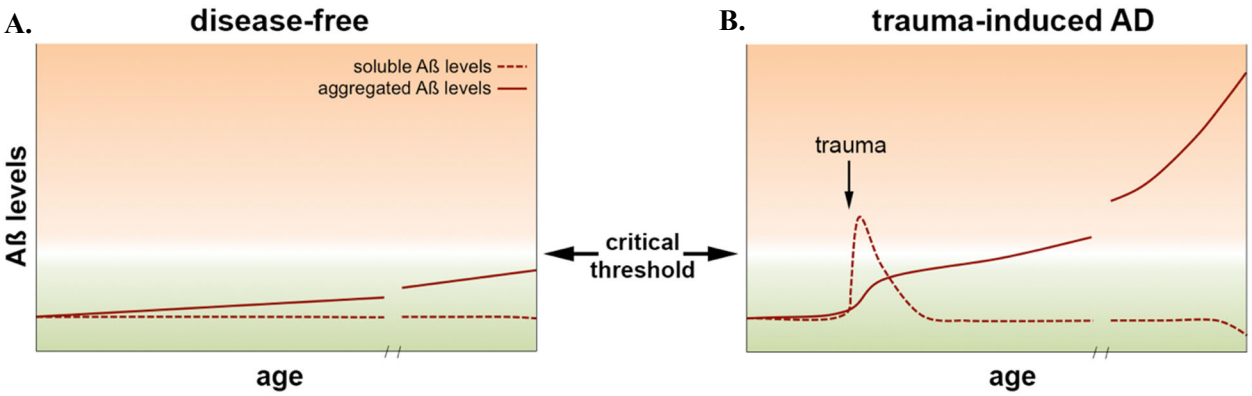

Figure 2.1. Hypothetical mechanism for the pathogenesis of LOAD. Cartoon illustrating several concepts underlying the hypothesis that will be tested in Aim 1. ***A***, In disease-free individuals, soluble Aβ levels (dashed line) remain steady across the lifetime, and insoluble Aβ levels (solid line) accumulate only slowly, never surpassing a hypothesized *critical threshold* (arrows, center) for the initiation of LOAD. ***B***, As a hypothesized mechanism for triggering LOAD, trauma induces a transient rise in soluble Aβ levels (dashed line) that surpass the critical threshold, and thereby trigger Aβ accumulation, causing insoluble Aβ levels (solid line) to increase and, over time, surpass the critical threshold for onset of LOAD.

This hypothesis is supported by the finding that insults such as TBI or stroke increase the risk for developing LOAD (27, 28). TBI, more commonly known as a concussion, is often viewed as a risk factor for AD and a common problem in aged individuals, but the current literature contains many contradictory lines of evidence, with some agreeing that TBI is, indeed, a real risk factor for altered cognition with aging (29, 30). On the other hand, other results suggest that TBI is not an *independent* risk factor, but instead merely accelerates ongoing aging and disease processes within the brain (31-33). Despite disagreements about the precise role of TBI in LOAD onset, there is strong evidence showing rapid elevation in Aβ accumulation and glial activation in humans shortly following a TBI (hours to days) (34-37). Numerous studies in AD mouse models have shown that these injuries trigger a transient increase in Aβ, which returns to basal levels shortly after injury (30, 38, 39) (Fig. 2.1). Though only transient, a substantial increase in Aβ can result in long-lasting cognitive and pathological sequelae (33, 40, 41). However, it is important to

emphasize that most of the mouse models used in the latter studies featured high levels of overexpression of APP via heterologous promoters, usually in the presence of EOAD-linked mutations. These features are not present in humans, and so can confound, amplify, or obscure the true effects of a TBI on endogenous Aβ levels. Additionally, in animal modeling studies, inflammation, a major component of AD pathology that can be triggered by Aβ increases, is differentially increased after TBI in an age-associated manner (41, 42). For example, work by Morin and colleagues has found that decreasing inflammation can improve recovery after TBI, identifying Aβ-induced inflammation as a critical element (43). In addition, other research has revealed significant sex differences in the short-term response to brain injury, wherein males have increased inflammation and pro-inflammatory cytokine release, while females seem to be protected against cell death (44, 45).

To investigate whether transient increases in Aβ per se are sufficient to trigger LOAD, it is critical to design experiments in which Aβ levels represent the independent variable, with downstream pathological sequelae representing the dependent variables. For the experiments in Aim 1B, we elected to increase cerebral Aβ levels by pharmacological inhibition of Aβ degradation. To that end, we elected to use phosphoramidon, a broad-spectrum metalloprotease inhibitor that targets several major AβDPs, which primarily regulate extracellular pools of Aβ (Table. 2.1). As discussed in Chapter 1, many of the AβDPs inhibited by phosphoramidon can degrade not only monomeric Aβ, but also oligomeric, fibrillar, and diffuse aggregates of Aβ. Notably, in a study by Eckman and colleagues, i.c.v. infusion of phosphoramidon for just two hours resulted in as much as a 5-fold increase in Aβ levels in WT mice (Fig. 2.2A), and a >2-fold increase in an AD mouse model (Tg2576) (Fig. 2.2B) (46).

Table 2.1. Multiple AβDPs are inhibited by phosphoramidon. Highlighted (yellow) are well-established AβDPs known to be inhibited by phosphoramidon. Note that all are localized in the extracellular space and the lumen of the endoplasmic reticulum (47). Reprinted via Open Access from Leissring and Turner, 2013 *Alzheimers Res Ther*.

Protease	Class	Location					
		Extracellular	ER/Golgi	Lysosomes	Cytosol	Mitochondria	Peroxisomes
NEP	Metallo	+	+				
ECE-1	Metallo	+	+				
ECE-2	Metallo	+	+				
MMP-2	Metallo	+	+				
MMP-9	Metallo	+	+				
IDE	Metallo	+			+	+	+
PreP	Metallo					+	
Plasmin	Serine	+					
CatB	Cysteine	+		+			
CatD	Aspartyl			+	+		

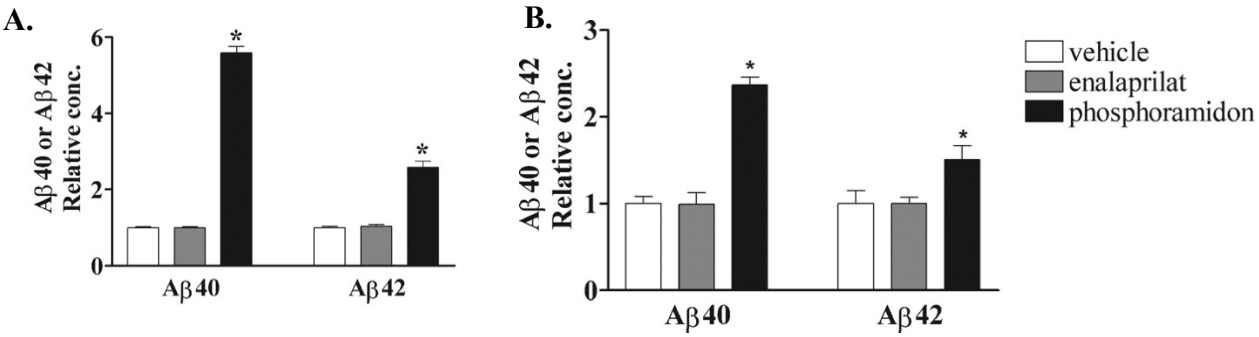

Figure 2.2. Effects of i.c.v administration of phosphoramidon on Aβ levels. Data show the levels of cerebral Aβ in WT (***A***) or Tg2576 (***B***) mice after i.c.v. infusion for 2 hours with: phosphoramidon (black bars; (***A)*** n=3; (***B)*** n=5); the angiotensin-converting enzyme (ACE) inhibitor, enalaprilat (grey bars; (***A)*** n=7; (***B)*** n=6); or vehicle only (white bars; normalized to 1; (***A)*** n=5; (***B)*** n=8). Note the dramatic increase in both Aβ40 and Aβ42 levels after phosphoramidon treatment in both WT and Tg2576 mice (46). ***(A)*** **P*< 0.0001; (***B)*** Aβ40 **P* 0.0001; Aβ42 **P*=0.04. Reprinted from Eckman et al., 2013 with permission from the American Soc for Biochemistry & Molecular Biology.

In this Aim we sought to interrogate the role of transient increases in Aβ as a common mechanism in risk factors for LOAD, questions that would be confounded by the use of common mouse models such as TG2576 that contain EOAD-linked mutations and develop AD-type

pathology inexorably. A new mouse model developed by the LaFerla laboratory, hAβ-KI, was generated in an attempt to better model LOAD in mice. The hAβ-KI line was generated by using homologous recombination to "knock in" (replace) one exon of the endogenous murine *APP* gene with a slightly modified version that "humanizes" the Aβ region by introducing 3 mutations that convert the mouse Aβ amino acid sequence to the wild-type human sequence (Fig. 2.3A). By virtue of this design, the resulting mouse line expresses human, wild-type Aβ at physiological levels under the endogenous promoter, exhibiting stable expression up to 22 months of age (Fig. 2.3B). Although this model develops modest increases in Aβ with age (Appendix A Fig. S2.1), importantly, there are no changes to the Aβ42/40 ratios (Fig. 2.4) or development of neuritic plaques up to 22 months of age. Interestingly, the LaFerla laboratory detected the presence of Aβ fibrils, beginning in 10-month-old animals, which were associated with astrocytes (there was no evidence of microglial activation) (Appendix A Fig. S2.2). Together, the characteristics of this model make it ideal for investigating triggers of LOAD that might initiate pathological Aβ accumulation later in life, in the context of aging, specifically in the absence of other factors (e.g., EOAD-linked mutations) that precipitate amyloidogenesis on their own.

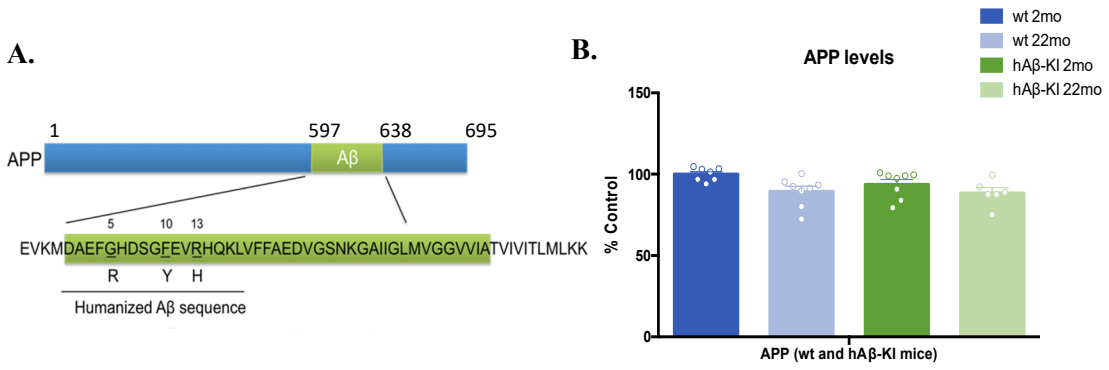

Figure 2.3. hAβ-KI mouse model of LOAD. ***A***, Cartoon showing the 3 amino acids mutated to convert murine Aβ to human Aβ in hAβ-KI mice. ***B***, APP levels in hAβ-KI mice are comparable to those in wild-type (wt) animals and are stable across a wide range of ages (Baglietto-Vargas et al., submitted).

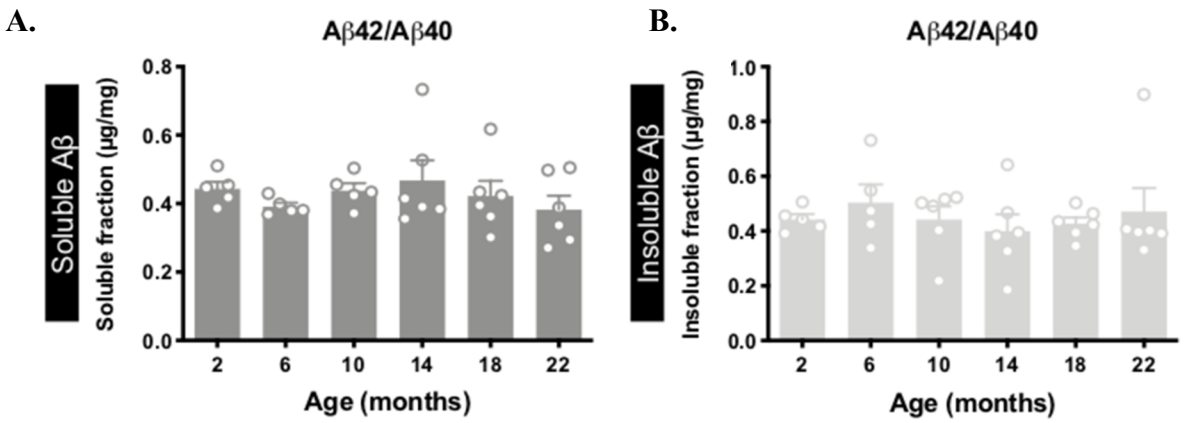

Figure 2.4. Consistent Aβ42/40 ratios in the hAβ-KI mouse model ***A***, ***B***, Aβ42/40 levels in hAβ-KI mice are stable over time. (Baglietto-Vargas et al., submitted).

Collectively, these results indicate that the hAβ-KI mouse model faithfully mimics the biological context in which LOAD emerges—i.e., with endogenous levels of human Aβ expressed via the endogenous *APP* promoter in the absence of EOAD-linked mutations. These features make this model appropriate for the study of risk factors that may cause or depend on transient increases in Aβ levels, whether due to changes in production or its clearance.

This study had two primary goals, investigating two independent hypotheses. The first hypothesis (Aim 1A) was that a known risk factor for AD, TBI, will trigger a transient increase in Aβ in the hAβ-KI mouse model of LOAD, as occurs in humans. To that end, TBI was administered to hAβ-KI mice, and Aβ levels and associated pathology were assessed before and 1 to 3 days after TBI. The second hypothesis (Aim 1B) was that a transient increase in Aβ administered early in life (mimicking an AD-risk factor like TBI) would be sufficient to trigger AD-type pathology later in life in the hAβ-KI model of LOAD. To that end, young hAβ-KI mice were administered either vehicle or phosphoramidon i.c.v. for 4 weeks, then the effects were examined immediately

afterward or at 15 and 22 months of age. In addition, in an attempt to rule out Aβ-independent effects of phosphoramidon, the γ-secretase inhibitor begacestat, which blocks on-going Aβ production (48), was co-administered to one half of both the phosphoramidon and control groups.

2.3.3 Results

Aim 1A.

Literature in the AD field using traditional AD mouse models has generally shown that immediately after TBI there is a transient (6 hours to 3 days) increase in Aβ levels, which returns to baseline levels shortly (3 to 7 days) after injury (49, 50). However, many of these animal models employ transgenic overexpression (and/or ectopic expression) of APP using heterologous promoters, which could drive increases in Aβ in non-physiological ways. It is therefore critical to first test whether TBI can trigger acute rises in Aβ in the hAβ-KI LOAD model, which expresses physiological levels of wild-type human Aβ under the control of the endogenous *APP* promoter. To that end, we administered a severe closed-head impact (sCHI) to 6-month-old hAβ-KI male and female mice, and tissues were collected 1- and 3-days post injury (1DPI, 3DPI), as well as from mice not receiving an impact (0DPI), but undergoing all other aspects of the procedure, including anesthetization. Figure 2.5 provides an overview of the experimental design.

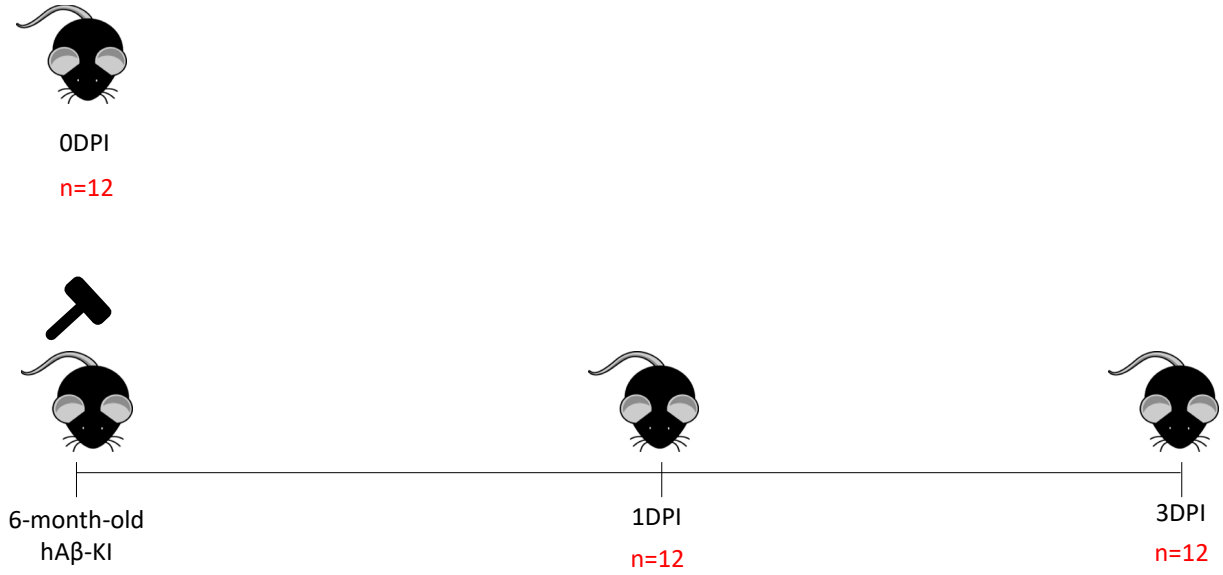

Sex/Timepoint	0DPI	1DPI	3DPI
Male	n=6	n=6	n=6
Female	n=6	n=6	n=6

Figure 2.5. Timeline for the experiments in Aim 1A. Cartoon illustrating the overall timeline (top) as well as the number male and female animals per group (bottom). DPI = days post-injury.

After collection, soluble and insoluble fractions of Aβ were extracted then quantified using a multiplex assay that simultaneously quantifies levels of Aβ38, Aβ40 and Aβ42 (Meso Scale Diagnostics (MSD); Rockland, MD). sCHI triggered acute increases in total soluble Aβ, with elevations in soluble Aβ42/40 (and Aβ42/38) ratios (Fig. 2.6A-C), together with corresponding decreases in both total insoluble Aβ and Aβ42/40 ratio (Fig. 2.6D-E).

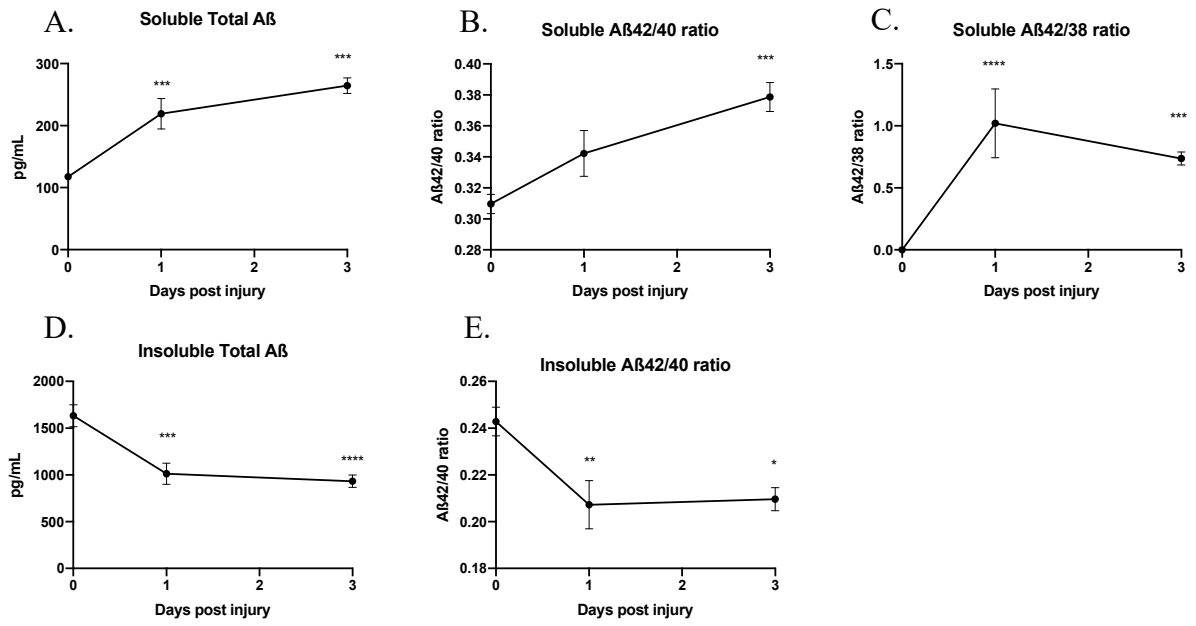

Figure 2.6. Effects of sCHI on cerebral Aβ in hAβ-KI mice. ***A-C***, sCHI triggered a significant increase in total soluble Aβ both 1- and 3-days following injury (***A***), along with corresponding increases in Aβ42/40 (***B***) and Aβ42/38 (***C***) ratios. ***D, E***, sCHI triggered a significant decrease in insoluble Aβ following injury (***D***), along with a decrease in the insoluble Aβ42/40 ratio (***E***). Note that Aβ42/38 ratios are not shown because this Aβ species does not typically form insoluble deposits. Data are mean ± SEM for 12 replicates per group. *$P< 0.05$; ** $P< 0.01$; *** $P< 0.001$; **** $P< 0.0001$.

Many studies of TBI in rodent models focus exclusively on males, as sexual dimorphisms in the brain have frequently led to conflicting results, owing in part to the protective effect of female hormones in injury (44, 51). We therefore analyzed whether females and males had differing responses to the injury in this study. As can be seen in Figures 2.7A and D, sCHI triggered an elevation in total soluble Aβ that was more prominent in females than in males 1DPI, although this did not affect the Aβ42/40 or Aβ42/38 ratios (Figs. 2.7B-C, E-F). Interestingly, in the case of total insoluble Aβ, both females and males exhibit a rapid drop in insoluble Aβ post injury (Figs. 2.8A, C), but a parallel decrease in Aβ42/40 ratios occurs two days earlier in females than it does in males (Figs. 2.8B, D).

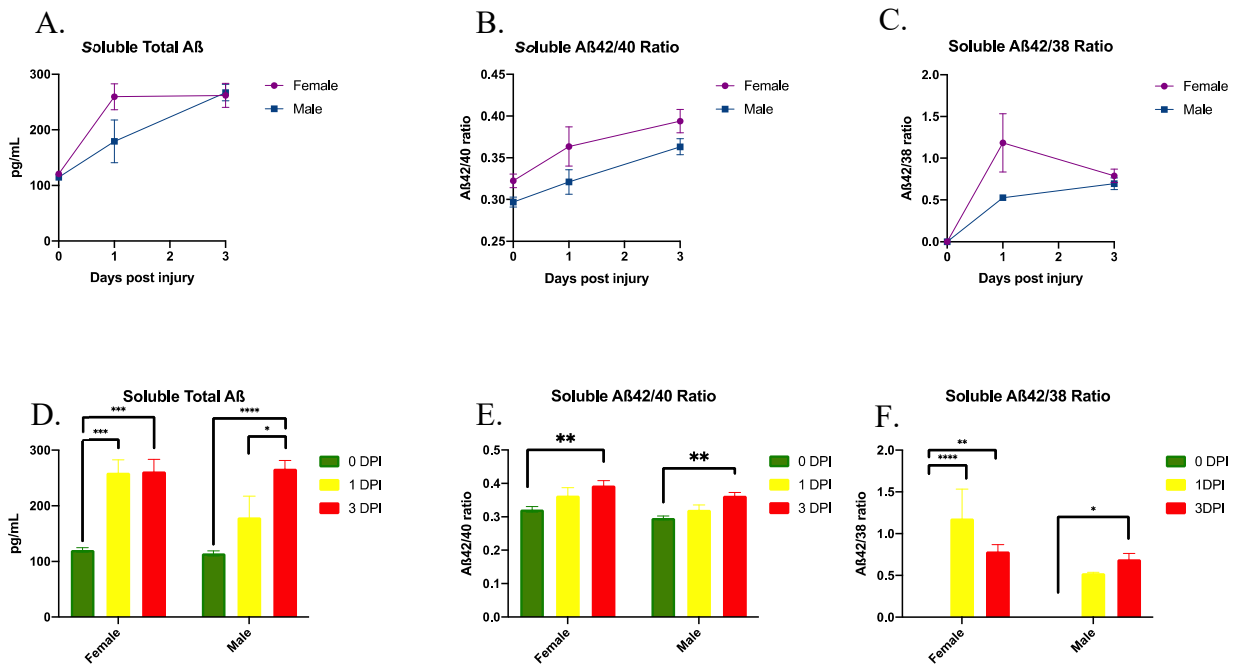

Figure 2.7. Effects of sCHI on soluble Aβ in male *vs.* female hAβ-KI mice. ***A-C***, Effects of sCHI on total soluble Aβ (***A***) as well as Aβ42/40 (***B***) and Aβ42/38 (***B***) ratios as a function of time in male and female mice. Note that there are no significant differences between sexes (as opposed to between time points). ***D-F***, Data in ***A-C*** graphed individually for each sex to demonstrate significant time-dependent changes. Data are mean ± SEM for 6 replicates per group. *$P< 0.05$; ** $P< 0.01$; *** $P< 0.001$; ****$P< 0.0001$.

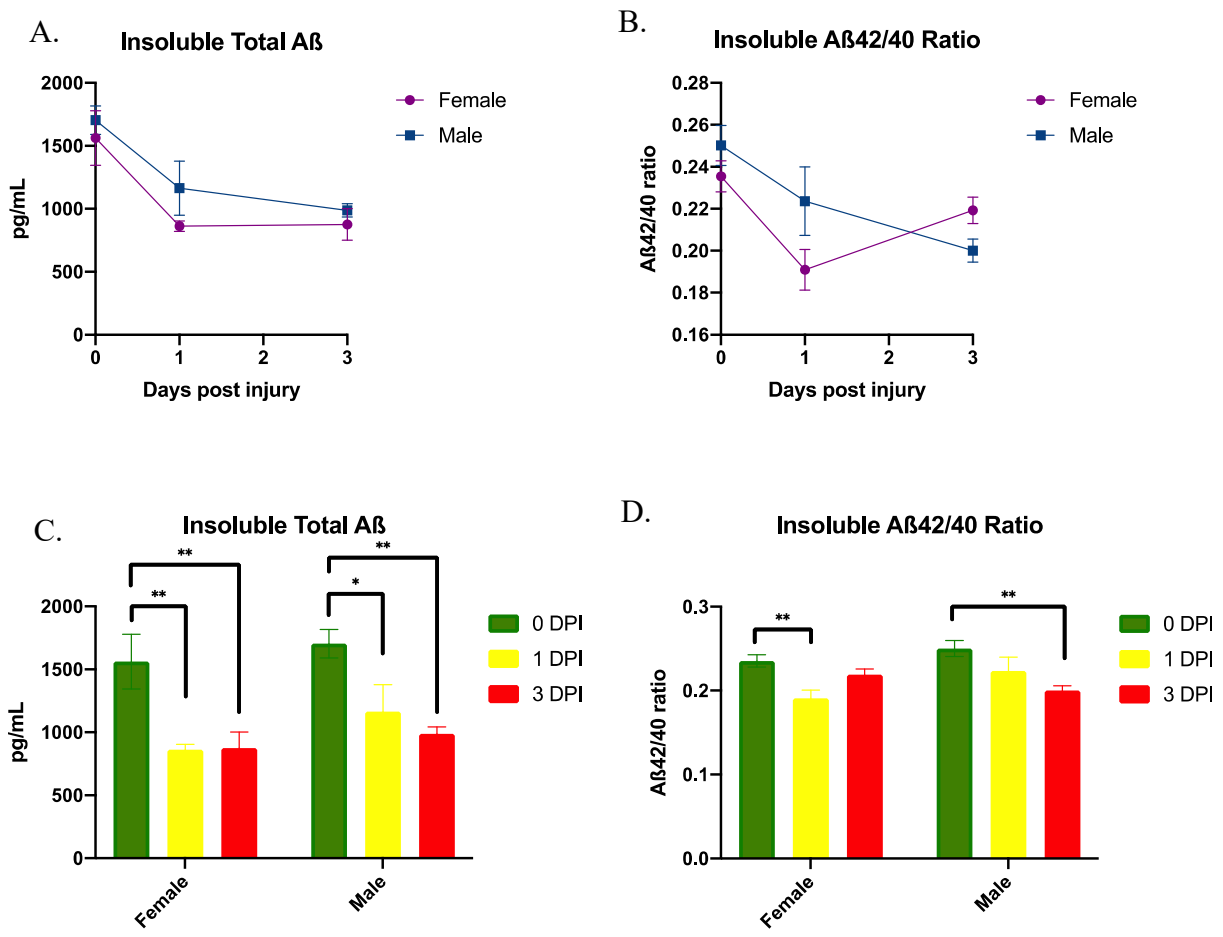

Figure 2.8. Effects of sCHI on insoluble Aβ in male *vs.* female hAβ-KI mice. ***A-B***, Effects of sCHI on total insoluble Aβ (***A***) as well as insoluble Aβ42/40 ratios(***B***) as a function of time in male and female mice. Note that Aβ42/38 ratios are not shown because this Aβ species does not typically form insoluble deposits. Note that there are no significant differences between sexes (as opposed to between time points). ***C,D***, Data in ***A*** and ***B*** graphed individually for each sex to demonstrate significant time-dependent changes. Data are mean ± SEM for 6 replicates per group. *$P< 0.05$; ** $P< 0.01$.

Upon closer examination of individual Aβ species, at 1DPI (but not 3DPI) we found no significant differences between males and females in the levels of soluble Aβ38 (Fig. 2.9A,D) or Aβ40 (Fig. 2.9B, E), but there was a significant between-sex difference for soluble Aβ42 (Fig. 2.9 C, F), with Aβ42 being significantly higher in females. Analysis of insoluble Aβ species shows that the change in female insoluble Aβ42/40 ratios reflects drops in both Aβ40 and Aβ42, whereas

the decrease in male insoluble Aβ42/40 ratios is primarily due to a change in Aβ42 levels (Fig. 2.10 A-D). Due to the limited duration and size of this initial study, these observations should be considered preliminary; however, we believe these data warrant further investigation.

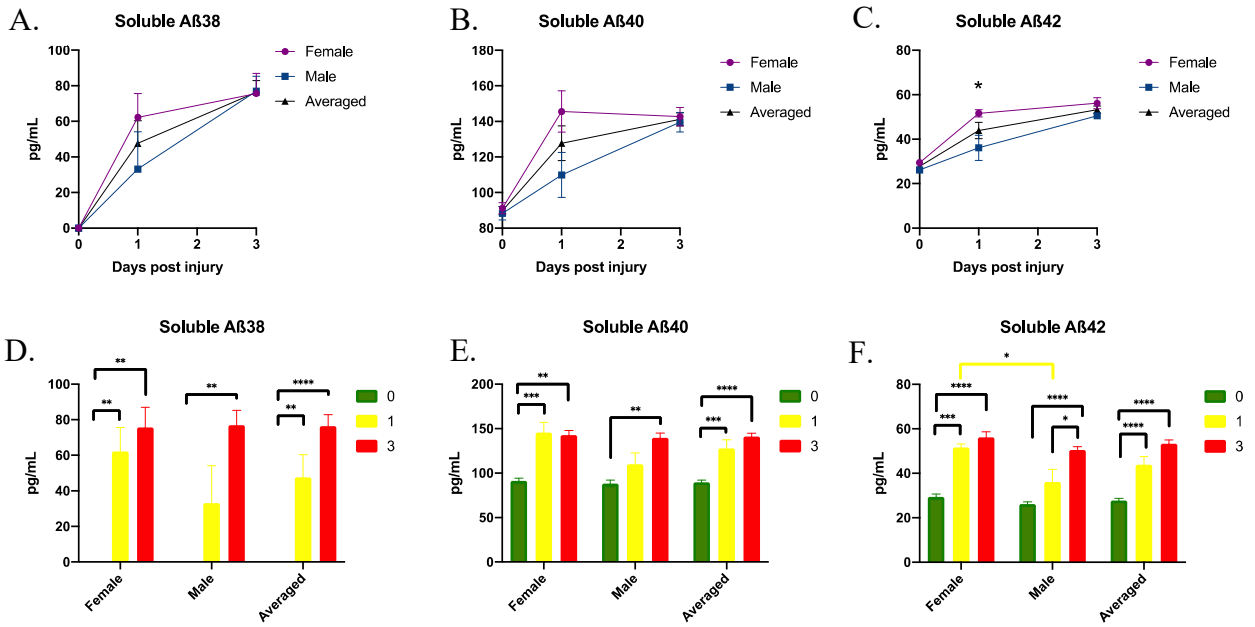

Figure 2.9. Effects of sCHI on individual soluble Aβ species in males *vs.* females. ***A-C***, Effects of sCHI on soluble Aβ38 (***A***), Aβ40 (***B***) and Aβ42 (***C***) plotted separately for males and females as a function of time. ***D-F***, The same data in ***A-C*** graphed by sex to demonstrate time-dependent effects for males and females separately and combined. Note that there are significant between-sex differences in the levels of Aβ42, but not Aβ38 or Aβ40, at 1DPI. Data are mean ± SEM for 6 replicates per group. *$P< 0.05$; ** $P< 0.01$; *** $P< 0.001$; ****$P< 0.0001$.

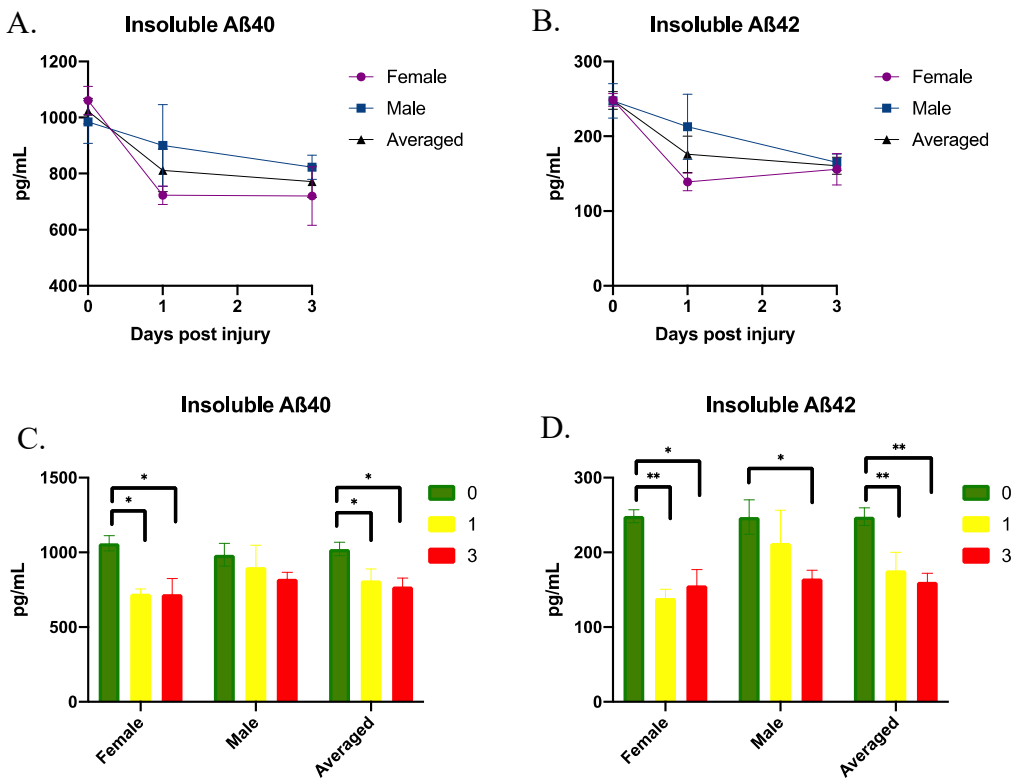

Figure 2.10. Effects of sCHI on insoluble Aβ40 and Aβ42 in males *vs.* females. ***A-C***, Effects of sCHI on insoluble Aβ40 (***A***) and Aβ42 (***B***) plotted separately for males and females as a function of time. Note that there were no between-sex differences at any time points for either Aβ species. ***C,D***, The same data in ***A*** and ***B*** graphed by sex to demonstrate time-dependent effects for males and females separately and combined. Data are mean ± SEM for 6 replicates per group. *$P< 0.05$; ** $P< 0.01$.

To further investigate the effects of sCHI in the hAβ-KI model, we used immunohistochemistry (IHC) to probe for amyloid Aβ plaques and fibrils, APP, as well as for activation of astrocytes and microglia. Predictably, we did not find any evidence of amyloid plaque formation in response to sCHI at any time points tested, and glial activation at 0DPI (Appendix A Fig. S2.3). However, we observed minimal microglial activation, but clear astrocytic migration to the injury site at both 1DPI (Fig. 2.11, Appendix A Fig. S2.4) and 3DPI (Fig. 2.12, Appendix A S2.5).

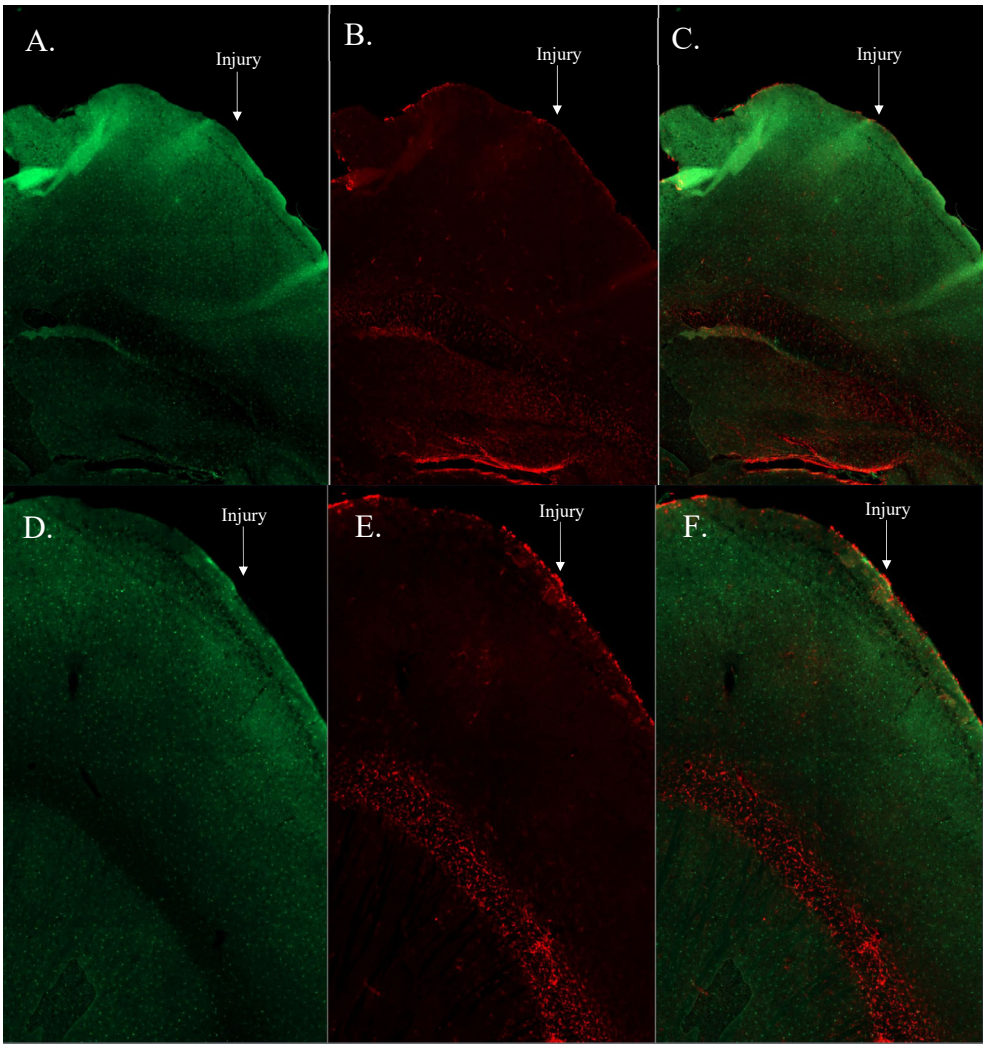

1DPI Male

1DPI Female

Figure 2.11. Microglial and astrocytic responses to sCHI at 1DPI. ***A-F*****,** Staining for the microglial marker, Iba1 (green, ***A, D***), and the astrocytic marker, GFAP (red, ***B, E***), in males (top, ***A-C***) and females (bottom, ***D-F***) at 1DPI. Panels ***C*** and ***F*** show both stainings merged. Note the presence of astrocytes near the site of injury (arrows), which is most prominent in females at this time point. Data are representative of 6 replicates per group.

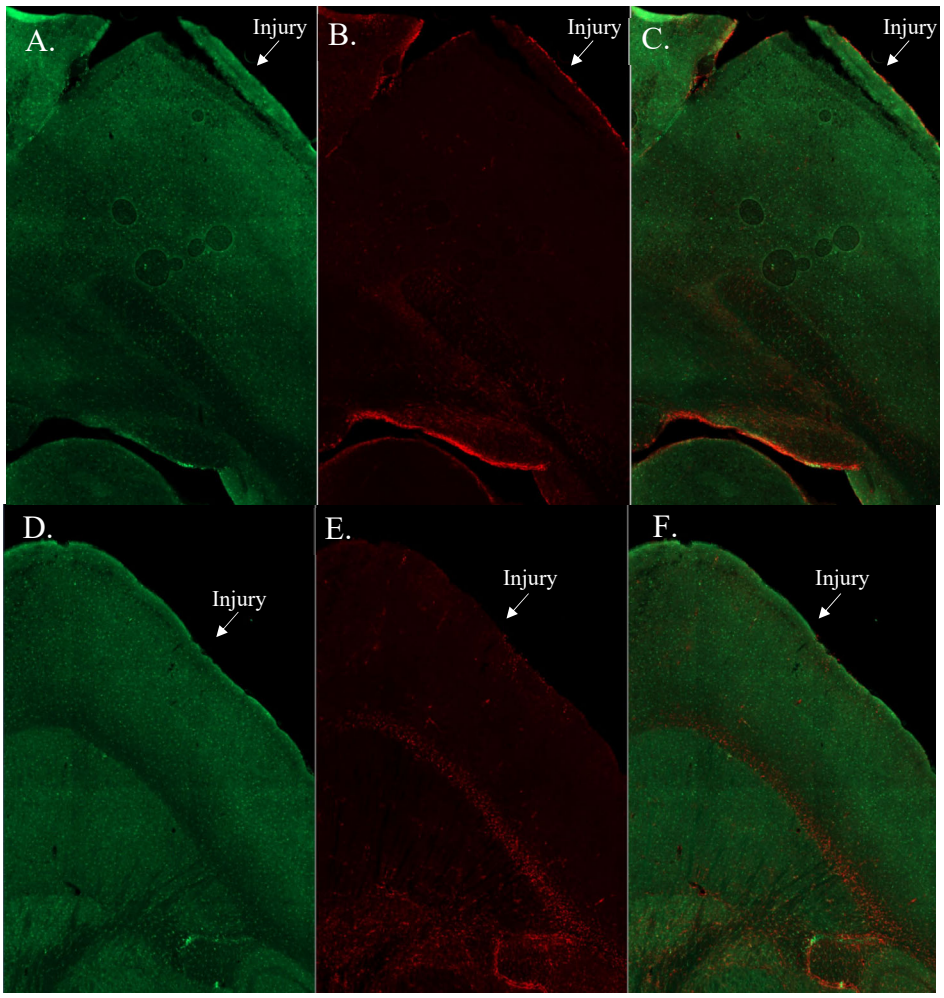

3DPI Male

3DPI Female

Figure 2.12. Microglial and astrocytic responses to sCHI at 3DPI. ***A-F*****,** Staining for the microglial marker, Iba1 (green, ***A, D***), and the astrocytic marker, GFAP (red, ***B, E***), in males (top, ***A-C***) and females (bottom, ***D-F***) at 3DPI. Panels ***C*** and ***F*** show both stainings merged. Note the presence of astrocytes near the site of injury (arrows), which is most prominent in females at this time point. Data are representative of 6 replicates per group.

To our surprise, Aβ fibrils were detected using the OC fibril antibody (52) in a small subset of male mice at 3DPI (Fig. 2.13). Significantly, the granular OC+ staining colocalizes with astrocytes (Fig. 2.13). The emergence of Aβ fibrils is especially notable given that this model does not develop such fibrils until later in life; research in humans, however, has shown the rapid formation of intermediary Aβ fibrils following a TBI (53).

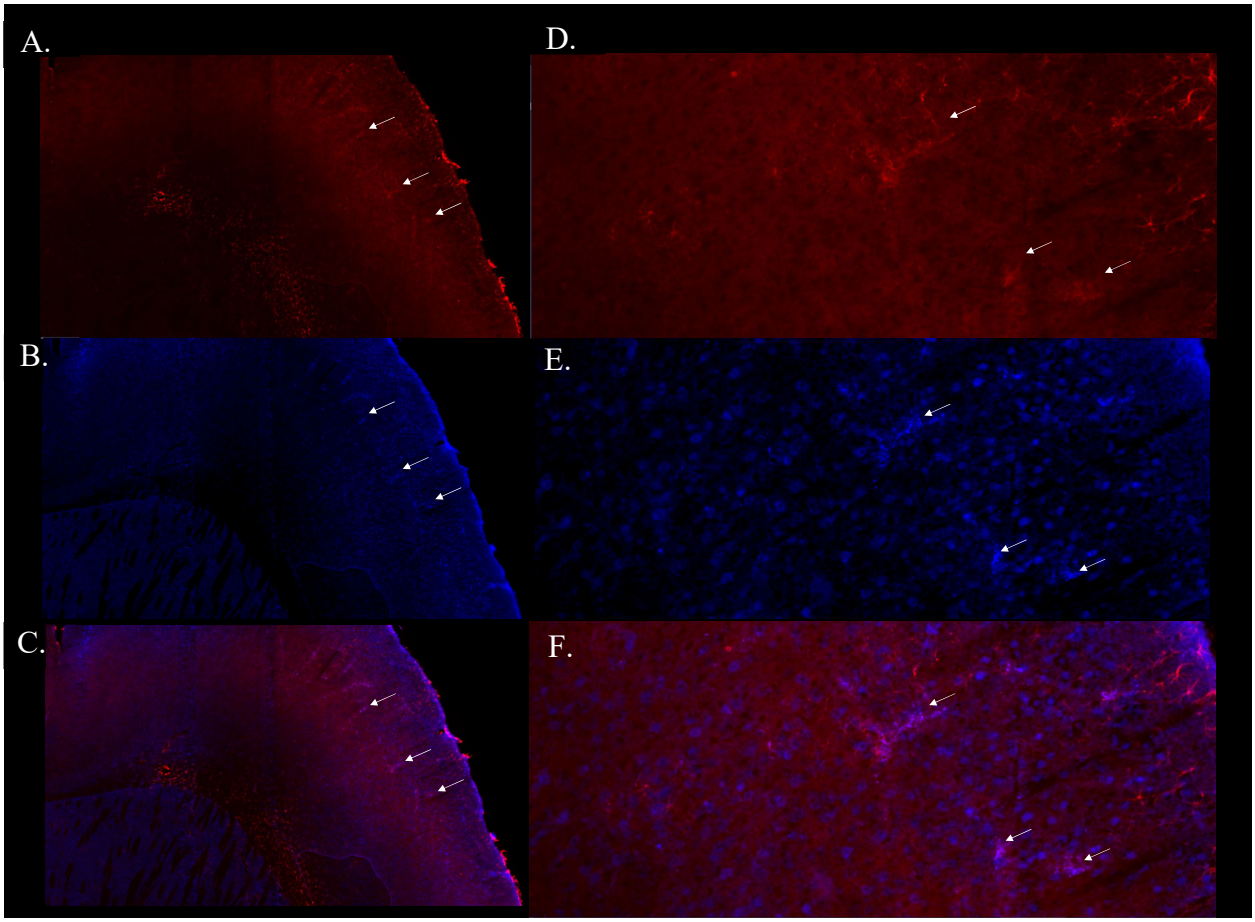

Figure 2.13. Detection of Aβ fibrils colocalized with astrocytes at 3DPI. ***A-F***, GFAP staining (red, ***A, D*)**, Aβ fibrils detected with the OC fibril antibody (blue, ***B, E***) and their colocalization (highlighted by arrows, ***C, F***). ***D-F*** show higher magnification images of the sections in ***A-C***, highlighting the "granular" pattern of the Aβ fibrils. Data are representative of 3 replicates.

Aim 1B.

Having confirmed that the hAβ-KI model exhibits acute increases in Aβ following TBI, we next wanted to establish whether an increase in Aβ levels *per se* might be sufficient to trigger amyloidogenesis in this LOAD mouse model. This is important, because sCHI and other forms of TBI have many other consequences besides those affecting Aβ levels, and our hypothesis is that a transient increase in Aβ specifically represents the common pathological mechanism linking a variety of AD risk factors. It was therefore critical to selectively induce an elevation in Aβ early in life (as the independent variable in our experiment) by some other means besides TBI, then assess whether this could trigger for AD-like pathology (the dependent variables) later in life. To that end, we administered the broad-spectrum metalloprotease inhibitor, phosphoramidon, intracerebroventricularly (i.c.v.) to 5-month-old hAβ-KI mice transiently (for 4 weeks), then examined the consequences immediately after (at 6 months) then in adult (15-month-old) and aged (22-month-old) animals (Fig. 2.14). Critically, to control for possible off-target effects of phosphoramidon (as opposed to the intended effect on Aβ levels), we also included groups of mice treated with the γ-secretase inhibitor, begacestat, to block Aβ production during the inhibitor treatment. Thus, four groups of mice were treated separately with either: (C) vehicle alone, (CB) vehicle plus begacestat, (P) phosphoramidon alone, or (PB) phosphoramidon plus begacestat (Fig. 2.14; Appendix A Fig. S2.6).

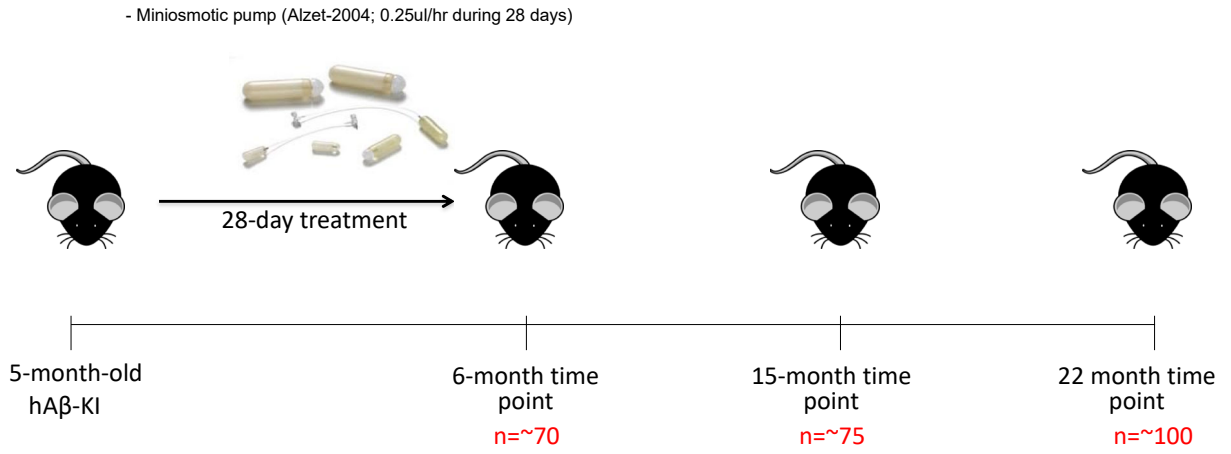

Drug/Group ID	C	CB	P	PB
Phosphoramidon	-	-	+	+
Begacestat	-	+	-	+

Figure 2.14. Timeline and treatment groups for the experiments in Aim 1B.Cartoon illustrating the overall timeline (top) as well as treatments given to the four experimental groups (bottom). Note: information on duration of treatment, survival rates, and changes in tissue with age can be viewed in Appendix A Figs. S2.7-S2.9. C = vehicle-only control; CB = vehicle plus begacestat; P = phosphoramidon; PB = phosphoramidon plus begacestat

Tissue from mice collected at each time point and condition was used to extract soluble and insoluble Aβ, which was then quantified. At the 6-month time point, significant elevations in both soluble and insoluble total Aβ were observed in phosphoramidon-treated versus control mice, indicating that phosphoramidon successfully inhibited the hydrolysis of Aβ by some AβDPs (Fig. 2.15A, C). However, both soluble and insoluble total Aβ returned to baseline levels at 15 and 22 months (Fig. 2.15A, C). Interestingly, animals that received phosphoramidon treatment had significantly lower Aβ42/40 ratios at 6-months, suggesting that the AβDPs inhibited by phosphoramidon preferentially cleave shorter Aβ fragments (Fig. 2.15B, D).

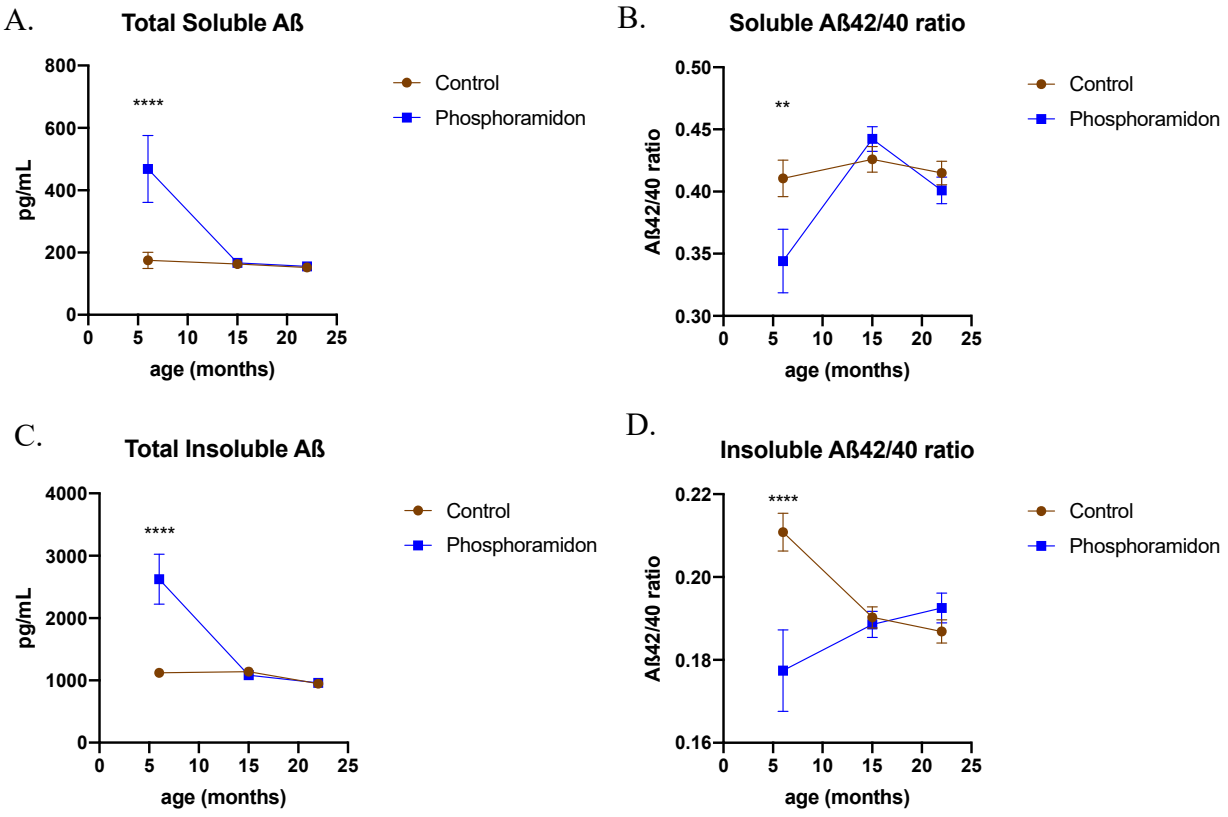

Figure 2.15. Change in total Aβ and Aβ42/40 ratio in response to phosphoramidon treatment. ***A***,***C***, Levels of total Aβ in soluble (***A***) and insoluble (***C***) fractions. Note that this fraction includes Aβ38, Aβ40 and Aβ42. ***C***,***D***, Changes in Aβ42/40 ratios in soluble (***C***) and insoluble (***D***) fractions. Note that both soluble and insoluble total Aβ increase at 6 months, but return to baseline at subsequent time points. Note also that soluble Aβ42/40 ratios increase, and insoluble Aβ42/40 ratios decrease, significantly only in the 6-month-old mice, with ratios returning to baseline at subsequent ages. Data are mean ± SEM for 12-16 replicates per group. ** $P< 0.01$; **** $P< 0.0001$.

Although phosphoramidon appeared to be effective, given that significant increases in Aβ were evident immediately after treatment (6P), we next wanted to investigate the effect of begacestat; if begacestat worked, phosphoramidon-treated animals should look similar to vehicle-only control mice. Regrettably, both the CB and PB groups were not statistically distinct from the counterpart groups not treated with begacestat (Fig. 2.16A-D). All following analyses will therefore combine these conditions (C and CB, P and PB) to increase the number of mice per group.

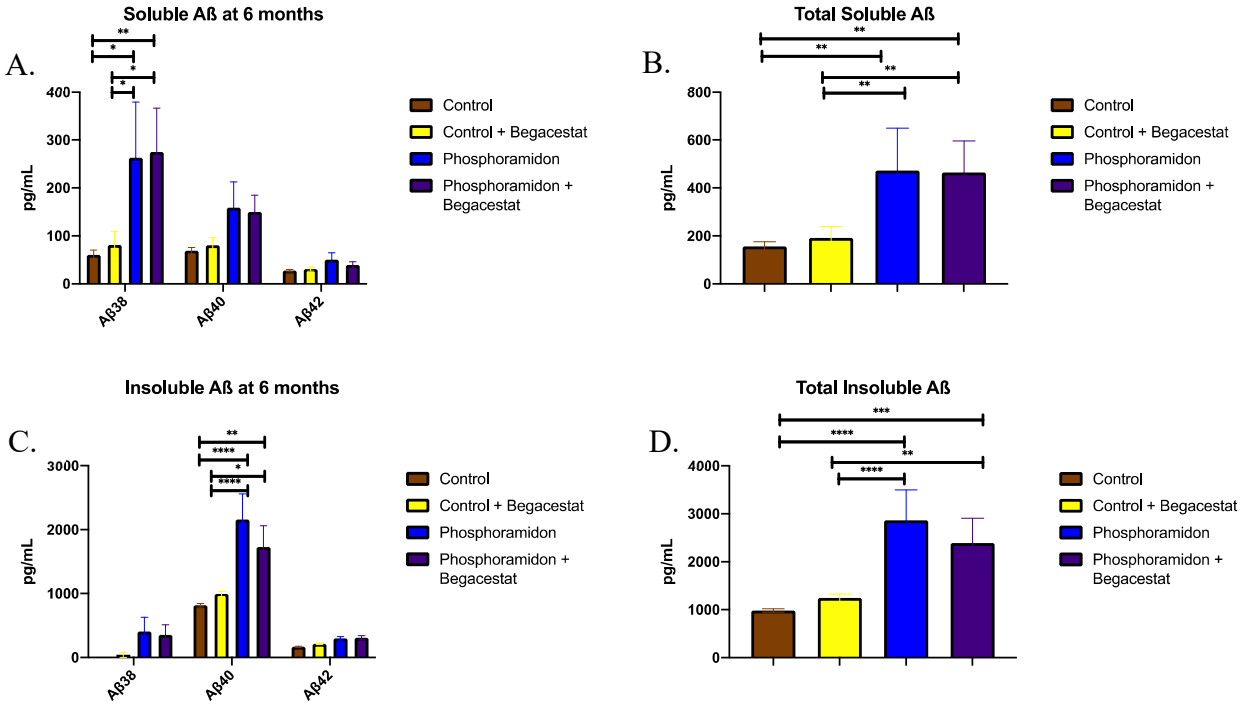

Figure 2.16. Effect of phosphoramidon on difference Aβ species immediately after treatment in the absence or presence of begacestat. ***A***, Levels of soluble total Aβ (Aβ38, Aβ40 and Aβ42) immediately after treatment (6 months) with the indicated inhibitors for 4 weeks. ***B***, Levels of soluble total Aβ (Aβ38, Aβ40 and Aβ42) immediately after treatment (6 months) with the indicated inhibitors for 4 weeks. ***C***, Levels of all soluble Aβ species combined at 6 months of age. ***D***, Levels of insoluble total Aβ immediately after treatment. Note that no significant effect of begacestat was observed. Data are mean ± SEM for 12 replicates per group. *P< 0.05; ** P< 0.01; *** P< 0.001; ****P< 0.0001.

The profound effect of phosphoramidon on total Aβ immediately after treatment (6 months) becomes more interesting when the individual Aβ species are considered. In particular, although phosphoramidon significantly increased all Aβ species, both soluble and insoluble, relative to controls (Fig. 2.17, Appendix A Fig. S2.10), this effect was disproportionately attributable to Aβ38 in the soluble fraction, and Aβ40 in the insoluble fraction (Fig. 2.17A, D). In addition, Aβ42 made only a minor contribution to the effects on total Aβ, both soluble and insoluble.

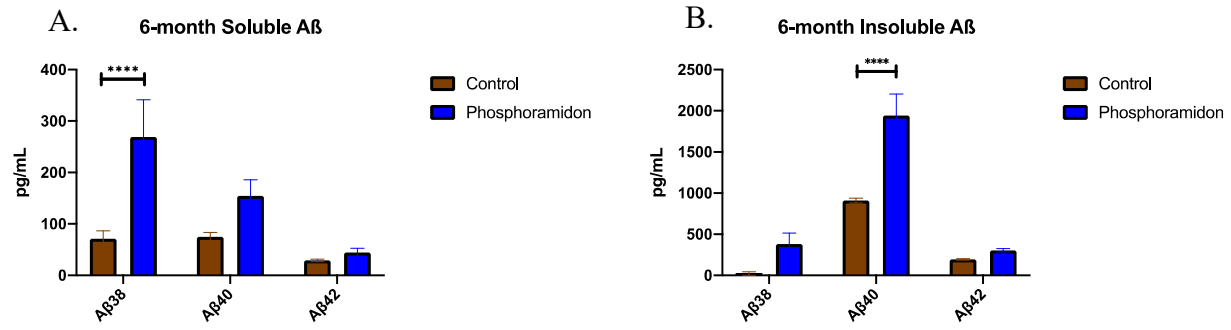

Figure 2.17. Effects of phosphoramidon on individual Aβ species. ***A***,***B***, Levels of soluble (***A***) and insoluble (***B***) Aβ38, Aβ40 and Aβ42 immediately after treatment with phosphoramidon (brown) or vehicle (blue) for 4 weeks (i.e., at 6 months of age). Note that Aβ38 is increased disproportionately by phosphoramidon in the soluble fraction, whereas Aβ40 is the only species increased significantly in the insoluble fraction. Data are mean ± SEM for 24 replicates per group. ****$P< 0.0001$.

Next, we wanted to establish whether the small sex differences found in our TBI project (Aim 1A) were recapitulated in this project. Surprisingly, we found that the effect on soluble Aβ seen with both sexes combined was disproportionately attributable to male mice (Fig. 2.18A-C), while males and females both contributed to the changes seen in insoluble Aβ (Fig. 2.18D-E).

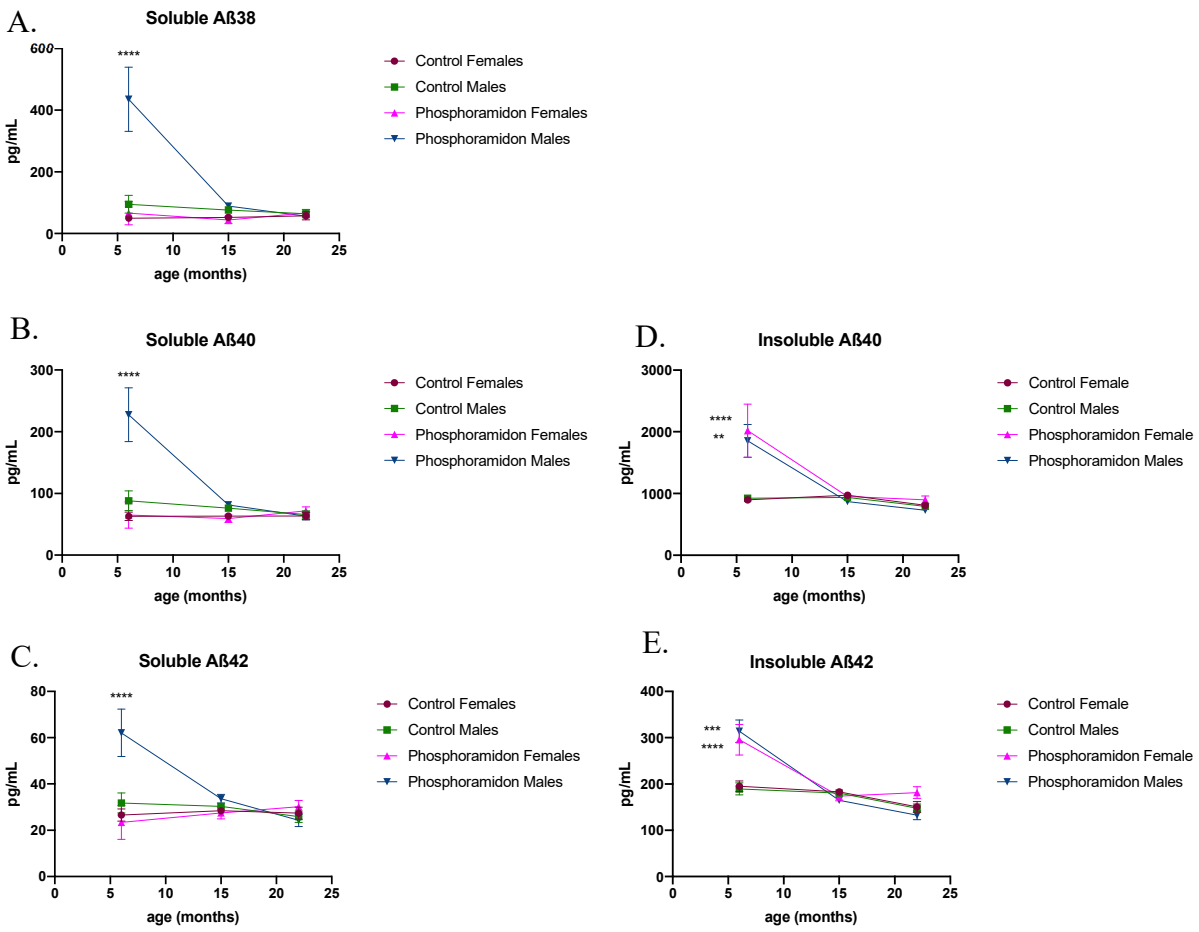

Figure 2.18. Sex differences in responsiveness of individual Aβ species to phosphoramidon treatment. ***A-C***, Levels of soluble Aβ38 (***A***), Aβ40 (***B***) and Aβ42 (***C***) in male and female control and phosphoramidon-treated mice as a function of age. Note that levels of all 3 Aβ species were disproportionately affected by phosphoramidon treatment in males, and only at 6 months of age. with no significant changes observed in females. ***D-E***, Levels of insoluble Aβ40 (***D***) and Aβ42 (***E***) in male and female control and phosphoramidon-treated mice as a function of age. Note that levels of both Aβ40 and Aβ42 were significantly increased by phosphoramidon at 6 months in both males and females**.** Data are mean ± SEM for 12-16 replicates per group. ** $P< 0.01$; *** $P< 0.001$; ****$P< 0.0001$.

Interestingly, these sex differences did not extend fully to Aβ42/40 ratios. For soluble Aβ42/40 ratios, we observed no significant sex-, treatment-, or age-dependent differences (Fig. 2.19A). However, insoluble Aβ42/40 ratios were significantly decreased in phosphoramidon-

treated females relative to controls at 6 months of age, but were not significantly different from males (Fig. 2.19B).

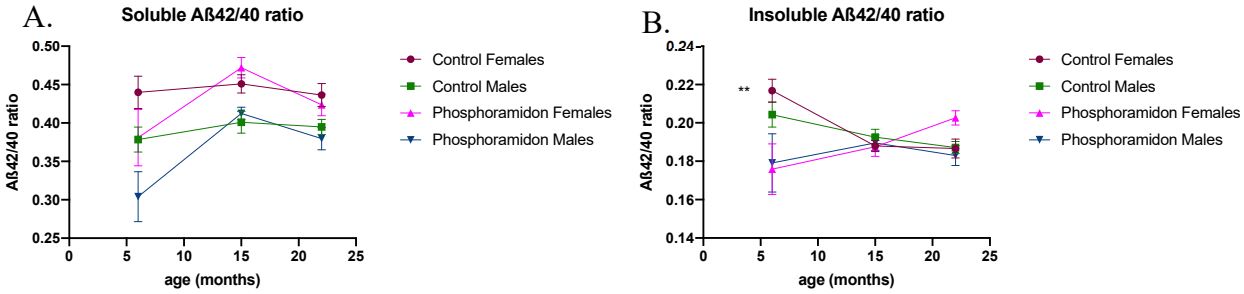

Figure 2.19. Sex differences in soluble and insoluble Aβ42/40 ratios. ***A***,***B***, Soluble (***A***) and insoluble (***B***) Aβ42/40 ratios in males and female control and phosphoramidon-treated mice as a function of age. Note that there were no significant differences between sex or treatment for soluble ratios, whereas for insoluble ratios, insoluble Aβ42/40 ratios were significantly reduced by phosphoramidon treatment in females relative to control females. Data are mean ± SEM for 12-16 replicates per group. ** $P< 0.01$.

Consistent with the biochemical results for insoluble Aβ, no plaques were detected at any time point or in any condition (Appendix A Fig. S2.11 and S2.12). However, consistent with the LaFerla laboratory's independent characterization of the hAβ-KI line, we detected Aβ fibrils in 22-month-old animals, with consistent levels irrespective of sex or condition (Fig. 2.20).

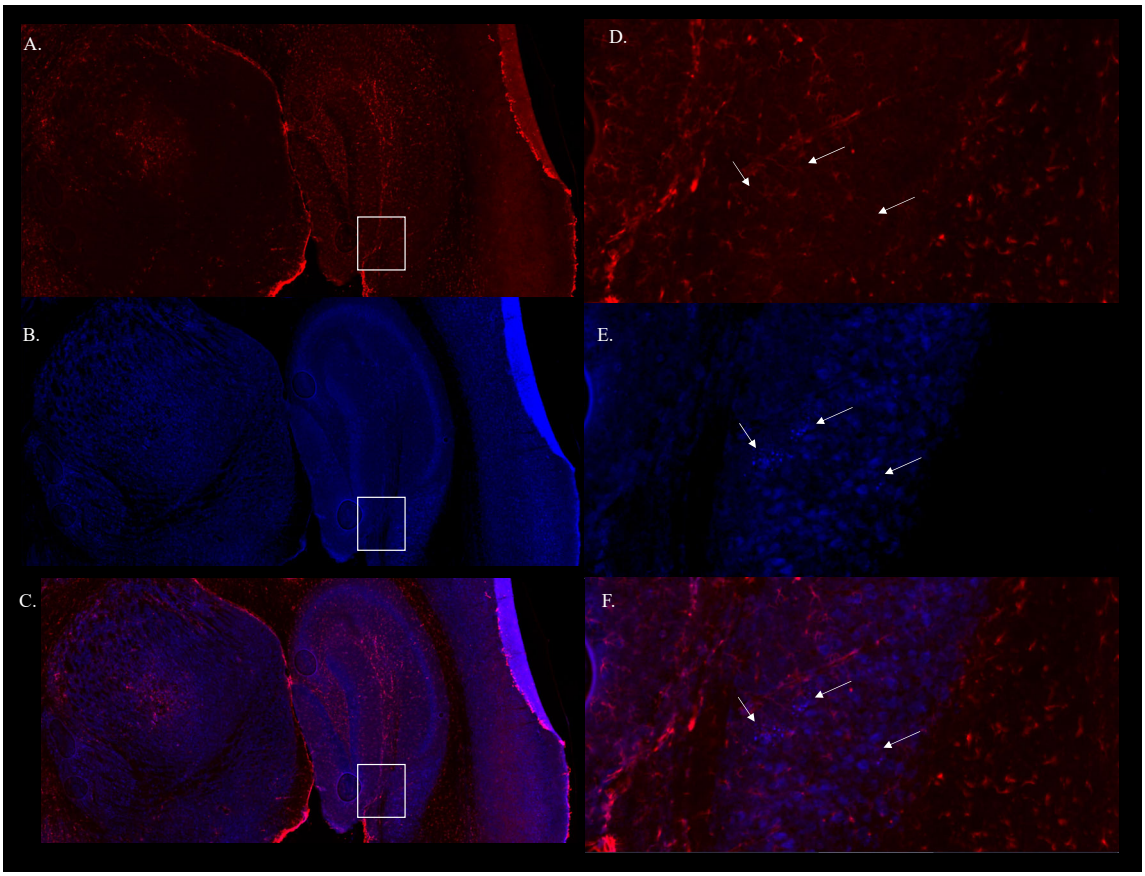

Figure 2.20. Detection of Aβ fibrils and colocalized astrocytes in 22-month-old hAβ-KI mice. ***A-F***, Hippocampal sections stained with the astrocytic marker**,** GFAP (red, ***A, D*****),** with the OC antibody for Aβ fibrils (blue, ***B, E***) and their colocalization (highlighted by arrows, ***C, F***). ***D-E*** show higher magnification images of the sections in ***A-C***, highlighting the "speckled" pattern of the Aβ fibrils. Data are representative of all 22-month animals.

2.3.4 Discussion

In humans, brain injury has been proposed as a candidate a risk factor for LOAD. Although contradictory evidence exists, many studies suggest that various types of head injury can trigger acute increases in cerebral Aβ. We assessed this idea using a novel model of LOAD, the hAβ-KI line, which closely models the biologic milieu in which LOAD emerges, with physiological levels of wild-type human Aβ expressed under the control of the endogenous *APP* promoter in the absence of EOAD-linked mutations. In Aim 1A, we assessed the consequences of a sCHI in this

model. Our results confirm that acute head injury can trigger transient Aβ elevations in the absence of APP overproduction or EOAD-linked mutations, thus validating the utility of the hAβ-KI mouse model for these experiments. At the same time, however, the response of insoluble Aβ in hAβ-KI mouse model differed in important ways from other published work. In conventional AD mouse models overexpressing mutant APP, TBI often triggers an increase in both soluble and insoluble Aβ following a concussion (30, 49). The increase in insoluble Aβ seen in most AD mouse models might be dependent on the high levels of APP expression and or elevated Aβ42/40 ratios usually present in these models, both of which would serve to promote Aβ deposition. This seems a satisfying explanation that suggests that new information can be gained using the hAβ-KI mouse model. However, Aβ aggregates have been found in human TBI patients that are composed of insoluble Aβ (34, 35, 54). This discrepancy may have several possible explanations, not mutually exclusive. It could be that the sCHI paradigm used in this case was insufficient to trigger insoluble aggregates; and/or insoluble aggregates might accrue later than 3DPI. In this regard, studies that use a single severe injury often observe Aβ returning to baseline after varying amounts of time post-injury: from 3 to 7 days (30, 49, 50, 55, 56). An extension of the current experiment including both earlier (e.g., 6- and 12-hour) and later (e.g., 5- and 7-day) timepoints may uncover a greater correspondence with other results within the field. Alternatively, or in addition, it may be that the hAβ-KI model does not have the characteristics needed to permit amyloidogenesis within the lifespan of a mouse and/or that it differs from humans in some other salient respect. Future studies investigating these questions are warranted. In this connection, it is notable that a recent TBI study conducted using another APP knock-in mouse model, the $APP^{NL\text{-}F/NL\text{-}F}$ line (57), which in this case has two copies of two different EOAD-linked mutations, found enhanced accumulation of both Aβ and phospho-tau following 14-day repeated mild closed head injury. This study did not

examine shorter term intervals after TBI, but it is significant that the pathology emerged from 3 to 8 months post-injury. Of particular importance to the study of TBI, this model also found activated microglia surrounding the newly developed plaques (58), something not observed in the hAβ-KI model.

The mechanisms underlying the rise in Aβ induced by TBI have yet to be completely determined. Clearly, much more work remains to be done; these results highlight just how complicated it can be to obtain a holistic view of Aβ proteostasis, requiring as it does a comprehensive analysis of all the components mediating both Aβ production and Aβ clearance, something that might not be achievable merely by quantifying protein levels. In a technical complication, we unfortunately were not able to assess the traditional markers of Aβ production (e.g., holo-APP, APP CTFs, BACE1, etc.), because the insoluble fraction, once solubilized with the very harsh formic acid, was not amenable to western blotting. This is an unforeseen but nevertheless significant flaw in our experimental design, and it should be addressed in future experiments revisiting this topic.

In Aim 1B, we sought to test the specific hypothesis that acute increases in Aβ represent a common pathogenic mechanism for TBI and potentially a variety of other AD risk factors. To test this, we increased cerebral Aβ levels pharmacologically for 4 weeks in young hAβ-KI mice, then examined the consequences immediately after treatment, as well as in middle-aged (15-month-old) and aged (22-month-old) mice. These experiments were very difficult to execute, involving approximately 250 delicate brain surgeries that did not always go as planned. Among the complications we encountered were: (1) problems with the integrity of the cannulae, which frequently fell out before the 4-week treatment period; (2) the emergence of a widespread skin pathology in the animal colony (59), and well as (3) much higher than expected premature lethality

(Appendix A Fig. S2.8). Although we planned for some degree of lethality, we had originally hoped to allow the animals to age to at least 24 months (Dr. Leissring hoped we could age them considerably longer). Despite our best efforts, it proved necessary to sacrifice the oldest animals at 22 months. Because we were most interested in the interaction between the elevation in Aβ and aging, this was a disappointing outcome. Moreover, it was not entirely expected. In published reports employing other APP knock-in mice developed by Dr. Takaomi Saido, very little premature lethality occurs (57). It may be relevant to note that construction work was being performed periodically in our vivarium. Although not quantified, we did notice a distinct increase in premature deaths when construction was most active. Given the lack of premature lethality seen with similar animal models, this suggests that our vivarium environment was less than ideal.

Given these caveats, and given the fact that phosphoramidon treatment did not trigger amyloidogenesis in aged animals as hoped, the conclusions we can make from the experiments in Aim 1B are necessarily tentative. First, regarding the treatment, on the one hand, it appeared to work as planned insofar as it produced significant elevations in both soluble and insoluble total Aβ. On the other hand, it did not result in any changes beyond the 6-month time point. In addition, relative to controls, phosphoramidon unexpectedly produced *decreases* in Aβ42/40 ratios in both soluble and insoluble fractions. This is different from that observed following sCHI, where soluble Aβ42/40 ratios increased, but insoluble ratios decreased. Additionally, this reduction in Aβ42/40 ratios is precisely the opposite of what would be likely to seed Aβ deposition. As to the mechanism underlying this effect, we can only speculate, but it is notable that phosphoramidon treatment disproportionately affected shorter Aβ species (e.g., Aβ38, Aβ40). Shorter Aβ species have actually been shown to be antiamyloidogenic. For example, selective overexpression of Aβ40 was found to reduce amyloidogenesis in APP transgenic mice (60). We speculate that the

disproportionate increase in antiamyloidogenic Aβ species induced by phosphoramidon was, at the very least, unhelpful to our objective of triggering amyloidogenesis. From a therapeutic perspective, however, this topic is highly deserving of further investigation; conceivably, it might be possible to prevent amyloidogenesis by inhibiting an AβDP, provided that AβDP preferentially degrades shorter, potentially anti-amyloidogenic species.

Second, we can speculate that the lack of amyloidogenesis we observed is attributable to characteristics of the hAβ-KI model. It is important to emphasize that this model was developed relatively recently, and its characterization is ongoing (with no publications yet emerging). However, by comparing this line to similar APP knock-in (KI) lines, it seems likely that hAβ-KI model might not be sufficiently aggressive to be useful as a model of LOAD. In particular, Saido and colleagues generated similar APP KI lines with humanized Aβ, but also containing either the Swedish double mutation (NL) alone or that mutation together with the Iberian (F) mutation (57). Significantly, mice with two copies of the EOAD-linked Swedish mutation exhibit ~3-fold increases in Aβ but nevertheless fail to show any signs of Aβ deposition up to 30 months of age (57). This demonstrates that even lifelong ~3-fold increases in total Aβ are insufficient to trigger amyloidogenesis in a model very similar to hAβ-KI mice. However, inclusion of the Iberian mutation, which increases the Aβ42/40 ratio, results in significant deposition. In mice with two copies of the NL-F double mutation, diffuse plaques develop by 6 months of age, converting to significant dense-core plaques by 15 months of age (57). Clearly, this is a less-than-ideal model of LOAD, not only because it contains EOAD mutations, but also because it inexorably develops amyloidogenesis. Intriguingly, however, it is notable that mice with just a single copy of the NL-F double mutation, develop diffuse plaques only at 14 months of age, with sparse dense-core plaques only emerging at very advanced ages (30 months). Because this time course of

amyloidogenesis mimics what is seen in cognitively normal humans, this model may be an appropriate animal for investigating the triggers for LOAD. In sum, given the characteristics of these other APP KI mice, it seems likely that the hAβ-KI line was likely not as permissive to the emergence of amyloidogenesis as hoped. As mentioned, however, we cannot exclude the possibility that more aggressive treatments, perhaps those increasing the Aβ42/40 ratio in particular, could trigger amyloidogenesis in the absence of EOAD mutations.

2.3.5 Methods/Experimental

Animals

Mice were bred and housed in American Association for Accreditation of Laboratory Animal Care -accredited facilities in accordance with the National Institutes of Health Guidelines for the Care and Use of Laboratory Animals. hAβ-KI mice were maintained as an inbred line in a C57Bl/6J genetic background.

Surgeries

ALZET® mini-osmotic pumps (Model 2004, Brain Infusion Kit 3; DURECT Corp., Cupertino, CA) were prepared according to manufacturer instructions and surgically implanted in anesthetized hAβ-KI mice as previously described (61). Phosphoramidon and begacestat were dissolved in ddH_2O and DMSO respectively and were then made up in artificial cerebrospinal fluid. The concentrations of phosphoramidon (10 mg/kg) and begacestat (1mg/kg) were adjusted to the weight of each mouse. Cannulae were surgically implanted to deliver compounds i.c.v. at the following coordinates, relative to bregma: -1.1 mm M/L, -0.5 mm A/P, -2.5 mm D/V. Pumps

were implanted subcutaneously in the backs of animals. Experimental compounds were delivered at 0.25 μL/h for up to 28-days, at which point the pump and cannulae were removed.

Traumatic brain injury

Parameters for sCHI were initially based on (44, 62). After preliminary tests were conducted to assess the severity of impact on the integrity of the skull, sCHI was administered on the midline, -2 mm A/P. Injuries were administered using a Leica Biosystems Impact One for Reproducible Neurotrauma using the following conditions: 3-mm tip size; 1-mm depth, 0.2 ms dwell time, and 6 m/s speed. Following injury, mice were allowed to fully recover on a warming pad before being returned to home cages.

Tissue collection

After cardiac perfusion with PBS in anesthetized mice, the right hemisphere was snap-frozen on dry ice and stored at -80 °C, and the left hemisphere was fixed for 3 days in 4% paraformaldehyde/PBS followed by immersion into 30% sucrose solution for a minimum of 24 h before storage at -80 °C.

Biochemical analyses

Frozen tissue was weighed, then homogenized using 1 mL TPER (plus protease inhibitor cocktail and phosphatase inhibitor) per 150 mg brain tissue, centrifuged at 100,000 g at 4 °C for 1 h. To isolate the insoluble fraction, 1 mL 70% formic acid per 300 mg original frozen brain weight was used to resuspend the pellet. This was centrifuged at 100,000 g at 4 °C for 1 h and diluted 1:15 with neutralization buffer (1M Tris Base, 0.5M Na_2HPO_4, 0.05% NaN_3 in ddH_2O_3) prior to subsequent analysis.

Aβ quantification

Levels of Aβ38, Aβ40 and Aβ42 were quantified simultaneously by multiplex assay using the V-PLEX Aβ Peptide Panel 1 (6E10) Kit (Meso Scale Diagnostics; Rockland, MD) according to manufacturer's recommendations, with the exception that samples were allowed to incubate at 4 °C overnight. Data were normalized by dilution factor.

Histochemistry and IHC

Following immersion in sucrose for 24 h and storage at -80 °C, serial sagittal sections (40-µm thickness) were cut using a freezing sliding microtome. Sliced tissue was stored at 4 °C in PBS supplemented with 0.01% sodium azide. For immunostaining, sections were pre-treated with 3% H_2O_2/3% MeOH in tris-buffered saline (TBS) for 30 min. Following washes in TBS, sections were incubated in TBS supplemented with 0.1% Triton X-100 (TBST) for 15 min, then in TBST with 2% bovine serum albumin (BSA, Sigma-Aldrich, St. Louis, MO) for 30 min. Next, tissue was incubated in 90% formic acid for 7 min. This was followed by incubation for 48 h at 4 °C, with 6E10 antibody (1:1000; BioLegend, San Diego, CA, USA; Catalog # 83001), for 48 h, followed by anti-mouse secondary (1:500) in TBS/2% BSA/5% normal horse serum for 1 h at room temp. Finally, sections were stained using the Vector ABC kit and 3,3'-diaminobenzidine (DAB) reagents (Vector Laboratories, Burlingame, CA, USA). For thioflavin-S (Thio-S) staining, tissue was washed and followed by 10-min treatment with 0.5% Thio-S in 50% EtOH (T-1892; Sigma-Aldrich, St. Louis, MO). For fluorescent staining, sections were pre-treated with 3% H_2O_2/3% MeOH in TBS for 30 min. Following washes in TBS, sections were incubated in TBST for 15 min, then in TBST with 2% BSA for 30 min. Next, tissue was incubated in 80% formic acid for 3 min. Sections were incubated with the following primary antibodies at the indicated dilutions in TBST: OC antibody (1:100; EMD Millipore Darmstadt, Germany; Catalog #ab2286); anti-GFAP antibody (1:5000; Abcam, Cambridge, MA, USA; Catalog #ab13443). After incubation in primary

antibody at 4 ºC overnight, sections were washed in TBST, then incubated in one of the following secondary antibodies (1:500 in TBST) for 1 h at room temperature: Alexa-fluor 647-tagged goat anti-rabbit antibody (Invitrogen, Carlsbad, CA; Catalog #A27040); Alexa-fluor 555-tagged goat anti-chicken antibody (Invitrogen, Carlsbad, CA; Catalog #A21437). Glial staining was performed similarly, but without formic acid treatment. Primary antibodies for glial staining included the following at the indicated concentrations: Iba1 (1:200; Wako Pure Chemical Industries, Irvine, CA; Catalog #019-19741) and anti-GFAP (1:500; Abcam PLC, Cambridge, MA; Catalog; Catalog #ab4674). The secondary antibodies indicated above were used for labeling. Sections were then mounted on silane-coated glass slides and cover-slipped with Fluoromount-G (Catalog # 0100-01 Southern Biotech, Birmingham, AL). Images were taken at 10X and 20X magnification using an automated slide scanner (ZEISS Axio Scan.Z1; Zeiss Group, Oberkochen, Germany).

2.4 Conclusion

In sum, we have used a novel model of LOAD lacking EOAD mutations to investigate mechanistic hypotheses about precisely how various AD risk factors introduced early in life might trigger the full-spectrum of AD-type pathology late in life, as occurs in LOAD. We succeeded in showing that sCHI results in transient increases in soluble Aβ but, unlike what is observed in humans and in other AD mouse models, we did not see an increase in insoluble Aβ. Surprisingly, however, sCHI did trigger the emergence of Aβ fibrils in a subset of male animals by 3DPI. We also used the model to test whether transient increases in Aβ induced pharmacologically can trigger the emergence of amyloid deposition in the context of aging. Although our treatment succeeded in increasing total soluble and insoluble Aβ, it also lowered the Aβ42/40 ratios, potentially due to a disproportionate increase in shorter, anti-amyloidogenic Aβ species. Our efforts also helped to

characterize a novel animal, confirming independent results that Aβ fibrils emerge at 22 months of age in hAβ-KI mice. Our findings, while not resulting in the outcome we had hypothesized, nevertheless have provided valuable insights that will inform future experiments addressing the hypotheses we have tested.

2.5 Acknowledgements

I would like to sincerely thank the staff of the UCI Biological Sciences III vivarium, with particular gratitude to Jenna A. Quintero-Castan, for their help in maintaining the mouse colony, treating ulcerative dermatitis, and overall helping me continually improve our animal care. I would like to acknowledge the efforts of Stefania Forner, Alessandra Martini, members of the Thompson laboratory, and UCI animal training for demonstrating and teaching appropriate surgery techniques and helping me develop the surgery/animal protocol. I would also like to thank David Baglietto-Vargas for providing information regarding the hAβ-KI model, as well as sharing much of his preliminary data with me as I was beginning this project. Furthermore, I would like to thank Shelley Lane and Monica K. Brizuela for their help with experimental execution, and Malcolm A. Leissring for his assistance and mentorship in this development of this project.

2.6 References

1. Thal DR, Walter J, Saido TC, Fandrich M. Neuropathology and biochemistry of Abeta and its aggregates in Alzheimer's disease. Acta Neuropathol. 2015;129(2):167-82.

2. Lanoiselee HM, Nicolas G, Wallon D, Rovelet-Lecrux A, Lacour M, Rousseau S, et al. APP, PSEN1, and PSEN2 mutations in early-onset Alzheimer disease: A genetic screening study of familial and sporadic cases. PLoS Med. 2017;14(3):e1002270.

3. Armstrong RA. A critical analysis of the 'amyloid cascade hypothesis'. Folia Neuropathol. 2014;52(3):211-25.

4. Castellani RJ, Plascencia-Villa G, Perry G. The amyloid cascade and Alzheimer's disease therapeutics: theory versus observation. Lab Invest. 2019.

5. Karran E, De Strooper B. The amyloid cascade hypothesis: are we poised for success or failure? J Neurochem. 2016;139 Suppl 2:237-52.

6. Leissring MA. Proteolytic degradation of the amyloid beta-protein: the forgotten side of Alzheimer's disease. Curr Alzheimer Res. 2006;3(5):431-5.

7. Saido T, Leissring MA. Proteolytic degradation of amyloid beta-protein. Cold Spring Harb Perspect Med. 2012;2(6):a006379.

8. Kline A. Apolipoprotein E, amyloid-ss clearance and therapeutic opportunities in Alzheimer's disease. Alzheimers Res Ther. 2012;4(4):32.

9. Mawuenyega KG, Sigurdson W, Ovod V, Munsell L, Kasten T, Morris JC, et al. Decreased clearance of CNS beta-amyloid in Alzheimer's disease. Science. 2010;330(6012):1774.

10. Lee CY, Tse W, Smith JD, Landreth GE. Apolipoprotein E promotes beta-amyloid trafficking and degradation by modulating microglial cholesterol levels. J Biol Chem. 2012;287(3):2032-44.

11. Prasad H, Rao R. Amyloid clearance defect in ApoE4 astrocytes is reversed by epigenetic correction of endosomal pH. Proc Natl Acad Sci U S A. 2018;115(28):E6640-E9.

12. Li J, Kanekiyo T, Shinohara M, Zhang Y, LaDu MJ, Xu H, et al. Differential regulation of amyloid-beta endocytic trafficking and lysosomal degradation by apolipoprotein E isoforms. J Biol Chem. 2012;287(53):44593-601.

13. Main BS, Villapol S, Sloley SS, Barton DJ, Parsadanian M, Agbaegbu C, et al. Apolipoprotein E4 impairs spontaneous blood brain barrier repair following traumatic brain injury. Mol Neurodegener. 2018;13(1):17.

14. Hellstrom-Lindahl E, Ravid R, Nordberg A. Age-dependent decline of neprilysin in Alzheimer's disease and normal brain: inverse correlation with A beta levels. Neurobiol Aging. 2008;29(2):210-21.

15. Iwata N, Takaki Y, Fukami S, Tsubuki S, Saido TC. Region-specific reduction of A beta-degrading endopeptidase, neprilysin, in mouse hippocampus upon aging. J Neurosci Res. 2002;70(3):493-500.

16. Nakanishi H. Neuronal and microglial cathepsins in aging and age-related diseases. Ageing Res Rev. 2003;2(4):367-81.

17. Cataldo AM, Nixon RA. Enzymatically active lysosomal proteases are associated with amyloid deposits in Alzheimer brain. Proc Natl Acad Sci U S A. 1990;87(10):3861-5.

18. Higashida T, Kreipke CW, Rafols JA, Peng C, Schafer S, Schafer P, et al. The role of hypoxia-inducible factor-1alpha, aquaporin-4, and matrix metalloproteinase-9 in blood-brain barrier disruption and brain edema after traumatic brain injury. J Neurosurg. 2011;114(1):92-101.

19. Shigemori Y, Katayama Y, Mori T, Maeda T, Kawamata T. Matrix metalloproteinase-9 is associated with blood-brain barrier opening and brain edema formation after cortical contusion in rats. Acta Neurochir Suppl. 2006;96:130-3.

20. Suehiro E, Fujisawa H, Akimura T, Ishihara H, Kajiwara K, Kato S, et al. Increased matrix metalloproteinase-9 in blood in association with activation of interleukin-6 after traumatic brain injury: influence of hypothermic therapy. J Neurotrauma. 2004;21(12):1706-11.

21. Truettner JS, Alonso OF, Dietrich WD. Influence of therapeutic hypothermia on matrix metalloproteinase activity after traumatic brain injury in rats. J Cereb Blood Flow Metab. 2005;25(11):1505-16.

22. Wang X, Jung J, Asahi M, Chwang W, Russo L, Moskowitz MA, et al. Effects of matrix metalloproteinase-9 gene knock-out on morphological and motor outcomes after traumatic brain injury. J Neurosci. 2000;20(18):7037-42.

23. Ikonomovic MD, Mi Z, Abrahamson EE. Disordered APP metabolism and neurovasculature in trauma and aging: Combined risks for chronic neurodegenerative disorders. Ageing Res Rev. 2017;34:51-63.

24. Miners JS, Baig S, Tayler H, Kehoe PG, Love S. Neprilysin and insulin-degrading enzyme levels are increased in Alzheimer disease in relation to disease severity. J Neuropathol Exp Neurol. 2009;68(8):902-14.

25. Takeda T, Klimov DK. Temperature-induced dissociation of Abeta monomers from amyloid fibril. Biophys J. 2008;95(4):1758-72.

26. Harrison PM, Chan HS, Prusiner SB, Cohen FE. Conformational propagation with prion-like characteristics in a simple model of protein folding. Protein Sci. 2001;10(4):819-35.

27. Dams-O'Connor K, Guetta G, Hahn-Ketter AE, Fedor A. Traumatic brain injury as a risk factor for Alzheimer's disease: current knowledge and future directions. Neurodegener Dis Manag. 2016;6(5):417-29.

28. Sahathevan R, Brodtmann A, Donnan GA. Dementia, stroke, and vascular risk factors; a review. Int J Stroke. 2012;7(1):61-73.

29. Sivanandam TM, Thakur MK. Traumatic brain injury: a risk factor for Alzheimer's disease. Neurosci Biobehav Rev. 2012;36(5):1376-81.

30. Washington PM, Morffy N, Parsadanian M, Zapple DN, Burns MP. Experimental traumatic brain injury induces rapid aggregation and oligomerization of amyloid-beta in an Alzheimer's disease mouse model. J Neurotrauma. 2014;31(1):125-34.

31. Deutsch MB, Mendez MF, Teng E. Interactions between traumatic brain injury and frontotemporal degeneration. Dement Geriatr Cogn Disord. 2015;39(3-4):143-53.

32. Lou D, Du Y, Huang D, Cai F, Zhang Y, Li T, et al. Traumatic Brain Injury Alters the Metabolism and Facilitates Alzheimer's Disease in a Murine Model. Mol Neurobiol. 2018;55(6):4928-39.

33. Shishido H, Kishimoto Y, Kawai N, Toyota Y, Ueno M, Kubota T, et al. Traumatic brain injury accelerates amyloid-beta deposition and impairs spatial learning in the triple-transgenic mouse model of Alzheimer's disease. Neurosci Lett. 2016;629:62-7.

34. Roberts GW, Gentleman SM, Lynch A, Graham DI. beta A4 amyloid protein deposition in brain after head trauma. Lancet. 1991;338(8780):1422-3.

35. Roberts GW, Gentleman SM, Lynch A, Murray L, Landon M, Graham DI. Beta amyloid protein deposition in the brain after severe head injury: implications for the pathogenesis of Alzheimer's disease. J Neurol Neurosurg Psychiatry. 1994;57(4):419-25.

36. DeKosky ST, Abrahamson EE, Ciallella JR, Paljug WR, Wisniewski SR, Clark RS, et al. Association of increased cortical soluble abeta42 levels with diffuse plaques after severe brain injury in humans. Arch Neurol. 2007;64(4):541-4.

37. McKenzie KJ, McLellan DR, Gentleman SM, Maxwell WL, Gennarelli TA, Graham DI. Is beta-APP a marker of axonal damage in short-surviving head injury? Acta Neuropathol. 1996;92(6):608-13.

38. Loane DJ, Pocivavsek A, Moussa CE, Thompson R, Matsuoka Y, Faden AI, et al. Amyloid precursor protein secretases as therapeutic targets for traumatic brain injury. Nat Med. 2009;15(4):377-9.

39. Van Nostrand WE, Davis J, Previti ML, Xu F. Clearance of amyloid-beta protein deposits in transgenic mice following focal cerebral ischemia. Neurodegener Dis. 2012;10(1-4):108-11.

40. Johnson VE, Stewart W, Smith DH. Traumatic brain injury and amyloid-beta pathology: a link to Alzheimer's disease? Nat Rev Neurosci. 2010;11(5):361-70.

41. Collins JM, King AE, Woodhouse A, Kirkcaldie MT, Vickers JC. The effect of focal brain injury on beta-amyloid plaque deposition, inflammation and synapses in the APP/PS1 mouse model of Alzheimer's disease. Exp Neurol. 2015;267:219-29.

42. Cheng WH, Stukas S, Martens KM, Namjoshi DR, Button EB, Wilkinson A, et al. Age at injury and genotype modify acute inflammatory and neurofilament-light responses to mild CHIMERA traumatic brain injury in wild-type and APP/PS1 mice. Exp Neurol. 2018;301(Pt A):26-38.

43. Morin A, Mouzon B, Ferguson S, Paris D, Saltiel N, Lungmus C, et al. Treatment With Nilvadipine Mitigates Inflammatory Pathology and Improves Spatial Memory in Aged hTau Mice After Repetitive Mild TBI. Front Aging Neurosci. 2018;10:292.

44. Villapol S, Loane DJ, Burns MP. Sexual dimorphism in the inflammatory response to traumatic brain injury. Glia. 2017;65(9):1423-38.

45. Roof RL, Hall ED. Gender differences in acute CNS trauma and stroke: neuroprotective effects of estrogen and progesterone. J Neurotrauma. 2000;17(5):367-88.

46. Eckman EA, Adams SK, Troendle FJ, Stodola BA, Kahn MA, Fauq AH, et al. Regulation of steady-state beta-amyloid levels in the brain by neprilysin and endothelin-converting enzyme but not angiotensin-converting enzyme. J Biol Chem. 2006;281(41):30471-8.

47. Leissring MA, Turner AJ. Regulation of distinct pools of amyloid beta-protein by multiple cellular proteases. Alzheimers Res Ther. 2013;5(4):37.

48. Martone RL, Zhou H, Atchison K, Comery T, Xu JZ, Huang X, et al. Begacestat (GSI-953): a novel, selective thiophene sulfonamide inhibitor of amyloid precursor protein gamma-secretase for the treatment of Alzheimer's disease. J Pharmacol Exp Ther. 2009;331(2):598-608.

49. Uryu K, Laurer H, McIntosh T, Pratico D, Martinez D, Leight S, et al. Repetitive mild brain trauma accelerates Abeta deposition, lipid peroxidation, and cognitive impairment in a transgenic mouse model of Alzheimer amyloidosis. J Neurosci. 2002;22(2):446-54.

50. Wang Y, Martinez-Vicente M, Kruger U, Kaushik S, Wong E, Mandelkow EM, et al. Tau fragmentation, aggregation and clearance: the dual role of lysosomal processing. Hum Mol Genet. 2009;18(21):4153-70.

51. Sun MK, Passaro AP, Latchoumane CF, Spellicy SE, Bowler M, Goeden M, et al. Extracellular Vesicles Mediate Neuroprotection and Functional Recovery after Traumatic Brain Injury. J Neurotrauma. 2020;37(11):1358-69.

52. Kayed R, Head E, Sarsoza F, Saing T, Cotman CW, Necula M, et al. Fibril specific, conformation dependent antibodies recognize a generic epitope common to amyloid fibrils and fibrillar oligomers that is absent in prefibrillar oligomers. Mol Neurodegener. 2007;2:18.

53. Abu Hamdeh S, Waara ER, Moller C, Soderberg L, Basun H, Alafuzoff I, et al. Rapid amyloid-beta oligomer and protofibril accumulation in traumatic brain injury. Brain Pathol. 2018;28(4):451-62.

54. Ikonomovic MD, Uryu K, Abrahamson EE, Ciallella JR, Trojanowski JQ, Lee VM, et al. Alzheimer's pathology in human temporal cortex surgically excised after severe brain injury. Exp Neurol. 2004;190(1):192-203.

55. Loane DJ, Washington PM, Vardanian L, Pocivavsek A, Hoe HS, Duff KE, et al. Modulation of ABCA1 by an LXR agonist reduces beta-amyloid levels and improves outcome after traumatic brain injury. J Neurotrauma. 2011;28(2):225-36.

56. Pajoohesh-Ganji A, Burns MP, Pal-Ghosh S, Tadvalkar G, Hokenbury NG, Stepp MA, et al. Inhibition of amyloid precursor protein secretases reduces recovery after spinal cord injury. Brain Res. 2014;1560:73-82.

57. Saito T, Matsuba Y, Mihira N, Takano J, Nilsson P, Itohara S, et al. Single App knock-in mouse models of Alzheimer's disease. Nat Neurosci. 2014;17(5):661-3.

58. Chiasseu M, Fesharaki-Zadeh A, Saito T, Saido TC, Strittmatter SM. Gene-environment interaction promotes Alzheimer's risk as revealed by synergy of repeated mild traumatic brain injury and mouse App knock-in. Neurobiol Dis. 2020;145:105059.

59. Hampton AL, Hish GA, Aslam MN, Rothman ED, Bergin IL, Patterson KA, et al. Progression of ulcerative dermatitis lesions in C57BL/6Crl mice and the development of a scoring system for dermatitis lesions. J Am Assoc Lab Anim Sci. 2012;51(5):586-93.

60. Kim J, Onstead L, Randle S, Price R, Smithson L, Zwizinski C, et al. Abeta40 inhibits amyloid deposition in vivo. J Neurosci. 2007;27(3):627-33.

61. Sanchez-Mendoza EH, Carballo J, Longart M, Hermann DM, Doeppner TR. Implantation of Miniosmotic Pumps and Delivery of Tract Tracers to Study Brain Reorganization in Pathophysiological Conditions. J Vis Exp. 2016(107):e52932.

62. Rubenstein R, Chang B, Grinkina N, Drummond E, Davies P, Ruditzky M, et al. Tau phosphorylation induced by severe closed head traumatic brain injury is linked to the cellular prion protein. Acta Neuropathol Commun. 2017;5(1):30.

CHAPTER 3

AIM 2

3.1 Background

Cerebral Aβ levels are potently regulated by a diverse group of Aβ-degrading proteases (AβDPs) that—importantly—differ in numerous ways relevant to AD pathogenesis. For example, individual AβDPs can be altered differentially in AD, with some showing decreasing levels with age (e.g., neprilysin (1)) and others (e.g., cathepsin D (CatD)) showing increasing levels (2, 3)). In addition, some AβDPs are quantitatively more important than others for Aβ proteostasis (e.g., neprilysin versus neprilysin-2) (4). Moreover, certain ADBPs (e.g. plasmin) are operative only in a pathological context (5). Finally, AβDPs can differ functionally in terms of their ability to degrade Aβ in different aggregation states (e.g., monomers, oligomers, protofibrils, etc.), with some proteases capable only of degrading monomers (e.g., IDE) (6) and others capable of degrading fully-formed plaques (e.g., matrix-metalloprotease-9 (MMP-9)) (7).

AβDPs also vary considerably in terms of subcellular location (e.g., extracellular, lysosomal, etc.), and this has extremely important ramifications for Aβ proteostasis and its role in AD pathogenesis. In contrast to perturbations in APP processing, which affect Aβ in all subcellular compartments equally, spatially distinct AβDPs can regulate Aβ levels within specific subcellular compartments, thus defining discrete "pools" of Aβ (8). This may be of very high relevance to elucidating the precise mechanisms by which Aβ impacts AD pathogenesis, and hence is deserving of detailed consideration. For instance, Golde and colleagues used a highly innovative transgenic system to target Aβ production exclusively to the extracellular space (9). These mice develop abundant extracellular deposits of Aβ, including dense-core plaques; however, unlike mice overexpressing APP and exhibiting similar Aβ plaque pathology, these mice show no cognitive

deficits (10). In marked contrast, exquisitely low concentrations of Aβ microinjected into the cytoplasm of cultured neurons was found to be profoundly neurotoxic (11). In general, there is emerging evidence that intracellular pools of Aβ may be particularly critical to AD pathogenesis (12). Nevertheless, it remains unknown precisely which intracellular pools (e.g. cytosolic vs. lysosomal) are most relevant to AD. Moreover, addressing this topic has proved considerably challenging, given the comparatively high levels of Aβ in the extracellular space. Given that spatially distinct AβDPs can regulate discrete intracellular pools of Aβ, it follows that the dysregulation of particular proteases could critically affect AD pathogenesis, irrespective of their quantitative impact on overall brain Aβ levels. In addition, manipulation of spatially distinct AβDPs provides a powerful way for investigating the role of specific pools of Aβ.

Among the various pools of Aβ, lysosomal Aβ may be of particular importance for AD pathogenesis. It has been recognized for decades that lysosomal perturbations represent some of the earliest molecular changes observed in the AD brain (Fig. 3.1). The lysosome is the compartment responsible for breaking down the vast majority of proteins, and numerous proteases are located there, several of which are AβDPs (e.g., CatD and cathepsin B (CatB)). With aging and in AD, the lysosome expands and eventually becomes leaky, resulting in its contents spilling into the cytoplasm (3, 13, 14). Importantly, Aβ accumulates in the lysosome with age (Fig. 3.1) as a large portion of Aβ produced within the endolysosomal pathway is trafficked to the lysosome. Significantly, cellular uptake and trafficking of Aβ to lysosomes appears to be mediated by the strongest known genetic risk factor for LOAD, ApoE, with the neutral ApoE ε3 allele being more efficient at facilitating Aβ trafficking and degradation than the risky ApoE ε4 allele (15)

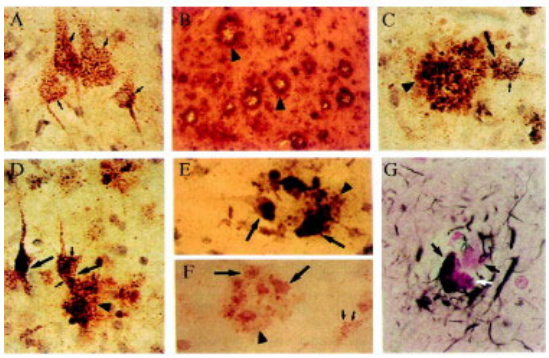

Figure 3.1. Lysosomal dysfunction in AD. IHC staining of the prefrontal cortex in AD brains show CatD staining in lysosomes (***A, C, D, F*** small arrow) and thioflavin S positive plaques (***B-F***) IHC of AD brain reveals that CatD is heavily localized in plaques and that plaques were commonly associated with degenerating neurons Reprinted with permission from Cataldo and Nixon, 1990 *Proc Natl Acad Sci* (3).

While the processing of Aβ in the lysosome is a normal part of Aβ proteostasis, the acidic environment present in the lysosome causes Aβ—particularly Aβ42—to aggregate extremely rapidly. To characterize this phenomenon more completely, we used circular dichroism to monitor the secondary structure of freshly prepared, size-exclusion purified monomeric Aβ40 and Aβ42. As shown in Figure 3.2, immediately after lowering the pH of the solution from pH=8 to pH=4, Aβ42 shows a very rapid increase in β-pleated sheet formation (evidenced by a drop in CD intensity). Aβ40 also forms β-pleated sheets at pH=4, albeit to a lesser extent, and at a much slower rate (Fig. 3.2). Notably, Aβ42 that has been treated for 1 hour at pH=4 remains aggregated after the pH is returned to pH=8. By contrast, Aβ40 treated similarly returns to an unaggregated state. Thus, the lysosome may be particularly important for Aβ proteostasis, not only because it is the site of degradation by multiple AβDPs, but also because Aβ aggregates rapidly in the acidic environment of the lysosome. Moreover, since Aβ42 aggregates irreversibly after even short exposure to low pH, it will remain aggregated if it is leaked into the cytoplasm, as is known to occur with normal aging and particularly in AD (3).

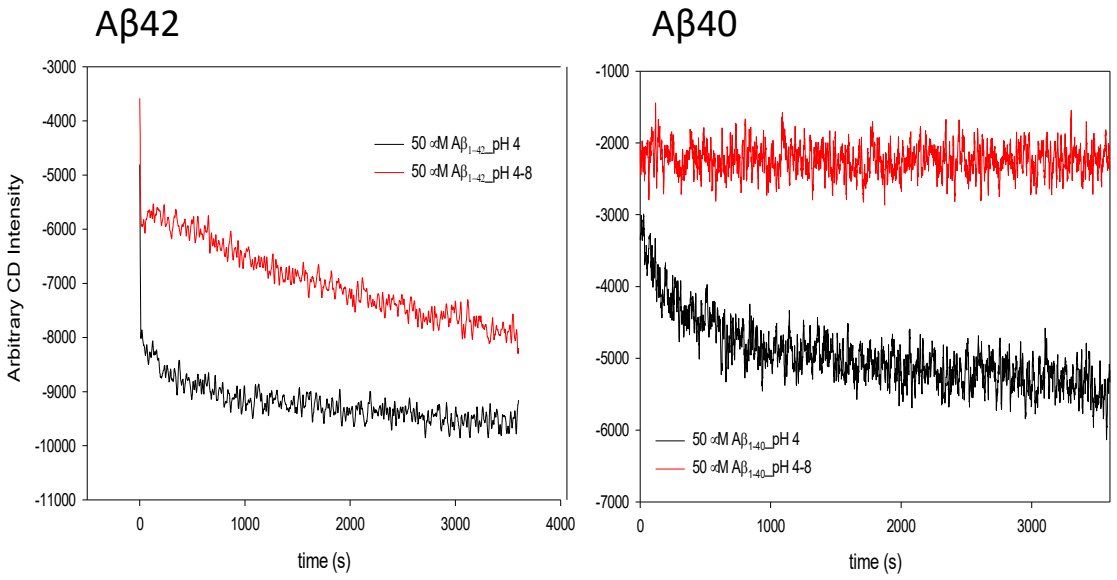

Figure 3.2. Rapid and irreversible fibrilization of Aβ42 at acidic pH. ***Black lines,*** Changes in circular dichroism, a method that detects β-pleated sheets, showing the rate of aggregation of Aβ42 and Aβ40 immediately after adjustment of the pH from 8.0 to 4.0. Note that Aβ42 aggregates within seconds, while Aβ40 also aggregates, but more slowly. ***Red lines,*** Comparable data obtained after treatment of Aβ42 or Aβ40 at acidic pH for 1 hour, then re-adjustment of the pH to 8.0. Note that Aβ42 exposed transiently to an acidic environment remains aggregated and continues to aggregate at neutral pH. By contrast, Aβ40 returns to an unaggregated state. Leissring, Unpublished observation.

CatD is an aspartyl protease located primarily in the lysosome and the cytosol and to lesser extents in the cytoplasm and extracellular space (13, 16) (Fig. 3.3A). CatD is part of the cathepsin family of enzymes that are ubiquitously expressed in all cell types and often found both intracellularly and extracellularly (17). They are located primarily within the lysosome and are pivotal for a variety of functions, including ion channel activity, autophagy, and cell proliferation (18). CatD degrades a variety of substrates including Aβ, fibronectin, laminin, and tau (18, 19). The lysosomal location of CatD, along with its ability to degrade both Aβ and tau, suggest it may play a particularly important role in AD pathogenesis (Fig. 3.3B). Nevertheless, the precise role of CatD in Aβ proteostasis remains almost completely unknown.

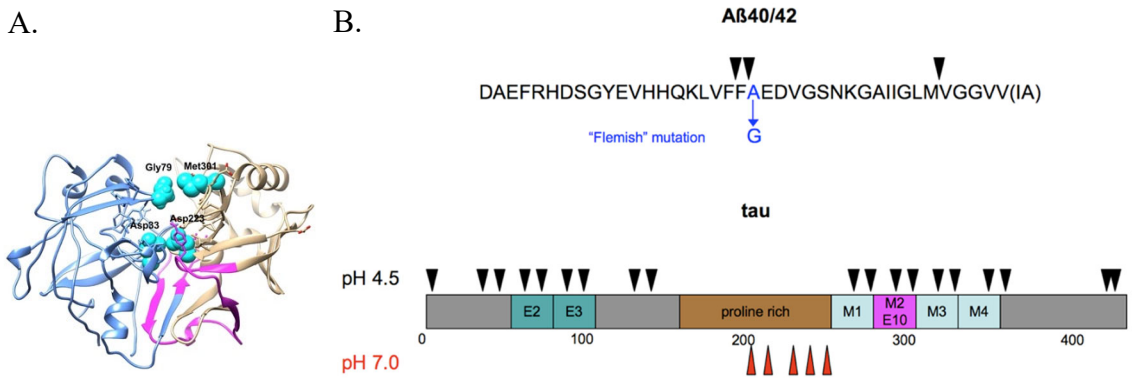

Figure 3.3. Cathepsin D degrades Aβ and tau. ***A***, Crystal structure of CatD showing the N-terminal domain (residues 1–188) in blue color, C-terminal domain (residues 189–346) in gold color, and an inter-domain region (residues 160–200) in pink color as well as the important aspartic acids and flap tip residues (also known as hairpin loop). ***B***, Cleavage sites within Aβ and tau mediated by CatD (20-22). Reprinted from Arodola and Soliman, 2016 *J Cell Biochem* with permission from John Wiley and Sons (23).

At the histopathological level, cathepsins are commonly found clustered around Aβ plaques and co-localized with tau, and enzymatically active CatD has been found in senile plaques (2, 3, 16, 24, 25). Additionally, researchers have found increases in inactive pro-CatD (the precursor to CatD) (26) and localized increases in CatD in AD brain (2). Notably, Perez and colleagues found that CatD was significantly upregulated in MCI patients compared to both control and AD patients (27). Intriguingly, ApoEε4 has been suggested to promote the expansion and permeability of lysosomes (28), lending further support to the idea that changes in the lysosome lead to modifications in Aβ proteostasis through alterations in CatD.

Considered exclusively as an AβDP, increases in CatD levels would be expected to be beneficial in AD in principle, but elevations in CatD can lead to deleterious consequences as well, including promotion of inflammation and apoptosis (18). Transcription of the CatD gene (*CTSD*) is triggered by cytokines (29), and other groups have found evidence that CatD may be proapoptotic. For instance, CatD is upregulated in degenerating neurons (14) and secreted by

activated microglia to induce cell death (30). Both pro-CatD and CatD are secreted in response to stress and inflammation (17). As an aspartyl protease, CatD should only be active at an acidic pH but more recent work has shown that CatD is enzymatically active in the cytosol and the extracellular space (13, 16). Nevertheless, CatD may in fact have nonproteolytic functions, as well.

Despite numerous studies implicating CatD in AD pathogenesis, most have been largely descriptive in nature, and only a few have addressed the role of CatD in Aβ proteostasis. The following publication is aimed to help close this large gap in our understanding, which we accomplished by characterizing Aβ proteostasis in mice with genetic deletion of CatD (Aim 2A) and by extensively characterizing CatD-mediated Aβ degradation *in vitro* (Aim 2B).

3.2 Aims and rationale

Aim 2A: Consequences of cathepsin D deletion on Aβ proteostasis

Rationale & Hypothesis: Dysregulation of spatially distinct AβDPs, by virtue of their ability to regulate discrete pools of Aβ, was predicted to affect Aβ proteostasis in ways that could differentially impact AD pathogenesis. We hypothesized that cathepsin D (CatD), a lysosomal protease shown to degrade Aβ *in vitro*, regulates lysosomal pools of Aβ, leading to quantitative or qualitative changes in Aβ proteostasis that are relevant to AD pathogenesis.

Aim 2B: Enzymological characterization of Aβ degradation by cathepsin D

Rationale & Hypothesis: Results from Aim 2A revealed that CatD-null (CatD-KO) brains have dramatic increases in insoluble Aβ42 and Aβ40 and—significantly—the Aβ42/40 ratio is consistently increased >25% compared to wild-type controls. It is hypothesized this increase in the Aβ42/40 ratio may be attributable to differences in the kinetics of degradation of Aβ42 and Aβ40 by CatD.

3.3 Publication 1:

Cathepsin D regulates cerebral Aβ42/40 ratios via differential degradation of Aβ42 and Aβ40

3.3.1 Abstract

Cathepsin D (CatD) is a lysosomal protease that degrades both the amyloid β-protein (Aβ) and the microtubule-associated protein, tau, and has been genetically linked to late-onset Alzheimer disease (AD). Here we sought to examine the consequences of genetic deletion of CatD on Aβ proteostasis *in vivo* and to more completely characterize the degradation of Aβ42 and Aβ40 by CatD. We quantified Aβ degradation rates and levels of endogenous Aβ42 and Aβ40 in the brains of CatD null (CatD-KO), heterozygous null (CatD-HET) and wildtype (WT) control mice. CatD-KO mice die by ~4 weeks of age, so tissues from younger mice, as well as embryonic neuronal cultures were investigated. Enzymological assays and surface plasmon resonance were employed to quantify the kinetic parameters (K_M, k_{cat}) of CatD-mediated degradation of monomeric human Aβ42 vs. Aβ40, and the degradation of aggregated Aβ42 species was also characterized. Competitive inhibition assays were used to interrogate the relative inhibition of full-length human and mouse Aβ42 and Aβ40, as well as corresponding p3 fragments. Genetic deletion of CatD resulted in 3- to 4-fold increases in insoluble, endogenous cerebral Aβ42 and Aβ40, exceeding the increases produced by deletion of insulin-degrading enzyme, neprilysin or both, together with readily detectable intralysosomal deposits of endogenous Aβ42—all by 3 weeks of age. Quite significantly, CatD-KO mice exhibited ~30% increases in Aβ42/40 ratios, comparable to those induced by presenilin mutations. Mechanistically, the perturbed Aβ42/40 ratios were attributable to pronounced differences in the kinetics of degradation of Aβ42 vis-à-vis Aβ40. Specifically, Aβ42 shows a low-nanomolar affinity for CatD, along with an exceptionally slow turnover rate that, together, render Aβ42 a highly potent competitive inhibitor of CatD. Notably,

the marked differences the processing of Aβ42 vs. Aβ40 also extend to p3 fragments ending at positions 42 vs. 40. Our findings identify CatD as the principal intracellular Aβ-degrading protease identified to date, one that regulates Aβ42/40 ratios via differential degradation of Aβ42 vs. Aβ40. The finding that Aβ42 is a potent competitive inhibitor of CatD suggests a possible mechanistic link between elevations in Aβ42 and downstream pathological sequelae in AD.

3.3.2 Introduction

Extracellular deposition of the amyloid β-protein (Aβ) is the most widely accepted pathognomonic marker of Alzheimer disease (AD). However, another early and invariant feature of AD is lysosomal dysfunction, and accruing evidence suggests that the lysosome may be a pivotal locus for the molecular pathogenesis of the disease (31, 32). Aβ is generated in the endolysosomal system by acidic proteases and secreted into the extracellular space, but an as-yet unquantified portion is also shuttled to lysosomes (33). Secreted Aβ is likewise trafficked to lysosomes in an ApoE-dependent manner (34). More recently, accruing evidence suggests that tau, particularly misfolded variants, is also trafficked to the lysosome via chaperone-mediated autophagy (35). Misfolded tau, in turn, is widely accepted as the proximal cause of neuronal cell loss and consequent cognitive disturbances in AD and multiple other neurodegenerative diseases (36). Collectively, these observations suggest that lysosomal disturbances may be highly relevant to the pathogenic role of Aβ and tau and, potentially, their interrelationship.

Cathepsin D (CatD) is a lysosomal aspartyl protease that degrades both Aβ (20, 22) and tau (37) *in vitro* and is strongly implicated in the pathogenesis of AD and multiple other neurodegenerative diseases (38). Loss-of-function mutations in CatD result in multiple forms of neurodegeneration in humans (39) and sheep (40). Moreover, a common variation in the CatD

gene (*CTSD*) has been linked to risk for late-onset AD (41) and to elevated levels of both Aβ42 and tau in cerebrospinal fluid (42, 43).

Multiple lines of evidence suggest that impaired Aβ degradation may play a role in the pathogenesis of AD (44, 45). Several specific Aβ-degrading proteases (AβDPs) have been identified that, when deleted *in vivo*, result in significant increases in cerebral Aβ levels, including neprilysin (NEP) (46-48), insulin-degrading enzyme (IDE) (49, 50) and many others (44, 45). Conversely, overexpression of several AβDPs has been shown to dramatically reduce AD-type pathology in mouse models of the disease (51, 52). Nevertheless, some proteases shown to degrade Aβ *in vitro*, including CatD, have not yet been thoroughly assessed *in vivo*.

This study sought to elucidate the role of CatD in Aβ proteostasis *in vivo*, using CatD null (CatD-KO) mice and several complementary approaches. CatD-KO mice die prematurely by ~4 weeks of age due to peripheral causes and are a well-established model of neuronal ceroid lipofuscinosis (53), but they remain healthy and comparable in body weight to WT mice until ~23 days of age (54, 55). Using tissue extracts from younger CatD-KO mice, cultured embryonic neurons, ELISA measurements in mice across a range of ages (15- to 26-days old), as well as extensive *in vitro* experiments, we provide compelling evidence that CatD plays a significant role in Aβ proteostasis *in vivo*. Although the premature lethality in these mice precludes the assessment of CatD deletion on all aspects of AD-type pathology, our findings suggest that future work on the role of CatD in Aβ proteostasis, using more sophisticated methods for manipulating CatD in a regulatable manner *in vivo*, is highly warranted.

3.3.3 Results

CatD is the major soluble Aβ-degrading protease at acidic pH

As an initial step toward elucidating the role of CatD in Aβ proteostasis, we quantified rates of Aβ degradation *in vitro* in soluble brain extracts from CatD-KO mice and wild-type

controls (54) as a function of pH, focusing on extracts from 15-day-old mice, due to the premature lethality of CatD-KO mice that occurs by ~4 weeks of age (54, 55). Consistent with previous results (20, 56), Aβ-degrading activity was present principally within two pH ranges: at neutral pH (pH 7.5 to 9.5) and—to a considerably larger extent—also at acidic pH (pH 2.5 to 4.5) (Fig. 3.4A). The Aβ-degrading activity at neutral pH was inhibited by excess insulin and reflects the activity of the neutral protease insulin-degrading enzyme (IDE), as shown previously by McDermott and Gibson (56). By contrast, the abundant Aβ-degrading activity at acidic pH in WT brain extracts was essentially absent in extracts from CatD-KO mice, strongly suggesting that CatD is the primary soluble AβDP in brain (Fig. 3.4A). To extend and confirm these findings, we quantified Aβ degradation at pH 4.0 in soluble brain extracts from CatD-KO and WT mice, as well as heterozygous null (CatD-HET) mice (Fig. 3.4B). As expected, the Aβ-degrading activity present in WT (and CatD-HET) extracts at acidic pH was inhibited almost completely by pepstatin A (PepA), a potent CatD inhibitor (Fig. 3.4B), reinforcing the conclusion that CatD is indeed the principal AβDP operative at acidic pH, and ruling out alternative explanations such as compensatory changes in other AβDPs. Confirming this, western blotting revealed that levels of the amyloid-precursor protein (APP), APP C-terminal fragments, and two other major AβDPs—IDE and NEP—were unchanged in CatD-KO brains relative to WT controls (Appendix B Fig. S3.1). Surprisingly, however, in CatD-HET extracts, Aβ-degrading activity (Fig. 3.4B) and CatD activity assessed by a selective substrate (Fig. 3.4B, inset) were not reduced to 50% of WT levels, as expected, but instead were reduced by considerably less (23.2 ± 10.7% and 26.4 ± 13.4%, respectively, for the two different activity assays; $P > 0.05$ in both cases), suggesting that some degree of compensatory upregulation of CatD occurs in the heterozygous state. Consistent with this, levels of both preprocathepsin D and mature CatD protein in the CatD-HET animals were

also determined to be >50% of WT levels (Fig. 3.4C, D), with mature CatD protein being reduced by only 26.0 ± 14.2% relative to WT controls *(P* > 0.05; Fig. 3.4D).

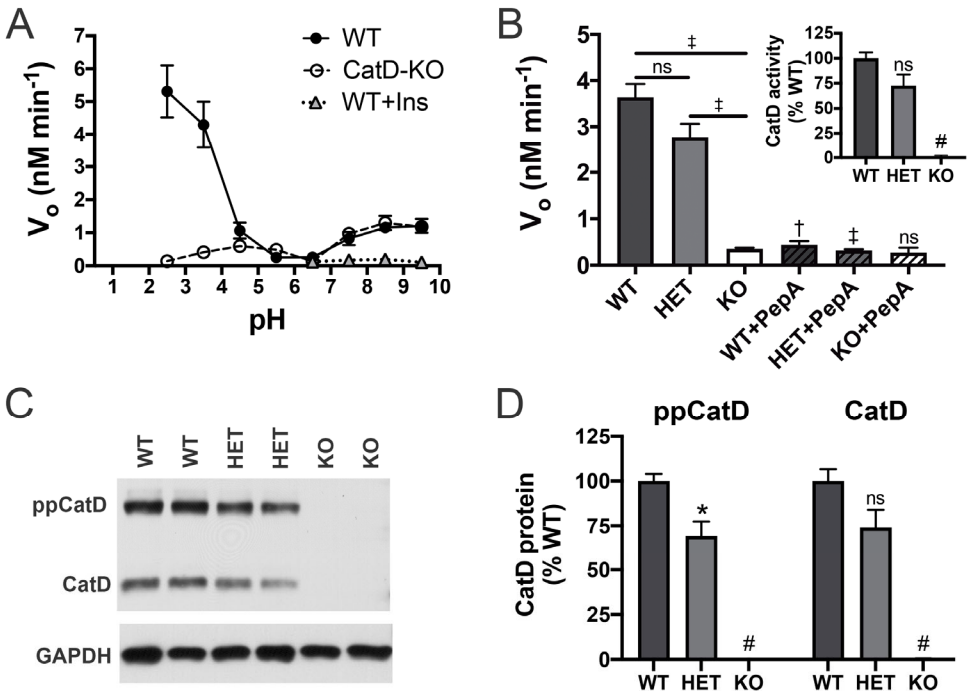

Figure 3.4. CatD activity and protein levels in brain extracts. ***A***, Aβ degradation in soluble brain extracts from 15-day-old WT and CatD-KO mice as a function of pH. Note that the abundant Aβ-degrading activity occurring at acidic pH is essentially absent in CatD-KO extracts. Note also that the smaller peak at neutral pH is inhibited by insulin (Ins), reflecting IDE activity (56). Data are mean ± SEM for 5 replicates. $^{\dagger}P$ <0.01. ***B***, Aβ-degrading activity in extracts from 15-day-old CatD-KO, -HET and -WT mice at pH 4.0. Note that the activity in WT and CatD-HET extracts is largely inhibited by the CatD inhibitor, pepstatin A (PepA). Data are mean ± SEM for 4 replicates. $^{\dagger}P$ <0.01; $^{\ddagger}P$ <0.001; $^{\#}P$ <0.0001. *Inset* shows CatD activity in brain extracts from WT, CatD-HET and CatD-KO mice measured directly using a selective substrate. Data are mean ± SEM for 4 replicates.; $^{\#}P$ <0.0001. Note also that Aβ-degrading activity in the CatD-HET extracts is not reduced by 50% as expected from deletion of one of two *CTSD* alleles. ***C***,***D***, Representative western blot (***C***) and quantification of multiple samples (***D***) showing relative CatD levels in CatD-KO, -HET and -WT mice. Note that, consistent with the activity data in (***B***), CatD levels in CatD-HET brains are not 50% of those in WT brains. Data in (***D***) are mean ± SEM for 6 samples per genotype. *P <0.05; $^{\#}P$ <0.0001.

Deletion of CatD increases insoluble Aβ42 and Aβ40 as well as Aβ42/40 ratios

To investigate whether CatD regulates cerebral Aβ levels *in vivo*, we quantified endogenous Aβ levels in the brains of CatD-KO, CatD-HET mice and WT controls, analyzing both diethylamine (DEA)-soluble and -insoluble (guanidinium extracted) cerebral extracts using

well-established Aβ42- and Aβ40-specific ELISAs (57-59). Soluble Aβ is generally believed to reflect primarily monomeric Aβ species, with insoluble Aβ reflecting aggregated forms (59). Because CatD-KO mice suffer from premature lethality by ~4 weeks of age (54, 55), we elected to analyze mice across a range of ages (15 to 26 days old). Relative to age-matched WT controls, levels of insoluble cerebral Aβ42 (Fig. 3.5A) and Aβ40 (Fig. 3.5B) were significantly increased in CatD-KO brains at all ages examined, including multiple time points well before any signs of moribundity (which first occurs at ~23 days of age 54, 55). In CatD-KO mice, the concentrations of both peptides rose in an age-dependent manner, culminating in a ~4-fold increase in insoluble Aβ42 and a ~2.5-fold increase in insoluble Aβ40 in CatD-KO mice relative to WT mice at 26 days of age (Fig. 3.5A, B). In marked contrast, insoluble Aβ42 and Aβ40 levels in CatD-HET mice were not significantly different from WT controls. The increases in insoluble Aβ42 and Aβ40 in CatD-KO relative to WT controls were highly significant at all ages, both in terms of pairwise comparisons between age-matched groups (Fig. 3.5A, B) and when analyzed by ANOVA using a mixed-effects model ($P<0.0001$ for age, genotype, and age x genotype for both Aβ42 and Aβ40). Of special interest, the percent increase in Aβ42 seemed consistently higher than that of Aβ40 at all ages examined, so we calculated the ratios of insoluble Aβ42 to Aβ40 for all mice examined.

Overall, CatD-KO mice showed a highly statistically significant ($P<0.0001$) ~30% increase in insoluble Aβ42/40 ratios relative to WT controls (Fig. 3.5C), an increase comparable in scale to that induced by many AD-linked presenilin mutations (57, 60, 61). In contrast, cerebral Aβ42/40 ratios were not significantly changed in mice lacking NEP (NEP-KO) or IDE (IDE-KO—or both NEP and IDE, simultaneously (NEP/IDE-DKO; Fig. 3.5C). In parallel, using the same methods, we also quantified insoluble Aβ42 and Aβ40 levels in age- and sex-matched NEP-KO, IDE-KO and NEP/IDE-DKO mice. Relative to their respective WT controls, the percent increases

in insoluble Aβ42 (Fig. 3.5D) and Aβ40 (Fig. 3.5E) in 26-day-old CatD-KO mice were found to be significantly higher than those in age-matched NEP-KO, IDE-KO and NEP/IDE-DKO mice, suggesting that the contribution of CatD to overall brain Aβ proteostasis *in vivo* exceeds that of both NEP and IDE.

In contrast to the consistently large increases in insoluble—likely aggregated—forms of Aβ seen in CatD-KO mice, levels of endogenous soluble Aβ42 (Appendix B Fig. S3.2A) and Aβ40 (Appendix B Fig. S3.2B) were lower overall, and consequently more variable, but nevertheless exhibited highly significant trends towards decreasing levels as a function of increasing age (P<0.0001 for age x genotype for both Aβ42 and Aβ40 using a mixed-effects multiple comparison ANOVA), with significant decreases in both peptides relative to WT mice evident at 26 days of age (Appendix B Fig. S3.2A, B). Similarly, opposite to the case for insoluble Aβ, soluble Aβ42/40 ratios were significantly decreased in CatD-KO mice relative to WT controls (Appendix B Fig. S3.2C). Nevertheless, because significantly less soluble vs. insoluble Aβ was extracted, the overall (soluble plus insoluble) Aβ42/40 ratios remained significantly elevated in CatD-KO mice (Appendix B Fig. S3.2D). NEP-KO, IDE-KO and NEP/IDE-DKO mice, by contrast, showed no significant changes in soluble or overall Aβ42/40 ratios (Appendix B Fig. S3.2C,D). Unlike 26-day-old CatD-KO mice, which exhibited lower soluble Aβ levels relative to their WT controls, age-matched NEP-KO and IDE-KO mice showed significant increases in both soluble Aβ42 (Appendix B Fig. S3.2E) and Aβ40 (Appendix B Fig. S3.2F) relative to their respective WT controls.

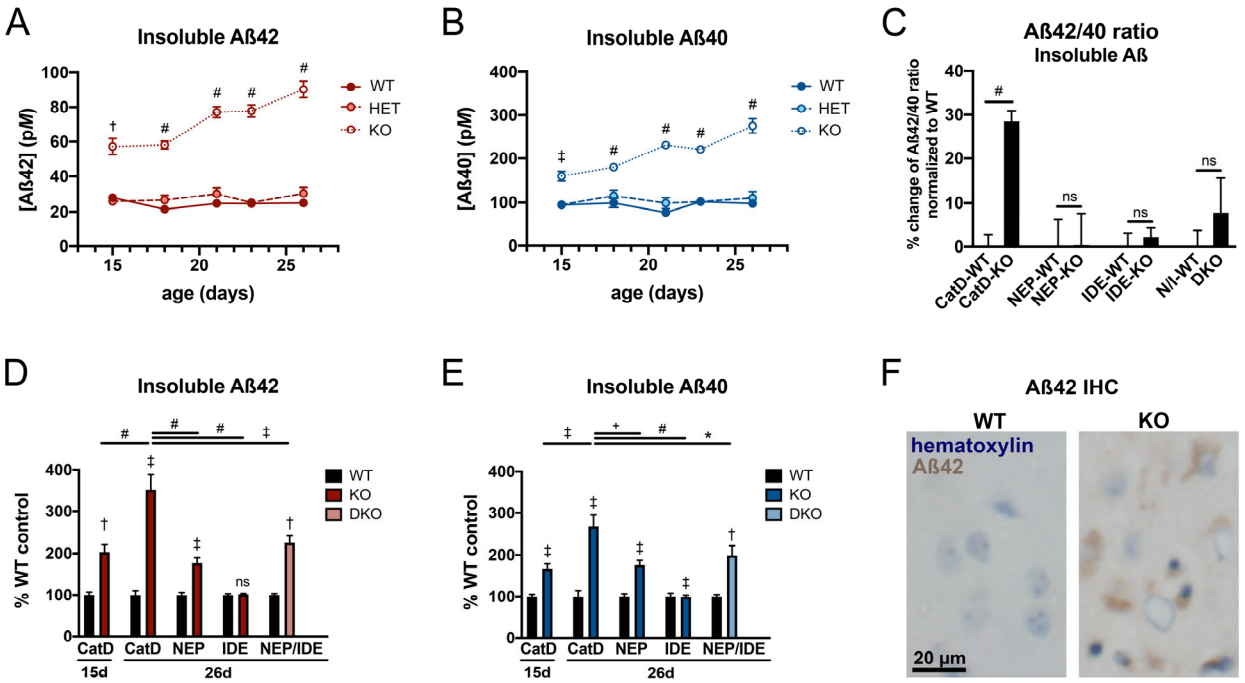

Figure 3.5. Insoluble Aβ42 and Aβ40 levels in CatD-KO, -HET and -WT brains. ***A***,***B***, Levels of insoluble, endogenous brain Aβ42 (***A***) and Aβ40 (***B***) in CatD-KO, -HET and -WT mice as a function of age. Note that levels of both Aβ species are markedly increased in CatD-KO, but not in CatD-HET, mice relative to WT controls at all ages examined. Data are mean ± SEM for 4-6 replicates per group. $^{\dagger}P$ <0.01; $^{\ddagger}P$ <0.001; $^{\#}P$<0.0001. ***C***, Insoluble Aβ42/40 ratios are significantly increased in CatD-KO mice, but not NEP-KO, IDE-KO or NEP/IDE-DKO mice, relative to their respective WT controls. Data are mean ± SEM for 28-30 replicates per group for CatD-KO and -WT mice and 6-11 replicates per group for the other genotypes. $^{\#}P$<0.0001. ***D***,***E***, Percent increases in insoluble, endogenous brain Aβ42 (***D***) and Aβ40 (***E***) in 15-d-old and 26-d-old CatD-KO mice as compared to 26-d-old NEP-KO, IDE-KO and NEP/IDE double-knockout (DKO) mice, all normalized to respective WT controls. Note that 26-d-old CatD-KO mice exhibit significantly higher increases in insoluble Aβ42 and Aβ40 above their WT controls than age-matched mice lacking NEP, IDE or both NEP and IDE. Data are mean ± SEM for 4-6 replicates per group. *P<0.05; $^{\dagger}P$<0.01; $^{\ddagger}P$<0.001; $^{\#}P$<0.0001. ***F***, Intracellular endogenous Aβ42 accumulation occurs in CatD-KO mice by 3 weeks of age. Shown is immunohistochemical staining of a 26-d-old CatD-KO mouse and age-matched WT control with an anti-Aβ42 end-specific antibody (59). Additional immunohistochemical characterization is provided in Appendix B Fig. S3.4.

In contrast to the consistently large increases in insoluble—likely aggregated—forms of Aβ seen in CatD-KO mice, levels of endogenous soluble Aβ42 (Appendix B Fig. S3.2A) and Aβ40 (Appendix B Fig. S3.2B) were lower overall, and consequently more variable, but nevertheless exhibited highly significant trends towards decreasing levels as a function of increasing age (P<0.0001 for age x genotype for both Aβ42 and Aβ40 using a mixed-effects multiple comparison

ANOVA), with significant decreases in both peptides relative to WT mice evident at 26 days of age (Appendix B Fig. S3.2A,B). Similarly, opposite to the case for insoluble Aβ, soluble Aβ42/40 ratios were significantly decreased in CatD-KO mice relative to WT controls (Appendix B Fig. S3.2C). Nevertheless, because significantly less soluble vs. insoluble Aβ was extracted, the overall (soluble plus insoluble) Aβ42/40 ratios remained significantly elevated in CatD-KO mice (Appendix B Fig. S3.2D). NEP-KO, IDE-KO and NEP/IDE-DKO mice, by contrast, showed no significant changes in soluble or overall Aβ42/40 ratios (Appendix B Fig. S3.2C,D). Unlike 26-day-old CatD-KO mice, which exhibited lower soluble Aβ levels relative to their WT controls, age-matched NEP-KO and IDE-KO mice showed significant increases in both soluble Aβ42 (Appendix B Fig. S3.2E) and Aβ40 (Appendix B Fig. S3.2F) relative to their respective WT controls.

The fact that CatD-KO mice die at such an early age raises the obvious concern that the elevated Aβ levels may represent a non-specific consequence, rather than a true reflection of the contribution of CatD to brain Aβ proteostasis. Towards the goal of addressing this concern, we quantified cerebral Aβ levels in another mouse model featuring both lysosomal dysfunction and premature lethality: the twitcher mouse. The twitcher mouse harbors a mutation in the galactosylceramidase gene (*GALC*), making it a model of human globoid cell leukodystrophy (Krabbe disease), a lethal lysosomal storage disorder (62, 63). Depending on the genetic background, twitcher mice die anywhere from 40 days of age to 3 months of age (62, 64) and, in our colony, 50% died at ~81 days of age. To assess whether Aβ accumulated in this mouse model, we quantified cerebral Aβ levels in CatD-KO and twitcher mice, both prior to onset of visible neurological symptoms (15 d) and 1-2 days prior to the typical date of death for each model (26 d for CatD-KO; 80 d for twitcher mice). As in previous experiments, relative to WT littermate

controls, CatD-KO mice exhibited statistically significant increases in insoluble Aβ42 and Aβ40 (Appendix B Fig. S3.3A, B) and significant decreases in soluble Aβ42 and Aβ40 (Appendix B Fig. S3.3C, D) at 26, but not 15, days of age. In marked contrast, twitcher mice showed no significant increase in soluble or insoluble Aβ42 or Aβ40 at any age tested relative to age- and sex-matched, colony-specific WT controls (Appendix B Fig. S3.3A-D). While the twitcher mouse model is not a perfect control for the specific phenotype in CatD-KO mice, these results lend support to the conclusion that CatD is a *bona fide* regulator of Aβ proteostasis *in vivo*.

CatD-KO mice develop intralysosomal Aβ42 deposits by 3 weeks of age

The preceding ELISA-based results reflect the levels of Aβ averaged over the entire volume of the cerebrum. The ~4-fold increase in whole-brain Aβ42 levels induced by deletion of CatD, however, might theoretically reflect a considerably larger, localized increase in Aβ42 if limited exclusively to lysosomes. Consistent with this prediction, intracellular deposits of endogenous Aβ42 could be readily detected in the brains of 3-week-old CatD-KO mice, but not WT mice, by conventional immunohistochemical methods (Fig. 3.5F; Appendix B Fig. S3.4A-F). Co-labeling experiments confirmed the presence of abundant Aβ42 in Lamp2-positive lysosomes, which was particularly prominent in neuronal cell bodies in cortical layers III and IV (Appendix B Fig. S3.4G) and in hippocampal CA1 pyramidal neurons (Appendix B Fig. S3.4H). Although Aβ42 is not the only protein expected to accumulate following deletion of CatD, it is notable that neurons containing abundant Aβ42 were also positive for several immunohistochemical markers of amyloid accumulation, including Congo Red, Thioflavin S, and Gallyas silver stains (Appendix B Fig. S3.4I-L).

Primary neurons lacking CatD show defects in intracellular Aβ catabolism

As an independent method of investigating the role of CatD in Aβ degradation, we studied cultured primary hippocampal neurons obtained from embryonic (E18) CatD-KO and WT littermate mice. Consistent with our *in vivo* results, significantly more Aβ42 (Appendix B Fig. S3.5A) was secreted into the conditioned medium of CatD-KO neurons relative to WT controls, with a similar, albeit statistically nonsignificant trend obtained for Aβ40 (Appendix B Fig. S3.5B). To explore whether the observed changes in extracellular Aβ reflected differences in intracellular catabolism *per se*, as opposed to possible effects on Aβ production or secretion, cultured neurons were incubated in the presence of fluorescently labeled Aβ42 and Aβ40, washed to remove excess extracellular Aβ peptides, then allowed to catabolize internalized Aβ for 2 h prior to microscopic analysis. CatD-KO neurons exhibited substantial defects in the catabolism of Aβ42 in particular, and to a lesser extent Aβ40, as determined from the relative amounts of fluorescently tagged Aβ peptides present after the 2-h incubation period (Appendix B Fig. S3.5C-E). Taken together with the findings above, these results strongly suggest that CatD is a powerful regulator of intralysosomal Aβ catabolism, independent of any deleterious phenotype triggered by CatD deletion *in vivo*.

Mechanistic basis for the increase in Aβ42/40 ratios

Given that deletion of CatD produced a highly consistent increase in insoluble (and total) cerebral Aβ42/40 ratios, and in light of differential effects of CatD on Aβ42 vs. Aβ40 levels seen in cultured neurons, we focused our attention on possible mechanisms to account for these seemingly selective effects. Mechanisms affecting the production of Aβ seemed unlikely, based on previous studies demonstrating that Aβ production is unperturbed in CatD-KO neurons (65), as well as our own data (e.g., Appendix B Fig. S3.1). CatD might alternatively affect Aβ42 levels through conversion of Aβ42 to Aβ40 or other shorter species through carboxypeptidase activity,

as has been shown previously for cathepsin B (66). To explore this possibility, we used mass spectrometry to determine the cleavage sites within human Aβ42 and Aβ40 induced by purified human CatD. Consistent with previous studies (20, 22), CatD hydrolyzed both Aβ40 and Aβ42 at the Phe^{19}-Phe^{20} and Phe^{20}-Ala^{21} peptide bonds (Appendix B Table S3.1; Appendix B Figs. S3.6, S3.7). A third cleavage site, which proved to be the major one, occurred at the Leu^{34}-Met^{35} peptide bond (Appendix B Table S3.1; Appendix B Figs. S3.6, S3.7). However, we found no evidence for conversion of Aβ42 to Aβ40.

As a logical step in the characterization of CatD as a novel AβDP, we sought to quantify the kinetics of its degradation of Aβ42 and Aβ40 at pH 4.0. For these and all other enzymological experiments, we were careful to use freshly prepared, well-characterized batches of monomeric human Aβ42 or Aβ40 peptides, which we routinely prepared by size-exclusion chromatography (67, 68). As assessed by multiple quantitative methods, the kinetics of Aβ42 and Aβ40 degradation were found to be strikingly dissimilar. For example, by ELISA, Aβ42 exhibited an unexpectedly strong, low-nanomolar affinity for CatD (K_M = 27.7 ± 6.0 nM), in marked contrast to Aβ40, which showed a low-micromolar value (K_M = 1.51 ± 0.26 μM) that is more typical of the interaction between Aβ and other AβDPs (Fig. 3.6A,B; Appendix B Table S3.2). The k_{cat} values obtained for Aβ42 and Aβ40 were likewise dramatically different (0.23 ± 0.01 *vs*. 20.8 ± 1.1 min^{-1}, respectively; Fig. 3.6A,B; Appendix B Table S3.2). The k_{cat} value for Aβ42 (0.23 min^{-1}) in particular stands out as being exceptionally low—indicating that it takes each molecule of CatD a remarkable ~4.3 mins to process just 1 molecule of Aβ42. The results obtained by ELISA were subsequently confirmed by multiple independent enzymological methods, including trichloroacetic acid-mediated precipitation of ^{125}I-labeled Aβ peptides, competition experiments with fluorogenic peptide substrates (69), and a novel homogeneous time-resolved fluorescence (HTRF)-based approach

using end-specific antibodies (see Appendix B Supplemental Methods). All of these methods yielded quantitative data in good agreement with the ELISA results (Appendix B Table S3.2). Finally, in an independent approach, surface plasmon resonance was used to quantify the affinity and dissociation constant of Aβ42 and Aβ40 to immobilized CatD, in this case at pH 4.5. In excellent agreement with the enzymological findings, Aβ42 showed a K_M of 47.7 + 0.041 nM and a k_d value (dissociation constant, comparable to k_{cat}) of 0.266 + 7.2x10^{-5} min^{-1} at pH 4.5, whereas, consistent with the other findings, the K_M for Aβ40 was outside the range of concentrations tested (>333 nM; Fig. 3.6C, D).

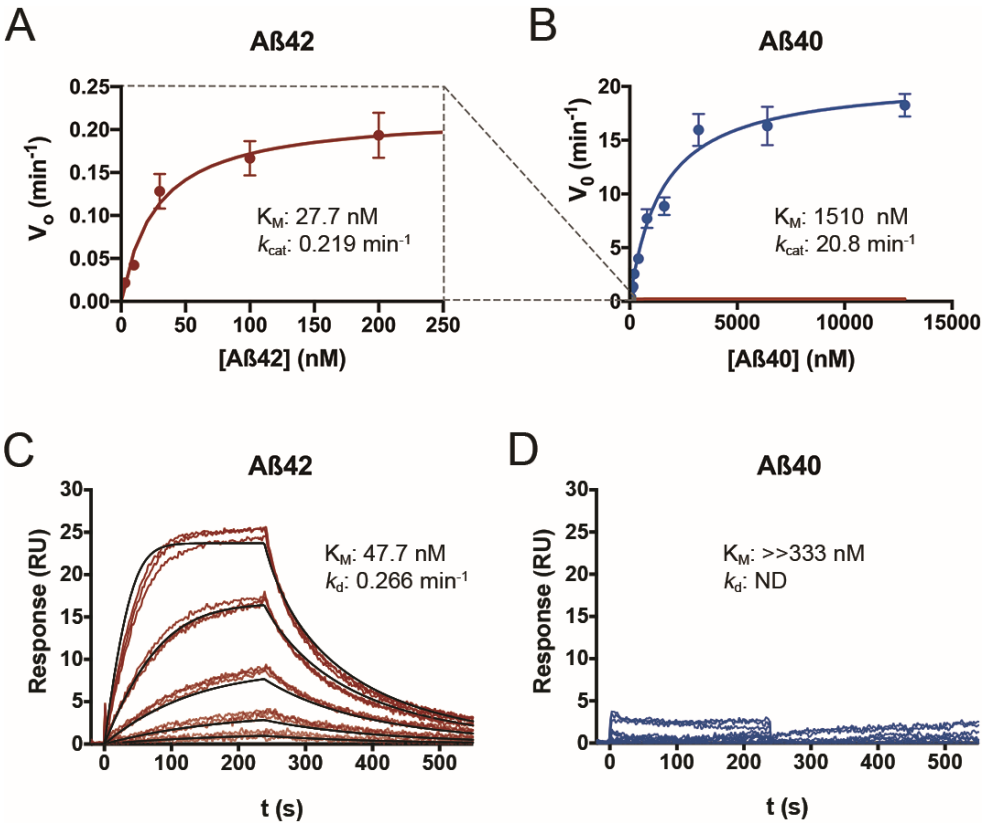

Figure 3.6. CatD degrades Aβ42 and Aβ40 with markedly different kinetics. ***A***,***B***, Plots of initial velocity (v_o) versus substrate concentration for Aβ42 (***A***, *red*) and Aβ40 (***B***, *blue*). The dashed lines (*gray*) show the relative position of the data in (***A***) when superimposed on the same scale as is used for the data in (***B***). Quantitative kinetic parameters are provided in Appendix B Table S3.2. ***C***,***D***, Surface plasmon resonance confirms that Aβ42 exhibits markedly higher affinity for CatD than Aβ40, independent of degradation. Traces obtained for 3-fold dilutions of Aβ42 (***C***) and Aβ40 (***D***) beginning at 333 nM. Analysis of the fitted curves in (***C***) yielded a K_M of 47.7 + 0.041 nM and a k_d value of 0.266 + 7.2x10^5 min^{-1} for Aβ42. Consistent with the kinetics of Aβ40 binding obtained by other methods (Appendix B Table S3.2), no significant binding of Aβ40 was observed within the conditions used. Note that, for technical reasons, these experiments were conducted at pH 4.5, precluding direct quantitative comparisons to kinetic parameters determined by other methods at pH 4.0.

To complete the characterization of CatD as a novel AβDP, we also investigated whether the protease was capable of degrading Aβ in various states of aggregation. On short time scales (≤1 d), no effect was observed on the degradation of Aβ42 fibrils, protofibrils or SDS-induced oligomers of Aβ42 (Appendix B Fig. S3.8A-C). However, over longer time scales (≥ ~4 d) fibrils

(Appendix B Fig. S3.8A) and protofibrils (Appendix B Fig. S3.8B) of Aβ42 were effectively degraded by CatD at pH 4.0, but not by trypsin at pH 4.0 or IDE at pH 7.4.

Low K_M and k_{cat} values render Aβ42 a potent competitive inhibitor of CatD

The very strong affinity (K_M) of Aβ42 for CatD, combined with its exceptionally slow turnover rate (k_{cat}), effectively renders Aβ42 a highly potent competitive inhibitor of CatD. To explore these inhibitory properties more quantitatively, we measured CatD activity in real time using a fluorescence dequenching assay in the presence of varying quantities of Aβ42 or Aβ40. Using this paradigm, Aβ40 inhibited CatD with an IC_{50} of 2.75 μM; whereas, in marked contrast, Aβ42 inhibited CatD $>10^3$ more potently, with a calculated IC_{50} of 0.96 nM (Fig. 3.7A,B). Given that the nominal concentration of CatD in these experiments was ~1 nM, this implies an essentially 1:1 interaction between Aβ42 and CatD that nevertheless potently inhibits the protease for prolonged periods. Similar results were obtained using a fluorescence polarization-based Aβ degradation assay (70), where 200 nM Aβ42 was found to essentially completely inhibit the degradation of fluorescent Aβ (200 nM) by CatD, while 200 nM Aβ40 inhibited its degradation only partially (Fig. 3.7C). Likewise, when Aβ42 and Aβ40 were combined together in equimolar quantities (100 nM), the degradation of Aβ42 was not slowed relative to Aβ42 alone, whereas the degradation of Aβ40 was significantly slowed relative to Aβ40 alone (Fig. 3.7D). In the latter experiment, we also note that Aβ42 alone was degraded more quickly than Aβ40 alone. Together, these results imply that, for a mixture of both peptides, Aβ42 is degraded more efficiently by CatD than Aβ40, providing a plausible mechanism explaining how deletion of CatD increases the Aβ42/40 ratio. Given that Aβ42 is usually present at concentrations ~10-fold lower than Aβ40 *in vivo*, we also tested whether Aβ40 degradation could be inhibited by 1/10 as much Aβ42. In fact, the degradation of 50 nM Aβ40 was significantly inhibited by just 5 nM Aβ42 (Fig. 3.7E).

In a final set of experiments, we aimed to test whether the marked differences in the kinetics of human Aβ42 vs. Aβ40 degradation might extend to full-length rodent Aβ or shorter Aβ fragments ending at positions 42 vs. 40. To address this, we tested the extent to which different peptides at identical concentrations inhibited CatD activity monitored with a fluorogenic substrate. CatD activity was inhibited >90% by 1 μM of human Aβ42, rodent Aβ42 as well as the α-secretase-derived p3 fragment of APP ending at position 42 ($A\beta_{(17-42)}$), but not by a short C-terminal peptide ($A\beta_{(33-42)}$; Fig. 3.7F). In contrast, the corresponding Aβ peptides ending at position 40 instead of 42, inhibited the degradation of the fluorogenic substrate to a significantly lesser extent (Fig. 3.7F). The result for the p3 fragment ending at position 42 is especially notable, since it is a naturally occurring product of endogenous APP processing, moreover, one that is produced at levels ~10-fold higher than Aβ42 (71).

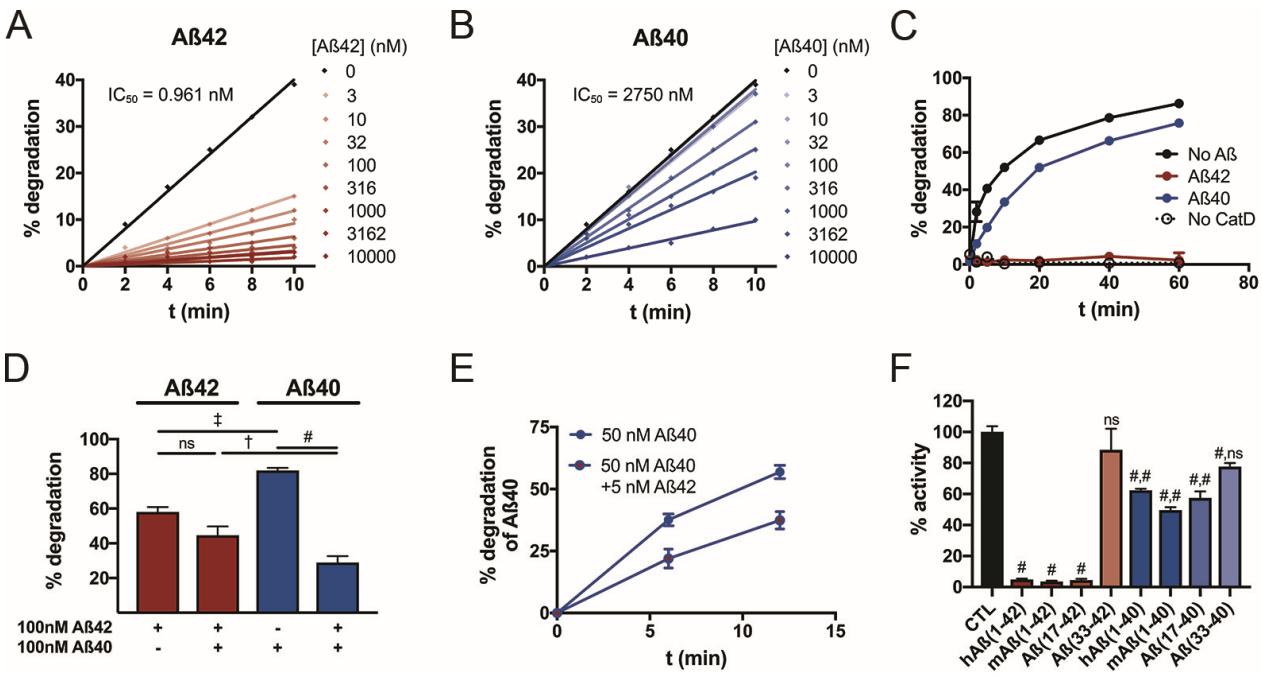

Figure 3.7. Aβ42 is a potent competitive inhibitor of CatD. ***A***,***B***, Competitive inhibition by Aβ42 (***A***) and Aβ40 (***B***) of CatD activity quantified by a fluorogenic substrate. Note that just 3 nM Aβ inhibits CatD (nominal concentration, ~1 nM) by more than 50%. ***C***, Comparable data for CatD activity quantified using an Aβ degradation assay, with 200 nM fluorescent Aβ alone (No Aβ) or in combination with 200 nM Aβ42 (*red*) or Aβ40 (*blue*). ***D***, Quantification of Aβ42 (*red*) and Aβ40 (*blue*) degradation either alone (100 nM) or in combination (100 nM each). Note that Aβ42 significantly inhibits Aβ40 degradation, but the converse is not true. Data are mean ± SEM for 4-8 replicates per group. $^{\dagger}P<0.01$; $^{\ddagger}P<0.001$; $^{\#}P<0.0001$. ***E***, Aβ40 degradation is significantly inhibited by 1/10 the concentration of Aβ42, a ratio representative of that present *in vivo*. ***F***, CatD is strongly inhibited by multiple Aβ peptides and fragments ending at position 42, including full-length murine Aβ (mAβ$_{(1-42)}$) and the p3 fragment (Aβ$_{(17-42)}$), more strongly than the corresponding peptides ending in Aβ40. The C-terminal fragment of Aβ42, Aβ$_{(33-42)}$, failed to inhibit significantly, while the corresponding fragment, Aβ$_{(33-40)}$, showed a modest but statistically significant inhibition under the conditions tested. Data are mean ± SEM for 4-8 replicates per group. $^{\#}P<0.0001$. For data on Aβ peptides ending at position 40, the 2 symbols reflect the statistical significance of comparisons to buffer-only control (here marked CTL) and to the corresponding fragments ending at position 42, respectively.

3.3.4 Discussion

Taken together, our findings support the twin conclusions that CatD is a key regulator of brain Aβ proteostasis *in vivo* and that a significant portion of Aβ is trafficked to lysosomes. CatD accounts for the vast majority of Aβ-degrading activity in soluble brain extracts; deletion of CatD *in vivo* results in marked increases in cerebral Aβ; and Aβ accumulates to high levels in lysosomes when CatD is absent. Collectively, these observations suggest that a significant fraction of Aβ is normally trafficked to lysosomes, where it is degraded primarily by CatD. In addition, our findings raise the compelling possibility that Aβ42/40 ratios can be regulated not only at the site of Aβ production, *via* presenilin/ γ-secretase (72), but also *via* differential degradation of different-length Aβ species by CatD, and perhaps also by other AβDPs.

Our results suggest that CatD may be, by several measures, the most pathologically significant AβDP yet identified. Quantitatively, the increases in endogenous Aβ42 and Aβ40 levels induced by deletion of CatD exceeds those induced by deletion of any other AβDP studied to date (45, 73) or, indeed, by simultaneous deletion of multiple AβDPs (74) (see also Fig. 3.5D,E). Qualitatively, moreover, CatD is the only AβDP that, when deleted, has been shown to trigger the frank deposition of endogenous murine Aβ by just 3 weeks of age. These findings strongly suggest that CatD's contribution to the overall economy of cerebral Aβ exceeds that of any previously characterized AβDP.

The involvement of CatD in the intralysosomal clearance of Aβ has potentially significant pathological implications. In particular, intracellular pools of Aβ have been hypothesized to play a disproportionately important role in AD pathogenesis (12), for example, initiating neuronal cell death at concentrations several orders of magnitude lower than extracellular Aβ (11). Nevertheless, this has been a technically challenging field of inquiry; manipulation of CatD could provide an

elegant means to assess the role of intralysosomal Aβ in the pathogenesis of AD. It is relevant to note in this context that Cheng and colleagues recently reported that deletion of one allele of *CTSD* in APP/PS1 transgenic mice had no effect on extracellular Aβ deposits (75). This lack of effect could have multiple potential explanations. First, it might reflect the fact that CatD only regulates intracellular pools of Aβ. Second, as our data suggest, it might instead be attributable to the apparent compensatory increases in CatD protein and activity we observed in the heterozygous state—although the decrease in CatD levels in CatD-HET mice was determined to be somewhat greater (~38%) in the study by Cheng and colleagues than what we found (~25%) (75). Third, CatD might not be rate-limiting in the determination of cerebral Aβ levels, such that a gene dosage-dependency would not be observed. Finally, we cannot entirely exclude the possibility that some other non-specific consequence of CatD deletion, perhaps involving neuronal ceroid lipofuscinosis or some other indirect consequence, could account for the increase in Aβ levels and Aβ42/40 ratios in CatD-KO mice. Given the lack of clarity on this and many other significant questions about the potential role of CatD in the pathogenesis of AD, research in this area would be greatly facilitated by future work with animal models that permit the manipulation of CatD conditionally, reversibly and/or cell-type specifically (55).

The finding that insoluble forms of Aβ were increased in CatD-KO mice, while soluble forms were decreased is also deserving of discussion. Insoluble forms of Aβ are generally considered to represent aggregated species (59). Notably, the aggregation of Aβ—and Aβ42 in particular—is dramatically accelerated under the acidic conditions present in the lysosomes (76). This fact, together with our immunohistochemical findings, strongly suggests that the insoluble pool of Aβ represents aggregates of Aβ within lysosomes. As to why soluble forms of Aβ decrease in CatD-KO mice, we can only speculate, but we note that it has been shown that the presence of

aggregated forms of Aβ acts to seed the aggregation of soluble pools of Aβ, thus reducing the concentration of monomeric Aβ species (77). In this connection, it is interesting to note that NEP-KO mice showed increases in soluble Aβ, while IDE-KO mice did not, perhaps reflecting the fact that NEP is present and active within the endolysosomal system, while IDE is not (78).

The most pathologically significant, and initially the most puzzling, consequence of CatD deletion was the highly consistent increase in the cerebral Aβ42/40 ratio. Although any number of indirect mechanisms might in principle have accounted for this effect *in vivo*, we discovered that CatD degrades Aβ42 and Aβ40 *in vitro* with strikingly different kinetics, implying that these enzymological parameters could potentially be operative *in vivo*. Depending on the specific methodology used, the K_M of Aβ42 for CatD at pH 4.0 was estimated to be from 3.2 to 28 nM, or from ~50 to ~600 times stronger than that for Aβ40 (Appendix B Table S3.2). The turnover number (k_{cat}) of Aβ42 was found to be unexpectedly slow, as well, with different methodologies yielding estimates of 0.22 to 1.1 min^{-1} (Appendix B Table S3.2). These values are from ~40- to ~110-fold lower than the corresponding values for Aβ40 and, quite significantly, are 10^2 to 10^3-fold slower than the k_{cat} of Aβ40 degradation by IDE, neprilysin, and plasmin (calculated from 70). Expressed differently, the processing of one molecule of Aβ42 requires the same amount of time as the processing of 10^2 to 10^3 molecules of Aβ40 by CatD or other well-characterized proteases.

Taken together with the strong affinity of Aβ42 for CatD, the slow turnover number essentially renders Aβ42 a very potent inhibitor of CatD, as confirmed by multiple experiments in this study. The possibility that aggregation of Aβ42 accounts for its potent inhibitory power is excluded by several observations. First, we showed that a mere 3 nM of monomeric Aβ42 inhibits 1 nM of CatD by >50%. If Aβ42 were in the form of aggregates, their average molarity would be decreased relative to the monomeric state, making such a potent interaction physically impossible.

Second, in the ELISA-based degradation experiments, we obtained absolute concentrations of Aβ in agreement with the nominal monomeric Aβ concentrations. Third, both murine Aβ42 and p3 fragments ending at position 42—which are both far less prone to aggregation than full-length human Aβ—were also shown to be effective inhibitors of CatD. Finally, the possibility that Aβ aggregated significantly when exposed to pH is similarly ruled out. Aggregation, if it did occur during the course of the degradation reactions, would *decrease* the apparent concentration of Aβ detected by ELISA, thereby resulting in an overestimate of the rates of degradation; to the contrary, Aβ42 levels remained quite stable throughout the course of the reactions, particularly for the highest concentrations. Collectively, these observations strongly suggest that Aβ42 potently inhibits CatD in an aggregation-independent manner.

Our findings imply an intriguing bidirectional relationship between Aβ42 and CatD activity. On the one hand, impaired CatD activity can trigger selective increases in Aβ42, and on the other hand, Aβ42—and the corresponding p3 fragment—can competitively inhibit CatD activity, in some instances with exquisite potency. This bidirectional interrelationship is especially notable from a pathological perspective and gives rise to some novel—albeit speculative—possibilities. Given that defects in CatD can trigger multiple neurodegenerative diseases (38), it is reasonable to ask whether the central role of elevated Aβ42 in AD pathogenesis may, in part, involve its potent ability to competitively inhibit CatD. While speculative, such a mechanism could conceivably be operative in the poorly understood link between elevated Aβ42 concentrations and tauopathy. In this context, it is especially notable that tau is degraded by CatD *in vitro* (37), and there is accruing evidence that disruptions to lysosomal clearance of tau may play a role in tau accumulation (35). Moreover, deletion of CatD in *Drosophila melanogaster* was shown to exacerbate the premature lethality induced by neuronal overexpression of tau (14), suggesting that

CatD may also protect against the pathological effects of tau. These findings, together with those of the present study, strongly suggest that CatD normally plays a protective role in AD, a function that can be selectively compromised by elevated concentrations of Aβ42.

There are many limitations inherent in the use of CatD-KO mice, due to their premature lethality and their development of profound neurodegeneration and lipofuscinosis. A proper assessment of the role of CatD in the pathogenesis of AD will require more sophisticated means for manipulating CatD. Because aging is the primary risk factor for AD—and because recent findings show that the maturation of and post-translational modifications of CatD can change in an age-dependent manner (79)—inducible expression systems will likely be needed.

If, as we propose, CatD plays a protective role in AD by virtue of a functional role as an AβDP, then we would predict that loss-of-function mutations in CatD would increase risk for AD. In fact, a large number of genetic association studies have investigated a single-nucleotide polymorphism present in exon 2 of the *CTSD* gene (rs17571; C→T224), which leads to an Ala→Val transition within the prodomain of the CatD zymogen (Appendix B Fig. S3.9A), and which has been reported to perturb the maturation and trafficking of CatD (80). Considered individually, these studies have yielded conflicting results. However, using data from AlzGene (81), meta-analysis of all 18 Caucasian-only reports published to date, excluding those with Hardy-Weinberg equilibrium violations, yields a statistically significant odds ratio estimate for the rs17571 polymorphism (OR = 1.20, 95% CI = 1.01 - 1.42, P= 0.038) (Appendix B Fig. S3.9B). Although the effect size of this association is comparatively modest, it is critical to emphasize that the functional consequences of this mutation are predicted to be relatively subtle, given that the rs17571 polymorphism results in a conservative amino acid substitution (A58V) in a non-functional, poorly conserved region of the latent CatD zymogen (Appendix B Fig. S3.9A). The

finding that such a subtle mutation nevertheless confers a statistically significant increase in AD risk lends support to the idea that CatD may play a relatively important pathophysiological role in the etiology of AD, as would be predicted from the functional findings of the present study.

3.3.5 Methods/Experimental

Aim, Design and Setting

The objective of the present study was to evaluate the role of CatD in Aβ proteostasis *in vivo* and to more completely characterize its Aβ-degrading function. To that end, homogenized brain extracts from 15- to 26-day-old CatD-KO, -HET and -WT mice were analyzed for Aβ degrading activity, protein levels, and steady state soluble and insoluble Aβ levels. Paraffin-embedded brain tissue from these mice was analyzed by immunohistochemistry for AD-related markers. Cultured embryonic (E18) hippocampal neurons were analyzed for Aβ secretion into the conditioned medium and the uptake and catabolism of fluorescently tagged synthetic Aβ peptides. Mass spectrometry was conducted to analyze the fragments of synthetic Aβ peptide fragments generated by recombinant CatD. Degradation of aggregated Aβ42 by recombinant CatD was assessed by thioflavin T fluorescence and western blotting. A variety of proteolytic degradation assays were performed in the absence or presence of different Aβ and p3 fragments, and binding assays were performed by surface plasmon resonance, all with recombinant human CatD. Research was conducted in multiple state-of-the-art biomedical laboratories.

Animals

Mice were bred and housed in American Association for Accreditation of Laboratory Animal Care -accredited facilities in accordance with the National Institutes of Health Guidelines for the Care and Use of Laboratory Animals. CatD-KO (54), IDE-KO (49), NEP-KO (47), APP-KO (82), BACE1-KO (83) and Twitcher mice (62) were maintained as inbred lines, each in a

mixed C57Bl/6J, DBA genetic background. The NEP/IDE-DKO line was derived from crosses between the NEP-KO and IDE-KO lines. Analyses were restricted to age- and sex-matched groups of littermates for all genotypes, except NEP/IDE-DKO mice, which were compared to age-and sex-matched NEP-WT and IDE-WT mice grouped together for statistical analysis. Due to the premature lethality present in CatD-KO mice, we focused our analyses on tissues extracted from 15- to 26-day-old mice, using age- and sex-matched littermate WT controls in all cases except the NEP/IDE-DKO line, for which littermate controls WT at both loci could not be obtained. These mice were instead compared to a group of both NEP-WT and IDE-WT animals, which did not differ from one another in terms of any analyte examined.

Aβ quantification

Endogenous murine Aβ40 and Aβ42 were extracted from frozen hemibrains with 0.2% diethylamine (DEA), as described (84), then quantified using Aβ42 and Aβ40 end-specific sandwich ELISAs (Wako) (59). For Aβ quantification in neuronal media, conditioned medium was supplemented with Complete Protease Inhibitor Cocktail (Roche) and analyzed without further extraction using in-house ELISA systems based on antibody pairs 33.1.1/13.1.1 and 2.1.3.35.86/33.1.1, respectively (58, 59). All ELISA measurements of brain Aβ were normalized to the average background signal obtained from APP-KO and BACE1-KO mouse brains processed and analyzed in parallel with other samples.

Enzymological studies

For determination of the pH dependence of Aβ degradation in soluble brain extracts, freshly harvested brain tissue from 15-day-old mice was dissociated in 20 mM Tris-HCl, pH 7.4 at 4 ºC using a Dounce homogenizer, then centrifuged at 1000 x g. The resulting supernatant was diluted 1:20 in Britton-Robinson buffers of different pHs, and CatD activity was quantified either

using a well-characterized fluorescence polarization-based Aβ degradation assay as described (70) or by monitoring hydrolysis of the CatD-specific fluorogenic substrate, Mca-GKPILFFRLK-Dnp. Kinetic experiments were conducted using freshly prepared, monomeric Aβ peptides separated from aggregated species by size-exclusion chromatography and characterized as described (67, 68). Aβ peptides and PepA were diluted in neutral Dilution Buffer (20 mM Tris, pH 8.0 supplemented with 0.1% BSA), with addition of DMSO as appropriate, and reactions were initiated by transfer into Assay Buffer (60 mM Na-citrate; 80 mM Na_2HPO_4, pH 4.0; Sigma) supplemented with purified human CatD (Enzo Life Sciences). Where required, reactions were terminated by adjustment to neutral pH with 10x Stop Buffer (0.2 M Tris-HCL, pH 9.5 supplemented with 10 μM PepA). For ELISA-based experiments, Aβ42 and Aβ40 were quantified by well-characterized sandwich ELISAs (Wako) (57). Competitive inhibition experiments were conducted using either ELISAs, an Aβ-degradation assay (70) or the fluorogenic substrate.

Surface Plasmon Resonance

Binding studies were performed using a Biacore S51 optical biosensor equipped with a CM5 sensor chip. Purified human CatD (Enzo Life Sciences) was diluted to 0.1 nM in Coupling Buffer (10 mM NaAc, pH 4.25) and amine-coupled to the chip surface. Aβ peptides were diluted in Running Buffer (50 mM Na-Citrate, 200 mM NaCl, 1 mM EDTA, 2 mM DTT, 0.005% Tween-20, pH 4.5) and tested in triplicate using a 3-fold dilution series beginning at 333 nM. Binding data were fitted to a simple 1:1 interaction model using manufacturer-supplied software (Biacore). Kinetic parameters were obtained by analysis of fitted curves using Anabel (85).

Statistical Analyses

Tests of significance between individual experimental and control groups were conducted using unpaired T tests, after F tests for equality of variances. For data in two or more groups and/or

also containing another variable (e.g., age), mixed-effects analysis via ANOVA was performed. Group sizes were determined by power analysis of comparable historical experimental data sets, using the Student's T test with the alpha level set at 0.05. All calculations were performed from the raw data in Prism 8 for Mac OS (Graphpad Software, LLC).

3.4 Conclusion

In conclusion, the totality of our results supports the hypothesis that CatD plays a protective role in the pathogenesis of AD by regulating intralysosomal Aβ levels as well as Aβ42/40 ratios through differential degradation of Aβ42 and Aβ40, an effect that is driven by aggregation-independent, enzymological mechanisms. More speculatively, the finding that Aβ42 competitively inhibits CatD at pathophysiologically relevant concentrations suggests a possible molecular mechanism linking elevations in Aβ42 to downstream neuropathological sequelae characteristic of AD.

3.5 Acknowledgements

I would like to acknowledge Samer O. Abdul-Hay, Tomoko Sahara, Dongcheul Kang, Monica K. Brizuela, Paul Saftig, Dennis W. Dickson, Terrone L. Rosenberry and Malcolm A. Leissring for their contributions to the work, experimental design, data analysis, and writing of the publication featured in **3.3**. This work has been published in *Alzheimer's Research and Therapy*, an open source journal (86).

3.6 References

1. Miners JS, Baig S, Tayler H, Kehoe PG, Love S. Neprilysin and insulin-degrading enzyme levels are increased in Alzheimer disease in relation to disease severity. J Neuropathol Exp Neurol. 2009;68(8):902-14.

2. Chai YL, Chong JR, Weng J, Howlett D, Halsey A, Lee JH, et al. Lysosomal cathepsin D is upregulated in Alzheimer's disease neocortex and may be a marker for neurofibrillary degeneration. Brain Pathol. 2019;29(1):63-74.

3. Cataldo AM, Nixon RA. Enzymatically active lysosomal proteases are associated with amyloid deposits in Alzheimer brain. Proc Natl Acad Sci U S A. 1990;87(10):3861-5.

4. Hafez D, Huang JY, Huynh AM, Valtierra S, Rockenstein E, Bruno AM, et al. Neprilysin-2 is an important beta-amyloid degrading enzyme. Am J Pathol. 2011;178(1):306-12.

5. Saido T, Leissring MA. Proteolytic degradation of amyloid beta-protein. Cold Spring Harb Perspect Med. 2012;2(6):a006379.

6. Schultz C, Rossi A, van Mieghem N, van der Boon R, Papadopoulou SL, van Domburg R, et al. Aortic annulus dimensions and leaflet calcification from contrast MSCT predict the need for balloon post-dilatation after TAVI with the Medtronic CoreValve prosthesis. EuroIntervention. 2011;7(5):564-72.

7. Yan P, Hu X, Song H, Yin K, Bateman RJ, Cirrito JR, et al. Matrix metalloproteinase-9 degrades amyloid-beta fibrils in vitro and compact plaques in situ. J Biol Chem. 2006;281(34):24566-74.

8. Turner AJ, Fisk L, Nalivaeva NN. Targeting amyloid-degrading enzymes as therapeutic strategies in neurodegeneration. Ann N Y Acad Sci. 2004;1035:1-20.

9. McGowan E, Pickford F, Kim J, Onstead L, Eriksen J, Yu C, et al. Abeta42 is essential for parenchymal and vascular amyloid deposition in mice. Neuron. 2005;47(2):191-9.

10. Kim J, Chakrabarty P, Hanna A, March A, Dickson DW, Borchelt DR, et al. Normal cognition in transgenic BRI2-Abeta mice. Mol Neurodegener. 2013;8:15.

11. Zhang Y, McLaughlin R, Goodyer C, LeBlanc A. Selective cytotoxicity of intracellular amyloid beta peptide1-42 through p53 and Bax in cultured primary human neurons. J Cell Biol. 2002;156(3):519-29.

12. LaFerla FM, Green KN, Oddo S. Intracellular amyloid-beta in Alzheimer's disease. Nat Rev Neurosci. 2007;8(7):499-509.

13. Boya P, Kroemer G. Lysosomal membrane permeabilization in cell death. Oncogene. 2008;27(50):6434-51.

14. Khurana V, Elson-Schwab I, Fulga TA, Sharp KA, Loewen CA, Mulkearns E, et al. Lysosomal dysfunction promotes cleavage and neurotoxicity of tau in vivo. PLoS Genet. 2010;6(7):e1001026.

15. Li J, Kanekiyo T, Shinohara M, Zhang Y, LaDu MJ, Xu H, et al. Differential regulation of amyloid-beta endocytic trafficking and lysosomal degradation by apolipoprotein E isoforms. J Biol Chem. 2012;287(53):44593-601.

16. Nixon RA, Cataldo AM. Lysosomal system pathways: genes to neurodegeneration in Alzheimer's disease. J Alzheimers Dis. 2006;9(3 Suppl):277-89.

17. Lowry JR, Klegeris A. Emerging roles of microglial cathepsins in neurodegenerative disease. Brain Res Bull. 2018;139:144-56.

18. Patel S, Homaei A, El-Seedi HR, Akhtar N. Cathepsins: Proteases that are vital for survival but can also be fatal. Biomed Pharmacother. 2018;105:526-32.

19. Wang Y, Martinez-Vicente M, Kruger U, Kaushik S, Wong E, Mandelkow EM, et al. Tau fragmentation, aggregation and clearance: the dual role of lysosomal processing. Hum Mol Genet. 2009;18(21):4153-70.

20. McDermott JR, Gibson AM. Degradation of Alzheimer's beta-amyloid protein by human cathepsin D. Neuroreport. 1996;7(13):2163-6.

21. Hamazaki H. A beta-amyloid peptide variant related with familial Alzheimer's disease and hereditary cerebral hemorrhage with amyloidosis is poorly eliminated by cathepsin D. FEBS Lett. 1996;397(2-3):313-5.

22. Hamazaki H. Cathepsin D is involved in the clearance of Alzheimer's beta-amyloid protein. FEBS Lett. 1996;396(2-3):139-42.

23. Arodola OA, Soliman ME. Molecular Dynamics Simulations of Ligand-Induced Flap Conformational Changes in Cathepsin-D-A Comparative Study. J Cell Biochem. 2016;117(11):2643-57.

24. Vandal M, Alata W, Tremblay C, Rioux-Perreault C, Salem N, Jr., Calon F, et al. Reduction in DHA transport to the brain of mice expressing human APOE4 compared to APOE2. J Neurochem. 2014;129(3):516-26.

25. Fernandez-Montoya J, Perez M. Cathepsin D in a murine model of frontotemporal dementia with Parkinsonism-linked to chromosome 17. J Alzheimers Dis. 2015;45(1):1-14.

26. Sadleir KR, Kandalepas PC, Buggia-Prevot V, Nicholson DA, Thinakaran G, Vassar R. Presynaptic dystrophic neurites surrounding amyloid plaques are sites of microtubule disruption, BACE1 elevation, and increased Abeta generation in Alzheimer's disease. Acta Neuropathol. 2016;132(2):235-56.

27. Perez SE, He B, Nadeem M, Wuu J, Ginsberg SD, Ikonomovic MD, et al. Hippocampal endosomal, lysosomal, and autophagic dysregulation in mild cognitive impairment: correlation with abeta and tau pathology. J Neuropathol Exp Neurol. 2015;74(4):345-58.

28. Zhang L, Sheng R, Qin Z. The lysosome and neurodegenerative diseases. Acta Biochim Biophys Sin (Shanghai). 2009;41(6):437-45.

29. Vidoni C, Follo C, Savino M, Melone MA, Isidoro C. The Role of Cathepsin D in the Pathogenesis of Human Neurodegenerative Disorders. Med Res Rev. 2016;36(5):845-70.

30. Nakanishi H. Neuronal and microglial cathepsins in aging and age-related diseases. Ageing Res Rev. 2003;2(4):367-81.

31. Cataldo AM, Hamilton DJ, Barnett JL, Paskevich PA, Nixon RA. Properties of the endosomal-lysosomal system in the human central nervous system: disturbances mark most neurons in populations at risk to degenerate in Alzheimer's disease. J Neurosci. 1996;16(1):186-99.

32. Wang Y, Martinez-Vicente M, Krüger U, Kaushik S, Wong E, Mandelkow EM, et al. Tau fragmentation, aggregation and clearance: the dual role of lysosomal processing. Hum Mol Genet. 2009;18(21):4153-70.

33. Haass C, Hung AY, Schlossmacher MG, Oltersdorf T, Teplow DB, Selkoe DJ. Normal cellular processing of the beta-amyloid precursor protein results in the secretion of the amyloid beta peptide and related molecules. Ann N Y Acad Sci. 1993;695:109-16.

34. Fuentealba RA, Liu Q, Zhang J, Kanekiyo T, Hu X, Lee JM, et al. Low-density lipoprotein receptor-related protein 1 (LRP1) mediates neuronal Abeta42 uptake and lysosomal trafficking. PLoS ONE. 2010;5(7):e11884.

35. Caballero B, Wang Y, Diaz A, Tasset I, Juste YR, Stiller B, et al. Interplay of pathogenic forms of human tau with different autophagic pathways. Aging cell. 2018;17(1).

36. Ballatore C, Lee VM, Trojanowski JQ. Tau-mediated neurodegeneration in Alzheimer's disease and related disorders. Nat Rev Neurosci. 2007;8(9):663-72.

37. Kenessey A, Nacharaju P, Ko LW, Yen SH. Degradation of tau by lysosomal enzyme cathepsin D: implication for Alzheimer neurofibrillary degeneration. J Neurochem. 1997;69(5):2026-38.

38. Vashishta A, Ohri SS, Vetvicka V. Pleiotropic effects of cathepsin D. Endocr Metab Immune Disord Drug Targets. 2009;9(4):385-91.

39. Steinfeld R, Reinhardt K, Schreiber K, Hillebrand M, Kraetzner R, Bruck W, et al. Cathepsin D deficiency is associated with a human neurodegenerative disorder. Am J Hum Genet. 2006;78(6):988-98.

40. Tyynela J, Sohar I, Sleat DE, Gin RM, Donnelly RJ, Baumann M, et al. A mutation in the ovine cathepsin D gene causes a congenital lysosomal storage disease with profound neurodegeneration. Embo J. 2000;19(12):2786-92.

41. Davidson Y, Gibbons L, Pritchard A, Hardicre J, Wren J, Tian J, et al. Genetic associations between cathepsin D exon 2 C-->T polymorphism and Alzheimer's disease, and pathological correlations with genotype. J Neurol Neurosurg Psychiatry. 2006;77(4):515-7.

42. Papassotiropoulos A, Lewis HD, Bagli M, Jessen F, Ptok U, Schulte A, et al. Cerebrospinal fluid levels of beta-amyloid(42) in patients with Alzheimer's disease are related to the exon 2 polymorphism of the cathepsin D gene. Neuroreport. 2002;13(10):1291-4.

43. Riemenschneider M, Blennow K, Wagenpfeil S, Andreasen N, Prince JA, Laws SM, et al. The cathepsin D rs17571 polymorphism: effects on CSF tau concentrations in Alzheimer disease. Hum Mutat. 2006;27(6):532-7.

44. Leissring MA, Saido TC. Aß degradation. In: Sisodia S, Tanzi R, editors. Alzheimer's disease: Advances in genetics, Molecular and Cellular Biology. New York: Springer Publishing Company; 2007. p. 157-78.

45. Nalivaeva NN, Turner AJ. Targeting amyloid clearance in Alzheimer's disease as a therapeutic strategy. Br J Pharmacol. 2019;176(18):3447-63.

46. Iwata N, Tsubuki S, Takaki Y, Watanabe K, Sekiguchi M, Hosoki E, et al. Identification of the major Abeta1-42-degrading catabolic pathway in brain parenchyma: suppression leads to biochemical and pathological deposition. Nat Med. 2000;6(2):143-50.

47. Iwata N, Tsubuki S, Takaki Y, Shirotani K, Lu B, Gerard NP, et al. Metabolic regulation of brain Abeta by neprilysin. Science. 2001;292(5521):1550-2.

48. Farris W, Schutz SG, Cirrito JR, Shankar GM, Sun X, George A, et al. Loss of neprilysin function promotes amyloid plaque formation and causes cerebral amyloid angiopathy. Am J Pathol. 2007;171(1):241-51.

49. Farris W, Mansourian S, Chang Y, Lindsley L, Eckman EA, Frosch MP, et al. Insulin-degrading enzyme regulates the levels of insulin, amyloid beta-protein, and the beta-amyloid precursor protein intracellular domain in vivo. Proc Natl Acad Sci U S A. 2003;100(7):4162-7.

50. Miller BC, Eckman EA, Sambamurti K, Dobbs N, Chow KM, Eckman CB, et al. Amyloid-beta peptide levels in brain are inversely correlated with insulysin activity levels in vivo. Proc Natl Acad Sci U S A. 2003;100(10):6221-6.

51. Leissring MA, Farris W, Chang AY, Walsh DM, Wu X, Sun X, et al. Enhanced proteolysis of beta-amyloid in APP transgenic mice prevents plaque formation, secondary pathology, and premature death. Neuron. 2003;40(6):1087-93.

52. Meilandt WJ, Cisse M, Ho K, Wu T, Esposito LA, Scearce-Levie K, et al. Neprilysin overexpression inhibits plaque formation but fails to reduce pathogenic Abeta oligomers and

associated cognitive deficits in human amyloid precursor protein transgenic mice. J Neurosci. 2009;29(7):1977-86.

53. Ahmed Z, Sheng H, Xu YF, Lin WL, Innes AE, Gass J, et al. Accelerated lipofuscinosis and ubiquitination in granulin knockout mice suggest a role for progranulin in successful aging. Am J Pathol. 2010;177(1):311-24.

54. Saftig P, Hetman M, Schmahl W, Weber K, Heine L, Mossmann H, et al. Mice deficient for the lysosomal proteinase cathepsin D exhibit progressive atrophy of the intestinal mucosa and profound destruction of lymphoid cells. EMBO J. 1995;14(15):3599-608.

55. Ketscher A, Ketterer S, Dollwet-Mack S, Reif U, Reinheckel T. Neuroectoderm-specific deletion of cathepsin D in mice models human inherited neuronal ceroid lipofuscinosis type 10. Biochimie. 2016;122:219-26.

56. McDermott JR, Gibson AM. Degradation of Alzheimer's beta-amyloid protein by human and rat brain peptidases: involvement of insulin-degrading enzyme. Neurochem Res. 1997;22(1):49-56.

57. Scheuner D, Eckman C, Jensen M, Song X, Citron M, Suzuki N, et al. Secreted amyloid beta-protein similar to that in the senile plaques of Alzheimer's disease is increased in vivo by the presenilin 1 and 2 and APP mutations linked to familial Alzheimer's disease. Nat Med. 1996;2(8):864-70.

58. Eckman EA, Watson M, Marlow L, Sambamurti K, Eckman CB. Alzheimer's disease beta-amyloid peptide is increased in mice deficient in endothelin-converting enzyme. J Biol Chem. 2003;278(4):2081-4.

59. Golde TE, Eckman CB, Younkin SG. Biochemical detection of Abeta isoforms: implications for pathogenesis, diagnosis, and treatment of Alzheimer's disease. Biochim Biophys Acta. 2000;1502(1):172-87.

60. Citron M, Westaway D, Xia W, Carlson G, Diehl T, Levesque G, et al. Mutant presenilins of Alzheimer's disease increase production of 42-residue amyloid beta-protein in both transfected cells and transgenic mice. Nat Med. 1997;3(1):67-72.

61. Cacace R, Sleegers K, Van Broeckhoven C. Molecular genetics of early-onset Alzheimer's disease revisited. Alzheimers Dement. 2016;12(6):733-48.

62. Duchen LW, Eicher EM, Jacobs JM, Scaravilli F, Teixeira F. Hereditary leucodystrophy in the mouse: the new mutant twitcher. Brain. 1980;103(3):695-710.

63. Igisu H, Shimomura K, Kishimoto Y, Suzuki K. Lipids of developing brain of twitcher mouse. An authentic murine model of human Krabbe disease. Brain. 1983;106 (Pt 2):405-17.

64. Taniike M, Mohri I, Eguchi N, Beuckmann CT, Suzuki K, Urade Y. Perineuronal oligodendrocytes protect against neuronal apoptosis through the production of lipocalin-type prostaglandin D synthase in a genetic demyelinating model. J Neurosci. 2002;22(12):4885-96.

65. Saftig P, Peters C, von Figura K, Craessaerts K, Van Leuven F, De Strooper B. Amyloidogenic processing of human amyloid precursor protein in hippocampal neurons devoid of cathepsin D. J Biol Chem. 1996;271(44):27241-4.

66. Mueller-Steiner S, Zhou Y, Arai H, Roberson ED, Sun B, Chen J, et al. Antiamyloidogenic and neuroprotective functions of cathepsin B: implications for Alzheimer's disease. Neuron. 2006;51(6):703-14.

67. Nichols MR, Moss MA, Reed DK, Lin WL, Mukhopadhyay R, Hoh JH, et al. Growth of beta-amyloid(1-40) protofibrils by monomer elongation and lateral association. Characterization of distinct products by light scattering and atomic force microscopy. Biochemistry. 2002;41(19):6115-27.

68. Rangachari V, Moore BD, Reed DK, Sonoda LK, Bridges AW, Conboy E, et al. Amyloid-beta(1-42) rapidly forms protofibrils and oligomers by distinct pathways in low concentrations of sodium dodecylsulfate. Biochemistry. 2007;46(43):12451-62.

69. Case A, Huskey WP, Stein RL. Enzymatic reaction of silent substrates: kinetic theory and application to the serine protease chymotrypsin. Biochemistry. 2003;42(16):4727-32.

70. Leissring MA, Lu A, Condron MM, Teplow DB, Stein RL, Farris W, et al. Kinetics of amyloid beta-protein degradation determined by novel fluorescence- and fluorescence polarization-based assays. J Biol Chem. 2003;278(39):37314-20.

71. Nhan HS, Chiang K, Koo EH. The multifaceted nature of amyloid precursor protein and its proteolytic fragments: friends and foes. Acta Neuropathol. 2015;129(1):1-19.

72. De Strooper B, Vassar R, Golde T. The secretases: enzymes with therapeutic potential in Alzheimer disease. Nat Rev Neurol. 2010;6(2):99-107.

73. Leissring MA, Saido TC. Degradation of amyloid-ß protein. In: Selkoe DJ, Mandelkow E, Holtzman DM, editors. The biology of Alzheimer disease. Cold Spring Harbor, New York: Cold Spring Harbor Laboratory Press; 2011. p. 387-404.

74. Eckman EA, Adams SK, Troendle FJ, Stodola BA, Kahn MA, Fauq AH, et al. Regulation of steady-state beta-amyloid levels in the brain by neprilysin and endothelin-converting enzyme but not angiotensin-converting enzyme. J Biol Chem. 2006;281(41):30471-8.

75. Cheng S, Wani WY, Hottman DA, Jeong A, Cao D, LeBlanc KJ, et al. Haplodeficiency of Cathepsin D does not affect cerebral amyloidosis and autophagy in APP/PS1 transgenic mice. J Neurochem. 2017;142(2):297-304.

76. Su Y, Chang PT. Acidic pH promotes the formation of toxic fibrils from beta-amyloid peptide. Brain Res. 2001;893(1-2):287-91.

77. Hong S, Quintero-Monzon O, Ostaszewski BL, Podlisny DR, Cavanaugh WT, Yang T, et al. Dynamic analysis of amyloid beta-protein in behaving mice reveals opposing changes in ISF

versus parenchymal Abeta during age-related plaque formation. J Neurosci. 2011;31(44):15861-9.

78. Hama E, Shirotani K, Iwata N, Saido TC. Effects of neprilysin chimeric proteins targeted to subcellular compartments on amyloid beta peptide clearance in primary neurons. J Biol Chem. 2004;279(29):30259-64.

79. Qureshi YH, Patel VM, Berman DE, Kothiya MJ, Neufeld JL, Vardarajan B, et al. An Alzheimer's Disease-Linked Loss-of-Function CLN5 Variant Impairs Cathepsin D Maturation, Consistent with a Retromer Trafficking Defect. Mol Cell Biol. 2018;38(20).

80. Touitou I, Capony F, Brouillet JP, Rochefort H. Missense polymorphism (C/T224) in the human cathepsin D pro-fragment determined by polymerase chain reaction--single strand conformational polymorphism analysis and possible consequences in cancer cells. Eur J Cancer. 1994;30A(3):390-4.

81. Bertram L, McQueen MB, Mullin K, Blacker D, Tanzi RE. Systematic meta-analyses of Alzheimer disease genetic association studies: the AlzGene database. Nat Genet. 2007;39(1):17-23.

82. Zheng H, Jiang M, Trumbauer ME, Sirinathsinghji DJ, Hopkins R, Smith DW, et al. beta-Amyloid precursor protein-deficient mice show reactive gliosis and decreased locomotor activity. Cell. 1995;81(4):525-31.

83. Luo Y, Bolon B, Kahn S, Bennett BD, Babu-Khan S, Denis P, et al. Mice deficient in BACE1, the Alzheimer's beta-secretase, have normal phenotype and abolished beta-amyloid generation. Nat Neurosci. 2001;4(3):231-2.

84. Chen F, Eckman EA, Eckman CB. Reductions in levels of the Alzheimer's amyloid beta peptide after oral administration of ginsenosides. Faseb J. 2006;20(8):1269-71.

85. Kramer SD, Wohrle J, Rath C, Roth G. Anabel: an online tool for the real-time kinetic analysis of binding events. Bioinform Biol Insights. 2019;13:1177932218821383.

86. Suire CN, Abdul-Hay SO, Sahara T, Kang D, Brizuela MK, Saftig P, et al. Cathepsin D regulates cerebral Abeta42/40 ratios via differential degradation of Abeta42 and Abeta40. Alzheimers Res Ther. 2020;12(1):80.

CHAPTER 4

AIM 3

4.1 Background

Insulin-degrading enzyme (IDE) is a structurally unusual zinc-metallopeptidase that is ubiquitously expressed in the cytosol and various other subcellular compartments (1). IDE can be found in soluble brain extracts (2), as well as conditioned medium of cultured cells (3, 4). IDE is the principal catabolizer of insulin, but is also capable of degrading glucagon, amylin, and monomeric amyloid β-protein (Aβ) (5). It has been predicted that pharmacological inhibition of IDE should boost insulin signaling in a manner beneficial for the treatment of type-2 diabetes mellitus (T2DM) (6-9). On the other hand, because IDE also degrades Aβ (10, 11) there is concern that IDE inhibitors may increase risk for the development of Alzheimer disease (AD).

Despite their significant therapeutic potential—and despite numerous outstanding questions about the biology of IDE that can only be addressed via a pharmacological approach—only a very limited number of IDE inhibitors have been described, consisting almost exclusively of peptidic compounds (12-15) and one thiol-modifying inhibitor (16). As discussed in greater detail, all of these compounds carry significant liabilities, including instability *in vivo*, lack of oral bioavailability, and/or strong potential for off-target effects. There is also a large number of outstanding questions about the relative roles of different pools of IDE, which exists both intracellularly and extracellularly, which can only be addressed with appropriate cell-penetrant and non-penetrant IDE inhibitors. Therefore, there is a strong need to generate improved inhibitors of IDE with greater potential for development into viable drug candidates, and with the properties needed to better elucidate the different physiological and pathophysiological roles of IDE.

The following publications detail some of the work we have conducted towards the goal of developing improved IDE inhibitors. Because pharmacological modulators of IDE can be exquisitely substrate-selective (12, 17), there is a need to develop assays for multiple IDE substrates that are accurate and compatible with high-throughput screening (HTS). This Chapter details our published work on the development of proteolytic degradation assays for glucagon (18), but we have also developed similar assays for amylin degradation that would be redundant to present here. Using these assays and others, we also describe the discovery of novel cyclic peptide inhibitors of IDE using phage display and the development of zinc-targeting IDE inhibitors using fragment-based drug discovery (FBDD).

4.2 Aims and rationale

Aim 3A: Development of substrate-specific high-throughput IDE activity assays

Rationale & Hypothesis: Insulin-degrading enzyme (IDE) degrades multiple substrates involved in diverse processes, many of which have opposite biological effects (e.g., insulin and glucagon). To investigate substrate-specific cleavage, there is a great need to develop multiple assays for proteolytic degradation of individual IDE substrates. We developed assays based on N-terminally fluoresceinated and C-terminally biotinylated glucagon (and amylin). Hydrolysis at any peptide bond separates the fluorescence group from the biotin moiety, which can be assayed by multiple methods involving avidin. We extensively characterized these assays to ensure they are quantitative, reliable, and suitable for HTS. Similar assays for amylin were generated, but are not presented here.

Aim 3B: Screening of small molecule libraries to find broad-spectrum and substrate-selective inhibitors and activators of IDE

Rationale & Hypothesis: IDE degrades multiple substrates, including Aβ, insulin, glucagon, and amylin. Through screening of peptide and small-molecule libraries, we hypothesized that we can discover and develop general and substrate-selective activators and inhibitors of IDE that can be beneficial in research and the treatment of diseases such as T2DM, AD and wound healing.

4.3 Publication 1:

Development and characterization of quantitative, high-throughput-compatible assays for proteolytic degradation of glucagon

4.3.1 Abstract

Glucagon is a vital peptide hormone involved in the regulation of blood sugar under fasting conditions. While the processes underlying glucagon production and secretion are well understood, far less is known about its degradation, which could conceivably be manipulated pharmacologically for therapeutic benefit. We describe here the development of novel assays for glucagon degradation, based on a modified glucagon peptide (FBG) labeled with fluorescein and biotin at the N- and C-termini, respectively. Proteolysis at any peptide bond within FBG separates the fluorescent label from the biotin tag, which can be quantified in multiple ways. In one method requiring no specialized equipment, intact FBG is separated from the cleaved fluoresceinated fragments using neutravidin-agarose beads, and hydrolysis is quantified by fluorescence. In an alternative, high-throughput-compatible method, the degree of hydrolysis is quantified using fluorescence polarization after addition of unmodified avidin. Using a known glucagon protease, we confirm that FBG is cleaved at similar sites as unmodified glucagon and utilize both methods to quantify the kinetic parameters of FBG degradation. We show further that the fluorescence

polarization-based assay performs exceptionally well (Z'-factor values >0.80) in high-throughput, mix-and-measure format.

4.3.2 Introduction

Glucagon is a 29-amino acid peptide hormone produced by alpha cells of the islet of Langerhans within the pancreas. Regarded as the principal catabolic hormone within the body, glucagon signals the liver to release glucose into the blood under fasting conditions by promoting glycogenolysis and gluconeogenesis, inhibiting glycogenesis, and other effects. Injected glucagon is also used therapeutically to treat a variety of conditions, including low blood sugar, anaphylaxis, and overdose by β-adrenergic receptor antagonists. Other therapeutic uses pertaining to the management of diabetes mellitus have been proposed (19).

While the mechanisms underlying the production and secretion of glucagon are well understood, considerably less is known about the catabolic fate of glucagon after its release from the pancreas. Glucagon is known to be hydrolyzed by a number of proteases, including dipeptidyl peptidase IV (20), neprilysin (21), and insulin-degrading enzyme (IDE) (22), with a recent study demonstrating that IDE regulates glucagon levels *in vivo* (15). The identification of pharmacological inhibitors of glucagon degradation will help elucidate the physiological and pathophysiological roles of this important hormone and its proteases, and may also hold value as therapeutic agents (19).

Although numerous assays for glucagon quantification exist, current assays are expensive, difficult to implement and/or less than ideal for high-throughput compound screening. Several ELISAs for glucagon are available, but these are costly, labor intensive to execute, and are normally provided only in 96-well format. Assays based on homogeneous time-resolved fluorescence are also available (e.g., ref. 23), but not all laboratories have the specialized

equipment required for this assay format. Moreover, in our hands, these assays performed poorly for compound screening, with Z'-factor values rarely exceeding 0.3. There is, therefore, a need to develop assays for glucagon degradation more suitable for high-throughput screening (HTS).

We report here on the development and characterization of versatile assays for glucagon degradation based on fluoresceinated and biotinylated glucagon (FBG). We describe assays based on two complementary formats, one that is readily implemented with no specialized equipment, and a second, mix-and-measure, HTS-compatible format based on fluorescence polarization (FP). Using IDE as a prototype glucagon protease, we show that FBG is cleaved at the same sites as unmodified glucagon and hydrolyzed with similar kinetics. Both assays are quantitative, highly sensitive, and usable across a wide range of substrate concentrations. The FP-based assay performs exceptionally well in high-throughput format, yielding Z'-factor values consistently >0.80. These assays will facilitate the discovery of chemical modulators of glucagon degradation and proteolytic processing, which may in turn lead to the development of novel therapeutics for controlling glucagon activity.

4.3.3 Results

We used a derivatized form of human glucagon, fluoresceinated at the N-terminus and biotinylated at the C-terminus (FBG), and a known glucagon protease, IDE, to develop novel glucagon degradation assays. We explored two formats, each with distinct advantages. In the first format, dubbed avidin-agarose precipitation (AP), the degree of hydrolysis is assessed by removing the intact, biotinylated and fluoresceinated species using neutravidin-agarose beads, then quantifying the amount of cleaved, fluoresceinated fragments remaining in the supernatant by fluorescence. This method has the advantage of requiring no specialized equipment other than a fluorescence plate reader; however, it entails comparatively complex manipulations, including

centrifugation and transfer steps (Fig. 4.1A) and thus is not readily adaptable to robotic automation. As expected, the AP method was a very effective means for detecting hydrolysis: intact FBG was nearly entirely removed by precipitation with neutravidin-agarose, while completely hydrolyzed FBG yielded a fluorescent signal >33-fold higher (Fig. 4.1B). As controls, we also quantified the fluorescence of intact and fully cleaved FBG in the absence of neutravidin-agarose. Hydrolyzed FBG unexpectedly fluoresced more strongly than the intact substrate even in the absence of neutravidin-agarose, albeit resulting in a significantly reduced relative signal change (~2.3-fold) as compared to the AP method. Using the AP method to monitor fluorescence as a function of time resulted in progress curves fitted well by hyperbolic curves (Fig. 4.1C).

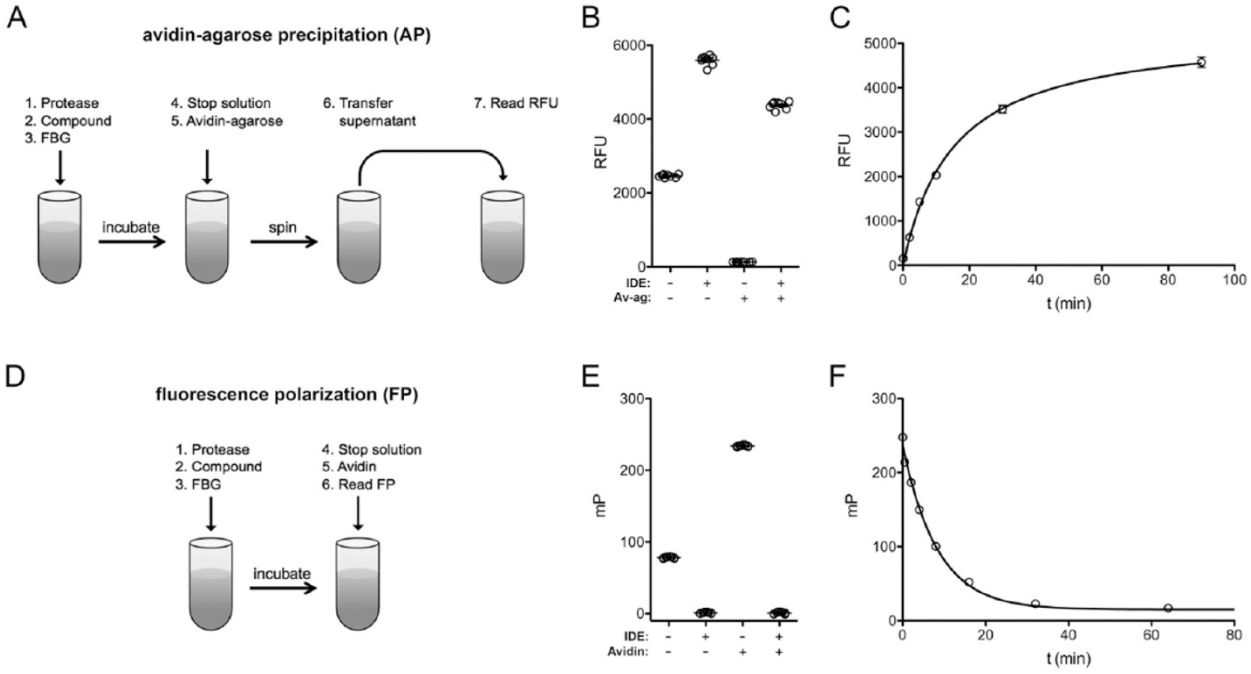

Figure 4.1. Overview of FBG-based glucagon degradation assays. Comparison of the experimental protocols and overall performance of the avidin-agarose precipitation (AP)-based method (***A***-***C***) and the fluorescence polarization (FP)-based method (***D***-***F***). ***A***, Cartoon showing the basic steps involved in carrying out the AP-based glucagon degradation assay. Note that both centrifugation and transfer steps are required. ***B***, Assessment of the minimal and maximal signal changes observed with uncleaved and fully hydrolyzed FBG (1 μM), respectively, before and after avidin-agarose (Av-ag) precipitation. Note that a >33-fold increase in signal is observed following AP, while a more modest signal change is seen even prior to this step (expressed in relative fluorescence units; RFU). ***C***, Typical progress curve observed with the AP-based assay using 2 μM FBG. ***D***, Cartoon illustrating the steps involved in carrying out the FP-based method, which is a true mix-and-measure procedure. ***E***, Changes in FP (expressed in millipolarization units; mP) obtained with intact versus fully hydrolyzed FBG (1 μM) in the absence or presence of avidin (4 μM). Note the large shift in depolarization by intact FBP effected by avidin, and the absence of change in fully cleaved FBG. ***F***, Typical progress curve observed with the FP-based assay using 2 μM FBG.

The second method we explored is based on the use of fluorescence polarization (FP) to monitor hydrolysis (24). Although specialized equipment is required, this approach has the advantage of being a simple mix-and-measure method requiring no centrifugation or transfer steps, making it much more amenable to automation vis-à-vis the AP method (Fig. 4.1D). FP has the further advantage of being a ratiometric rather than an absolute measure and thus less sensitive to

changes in volume or interference by experimental compounds (24). The FP method exploits the fact that fluorescent species in solution tumble at a rate inversely proportional to their size. Cleaved fragments tumble quickly and hence depolarize polarized light strongly (Fig. 4.1E). Intact FBG, being larger, tumbles more slowly and, by virtue of the C-terminal biotin moiety, this rate of tumbling of intact FBG can be slowed further by addition of avidin, a 64-kDa tetrameric protein (Fig. 4.1E). A typical progress curve obtained with the FP method is shown in Figure 4.1F.

Although the foregoing results established the functionality of FBG in both the AP and FP formats, it was critical to establish whether FBG was cleaved at the same sites as underivatized glucagon. To explore this, we used MALDI-TOF to analyze the fragments obtained after various lengths of incubation of FBG or human glucagon with IDE. Consistent with previous findings (22), we obtained fragments with masses indicative of cleavage occurring C-terminal to Ser16, Arg17 and Trp25 (Table 4.1; Appendix C Fig. S4.1) for both derivatized and underivatized glucagon. These data suggest that the biotin and fluorescein tags do not interfere with the processing of FBG.

Table 4.1. Cleavage sites of FBG and unmodified glucagon determined by mass spectrometry. MALDI-TOF mass spectrometry of FBG and unmodified human glucagon degraded partially by IDE was conducted and used to infer the cleavage sites (arrows) within the peptide sequence of both FBG and underivatized human glucagon. Note that the inferred cleavage sites match those reported previously (22). The mass spectra used to derive these data are shown in Appendix C Fig. S4.1. ND = not detected (below the minimum mass threshold for detection by MALDI-TOF).

HSQGTFTSDYSKYLDS↓↓RRAQDFVQW↓LMNT

		Unmodified glucagon			FBG		
Fragment	**Sequence**	**Exp.**	**Obs.**	**Diff.**	**Exp.**	**Obs.**	**Diff.**
1-29	HSQGTFTSDYSKYLDSRRAQDFVQWLMNT	3481.62	3481.23	0.39	4306.57	4306.19	0.38
1-17	HSQGTFTSDYSKYLDSR	1991.91	1991.76	0.15	2350.21	2350.45	-0.24
17-29	RRAQDFVQWLMNT	1664.83	1664.70	0.13	2131.48	2130.62	0.86
18-25	RAQDFVQW	1049.52	1049.42	0.10	1049.52	1049.42	0.10
18-29	RAQDFVQWLMNT	1508.73	1508.61	0.12	1975.38	1974.55	0.83
26-29	LMNT	478.23	ND	—	944.88	944.17	0.71

Despite the clear advantages of the FP method from the standpoint of automation, there are additional complications that must be taken into account when it is used for quantitative assays. To illustrate this, we compared the signal changes obtained by the AP versus the FP methods in response to fixed percentages of hydrolyzed versus intact FBG (Fig. 4.2A). As expected, the percent change in RFU obtained using the AP method varies in direct proportion with the percent hydrolyzed FBG. In contrast, the percent change in mP obtained with the FP method departs significantly from linearity, effectively overestimating changes in hydrolysis at all time points (Fig. 4.2A). For quantitative assays, data expressed in mP must therefore be converted to percent hydrolysis (Fig. 4.2B), which is readily accomplished via a 3rd-order polynomial equation fitted to the data in Figure 4.2A (see Eq. 1 and Appendix C Fig. S4.2).

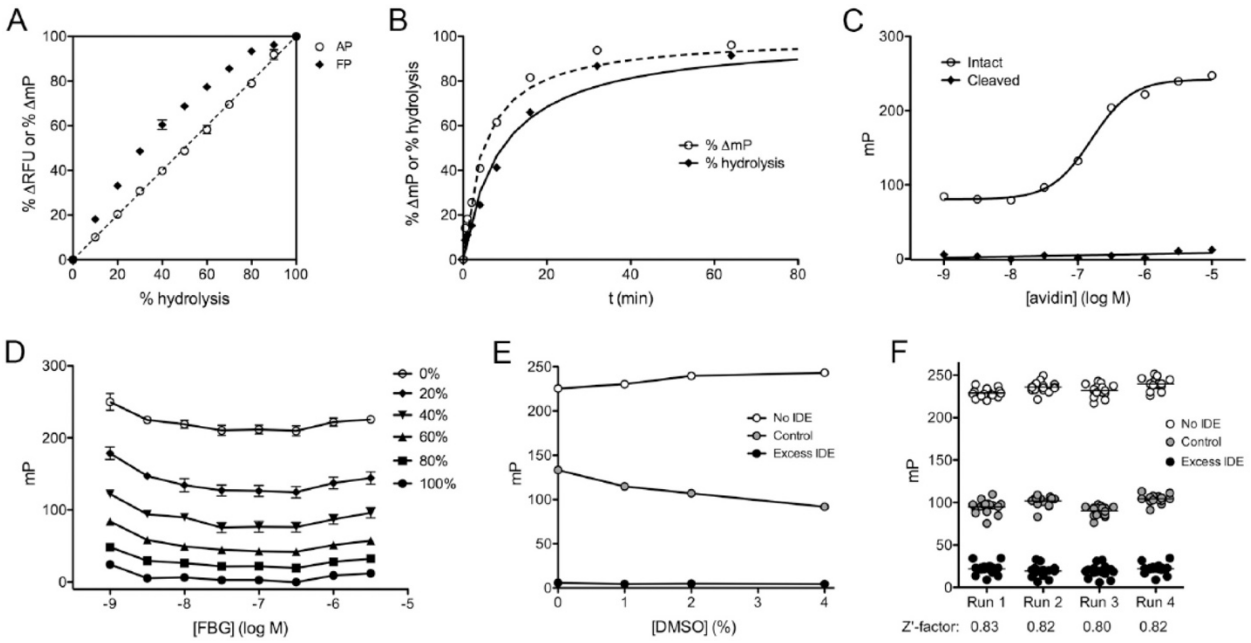

Figure 4.2. Characterization of the FP-based glucagon degradation assay. ***A***, Relationship between percent signal change and percent hydrolysis of FBG for the FP- and AP-based methods. Note that, unlike the AP-based assay, the FP-based assay shows a non-linear relationship. These data were used to generate a formula for conversion of raw FP data to percent hydrolysis for quantitative analyses (see section 4.3.5 and Appendix C Fig. S4.2). Data are mean ± SEM for 3 independent experiments. ***B***, Progress curve from the FP-based assay showing raw percent change in mP values (*dashed line*) and the same data converted to percent hydrolysis (*solid line)*, using the equation derived from the data in (***A)*** (Eq. 1). ***C***, Effect of avidin concentration on measured mP values for a fixed concentration of FBG (500 nM). Note that fully cleaved fragments are unaffected by avidin. Data are mean ± SEM for 3 independent experiments. ***D***, Relationship between raw mP values and FBG concentration for different degrees of hydrolysis. Note that only slight changes in mP are observed between 10 nM and 300 nM. The relationship between percent signal change and percent hydrolysis for these data are shown in Appendix C Fig. S4.3. Data are mean ± SEM for 3 independent experiments. ***E***, Effect of DMSO concentration on performance of the FP-based assay. Data are mean ± SEM for 16 replicates. ***F***, Raw data and calculated Z'-factor values for 4 independent experiments conducted in high-throughput (384-well) format on separate days.

As is evident from Figure 4.1D, the absolute mP values obtained using the FP method depend critically upon the avidin concentration. To explore this, we tested the mP values for intact and fully cleaved FBG in the presence of varying concentration of avidin (Fig. 4.2C). For intact FBG at a nominal concentration of 500 nM, the EC_{50} for avidin (monomer) was found to be 160 ± 6.1 nM (n=3), a value in good agreement with expectations, and essentially complete saturation

was obtained with ~1 to 3 μM avidin. Avidin had no effect on the FP signal of fully hydrolyzed FBG, as expected. In practice, we used at least 4 equivalents of avidin monomer (i.e., equimolar quantities of tetrameric avidin) per FBG equivalent in our stop solutions.

We also quantified how the FP signal varies as a function of FBG concentration, examining intact and fully cleaved FBG, as well as several fixed percentages of cleaved substrate across a wide range of concentrations (1 nM to 3 μM; Fig. 2D). The raw mP values varied only slightly as a function of concentration, being especially consistent between 10 nM and 300 nM (Fig. 4.2D). In addition, we examined whether FBG concentration affected the relationship between percent change in mP and percent hydrolysis. With the exception of the very lowest concentrations tested (1 and 3 nM), which showed slightly smaller deviations from linearity relative to all other concentrations, this relationship was essentially unchanged from that shown in Figure 4.2A (i.e., with 1 μM FBG) at all concentrations at or above 10 nM (Appendix C Fig. S4.3).

To assess the effect of DMSO on the FP-based assay, we tested the assay in the presence of 0, 1, 2 and 4% DMSO. Increasing concentrations of DMSO resulted in increased rates of FBG hydrolysis by a fixed amount of IDE, but the effect on uncleaved and fully cleaved substrate was modest (Fig. 4.2E), suggesting the assay is highly tolerant of DMSO.

To assess quantitatively the suitability of the FP-based glucagon degradation assay in high-throughput format, we conducted 4 independent experiments in 384-well format (30 μL/well) on separate days, quantifying the maximum and minimum changes in mP values, obtained from intact and fully hydrolyzed FBG, respectively, as well as testing the percent hydrolysis obtained using a fixed quantity of IDE terminated at a fixed interval of time (Fig. 4.2F). The percent hydrolysis achieved by control reactions was highly consistent (44 ± 1.4 %) among the independent runs (Fig.

2F). Z'-factor values (25) calculated from the resulting data exceeded 0.80 in all cases and averaged 0.82 ± 0.007 (Fig. 4.2F).

To assess the utility of FBG-based assays for obtaining quantitative data, we determined the kinetic parameters of FBG degradation using both the AP and FP methods. To that end, progress curves were obtained at different substrate concentrations, from which the initial velocity (v_o) of each reaction was quantified. As expected, plots of v_o as a function of FBG concentration followed a hyperbolic relationship for both the AP (Fig. 4.3A) and FP (Fig. 4.3B) methods, yielding apparent K_M values (800 ± 110 nM and 380 ± 72 nM, respectively) and k_{cat} values (1.76 ± 0.19 s^{-1} and 1.16 ± 0.11 s^{-1}, respectively) in good agreement (Appendix C Table S4.1).

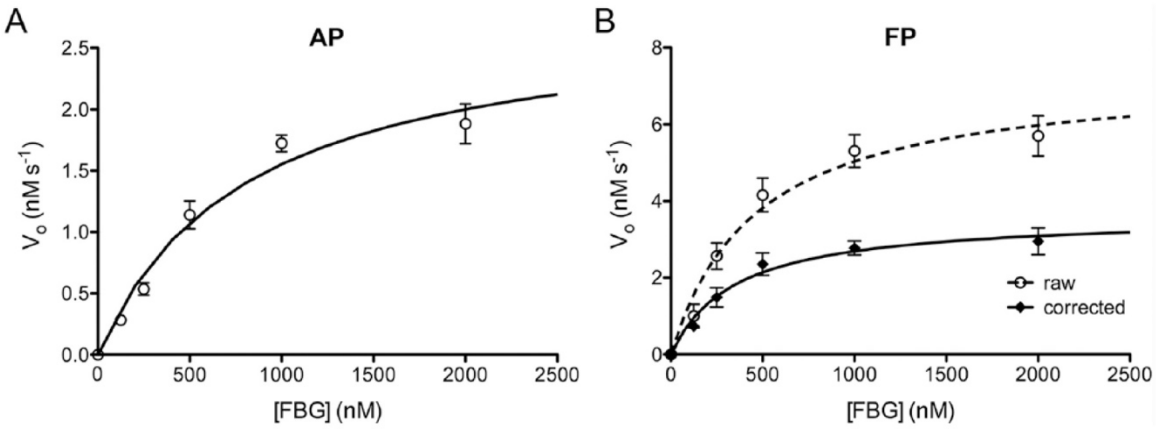

Figure 4.3. Kinetics of FBG degradation by IDE. Results obtained using the AP ***A***, and FP ***B***, -based assays, showing initial velocity (v_o) plotted as a function of FBG concentration. Data from the FP-based assay are plotted both in terms of raw percent change in mP (*dashed line*) and those data converted to percent hydrolysis using Eq. 1 (*solid line*). Note that uncorrected, raw data significantly overestimate the v_{max} of the reaction. Data are mean ± SEM for 4 independent experiments and are fitted to hyperbolae. Kinetic parameters derived from these results are provided in Appendix C Table S4.1.

To further validate the FP-based glucagon degradation assay, we used it to characterize a previously described IDE inhibitor in terms of potency and mechanism of action, conducting experiments on separate days to verify whether the assay obtains consistent results. To that end, we conducted dose-response curves on **ML345**, a small-molecule, thiol-modifying, irreversible

inhibitor of IDE (16, 26). In excellent agreement with previous results (16, 26, 27), we obtained K_i values of 70.6 ± 9.0 nM for **ML345** (Fig. 4.4A). To assess whether the FP-based FBG assay could be used to distinguish the mechanism of action of the inhibitor, we conducted kinetics analyses in the absence or presence of **ML345** (50 nM). As is evident from Lineweaver-Burk plot (Fig. 4.4B), as well as quantitative analysis of the resulting data (Appendix C Table S4.2), we obtained results consistent with irreversible inhibition for **ML345**.

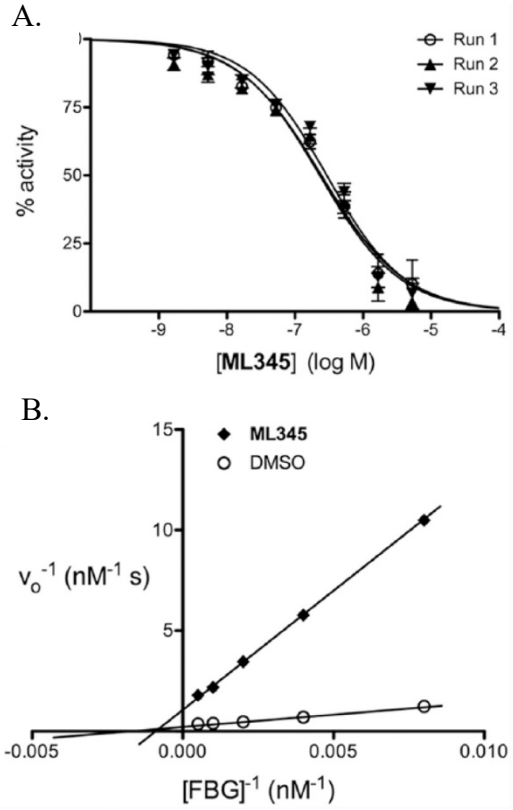

Figure 4.4. Validation of FP-based glucagon assay using known IDE inhibitor. Dose-response curves ***A***, and kinetic analyses ***B***, conducted in the absence or presence of a well-characterized IDE inhibitor: **ML345**. For dose-response curve, data are mean ± SEM for each of 3 independent experiments conducted on separate days. For kinetic experiments, data are expressed as double-reciprocal plots; for clarity, we show a single linear regression curve is drawn from the mean ± SEM of 3 independent experiments. Kinetic parameters derived from these results are provided in Appendix C Table S4.2.

To establish the suitability of the FP-based glucagon degradation assay for HTS, we used it to screen a collection of 753 compounds, in duplicate, at two different concentrations (500 μM and 50 μM), for a total of 3012 separate reads plus controls. In parallel, we screened the same compounds using a well-characterized FP-based Aβ degradation assay(28) and a fluorogenic peptide substrate (Substrate V; Sub V). As expected, strong correlations were observed between replicate readings at both 500 μM (Fig. 4.5A) and 50 μM (Fig. 4.5D). Correlations with other assays confirmed the validity of the FBG-based assay and the advantage of the FP format over fluorescence-based screens. Comparison with the Aβ degradation assay, another FP-based assay, revealed strong, but not perfect, correlations at both 500 μM (Fig. 4.5B) and 50 μM (Fig. 4.5E). In marked contrast, almost no correlation was observed at either compound concentration between the FBG-based assay and the fluorogenic assay utilizing Sub V (Fig. 4.5C, F), with the latter assay exhibiting evidence of strong activation by some compounds. These results are consistent with previous findings showing that screens conducted with fluorogenic peptide substrates often uncover compounds that exhibit markedly dissimilar activity when tested against endogenous substrates (14, 29).

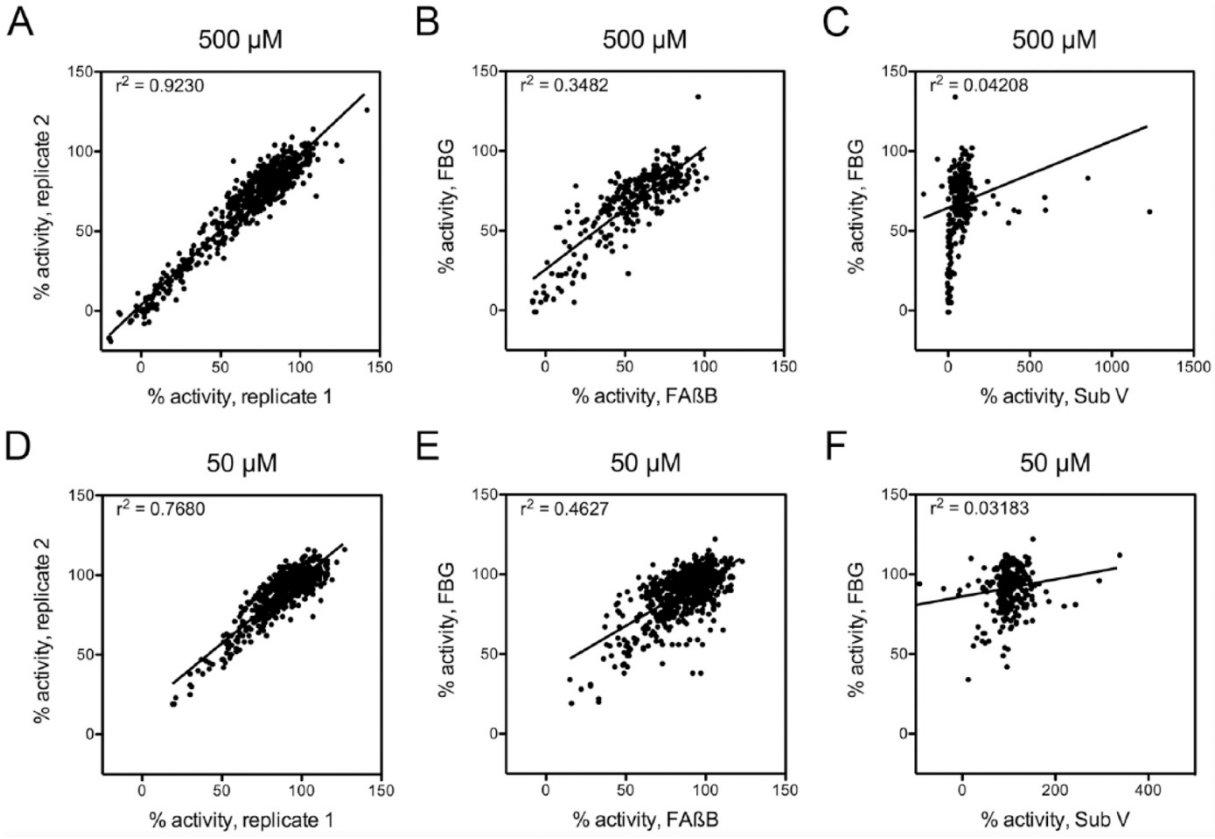

Figure 4.5. Performance of the FP-based glucagon degradation assay in HTS. Results from screening of 753 compounds with the FP-based FBG assay at 500 µM (***A***-***C***) and 50 µM (***D***-***F***). ***A***, Correlation between replicates conducted at 500 µM. ***B***, Correlation between results obtained with FBG and an Aβ-degradation assay (FAβB) at 500 µM. ***C***, Correlation between results obtained with FBG and Substrate V (Sub V) at 500 µM. ***D***, Correlation between replicates conducted at 50 µM. ***E***, Correlation between results obtained with FBG and FAβB at 50 µM. ***F***, Correlation between results obtained with FBG and Sub V at 50 µM.

4.3.4 Discussion

Using a dual-labeled form of glucagon, containing N-terminal fluorescein and C-terminal biotin moieties (FBG), we have succeeded in developing novel glucagon degradation assays that are versatile, quantitative, sensitive, and easily and inexpensively implemented. Notably, we demonstrate that the FP-based format of this assay is highly suitable for automated HTS.

Several lines of evidence suggest that FBG is processed similarly to unmodified glucagon, at least for IDE, which has been demonstrated to degrade glucagon *in vivo* (15). Consistent with previous results (22), MALDI-TOF analysis reveals that FBG is cleaved by IDE at the same sites

as human glucagon, specifically C-terminal to Ser16, Arg17 and Trp25. Furthermore, the kinetic parameters of FBG degradation obtained with both assay formats are in close agreement with one another and, with certain qualifications, reasonably similar to those reported in a previous study (30). The latter study, conducted in 1985 by Shroyer and colleagues, reported that glucagon was degraded with an apparent K_M of 3.46 μM and k_{cat} of 38.5 min^{-1} (0.641 s^{-1}) by a semi-purified protease that has been inferred—but not definitively proven—to be IDE. More specifically, the protease in this study, purified by affinity chromatography from rat liver, exhibited some characteristics consistent with IDE and others that are inconsistent. As is true for IDE, the purified protease was susceptible to inhibition by bacitracin (31) and thiol-alkylating agents such as N-ethylmaleimide (32), and was partially, but not completely, inhibited by zinc-chelating agents such as EDTA (33). On the other hand, the protease purified by Shroyer et al. was reported to exhibit a native size of ~180 kDa, rather than the correct value of ~220 kDa for the native, homodimeric form of IDE and, more troublingly, was composed of two non-identical subunits with different isoelectric points (30), findings that are inconsistent with the purified protease being (exclusively) IDE. These considerations, together with other limitations inherent to the methodology available at the time, raise some doubts about the reliability of the kinetic parameters reported by Shroyer and colleagues, and may account for the modest discrepancy with the results obtained with the AP and FP assays.

The kinetic parameters of FBG degradation by IDE are also consistent with those reported for other IDE substrates. In multiple previous studies performed with the same form of purified recombinant IDE, amyloid-β protein (Aβ) was degraded with K_M values of 0.8 – 1.2 μM and k_{cat} values of 0.88 – 4.27 s^{-1} (28, 34), values in excellent agreement with those obtained in the present study (see Appendix C Table S4.1). The notable exception is insulin, which was degraded with a

K_M of 65.7 ± 3.4 nM and a k_{cat} value of 0.025 s^{-1} (28, 34). The significantly lower K_M value for insulin reflects the known high affinity of insulin for IDE (35), whereas the remarkably slower turnover rate of insulin vis-à-vis other substrates is thought to be attributable to the unusually large and rigid structure of insulin, a 2-chain, disulfide-bonded substrate that makes extensive contacts with the internal chamber of IDE during processing (22), thus slowing the rate of release of incompletely hydrolyzed insulin from the protease (36).

As is evident from the performance of the FP-based glucagon degradation assay in HTS format, the assay is highly tolerant of compound screening even at concentrations as high as 500 μM. Due to the ratiometric nature of FP-based assays, the assay is generally unaffected by compounds that absorb strongly, and it also corrects for changes in volume. Because of the relatively long wavelength used for excitation of FITC (~488 nm), issues with compound fluorescence are largely obviated. However, the assay could conceivably be subject to artifacts in the case of compounds that fluoresce strongly in the same wavelengths as FITC. As a convenient counterscreening strategy, such compounds can be readily identified by examination of the raw fluorescence data in either the S or the P plane, then tested in orthogonal assays.

The assays described in the present study will facilitate the discovery of chemical modulators of glucagon degradation, which are expected to have multiple experimental and possibly therapeutic applications (19). Given that IDE has been confirmed to mediate glucagon degradation *in vivo* (15), it would seem to be an attractive target for such an effort. This idea might appear complicated, however, by the fact that IDE also avidly degrades glucagon's anabolic counterpart, insulin (33). While true, more than a decade of compound screening campaigns with IDE have shown that chemical modulators of IDE can be exquisitely substrate selective, with inhibitors showing widely varying K_i values for different substrates (32, 37), in some cases

differing by orders of magnitude (12). Indeed, certain compounds that inhibit the degradation of some IDE substrates can actually activate the degradation of other substrates (29, 38-40). These unusual substrate-selective effects arise as a consequence of the unique structure of IDE, which resembles a clamshell that completely encapsulates its substrates during a catalytic cycle (22). Substrates interact with the inner chamber of the protease at multiple sites besides the region near the active site, thereby permitting additional sites for chemical modulation. The assays developed in the present study will be instrumental, therefore, in the effort to identify compounds that selectively inhibit IDE-mediated glucagon degradation. In addition, the versatile nature of the assay format suggests it could be used for the discovery of chemical modulators of other glucagon proteases and/or the discovery of novel proteases mediating the degradation and/or processing of glucagon.

4.3.5 Methods/Experimental

Materials

FBG ([5FAM]HSQGTFTSDYSKYLDSRRAQDFVQWLMNT[Lys(Ahx-biotin)]-amide) was synthesized via solid-phase peptide synthesis by Thermo Fisher Scientific, Inc. (Whatham, MA, USA) and provided at 95% purity (Appendix C Fig. S4.4). Underivatized human glucagon and neutravidin-agarose beads were purchased from Thermo Fisher Scientific, Inc. (Whatham, MA, USA). Recombinant human IDE was generated as described (41). Unless otherwise noted, all other reagents and supplies were purchased from Sigma-Aldrich (St. Louis, MO, USA).

Mass spectrometry

To establish the cleavage sites within FBG and human glucagon, peptides (20 μM) were hydrolyzed by IDE in PBS for varying lengths of time, and the reactions were terminated by addition of 1% formic acid. Excess salts were removed using Millipore® C_{18} Ziptips (Sigma-

Aldrich, St. Louis, MO, USA) according to manufacturer's recommendations. The intact and digested peptides were eluted in a 1:3 mixture of water:acetonitrile supplemented with 0.1% trifluoroacetic acid, spotted 1:1 with 2,5-dihydroxybenzoic acid or alpha-cyano-4-hydroxycinnamic acid onto a steel sample plate, and subjected to matrix-assisted laser desorption/ionization-time-of-flight (MALDI-TOF) mass spectroscopy using positive reflection mode on an AB SCIEX TOF/TOF™ 5800 System (AB Sciex Pte. Ltd., Framingham, MA, USA). Observed masses were compared to monoisotopic $[M+H]^+$ masses predicted using PEPTIDEMASS (42).

Degradation assays

Except where otherwise noted, reactions were performed in Assay Buffer (PBS supplemented with 0.05% biotin-free BSA) with a final FBG concentration of 1 μM. For AP experiments, reactions were performed in 1.5-mL microfuge tubes and terminated by addition of 1,10-phenanthroline (2 mM). Biotinylated species were removed by addition of excess neutravidin-agarose beads (≥4 eq. biotin binding sites), followed by gentle rocking for 30 min and centrifugation at 14,000 X g for 10 min. The supernatant solution was carefully transferred to 384-well plates (30 μL/well), and fluorescence (λ_{ex} = 485 nm, λ_{em} = 515 nm) was quantified using a multilabel plate reader (SpectraMAX Gemini EM, Molecular Devices Corp., San Jose, CA, USA). For FP-based experiments, medium-throughput reactions were typically performed in 96-well, polypropylene plates and terminated by transfer to 384-well plates containing FP Stop Buffer (2 mM 1,10-phenanthroline; 4 eq. of avidin in Assay Buffer). Fluorescence polarization (λ_{ex} = 485 nm, λ_{em} = 515 nm) was quantified on a multilabel plate reader (SpectraMAX M5^e; Molecular Devices Corp., San Jose, CA, USA).

High-throughput screening

High-throughput FP-based assays were performed by successive addition of protease, experimental compounds or DMSO, FBG and, after a fixed incubation time, FP Stop Buffer in low-volume (30 μL/well) 384-well plates. To demonstrate the feasibility of using the assay for HTS, we screened a collection of 753 samples dissolved in DMSO, including known peptidic and nonpeptidic IDE inhibitors and a library of metal-binding pharmacophores (27, 43, 44), in duplicate at two different concentrations. The same compounds were also tested in parallel using an amyloid β-protein (Aβ) degradation assay (28) and a fluorescence dequenching assay based on Substrate V (Sub V; Mca-RPPGSFAFK(Dnp)-OH), performed as described (22). FP was quantified as described above.

Data analysis

Curve fitting was conducted using Prism 5 for Mac OS X (v. 5b). Percentage changes in mP values were converted to percent hydrolysis using the formula:

$$Y = 0.672622X - 0.00522939X^2 + 0.0000844959X^3 \quad \text{(Eq. 1)}$$

where Y = percent hydrolysis and X = percent change in mP. Z'-factor values were calculated according to Zhang and colleagues (25) using the following formula:

$$Z' = 1 - \frac{3(\sigma_{HI} + \sigma_{LO})}{(\mu_{HI} - \mu_{LO})} \quad \text{(Eq. 2)}$$

where σ_{HI} and σ_{LO} refer to the standard deviations and μ_{HI} and μ_{LO} the means for the high and low data, respectively.

4.4 Publication 2:

Peptidic inhibitors of insulin-degrading enzyme with potential for dermatological applications discovered *via* phage display

4.4.1 Abstract

Insulin-degrading enzyme (IDE) is an atypical zinc-metalloendopeptidase that hydrolyzes insulin and other intermediate-sized peptide hormones, many of which are implicated in skin health and wound healing. Pharmacological inhibitors of IDE administered internally have been shown to slow the breakdown of insulin and thereby potentiate insulin action. Given the importance of insulin and other IDE substrates for a variety of dermatological processes, pharmacological inhibitors of IDE suitable for topical applications would be expected to hold significant therapeutic and cosmetic potential. Existing IDE inhibitors, however, are prohibitively expensive, difficult to synthesize and of undetermined toxicity. Here we used phage display to discover novel peptidic inhibitors of IDE, which were subsequently characterized *in vitro* and in cell culture assays. Among several peptide sequences tested, a cyclic dodecapeptide dubbed **P12-3A** was found to potently inhibit the degradation of insulin (K_i = 2.5 ± 0.31 μM) and other substrates by IDE, while also being resistant to degradation, stable in biological milieu, and highly selective for IDE. In cell culture, **P12-3A** was shown to potentiate several insulin-induced processes, including the transcription, translation and secretion of alpha-1 type I collagen in primary murine skin fibroblasts, and the migration of keratinocytes in a scratch wound migration assay. By virtue of its potency, stability, specificity for IDE, low cost of synthesis, and demonstrated ability to potentiate insulin-induced processes involved in wound healing and skin health, **P12-3A** holds significant therapeutic and cosmetic potential for topical applications.

4.4.2 Introduction

Insulin is a pleiotropic peptide hormone that, although best known for its role in blood sugar regulation, is implicated in a wide array of physiological processes relevant to skin health and wound repair (45). Insulin stimulates the proliferation (46, 47), differentiation (48) and migration (49, 50) of skin fibroblasts and keratinocytes, as well as the production and secretion of extracellular matrix (ECM) proteins, particularly collagen (51-57). Conversely, all of these processes are impaired in the skin of mice with genetic deletion of the insulin receptor (58). Moreover, impairments in wound healing and other skin disorders are common among patients with diabetes (59), a disease characterized by defects in insulin production or action.

Given the importance of insulin signaling to wound healing, topical insulin has been investigated in numerous studies in animals (50, 60-64) and humans (65), including several clinical trials (66-68). However, the routine clinical use of topical insulin for wound management is not generally accepted as a first-line treatment, and significant adverse effects—including life-threatening hypoglycemia—have been reported (69).

Our group has been exploring an alternative approach to boosting insulin signaling that obviates the risk of hypoglycemia: namely, pharmacological inhibition of insulin-degrading enzyme (IDE) (70), the principal protease implicated in the catabolism and inactivation of insulin (33). IDE inhibitors have been shown to potentiate insulin action in cultured cells (14) and *in vivo* (8, 15, 71). Recently developed, highly selective IDE inhibitors exhibited potent antidiabetic properties (15), effects that were attributable to reduced catabolism of insulin. Importantly, mice with genetic deletion of IDE are viable (6, 10, 72); thus—unlike insulin—IDE inhibitors possess no intrinsic risk of triggering life-threatening hypoglycemia. IDE is expressed to high levels in skin (34, 73) and—notably—is especially abundant in wound fluid (74, 75) where it degrades

insulin (74, 75). Thus, topical application of IDE inhibitors is strongly predicted to enhance insulin signaling in skin.

Although a number of IDE inhibitors have been developed (12-15, 76-78), existing compounds are not ideal for topical applications due to their high cost of synthesis and undetermined toxicity. To overcome these limitations, we sought here to develop peptidic inhibitors of IDE that, by their intrinsic nature, would be inexpensive to manufacture and unlikely to be toxic. To that end, we used phage display to discover cyclic and linear peptide sequences that bind with high affinity to IDE. Among the sequences analyzed, a dodecameric, cyclic peptide dubbed **P12-3A**, proved to be a potent inhibitor of IDE that was stable in biologic milieu and highly selective for IDE. **P12-3A** was found to potentiate a number of insulin-stimulated processes in cultured skin cells, including collagen production in fibroblasts and migration of keratinocytes in a scratch wound assay. Given its high potency, selectivity for IDE, minimal potential for toxicity, and its low cost of manufacture, **P12-3A** possesses the characteristics needed to further explore the therapeutic and cosmetic potential of topical IDE inhibition.

4.4.3 Results

To identify novel peptidic inhibitors of IDE, we utilized phage display technology (79) to search for sequences that bind with high affinity to immobilized recombinant human IDE. Reasoning that IDE possesses an intrinsic affinity for cyclic peptides, we screened a library of cyclic peptides (Ph.D.^{TM}-C7C, New England Biolabs) comprised of essentially all combinations of seven natural amino acids flanked by two cysteines (ACXXXXXXXCGGG…, where X represents any amino acid). The two cysteines form a disulfide bond that cyclizes each peptide, the alanine serves to protect the N-terminal cysteine from off-target interactions, and the three glycines form a flexible linker with the bacteriophage coat protein. Three rounds of panning were

conducted using immobilized recombinant human IDE, with elution performed by addition of excess insulin in order to enrich for sequences that bind to the internal chamber of IDE. Twenty clones were selected for DNA sequencing, yielding sixteen unique amino acid sequences, some of which appeared more than once (Fig. 4.6A). From analysis of all sequences (Fig. 4.6B), a clear consensus sequence emerged (ACSWWSIHLCGGG…). This sequence, dubbed **C7C-1** (Fig. 4.6C, Appendix C Fig. S4.5A), was selected for subsequent synthesis and testing, together with another that appeared two times (ACNAGHLSQCGGG…), dubbed **C7C-2** (Fig. 4.6C, Appendix C Fig. S4.5B).

Ph.D.™-C7C

A

Clone	AA Sequence
Seq-C7C-01	CNWMNIHMC
Seq-C7C-02	CSKNFPRNC
Seq-C7C-03	CDWMRIWNC
Seq-C7C-04	CIHSPTALC
Seq-C7C-05	CLPWPLSLC
Seq-C7C-06	CSWWMLHHC
Seq-C7C-07	CSWWNIHLC
Seq-C7C-08	CLWWQLHLC
Seq-C7C-09	CSWMSIHLC
Seq-C7C-10	CGFTTTFVC
Seq-C7C-11	CSWWNIHLC
Seq-C7C-12	CNAGHLSQC
Seq-C7C-13	CSWMSIHLC
Seq-C7C-14	CSWMSIHLC
Seq-C7C-15	CSWWSIHVC
Seq-C7C-16	CLLLLNNTC
Seq-C7C-17	CNWWTIHNC
Seq-C7C-18	CNSIKKWSC
Seq-C7C-19	CNAGHLSQC
Seq-C7C-20	CISSSINHC

B

C

Peptide Name	Peptide Sequence	Repeats (among 20)	Prevalence (%)
C7C-1	ACSWWSIHLCG	consensus	consensus
C7C-2	ACNAGHLSQCG	2	10.0

Ph.D.™-12

D

Clone	AA Sequence
Seq-12A-01	VHWDFRQWWQPS
Seq-12A-02	NQLLTQRTPFQD
Seq-12A-03	SSNVISPFEQLL
Seq-12A-04	WVPWSTPFWLQQ
Seq-12A-05	VHWDFRQWWQPS
Seq-12A-06	VHWDFRQWWQPS
Seq-12A-07	
Seq-12A-08	NSPSGLIGWTSR
Seq-12A-09	WVPWSYEYFVST
Seq-12A-10	VHWDFRQWWQPS
Seq-12A-11	VHWDFRQWWQPS
Seq-12A-12	VHWDFRQWWQPS
Seq-12A-13	VHWDFRQWWQPS
Seq-12A-14	VHWDFRQWWQPS
Seq-12A-15	VHWDFRQWWQPS
Seq-12A-16	GPYVLGEHLRSN
Seq-12A-17	VHWDFRQWWQPS
Seq-12A-18	VHWDFRQWWQPS
Seq-12A-19	VHWDFRQWWQPS
Seq-12A-20	VHWDFRQWWQPS

E

Clone	AA Sequence
Seq-12B-01	LNFPMPSRPHSS
Seq-12B-02	VHWDFRQWWQPS
Seq-12B-03	VHWDFRQWWQPS
Seq-12B-04	VHWDFRQWWQPS
Seq-12B-05	LNFPMPSRPHSS
Seq-12B-06	LNFPMPSRPHSS
Seq-12B-07	SPLWSGWALEIL
Seq-12B-08	SFTWLHGSLTER
Seq-12B-09	VHWDFRQWWQPS
Seq-12B-10	WSPISGKFFQRF
Seq-12B-11	LNFPMPSRPHSS
Seq-12B-12	SNTQNVYWERWI
Seq-12B-13	QSLPWCYPHCVT
Seq-12B-14	RFPGPIEPDLRF
Seq-12B-15	WSPISGKFFQRF
Seq-12B-16	VHWDFRQWWQPS
Seq-12B-17	VHWDFRQWWQPS
Seq-12B-18	QSLPWCYPHCVT
Seq-12B-19	QSLPWCYPHCVT
Seq-12B-20	LNFPMPSRPHSS

F

Peptide Name	Peptide Sequence	Repeats (among 39)	Prevalence (%)
P12-1	VHWDFRQWWQPS	19	48.7
P12-2	LNFPMPSRPHSS	5	12.8
P12-3	QSLPWCYPHCVT	3	7.7
P12-4	WSPISGKFFQRF	2	5.1

Figure 4.6. Peptides derived by phage display. ***A,*** Peptide sequences deduced from DNA sequencing of 20 clones from the Ph.D.™-C7C library. ***B,*** Consensus sequence derived from analysis of all data. ***C***, Parent peptides selected for synthesis and testing. ***C,D,*** Peptide sequences deduced from DNA sequencing of 39 clones from the Ph.D.™-12 library, conducted as two independent runs (***D*** and ***E***). Note that Seq-12A-07 did not yield a decipherable sequence. ***F,*** Parent peptides selected for subsequent synthesis and testing based on prevalence.

A second library of dodecapeptides (Ph.D.^{TM}-12, New England Biolabs), consisting of ~10^9 possible combinations of twelve amino acids, was also screened, in this case two separate times, yielding the sequences in Figs. 1D and 1E. In this case, four sequences appeared multiple times (dubbed **12-1**, **12-2**, **12-3** and **12-4**), and these dodecapeptides were selected for subsequent synthesis and testing (Fig. 4.6F, Appendix C Figs. S4.5C-F).

The six selected peptide sequences (**C7C-1**, **C7C-2**, **12-1**, **12-2**, **12-3** and **12-4**) were synthesized, together with a variety of modifications, yielding a total of 25 peptides (Table 4.2). For the 12-mer peptides, we synthesized variants of the parent peptides truncated at one or both termini, to test whether the entire sequence was necessary or not, in the hope that shorter, and thus less expensive, sequences might be effective. Other modifications included N-terminal acetylation and C-terminal amidation, included to mimic the charge state of the peptides when incorporated in the phage coat protein (Table 4.2). To assess the extent to which these peptide sequences inhibit IDE, we quantified their potency in protease activity assays using recombinant human IDE and two different substrates: FRET1, a fluorogenic peptide (80), and recombinant human insulin. Peptides were initially tested at a few concentrations (10 μM, 100 μM and/or 500 μM) then, for those peptides showing good potency, dose-response relationships were obtained to quantify IC_{50} values, which were subsequently converted to inhibitory constants (K_i values) with the Cheng-Prusoff equation (81).

Table 4.2. Peptide sequences synthesized and their potency in activity assays with FRET1 and insulin.

Name	N-term	Sequence	C-term	$K_{i\ FRET1}$ (μM)	$K_{i\ Insulin}$ (μM)
C7C-1	NH_3^+	**ACSWWSIHLCG**	COO^-	112 ± 6	3.7 ± 0.7
C7C-1A	NH_3^+	**ACSWWSIHLCG**	amide	>100	>10
C7C-1B	NH_3^+		COO^-	>100	>10
C7C-2	NH_3^+	**ACNAGHLSQCG**	COO^-	>500	>10
C7C-2A	NH_3^+	**ACNAGHLSQCG**	amide	>500	>10
P12-1	NH_3^+		COO^-	7.7 ± 0.7	0.8 ± 0.04
P12-1A	NH_3^+		amide	5.0 ± 0.3	1.3 ± 0.2
P12-1B	NH_3^+	**VHWDFRQW**	amide	41 ± 6.4	7.0 ± 1.7
P12-1C	acetyl	**FRQWWQPS**	COO^-	139 ± 21	>10
P12-1D	acetyl	**WDFRQWWQ**	amide	140 ± 28	>10
P12-2	NH_3^+	**LNFPMPSRPHSS**	COO^-	>100	>10
P12-2A	NH_3^+	**LNFPMPSRPHSS**	amide	>100	>10
P12-2B	NH_3^+	**LNFPMPSR**	amide	>500	>10
P12-2C	acetyl	**MPSRPHSS**	COO^-	>500	>10
P12-2D	acetyl	**FPMPSRPH**	amide	>500	>10
P12-3	NH_3^+	**QSLPWCYPHCVT**	COO^-	8.9 ± 0.3	3.9 ± 1.6
P12-3A	NH_3^+	**QSLPWCYPHCVT**	amide	10 ± 0.4	4.1 ± 0.3
P12-3B	NH_3^+	**QSLPWCYP**	amide	39 ± 20	>10
P12-3C	acetyl	**WCYPHCVT**	COO^-	35 ± 4.7	>10
P12-3D	acetyl	**LPWCTPHC**	amide	102 ± 14	>10
P12-4	NH_3^+	**WSPISGKFFQRF**	COO^-	3.9 ± 0.5	1.5 ± 0.3
P12-4A	NH_3^+	**WSPISGKFFQRF**	amide	4.2 ± 1.3	2.6 ± 0.7
P12-4B	NH_3^+	**WSPISGKF**	amide	>500	>10
P12-4C	acetyl	**SGKFFQRF**	COO^-	>500	>10
P12-4D	acetyl	**PISGKFFQ**	amide	>500	>10

Among the cyclic peptides tested, **C7C-1** exhibited a modest K_i value of 112 ± 6 μM against FRET1 but yielded considerably improved potency against insulin (K_i = 3.7 ± 0.7 μM) (Table 4.2). None of the other **C7C-1** derivatives exhibited K_i values below 100 μM for FRET1 or 10 μM for insulin, nor did **C7C-2** or its amidated derivative (Table 4.2).

Relative to the cyclic peptides **C7C-1** and **C7C-2** and their derivatives, the unmodified linear peptide **P12-1** exhibited significantly lower K_i values against FRET1 (7.7 ± 0.7 μM) as well as insulin (0.8 ± 0.04 μM) (Table 4.2). The C-terminally amidated version of **P12-1**, **P12-1A**,

exhibited comparable K_i values against FRET1 and insulin (5.0 ± 0.3 μM and 1.3 ± 0.2 μM, respectively) (Table 4.2). Among three different 8-amino acid truncated versions of **P12-1**, the C-terminally truncated variant (**P12-1B**) exhibited slightly higher K_i values (41 ± 6.4 μM and 7.0 ± 1.7 μM for FRET1 and insulin, respectively), while the other N-terminally truncated (**P12-1C**) and N- and C-terminally truncated (**P12-1D**) variants exhibited relatively poor potency, with K_i values >100 μM for FRET1 and >10 μM for insulin (Table 4.2). These results suggest the N-terminal residues of **P12-1** (VHWD…) are the most critical determinants of its potency.

The dodecapeptide **P12-2** contained 3 proline residues (Table 4.2), which constrain the flexibility of the peptide backbone (Appendix C Fig. S4.5D) and, in general, tend to render peptides less vulnerable to proteolytic degradation. However, **P12-2** and all its variants exhibited K_i values >100 μM for FRET1 and >10 μM for insulin (Table 4.2) and were not characterized further.

Peptide **P12-3** is noteworthy for containing two cysteine residues (Table 4.2), which are predicted to form a disulfide bond that cyclizes the peptide, together with 2 proline residues (Appendix C Fig. S4.5E). The unmodified peptide, **P12-3**, and its C-terminally amidated variant, **P12-3A**, both potently inhibited the degradation of both FRET1 (K_i = 8.9 ± 0.3 μM and 10 ± 0.4 μM, respectively) and insulin (K_i = 3.9 ± 1.6 μM and 4.1 ± 0.3 μM, respectively) (Table 4.2). For the FRET1 substrate, the 8-amino acid truncated variants exhibited poorer potency, with the C-terminally (**P12-3B**) and N-terminally (**P12-3C**) truncated variants exhibiting of K_i values of 39 ± 20 μM and 35 ± 4.7 μM, respectively, and the dual N- and C-terminally truncated variant (**P12-3D**) exhibiting even higher K_i values of 102 ± 14 μM (Table 4.2). When insulin was used as a substrate, none of the truncated variants of **P12-3** exhibited K_i values <10 μM.

For the final peptide series, **P12-4** and its derivatives (Table 4.2, Appendix C Fig. S4.5F), the full-length unmodified (**P12-4**) and amidated (**P12-4A**) versions showed good potency against FRET1 (K_i = 3.9 ± 0.5 μM and 4.2 ± 1.3 μM, respectively) and insulin (K_i = 1.5 ± 0.3 μM and 2.6 ± 0.7 μM, respectively), while none of the truncated variants (**P12-4B**, **P12-4C** and **P12-4D**) exhibited K_i values below 500 μM or 10 μM for FRET1 or insulin, respectively (Table 4.2).

The sequences exhibiting high potency could be used either as conventional peptides—a preferred outcome due to their low cost of synthesis and low intrinsic toxicity—or, instead, as the starting point for the development of derivatives containing modifications that confer resistance to degradation (e.g., D-amino acids, beta-amino acids, etc.). To determine which peptides were susceptible to degradation by IDE, we incubated twelve peptides showing quantifiable inhibitory potency together with IDE for an extended period (4 h), then the potency of each was determined and compared to the potency immediately after addition of the enzyme (0 h). As shown in Fig. 4.7, most peptides exhibited significant reductions in potency (i.e., increases in K_i values) after a 4-h incubation with IDE, reflecting proteolytic degradation by IDE. Notable exceptions to this trend included **P12-3A** and **P12-3B**, particularly **P12-3A** (QSLPWCYPHCVT-amide).

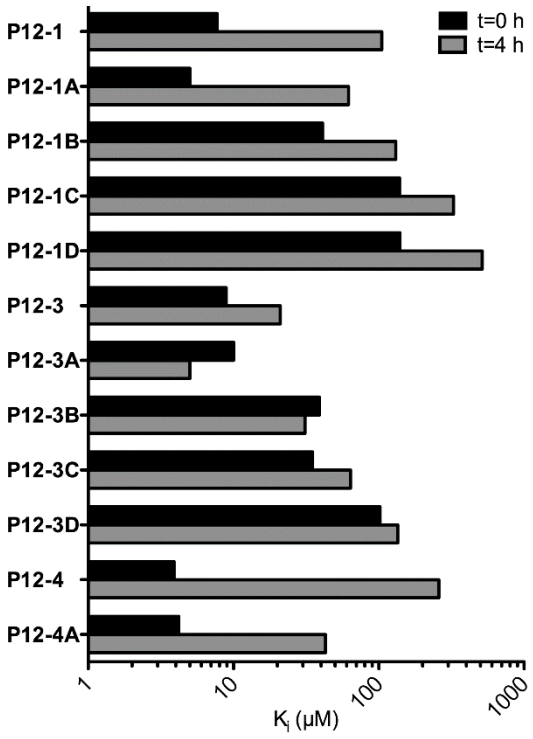

Figure 4.7. Vulnerability of peptides to degradation by IDE assessed by activity assays. IC_{50} values obtained for selected peptides pre-incubated with IDE 0 or 4 h before testing with the FRET1 assay. Note that all peptides except **P12-3A** and **P12-3B** showed reductions in apparent potency after prolonged incubation with IDE, reflecting degradation. Data are the average of duplicate assays that did not differ by more than 5%.

Taken together with the potency of all peptides against insulin (Table 4.2), we concluded that **P12-3A** represented the best inhibitor for further studies, and a highly purified, deliberately cyclized version (Fig. 4.8A) was synthesized. This cosmetic-grade version of **P12-3A** was found to be soluble up to ~500 μM in assay medium (PBS/0.05%BSA) and up to ~100 μM in cell culture medium, and was confirmed to exhibit similar potency against insulin degradation (K_i = 2.5 ± 0.31 μM, n = 5) (Fig. 4.8B), and highly consistent inhibition constants were also observed for the degradation of two other substrates, FRET1 (K_i = 2.7 ± 0.50 μM, n = 6) and amyloid β-protein (Aβ) (K_i = 2.1 ± 0.34 μM, n = 6). Notably, **P12-3A** exhibited essentially no inhibition against 15

different proteases tested (Appendix C Fig. S4.6) , suggesting it is highly selective for IDE. Based on its potency, stability and selectivity for IDE, **P12-3A** was selected for use in downstream assays.

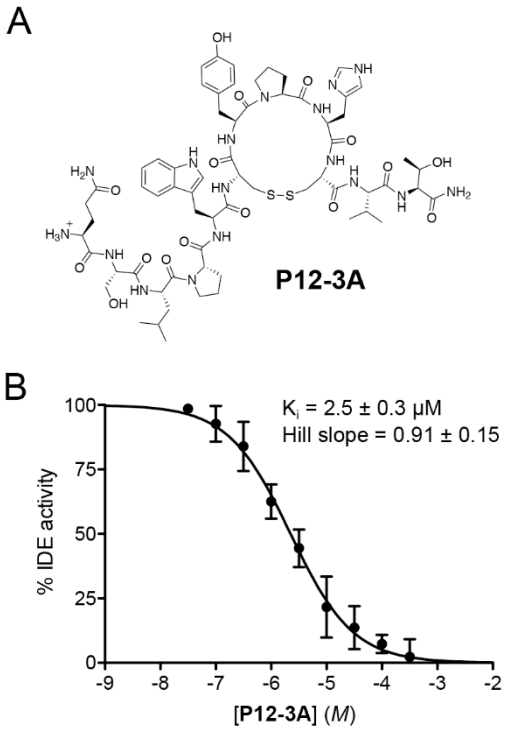

Figure 4.8. Structure and activity of P12-3A. ***A***, Structure of cyclized **P3-12A**. ***B***, Dose-response of **P12-3A** against insulin degradation by IDE. Data are mean ± SEM of 5 independent experiments.

Insulin promotes wound healing and overall skin health by affecting a number of processes, including cell proliferation (46, 47), cell migration (49, 50), and the production and secretion of ECM components, particularly type I collagen (51-57). We therefore assessed the ability of **P12-3A** to influence these processes in cultured skin fibroblasts and keratinocytes. To that end, primary mouse skin fibroblasts were grown for 4 d in multiple concentrations of insulin in the presence or absence of **P12-3A,** and insulin concentration over time was monitored by ELISA. In untreated cells, 10 nM insulin was degraded approximately 90% by day 4 in logarithmically growing cells, whereas insulin levels remained constant in cells treated with either 100 μM **P12-3A** (Fig. 4.9A).

These results demonstrate that **P12-3A** is effective at inhibiting insulin degradation by skin fibroblasts and, moreover, confirm that the compound is stable in biological milieu. Relative to control cells, cell proliferation in the presence of 10 nM insulin was found to be modestly increased in the presence of 100 μM **P12-3A** (Fig. 4.9B), but this did not achieve statistical significance. Finally, the effects of **P12-3A** on collagen production in were assessed at both the transcriptional and the posttranslational level in confluent monolayers of fibroblasts. After 4 d of treatment with **P12-3A** (100 μM), mRNA levels for the major form of collagen, alpha-1 type I collagen (*COL1A1*), were quantified by RT-PCR and found to be increased to ~2.6 times the levels of untreated cells (Fig. 4.9C). To assess overall levels of collagen production and secretion, we quantified levels of hydroxyproline, a modified amino acid present almost exclusively in collagen proteins (82). In the presence of **P12-3A**, hydroxyproline levels secreted into the medium were found to be increased to levels ~4.6 times that secreted by untreated cells (Fig. 4.9D). Western blotting also confirmed that mature, cell-associated collagen levels were increased in the presence of **P12-3A** (Fig. 4.9E). Finally, using an *in vitro* scratch wound assay, **P12-3A** (100 μM) was found to result in statistically significant increases in the migration of keratinocytes in the presence of different concentrations of insulin (Fig. 4.9F).

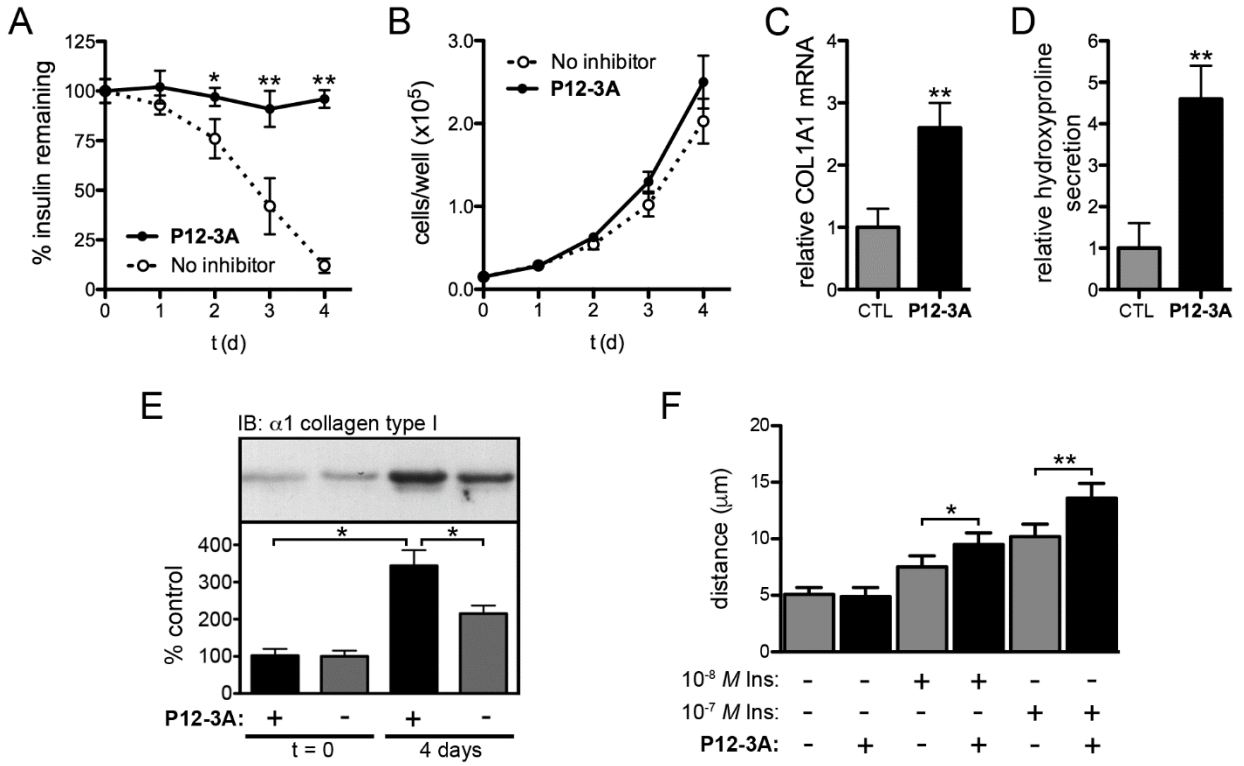

Figure 4.9. Effects of P12-3A on cultured skin cells. ***A,*** Insulin concentrations as a function of time in logarithmically growing primary murine skin fibroblasts in the absence or presence of **P12-3A** (100 μM). Note that insulin levels remain constant in the presence of **P12-3A**, reflecting both the effectiveness of the peptide inhibiting insulin degradation and also the stability of the peptide in biological milieu. Data are mean ± SEM of 4 independent replications. **P<0.05,* ***P<0.01.* ***B***, Proliferation of cells in the absence or presence of **P12-3A** (100 μM). Data are mean ± SEM of 6 independent replications. No significant differences were observed. ***C***,***D***,***E***, **P12-3A** (100 μM) potentiates insulin-induced collagen production in skin fibroblasts. Collagen production was assessed by *COL1A1* mRNA levels (***C***), levels of hydroxyproline secreted into the medium (***D***), and cell-associated mature alpha-1 type I collagen levels detected by Western blotting (***E***). Data are mean ± SD of 4 independent replications. **P<0.05,* ***P<0.01.* ***F***, **P12-3A** (100 μM) potentiates the migration of keratinocytes in a scratch wound assay. Migration of HaCaT cells 48 h after induction of a scratch wound in the presence of the indicated quantities of insulin and/or **P12-3A** (100 μM). Data are mean ± SEM of 6 independent replications. **P<0.05,* ***P<0.01.*

4.4.4 Discussion

Although a variety of potent and selective IDE inhibitors have been developed (12-15, 76-78), current inhibitors are difficult to synthesize, expensive to generate and/or contain chemical moieties or constituents with established or undetermined potential for toxicity. Due to these and other considerations, existing IDE inhibitors are poorly suited for topical applications. To

overcome these limitations, in the present study we aimed to develop peptidic inhibitors of IDE suitable for use in wound healing or cosmetic applications. Peptides are easy to manufacture and therefore inexpensive to scale up and, being composed solely of all-natural amino acids, are unlikely to possess any degree of toxicity. To that end, we used phage display technology to select for a range of peptides that bind to IDE with strong affinity, which were then screened for resistance to degradation by IDE. One cyclic dodecapeptide in particular, **P12-3A**, proved to be a potent and stable inhibitor of IDE that showed excellent selectivity and also showed no evidence of toxicity in cell culture experiments. Critically, **P12-3A** was found to potentiate a number of insulin-stimulated processes relevant to wound healing and skin health, including collagen production by fibroblasts and migration of keratinocytes in response to scratch wounds.

Phage display proved to be a highly effective approach for developing peptidic inhibitors. From among six parent peptides selected for further testing, four exhibited low-micromolar K_i values against insulin, and one (**P12-1**) exhibited sub-micromolar potency ($K_i = 0.8 \pm 0.04$ μM). Among the modified versions of these parent peptides, an additional five exhibited K_i values <10 μM; thus nine of the twenty-five peptides tested (36%) showed good activity. These hit rates are markedly higher than those obtained through high-throughput compound screening (78, 80, 83) or other approaches (15). Notably, the potency of **P12-1** (K_i = 800 nM) compares favorably to that of the highly optimized and extensively characterized macrocyclic IDE inhibitor, **6bK**, which shows a IC_{50} value of ~100 nM against insulin (15). Given that **6bK** underwent considerable optimization (15), the potency of **P12-1**, a simple, unmodified dodecapeptide, is notable.

Although the majority of peptides showed good affinity for IDE, most were also degraded by it. Due to the peculiarities of its structure (22, 32, 70, 84), IDE is a pure peptidase that cannot degrade proteins; thus it is unsurprising that phage display would reveal sequences that bind

strongly while attached to the bacteriophage coat protein but are nevertheless degraded when synthesized as a short peptide. The particular stability of **P12-3A** (and related peptides) likely derives from the fact that it contains two cysteines and can therefore form a cyclic peptide. Of note, it is unusual for cyclic peptides to emerge from a library of linear peptides, because cyclization tends to slow the maturation of the bacteriophage, leaving the phage expressing them at a competitive disadvantage when grown in parallel with phage expressing linear peptides. This suggests this peptide sequence was strongly favored during the selection process.

Based on the ability of **P12-3A** to potentiate insulin-stimulated collagen production and cell migration, topical IDE inhibition would appear to hold significant therapeutic potential in wound healing, particularly for diabetic patients (45). Given the accruing evidence that insulin signaling pathways are critical for wound healing (45, 66) and, given that IDE is abundant in wound fluid (74, 75), where it actively degrades insulin, there is a strong prediction that pharmacological inhibition of IDE will promote wound healing (14). This prediction is strongly supported by the finding that IDE inhibitors potentiate insulin action *in vivo* in part by preserving endogenous insulin (6, 10) and possibly *via* actions downstream of insulin receptor binding (14). Importantly, by contrast to direct topical administration insulin, which can cause life-threatening hypoglycemia (69), pharmacological inhibition of IDE possesses no intrinsic risk of triggering hypoglycemia (6, 10, 72).

One of the most immediately implementable potential cosmetic applications for **P12-3A** may be as an adjuvant for microneedling procedures (85). Also known as percutaneous collagen induction (86, 87), microneedling is a minimally invasive, widely used technique by which production of ECM proteins in the dermis can be stimulated by introducing uniform, sterile wounds in a controlled manner (85). Although originally developed for skin rejuvenation, this

technique is now being used as a novel treatment for a wide range of cosmetic and medical conditions, including acne, alopecia, stretch marks, hyperhidrosis and scarring of multiple types (85, 86). Topical application of **P12-3A** prior to microneedling would permit the delivery of the peptide subcutaneously (85), thus maximizing its impact on the processes involved in wound repair.

In sum, using phage display technology, we have generated novel peptidic inhibitors of IDE that, by virtue of their low cost of synthesis and minimal risk of toxicity, have the properties needed to explore the therapeutic and cosmetic potential of topical IDE inhibition. Given the importance of insulin in wound healing and normal skin health, these novel inhibitors, as well as future derivatives thereof, will be useful for exploring the involvement of IDE in these processes, and may also hold significant value as adjuvants for medicinal and cosmetic treatments.

4.4.5 Methods/Experimental

Materials

Anti-alpha-1 type I collagen antibody (Cat. No. AB765P) and horseradish peroxidase (HRP)-conjugated anti-rabbit IgG antibody (Cat. No. A0545) were from Sigma-Aldrich (St. Louis, MO, USA). Anti-glyceraldehyde-3-phosphate dehydrogenase (GAPDH; Cat. No. AF5718) antibody was from R&D Systems (Minneapolis, MN, USA). HRP-conjugated anti-goat IgG antibody (Cat. No. sc-2354) was from Santa Cruz Biotechnology (Santa Cruz, CA, USA). Materials for Western blotting and cell culture were from Thermo Fisher Scientific (Waltham, MA, USA). Insulin ELISAs (Cat. No. 90082) were from Crystal Chem (Downers Grove, IL, USA). Primary murine skin fibroblasts were a generous gift from Dr. Jorge Busciglio (UC Irvine). HaCaT cells and optimized growth medium were purchased from AddexBio Technologies (San Diego, CA, USA). Unless specified, all other reagents were from Sigma-Aldrich (St. Louis, MO, USA).

Phage Display

The selection of IDE-binding peptide sequences was conducted by phage display using the Ph.D.™-C7C and Ph.D.™-12 Phage Display Library Kits from New England Biolabs (Ipswich, MA, USA) according to manufacturer's recommendations. Briefly, purified, glycerol-free, recombinant human IDE (100 μg/mL) (34) was immobilized onto Corning® High Bind, 96-well, round-bottom plates (Cat. No. CLS3366). After washing and prior to addition of bacteriophage, activity assays with FRET1 (see below) were used to confirm the presence of proteolytically active IDE in wells coated in parallel with those used for panning. Three rounds of panning were conducted, with 2 x 10^{11} phage/well added at each step. After incubation at room temperature for 60 min, bound phage were eluted by addition of excess recombinant human insulin (100 μg/mL) and amplified for the subsequent round of panning. After the third round of panning, the eluate was titered and individual clones were selected for DNA sequencing. Peptide sequences were decoded, and consensus sequences searched for using CLC Sequence Viewer (Version 7.5).

Peptide Synthesis

Peptides were synthesized by automated solid-phase peptide synthesis by Sigma-Aldrich, with the exception of **C7C-1**, which was synthesized in-house essentially as described (14) and analyzed by electrospray-ionization mass spectrometry (ESI-MS; Appendix C Fig. S4.7) and HPLC (Appendix C Fig. S4.8). Cosmetic-grade, gram-scale quantities of **P12-3A** were synthesized by GenScript Biotechnology Corp. (Piscataway Township, NJ, USA).

Degradation Assays

IDE activity was quantified by monitoring the degradation of Mca-GGFLRKVGQK(Dnp) (FRET1, 5 μM) (32, 40), fluoresceinated and biotinylated amyloid β-protein (FAβB; 500 nM) or recombinant human insulin (50 nM) in PBS supplemented with 0.05% BSA. FRET1 degradation

was measured by changes in fluorescence (λ_{ex} = 340 nm, λ_{em} = 420 nm); FAβB degradation was monitored by fluorescence polarization (λ_{ex} = 488 nm, λ_{em} = 525 nm), as described (28); and insulin degradation was quantified by ELISA. *In vitro* activity assays incorporated recombinant human IDE (1 nM) purified from bacteria (34). For quantitation of insulin degradation in primary murine skin fibroblasts, cells (1 x 10^5/well) were plated in 96-well plates and maintained in DMEM supplemented with 10% fetal bovine serum (FBS), 2mM glutamine, penicillin and streptomycin. After addition of insulin (10 nM or 100 nM), samples of conditioned medium were removed daily and quickly frozen, then insulin levels were quantified in parallel by ELISA according to manufacturer's recommendations (Crystal Chem, Downers Grove, IL, USA). Assessment of the activity of **P12-3A** against a variety of matrix-metalloproteases was conducted using the Matrix Metalloproteinase (MMP) Inhibitor Profiling Kit, Fluorometric RED (Enzo Life Sciences, Inc., Farmingdale, NY, USA) according to manufacturer's recommendations using the broad-spectrum MMP inhibitor, NNGH, as a positive control. Activity assays on additional proteases were conducted using the FAβB degradation assay, using a custom protease inhibitor cocktail (PIC) comprised of cOmplete™, Mini, EDTA-free Protease Inhibitor Cocktail supplemented with 1,10-phenanthroline (2 mM) and pepstatin A (5 μM).

Cell Proliferation

Primary murine skin fibroblasts cells (1 x 10^5/well) were plated in 96-well plates, using separate plates for each timepoint and endpoint. Cell proliferation was quantified using the CellTiter 96® AQueous Non-Radioactive Cell Proliferation Assay (Promega Corp., Madison, WI, USA) according to manufacturer's recommendations.

RNA Quantification

RNA was extracted from freshly lysed cells, reverse transcribed and amplified using the Ambion® Fast SYBR® Green Cells-to-C_T™ Kit according to manufacturer's recommendations (Thermo Fisher Scientific, Waltham, MA, USA). The quantitative real-time PCR reaction was conducted using a 7500 real-time PCR system and analyzed using System SDS software v2.0.5 (Applied Biosystems). Murine COL1A1 mRNA was detected using the following primers (forward: 5'-ACCTAAGGGTACCGCTGGA and reverse: 5' TCCAGCTTCTCCATCTTTGC). Fold change differences between samples were determined using the comparative C_t ($\Delta\Delta C_t$) method, normalized to internal standards detected with the SYBR® Green Cells-to-C_T™ Control Kit according to manufacturer's recommendations (Thermo Fisher Scientific, Waltham, MA, USA) calculated by $2^{-\Delta\Delta Ct}$.

Hydroxyproline Quantification

For quantitation of hydroxyproline secretion by primary murine skin fibroblasts, cells (1 x 10^5/well) were plated in 24-well plates DMEM supplemented with 10% FBS, 2mM glutamine, penicillin, streptomycin and 100 nM insulin, in the absence or presence of 100 μM **P12-3A**. After incubation for 4 days, the conditioned medium was removed, centrifuged at 1000 x g for 10 min to remove cellular debris, and hydroxyproline levels were quantified using the Hydroxyproline Assay Kit according to manufacturer's recommendations (Sigma-Aldrich, St. Louis, MO, USA).

Western Blotting

Protein was collected using the M-Per Mammalian Extraction Reagent and the concentration was quantified using the Pierce™ BCA Protein Assay Kit according to manufacturer's recommendations (Thermo Fisher Scientific, Waltham, MA, USA). Protein (30 μg/well) was separated SDS-PAGE under reducing conditions using Novex™ 10%

polyacrylamide tris-glycine mini gels and transferred to nitrocellulose membranes as described (41). Briefly, membranes were blocked in 5% non-fat milk in tris-buffered saline supplemented with 0.2% Tween-20 (TBST), cut into segments and incubated for 1 h at room temperature with anti-alpha-1 type I collagen (1:5000) and anti-GAPDH (1:10,000) antibodies, washed extensively in TBST, then probed with anti-rabbit (1:20,000) or anti-goat (1:50,000) secondary antibodies, respectively, and detected by enhanced chemoluminescence using SuperSignal West Pico Substrate. Protein expression, normalized to GAPDH levels, was quantified using the band analysis tools of ImageLab software, version 4.1 (Bio-Rad Laboratories, Inc., Hercules, CA, USA).

***In Vitro* Scratch Wound Assay**

Cell migration in HaCaT cells after induction of scratch wounds was quantified essentially as described (88). Briefly, HaCaT cells maintained in optimized DMEM (AddexBio Technologies, San Diego, CA, USA) supplemented with 10% FBS, penicillin and streptomycin, were grown to confluency in 24-well tissue culture plates, and scratch wounds were induced with a 200-µL pipette tip. After growth for 48 h in the absence or presence of insulin (10 nM or 100 nM) and/or **P12-3A** (100 µM), cell migration distance was quantified by two independent, blinded observers using a Nikon TMS inverted light microscope (Nikon Corp., Melville, NY, USA) fitted with a ruler reticle.

Statistical Analyses

Tests for statistical significance were performed by using the two-tailed Student's *t* test with various levels of significance (P = 0.05, 0.01). For comparisons with unequal numbers of replications per group, Hartley's F_{max} was calculated to check for homogeneity of variance. All calculations and curve fitting were performed in Prism for Mac OS X, version 5.0b (GraphPad Software, Inc., La Jolla, CA, USA).

4.5 Publication 3:

Isosteres of hydroxypyridinethione as inhibitors of human insulin-degrading enzyme

4.5.1 Abstract

Insulin-degrading enzyme (IDE) is a human mononuclear Zn^{2+} metalloenzyme that is widely regarded as the primary peptidase responsible for insulin degradation. Despite its name, IDE is also critically involved in the hydrolysis of several other disparate peptide hormones, including glucagon, amylin, and the amyloid β-protein. As such, the study of IDE inhibition is of particular relevance for conditions such as type 2 diabetes mellitus and Alzheimer disease. There have been few reported IDE inhibitors, and of these, inhibitors that directly target the active-site metal ion have yet to be fully explored. In an effort to discover new, metal-binding inhibitors of IDE, a library of ~350 metal-binding pharmacophores was screened against IDE, resulting in the identification of the 1-hydroxypyridine-2-thione (1,2-HOPTO) as an effective metal-binding scaffold. Screening of a focused library of druglike HOPTO isosteres found 3-sulfonamide derivative of 1,2-HOPTO to have good activity against IDE (K_i values of ~50 μM). Further structure-activity relationship studies yielded several thiophene-sulfonamide HOPTO derivatives with good, broad-spectrum activity against IDE that have the potential to be useful pharmacological tools for future studies of IDE.

4.5.2 Introduction

Insulin-degrading enzyme (IDE, EC 3.4.24.56), also known as insulysin and insulinase, is found across nearly all domains of life, and within mammals, is widely considered to be the primary protease responsible for insulin degradation (89). IDE belongs to the inverzincin family of metalloproteases, which utilize an active site Zn^{2+} metal ion to catalyze the hydrolysis of peptide bonds (89). The protease is also inhibited by thiol-modifying compounds, and was at one point

miscategorized as a cysteine-dependent protease, but it is now known that the cysteine residues within IDE are not involved directly in the proteolytic activity of the enzyme (32, 89).

Human IDE is a ~113-kDa Zn^{2+}-metalloendopeptidase (Fig. 4.10) that is classified as cryptidase-type protease, as it uses a clamshell-like mechanism to encapsulate substrate peptides within its abnormally large, 13,000-$Å^3$ internal chamber (90). IDE is comprised of two bowl-shaped N- and C-terminal domains (NTD, CTD) linked by a hinge that can adopt "open" and "closed" conformations (90). Notably, the active site is bipartite, comprised of regions within both the NTD and CTD, and is fully formed only when the protease is in the closed conformation (32, 90). Because substrates must fit completely within the internal chamber to be hydrolyzed, this constrains the size of the substrates that can be processed, rendering it a true peptidase and also resulting in exquisite substrate selectivity both for the protease itself and also for inhibitors thereof (12, 89). The catalytic Zn^{2+} is coordinated by His108, His112, and Glu188, with an axial bound water that completes the tetrahedral coordination geometry of the metal center (Fig. 4.10B) (90). To aid in substrate binding, IDE utilizes an exosite ~30 Å away from the catalytic site to anchor the N-terminus domain of the various substrates and facilitate substrate unfolding (91, 92). Mechanistically, IDE is believed to operate by first enveloping its peptide substrates, with hydrolysis occurring only upon complete encapsulation of the substrate (91, 92). In the case of insulin, IDE is able to perform multiple peptide cleavages without impacting the disulfide bonds that hold the hormone peptide together (91). Following substrate cleavage, IDE re-opens to release the hydrolyzed products, and the cycle begins anew (91, 92).

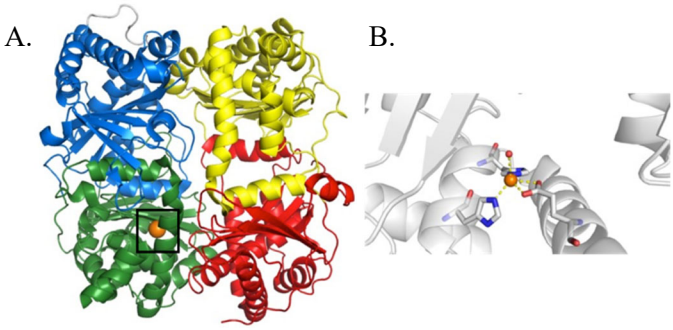

Figure 4.10. Structure of IDE. ***A***, The complete structure of IDE, with the NTD in blue and green, the CTD in yellow and red, and the connecting hinge in white. ***B***, Magnified image of the buried catalytic Zn^{2+} and metal coordinating residues within the active site (highlighted in box in '***A***'), with Zn^{2+} shown as an orange sphere, water as a red sphere, and coordination bonds as yellow dashes. Images produced from PDB structure PDB 4NXO.

Homologues of IDE are found across all domains of life, but within humans, misregulation of this mononuclear Zn^{2+} metallopeptidase has been implicated in both type-2 diabetes mellitus (T2DM) and Alzheimer disease (AD) (93, 94). While the biological roles of IDE are not yet fully understood, this metalloenzyme is expressed throughout the body, and is found in both the intra- and extra-cellular compartments (95). IDE functions to hydrolyze a broad range of peptide hormones, yet paradoxically only hydrolyzes certain members of these disparate peptide families (90). Chief among the known IDE substrates are insulin, glucagon, amylin, and the amyloid β-protein (Aβ) (96, 97). Of these, three are relevant to T2DM, as amylin promotes satiety (98), and insulin and glucagon work in tandem to down- and up-regulate blood glucose, respectively (99). Additionally, Aβ accumulates abnormally in AD (100, 101).

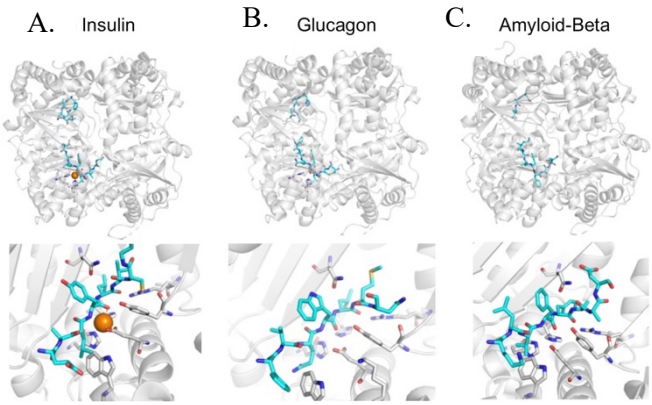

Figure 4.11. Binding of IDE to a broad range of substrates. Exemplified by: ***A***, insulin, ***B***, glucagon, and ***C***, Aβ (90). The full structure of IDE bound to each substrate is shown on the top, with a close-up of the catalytic site below. For glucagon and Aβ, apo-IDE was used so as to prevent substrate hydrolysis. Images produced from PDB structures 2G54, 2G49, and 2G47, respectively.

Considering the relevance of IDE to various disease states, there has been great interest in developing substrate-selective inhibitors of IDE (17), with a particular emphasis on the development of tool compounds to disentangle the different biological roles of IDE in relation to its various substrates. Among the more sought-after goals related to IDE are compounds that act as activators in respect to Aβ degradation, as a means to decrease levels of this neurotoxic peptide (100, 101). In addition, there is particular interest in the discovery of compounds that inhibit insulin degradation, while retaining IDE activity against other substrates. Such a strategy would theoretically provide a novel pharmacological approach to boosting insulin signaling and thereby treating T2DM (93, 102, 103). Selective inhibitors of either glucagon or amylin would be of considerable value as pharmacological tools to aid in evaluating the biological roles of IDE. However, few substrate selective inhibitors of IDE are available. Of the reported IDE inhibitors, most are peptidic and bind at the exosite distal to the catalytic Zn^{2+} (Fig. 4.12). The current best-in-class inhibitor is a small molecule that is both potent and selective for IDE inhibition for insulin hydrolysis (Fig. 4.12C) (17); however, this compound is difficult to synthesize and has yet to be examined in cellular studies, so that its clinical value is undetermined. Finally, there remains a

great experimental need for broad-spectrum inhibitors of IDE that are inexpensive to synthesize at scale.

Metal-binding inhibitors of IDE have the potential to provide alternative avenues for IDE inhibition, but such classes of inhibitor have not been thoroughly explored. Only two hydroxamic acid peptide compounds and 1,10-phenanthroline have been reported as metal-binding inhibitors of IDE (Fig. 4.12) (104, 105). Hydroxamic acids are known to have potential issues with selectivity, pharmacokinetics, and metabolism and 1,10-phenanthroline is a broad-spectrum metal-stripping agent.

To develop new inhibitors against IDE, a library of metal-binding pharmacophores (MBPs) was screened against IDE. MBPs are small molecules (<300 MW) containing one or more donor atoms suited for metal binding (106). As metal binding (a.k.a., dative bond, coordination bond) represents a strong, but reversible bond, MBPs are ideally suited for making strong interactions with the metalloenzyme active site and thus presents a favorable starting point for further drug discovery efforts. The results of screening this library against IDE are described here, revealing that 1,2-hydroxypyridine thione (1,2-HOPTO) as a promising fragment lead against this important metalloenzyme.

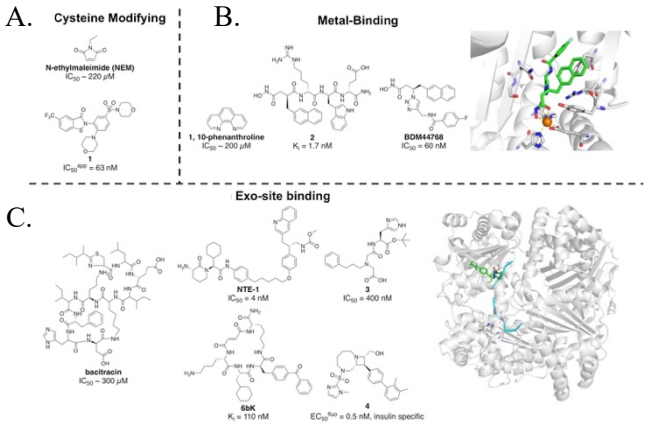

Figure 4.12. Structures and inhibition values of previously reported IDE inhibitors (17, 104, 105, 107-112). ***A***, Cysteine-modifying IDE inhibitors. ***B***, Metal-binding IDE inhibitors, with inset showing crystal structure of hydroxamate-based **2** coordinating to the active site Zn^{2+}, PDB 4NXO (105)**.** ***C***, Exosite-binding IDE inhibitors, with inset showing the crystal structure of **4** bound to the exosite and co-crystallized with insulin (cyan) PDB 6EDS (17).

4.5.3 Results and Discussion

Screening of the MBP Library

In an effort to broaden the scope of available MBP inhibitors for metalloenzymes, we have developed a ~350-component library of small molecules each bearing a unique metal-binding group (113, 114). To identify MBPs with the potential for inhibitor development against IDE, this library was screened against IDE, testing for inhibition against the degradation of several key biological IDE substrates, including insulin, glucagon, amylin, and Aβ, as well as the synthetic fluorogenic peptide, Substrate V (115). Compounds were initially screened against all 5 substrates at 500 μM and 50 μM, then for compounds showing good inhibitory activity, K_i values were established via dose-response experiments. Approximately 14 compounds exhibited average K_i values <100 μM across the 5 different substrates. Based on potency, synthetic tractability and other considerations, 1,2-hydroxypyridine thione (1,2-HOPTO, **5**, Fig. 4.13) was identified as a fragment lead against IDE with an average K_i value of 86 μM against the evaluated substrates.

Screening of the Elaborated HOPTO Sublibrary

HOPTOs are a known class of powerful metal ligands, particularly suited for Zn^{2+} binding based on hard-soft, acid-base theory (116, 117). They have been established to have bidentate-binding through a set of oxygen and sulfur donor atoms, where the sulfur has been demonstrated to exist predominately in the thione isomer (118). In an effort to broaden the utility of HOPTOs as warheads for metalloenzyme inhibition, an expanded library of HOPTO derivatives (Fig. 4.13) was prepared and demonstrated to have druglike qualities while maintaining the core metal-binding capacities (119). As 1,2-HOPTO was identified as a broad-spectrum scaffold for IDE inhibition, it was decided to employ this elaborated HOPTO sublibrary against IDE to better optimize the MBP warhead before pursuing furthering inhibitor elaboration. Screening of this focused HOPTO sublibrary revealed both 3-sulfonamide-1,2-HOPTO (**8**) and isoquinoline-1,2-HOPTO (**10**) to have improved inhibition activity with K_i values of ~50 μM for both compounds. It was decided to pursue **8** for further use against IDE, as **8** had better experimentally determined aqueous solubility compared to **10**.

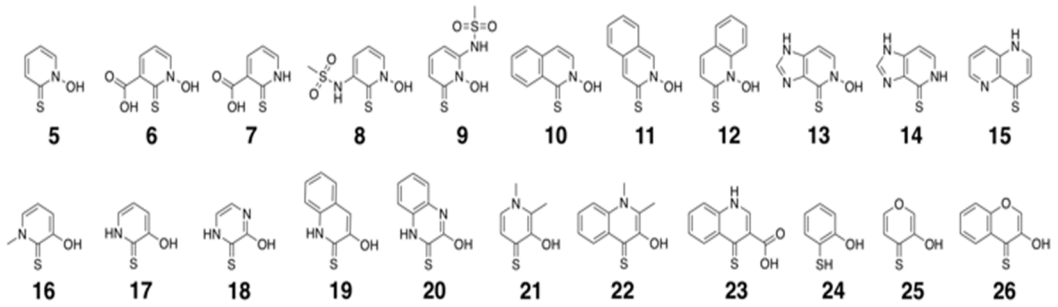

Figure 2.13. Previously prepared HOPTO compounds tested for IDE inhibition.

Modeling of 8 in the IDE Active Site

In the absence of a co-crystal structure, **8** was modeled in the active site of IDE to gain some rudimentary idea of the compound could potentially bind the IDE active site. The lead

fragment **8** has been previously crystallized in a model hydrotris(3,5-phenylmethylpyrazolyl)-borate [($Tp^{Ph,Me}$)Zn(**8**)] complex, demonstrating a preferred Zn^{2+} metal-coordination through donor atoms of an axial thione and equatorial hydroxyl (119). Additionally, there have been previously reported crystal structures of hydroxamic acid based inhibitors of IDE, showing that these compounds bind the active-site Zn^{2+} through axial carbonyl and equatorial hydroxyl (Fig. 4.12B) (105). Considering the 1,2-HOPTO MBP core is a cyclized thione hydroxamic acid, the structure of hydroxamic acid **2** bound to IDE was used to model the binding of **8** in the IDE active site. To prepare the in silico model, the Molecular Operating Environment (MOE) software suite was employed (120), using the structure of **8** from the crystal structure of [($Tp^{Ph,Me}$)Zn(**8**)] and superposing it over the hydroxamate of **2** bound in IDE by aligning the thione of **8** with the carbonyl of **2**, and the hydroxyl of **8** with the hydroxyl of **2**. This resulted in the model displayed in Figure 4.14, with compound **8** being predicted to bind IDE through the thione and hydroxyl donor atoms in a manner consistent with both the model [($Tp^{Ph,Me}$)Zn(**8**)] and previous hydroxamic crystal structures.

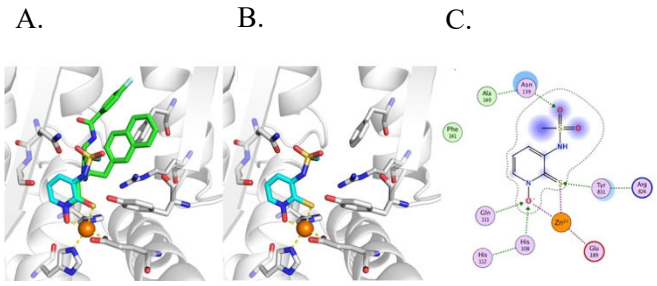

Figure 4.14. Model of 8 **bound to the Zn^{2+} within the active site of IDE**. ***A***, Superposition of **8** and **2**, which was used to create ***B***, a model of **8** bound to the Zn^{2+} in the IDE active site. ***C***, A 2-D representation of the model of **8** binding, with Zn^{2+} in orange, coordination bonds as pink dashes, interactions as green arrows, and solvent exposed regions as blue spheres.

Sulfonamide HOPTO Derivative Synthesis and Inhibitory Activity

To facilitate the use of these sulfonamide derivatized HOPTOs as tool compounds, a readily adaptable and simple 3-step synthetic route amenable towards rapid derivatization was developed, as detailed in Figure 4.16. Combining a sulfonyl chloride with a suitable amine heterocycle starting material in a microwave reactor yielded the desired sulfonamide product. It was found that using excess amine relative to sulfonyl chloride aided in decreasing the amount of undesired disulfonamide side products generated. This step is highly adaptable to a broad scope of both amine and sulfonyl chloride partners, as evidenced by the scope of sulfonamide HOPTOs prepared in this study (Fig. 4.15). The subsequent step of oxidation using mCPBA achieves selective oxidation at the pyridine nitrogen. The final step of thionation was achieved by heating the oxidized product in a solution of freshly prepared saturated NaSH in the presence of KI. This reaction was quenched with aqueous HCl, and subsequent work-up of chromatography followed by recrystallization from iPrOH with varying amounts of H_2O yielded final HOPTO products. In the case of compounds **47** and **48** (which are designed as negative controls because they lack one donor group), thionation was instead achieved by heating the halogenated sulfonamide to reflux at 150 °C in DMF in the presence of excess thiourea. Finally, it should be noted that some HOPTO products were isolated as mixtures with the oxidized dimer (through the sulfur atom). This dimer is easily reverted to back the active thione in the presence of DTT as a reductant. Considering IDE requires DTT in the assay buffer to ensure reduction of its 13 Cys residues, DTT in the biochemical assays served the dual function of also ensuring the HOPTO species were in the active thione form.

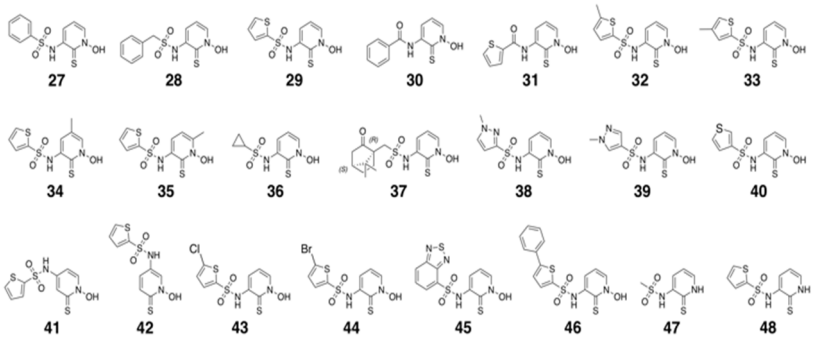

Figure 4.15. Sulfonamide HOPTO compounds prepared and tested against IDE. Compounds **30** and **31** are amide controls, and **47** and **48** are controls lacking the hydroxyl moiety proposed to be essential for metal binding.

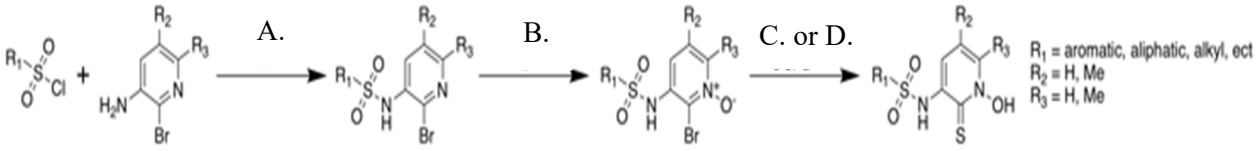

Figure 4.16. Synthesis of sulfonamide HOPTO derivatives. Reagents and conditions: ***A***, sulfonyl chloride, pyridine, microwave irradiation, 120 °C, 15 min, 25 – 71%; ***B***, mCPBA, CH_2Cl_2, MeOH, 25 – 35 °C, 16 – 72 h, 28 – 64%; ***C***, sat. aq. NaSH, KI, MeOH, 50 – 100 °C, 4 – 16 h, 6 – 58%; ***D***, thiourea, DMF, 150 °C, followed by 6 M HCl, 110 °C, 2 h, 22 – 40 %.

To further elaborate the lead **8**, it was decided to investigate the SAR of the sulfonamide moiety to explore other potential interactions within the active site. A preliminary test of phenyl (**27**) and benzyl (**28**) derivatives showed some improvement relative to parent **8**, with **27** having an average K_i value (over all tested substrates) of 22 μM, and **28** having an average K_i value of 35 μM. Utilizing an aromatic isostere replacement of the phenyl ring to a thiophene substituent yielded **29** with a further improved average K_i value of 9 μM.

Table 4.3 K_i **values (in μM) of parent HOPTO compounds against IDE substrates**. Compounds **30** and **31** are included as amide variants of the sulfonamide.

Compound	Insulin	Glucagon	Amylin	Amyloid-β	Substrate V	Average	Average without Substrate V
5	39	217	41	108	25	86	101
8	24	114	31	61	19	50	58
27	26	10	26	13	36	22	19
28	57	14	40	19	47	35	33
29	9	3	10	6	15	9	7
30	23	26	63	33	140	57	37
31	27	26	62	36	126	55	38

In addition, to validate the contribution of the sulfonamide to the overall activity of **29**, amide controls **30** and **31** were prepared as respective analogs of **27** and **29**. As shown in Table 4.3, **30** had an average K_i value of 57 μM (37 μM without substrate V) rendering **30** ~2.5-fold less active than **27**, and **31** had average K_i values of 55 μM (38 μM without substrate V) making **31** ~6-fold less active than **29**. As a whole, these data suggest that the sulfonamide moiety makes more favorable interactions with the active site relative to amide derivatives.

Sulfonamide HOPTO SAR Analysis

In an effort to further improve the activity of the lead thiophene **29**, **32** – **46** were synthesized (Fig. 4.15). The methyl derivative compounds **32 – 35**, were prepared to probe which positions would be amenable to further elaboration. These methyl derivatives exhibited flat SAR with neither improvement nor loss in activity against IDE and the degradation of its substrates. Within the next set of tested alkyl substituents, cyclopropane **36** had a comparatively high average K_i of 45 μM, whereas the bulky camphor **37**, was slightly more on par with the thiophene, with an average K_i value of 16 μM. Pyrazole derivatives **38** and **39** were prepared as analogues of the 5-member thiophene ring and, again, these showed somewhat flat SAR with average K_i values of 16

and 23 μM, respectively. To explore alternate variations of the position of the thiophene, the 3-thiophene **40** and alternate position 2-thiophene compounds **41** and **42** were prepared. Of these, **42** was the most interesting: although it had a higher average K_i value of 43 μM, it was the most selective in this study towards sparing amylin degradation, making **42** of potential interest as a tool compound in this regard.

To examine more lipophilic substituents, **43 – 46** were synthesized. The thiadiazole **45** and 2-phenyl thiophene **46** showed no improvement relative to **29**, but the halogenated derivatives **43** and **44** showed improvement relative to the parent thiophene, with respective average K_i values of 11 and 7 μM, and averages of 11 and 5 μM when excluding the synthetic Substrate V. Between the halogenated derivatives, the brominated thiophene **44** displayed slightly more broad-spectrum activity, with somewhat consistent inhibition levels across the tested substrates, whereas the chlorinated thiophene **43** displayed slightly more selectivity, inhibiting the degradation of glucagon ~15-fold more potently than insulin.

Table 4.4 Inhibitory activity (K_i, μM) of thiophene sulfonamide derivatives against IDE substrates. Validation of Metal-Binding Mechanism

Compound	Insulin	Glucagon	Amylin	Amyloid-β	Substrate V	Average	Average without Substrate V
32	11	6	13	8	27	13	10
33	23	5	12	6	22	14	11
34	18	6	13	7	18	12	11
35	21	5	14	7	27	15	12
36	51	20	35	22	95	45	32
37	7	7	19	11	46	18	11
38	15	6	15	8	36	16	11
39	21	7	19	13	54	23	15
40	16	8	14	9	26	15	12
41	8	11	27	13	29	17	15
42	27	20	64	20	84	43	33
43	30	2	7	3	13	11	11
44	9	2	7	3	14	7	5
45	26	5	11	10	31	16	13
46	55	2	28	13	10	23	25
47	>200	172	>200	>200	61	-	-
48	>200	62	84	102	77	-	-

To validate the mechanism of action as metal-binding at the active site Zn^{2+}, and ensure the compounds were not binding elsewhere, a set of non-metal binding controls were prepared (Fig. 4.15). Control compounds **47** and **48** were prepared as respective methyl and thiophene sulfonamide derivatives lacking the oxygen donor atom of the HOPTO. These controls represent a deletion of a crucial portion of the donor atoms required for the bidentate metal-coordination of the 1,2-HOPTO ligand, and neither should be capable of strong metal coordination, and as expected, did not display strong inhibition against IDE (Table 4.4).

4.5.4 Conclusion

The goal of this work was to develop novel, easy-to-synthesize metal-binding inhibitors of IDE useful as pharmacological tools and potentially as pharmacophores for future therapeutic development. IDE relies on an active site Zn^{2+} for catalytic activity, and controls the levels of several biologically important peptide substrates, making IDE inhibition of high importance towards conditions such as T2DM as well as AD. Screening an MBP library of ~350 unique compounds led to the identification of the HOPTO scaffold as a novel zinc-binding moiety having good activity against IDE. Further testing of a specialized druglike HOPTO library resulted in the discovery of 3-sulfonamide-1,2-HOPTO as a novel IDE inhibitor, with an average K_i value of 50 μM against the tested IDE substrates, and derivatization of the sulfonamide resulted in thiophene sulfonamide **29**, with an average K_i of 9 μM against the IDE substrates. Further SAR studies yielded halogen derivatives **43** and **44**, of which the bromine **44** had broad-spectrum activity, with average K_i value of 5 μM against the physiological IDE substrates, and chlorine **43** was notably ~15-fold more active against glucagon degradation than insulin degradation. Overall, these compounds represent a new class of metal-binding IDE inhibitors, and due to their rapid, facile syntheses, can be readily made available to serve as useful pharmacological tools for investigating the role of IDE and the various substrates it regulates in numerous biological processes.

4.5.5 Methods/Experimental Section

Synthesis

Unless otherwise noted, all reagents and solvents were purchased from commercial suppliers and used with no additional purification. Microwave reactions were performed using a CEM Discover series S-class microwave reactor in pressure-sealed vessels. Silica gel column chromatography was performed using a CombiFlash Rf^+ Teledyne ISCO system, using hexane, ethyl acetate, CH_2Cl_2 or MeOH as eluents. Separations were monitored via a Teledyne ISCO RF^+ PurIon ESI-MS detector with 1-Da resolution. ^1H NMR spectra were obtained using Varian 400-MHz and 500-MHz spectrometers at the Department of Chemistry and Biochemistry at UC San Diego. ^1H NMR data is reported in parts per million relative to the residual non-deuterated solvent signals, and spin multiplicities are given as s (singlet), *br* s (broad singlet), d (doublet), dd (doublet of doublets), t (triplet), dt (doublet of triplets), q (quartet), and m (multiplet). When available, coupling constants (J) are reported in hertz (Hz). Standard resolution mass spectrometry was performed at either the UC San Diego Molecular Mass Spectrometry Facility or on the previously described Teledyne ISCO RF^+ PurIon ESI-MS detector.

The synthesis of **5** – **28** was previously reported in Adamek et al. (119). While **29** was previously reported in Adamek et al., this key compound was prepared again for this work. The purity of compounds **29 – 48** was determined to be at least 90% by analytical HPLC analysis, or at least 99.6% by elemental analysis when noted.

Generation of Sulfonyl Chloride

5-Phenylthiophene-2-sulfonyl chloride (46a)

To a solution of DMF (0.87 mL, 11.2 mmol) cooled to 0 °C while under a nitrogen atmosphere, sulfuryl chloride (913 μL, 11.2 mmol) was added dropwise, and the reaction was stirred for 15 min, until the mixture formed a white solid. Then 2-phenylthiophene (1.50 g, 9.36 mmol) was added in one portion, and the solids were heated as a melt at 100 °C for 45 min, noting that upon initial addition of the white thiophene, the solid mixture turned yellow, and upon heating, melt was observed to occur at 55 °C. Upon reaching 100 °C, the reaction mixture had turned from clear yellow to clear green. After heating at 100 °C for 45 min, upon reaction completion, the melt was cooled to 25 °C, diluted with ethyl acetate, and ice water was added. With a chilled separatory funnel, the product was extracted into organic using 2×15 mL ethyl acetate, and the combined organic was washed with brine and dried over magnesium sulfate. The solids were filtered off and discarded, and the resulting filtrate was concentrated under reduced pressure to yield a blue liquid. The product was then purified by column chromatography, running an isocratic in gradient 100% hexanes. Like fractions of the desired product were combined and concentrated under reduced pressure, until there was a remaining volume of ~5 mL hexanes, containing a solid precipitate of the desired product. The precipitate was collected via vacuum filtration and washed with hexanes to obtain **46a** (1.25 g, 4.81 mmol, 51%) as a powdery solid that was pale yellow with a greenish tint in color. ^{1}HNMR (400 MHz, $(CD_3)_2SO$): 7.60 (d, J = 7.6, 2H), 7.39 (t, J = 7.6, 2H), 7.31 – 7.27 (m, 2H), 7.11 (d, J = 2.8, 1H).

Sulfonamide Coupling

General Sulfonamide Coupling Protocol

Unless otherwise noted, the following protocol was used for sulfonamide coupling. To a heat-gun dried microwave vessel equipped with stir bar and charged with a solution of starting

amine (1.3 eq) in 2 mL dry pyridine, sulfonyl chloride (1.0 eq) was added in one portion. The mixture was placed in a microwave reactor and irradiated at 120 °C for 15 min. Upon cooling, the reaction mixture was diluted with 15 mL ethyl acetate, and washed with 2×15 mL 4 M HCl. The aqueous was back-extracted with an additional 15 mL ethyl acetate, and the combined organic was washed with brine, dried over magnesium sulfate, and the solids were filtered off and discarded. The filtrate was concentrated under reduced pressure, and the resulting crude was purified by column chromatography, running gradient from 100% hexanes to 100% ethyl acetate. The desired sulfonamide product typically eluted in 50% ethyl acetate in hexanes. Like fractions were combined and concentrated under reduced pressure to obtain the desired sulfonamide product that was used directly in the subsequent step. As previously noted, some coupling reactions resulted in an inseparable mix of sulfonamide and disulfonamide products. These mixtures were carried over directly into the next step with no additional purification.

N-(2-Bromopyridin-3-yl)thiophene-2-sulfonamide (29a)

Following the general method for sulfonamide coupling, from 2-bromopyridin-3-amine (1.50 g, 8.67 mmol) and thiophene-2-sulfonyl chloride (1.27 g, 6.94 mmol), the desired product **29a** (1.53 g, 4.80 mmol, 55%) was obtained as a peach colored solid. ^{1}H NMR (400 MHz, DMSO-d_6): δ 10.41 (*br* s, 1H), 8.25 (d, J = 4.4, 1H), 7.97 (d, J = 5.2, 1H), 7.70 (d, J = 7.6, 1H), 7.49 – 7.44 (m, 2H), 7.16 (t, J = 4.4, 1H); ESI-MS(-): *m/z* 317.18 $[M - H]^-$.

N-(2-Bromopyridin-3-yl)benzamide (30a)

To a 0 °C solution of 2-bromopyridin-3-amine (0.600 g, 3.47 mmol) and pyridine (0.56 mL, 6.9 mmol) in 10 mL CH_2Cl_2, a mixture of benzoyl chloride (269 µL, 2.31 mmol) in 5 mL CH_2Cl_2 was added dropwise. The reaction mixture was allowed to slowly warm to 25 °C for 16 h,

and was then diluted with an additional 15 mL CH_2Cl_2, and was washed with 20 mL 4 M HCl. The aqueous was back-extracted with 10 mL CH_2Cl_2, and the combined organic phase was washed with brine, dried over magnesium sulfate, and the solids were filtered off and discarded. The filtrate was concentrated under reduced pressure, and the resulting crude was purified by column chromatography, running gradient from 100% hexanes to 100% ethyl acetate. The desired product eluted in 50% ethyl acetate in hexanes. Like fractions were combined and concentrated under reduced pressure to obtain **30a** (0.549 g, 1.98 mmol, 86 %) as a clear oil that solidified upon standing. ^{1}H NMR (400 MHz, DMSO-d_6): δ 10.10 (*br* s, 1H), 8.30 (dd, J_1 = 4.4, J_2 = 1.2, 1H), 8.01 (d, J = 7.2, 3H), 7.65 – 7.47 (m, 4H); ESI-MS(+): *m/z* 277.12 $[M + H]^+$.

N-(2-Bromopyridin-3-yl)thiophene-2-carboxamide (31a)

Following the same protocol used in **30a**, from 2-bromopyridin-3-amine (0.600 g, 3.47 mmol), pyridine (0.56 mL, 6.9 mmol), and thiophene-2-carbonyl chloride (247 µL, 2.31 mmol), the desired **31a** (0.536 g, 1.89 mmol, 82%) was obtained as a clear oil that solidified upon standing. ^{1}H NMR (400 MHz, DMSO-d_6): δ 10.23 (*br* s, 1H), 8.30 (d, J = 4.8, 1H), 8.02 (d, J = 3.6, 1H), 7.96 (d, J = 7.6, 1H), 7.90 (d, J = 5.2, 1H), 7.51 (dd, J_1 = 7.6, J_2 = 0.8, 1H), 7.25 (t, J = 5.2, 1H); ESI-MS(+): *m/z* 283.11 $[M + H]^+$.

N-(2-Bromopyridin-3-yl)-5-methylthiophene-2-sulfonamide (32a)

Following the general method for sulfonamide coupling, from 2-bromopyridin-3-amine (0.600 g, 3.47 mmol) and 5-methylthiophene-2-sulfonyl chloride (608 µL, 4.51 mmol), the desired product **32a** (0.380 g, 1.14 mmol, 33%) was obtained as a light yellow oil that solidified upon standing. ^{1}H NMR (400 MHz, DMSO-d_6): δ 10.31 (*br* s, 1H), 8.24 (dd, J_1 = 4.8, J_2 = 1.6, 1H),

7.68 (dd, J_1 = 7.6, J_2 = 1.6, 1H), 7.45 (dd, J_1 = 8.0, J_2 = 4.8, 1H), 7.30 (d, J = 3.6, 1H), 6.87 (dd, J_1 = 4.0, J_2 = 1.2, 1H), 2.48 (s, 3H); ESI-MS(+): *m/z* 333.10 $[M + H]^+$.

N-(2-Bromopyridin-3-yl)-4-methylthiophene-2-sulfonamide (33a)

Following the general method for sulfonamide coupling, from 2-bromopyridin-3-amine (0.484 g, 2.80 mmol) and 4-methylthiophene-2-sulfonyl chloride (0.500 g, 2.54 mmol), the desired product **33a** (0.560 g, 1.68 mmol, 66%) was obtained as a slightly impure white solid that was used directly in the next step without any additional purification. ^{1}H NMR (400 MHz, DMSO-d_6): δ 10.39 (*br* s, 1H), 8.24 (dd, J_1 = 4.4, J_2 = 1.2, 1H), 7.67 (dd, J_1 = 8.0, J_2 = 1.2, 1H), 7.55 – 7.54 (m, 2H), 7.45 (dd, J_1 = 7.6, J_2 = 4.4, 1H), 7.35 (s, 1H), 2.19 (s, 3H); ESI-MS(-): *m/z* 333.15 $[M - H]^-$.

N-(2-Bromo-5-methylpyridin-3-yl)thiophene-2-sulfonamide (34a)

Following the general method for sulfonamide coupling, from 2-bromo-5-methylpyridin-3-amine (0.500 g, 2.67 mmol) and thiophene-2-sulfonyl chloride (0.635 g, 3.48 mmol), the desired product **34a** (0.513 g, 1.20 mmol, 43%) was obtained as a white solid contaminated with approximately 25% disulfonamide product. The product was used directly in the next step without any additional purification. ^{1}H NMR (400 MHz, DMSO-d_6): δ 10.31 (*br* s, 1H), 8.10 (s, 1H), 7.96 (d, J = 5.2, 1H), 7.52 (s, 1H), 7.48 (d, J = 3.6, 1H), 7.16 (t, J = 4.8, 1H), 2.25 (s, 3H); ESI-MS(+): *m/z* 331.29 $[M + H]^+$.

N-(2-Bromo-6-methylpyridin-3-yl)thiophene-2-sulfonamide (35a)

Following the general method for sulfonamide coupling, from 2-bromo-6-methylpyridin-3-amine (0.500 g, 2.67 mmol) and thiophene-2-sulfonyl chloride (0.635 g, 3.48 mmol), the desired

product **35a** (0.746 g, 1.90 mmol, 71%) was obtained as a white solid contaminated with approximately 15% disulfonamide product. The product was used directly in the next step without any additional purification. ^{1}H NMR (400 MHz, DMSO-d_6): δ 10.25 (*br* s, 1H), 7.96 (d, J = 4.8, 1H), 7.53 (d, J = 8.0, 1H), 7.45 (d, J = 3.6, 1H), 7.30 (d, J = 7.6, 1H), 7.15 (t, J = 4.8, 1H), 2.41 (s, 3H); ESI-MS(-): *m/z* 331.26 $[M - H]^-$.

N-(2-Bromopyridin-3-yl)cyclopropanesulfonamide (36a)

Following the general method for sulfonamide coupling, from 2-bromopyridin-3-amine (0.750 g, 4.34 mmol) and cyclopropanesulfonyl chloride (662 µL, 6.50 mmol), the desired product **36a** (0.850 g, 3.07 mmol, 71%) was obtained as a light yellow solid. ^{1}H NMR (400 MHz, DMSO-d_6): δ 9.70 (*br* s, 1H), 8.26 (dt, J_1 = 4.4, J_2 = 1.6, 1H), 7.84 (dt, J_1 = 8.0, J_2 = 1.6, 1H), 7.46 (qd, J_1 = 4.4, J_2 = 1.6, 1H), 2.77 – 2.70 (m, 1H), 1.01 – 0.96 (m, 2H), 0.90 – 0.86 (m, 2H); ESI-MS(+): *m/z* 279.12 $[M + H]^+$.

N-(2-Chloropyridin-3-yl)-1-((1R,4S)-7,7-dimethyl-2-oxobicyclo[2.2.1]heptan-1-yl)methanesulfonamide (37a)

Following the general method for sulfonamide coupling, from 2-chloropyridin-3-amine (0.350 g, 2.02 mmol) and ((1R,4S)-7,7-dimethyl-2-oxobicyclo[2.2.1]-heptan-1-yl)methanesulfonyl chloride (0.650 g, 2.59 mmol), the desired product **37a** (0.382 g, 1.11 mmol, 43%) was obtained as a pale yellow solid. ^{1}H NMR (400 MHz, DMSO-d_6): δ 9.79 (*br* s, 1H), 8.25 (d, J = 4.8, 1H), 7.95 (d, J = 8.0, 1H), 7.47 (dd, J_1 = 8.0, J_2 = 4.8, 1H), 3.50 (d, J = 14.8, 1H), 3.15 (d, J = 14.8, 1H), 2.38 – 2.29 (m, 2H), 2.06 (t, J = 4.4, 1H), 1.97 – 1.91 (m, 2H), 1.59 – 1.52 (m, 1H), 1.43 – 1.37 (m, 1H), 1.01 (s, 3H), 0.79 (s, 3H); ESI-MS(+): *m/z* 343.31 $[M + H]^+$.

N-(2-Bromopyridin-3-yl)-1-methyl-1H-pyrazole-3-sulfonamide (38a)

Following the general method for sulfonamide coupling, from 2-bromopyridin-3-amine (0.500 g, 2.89 mmol) and 1-methyl-1H-pyrazole-3-sulfonyl chloride (0.475 g, 2.63 mmol), the desired product **38a** (0.354 g, 1.12 mmol, 43%) was obtained as a pale tan oil that solidified upon standing. ^{1}H NMR (400 MHz, DMSO-d_6): δ 10.18 (*br* s, 1H), 8.21 (dd, J_1 = 4.8, J_2 = 1.6, 1H), 7.88 (d, J = 2.0, 1H), 7.72 (dd, J_1 = 8.0, J_2 = 1.6, 1H), 7.42 (dd, J_1 = 8.0, J_2 = 4.8, 1H), 6.57 (d, J = 2.4, 1H), 3.91 (s, 3H); ESI-MS(+): *m/z* 317.25 $[M + H]^+$.

N-(2-bromopyridin-3-yl)-1-methyl-1H-pyrazole-4-sulfonamide (39a)

Following the general method for sulfonamide coupling, from 2-bromopyridin-3-amine (0.500 g, 2.89 mmol) and 1-methyl-1H-pyrazole-4-sulfonyl chloride (0.626 g, 3.47 mmol), the desired product **39a** (0.611 g, 1.93 mmol, 67%) was obtained as a clear oil that solidified upon standing to a white solid. ^{1}H NMR (400 MHz, DMSO-d_6): δ 9.97 (*br* s, 1H), 8.23 (s, 1H), 8.21 (dd, J_1 = 4.8, J_2 = 1.6, 1H), 7.69 (s, 1H), 7.67 (d, J = 1.6, 1H), 7.42 (dd, J_1 = 8.0, J_2 = 4.8, 1H), 3.85 (s, 3H); ESI-MS(-): *m/z* 315.20 $[M - H]^-$.

N-(2-Bromopyridin-3-yl)thiophene-3-sulfonamide (40a)

Following the general method for sulfonamide coupling, from 2-bromopyridin-3-amine (0.600 g, 3.47 mmol) and thiophene-3-sulfonyl chloride (823 mg, 4.51 mmol), the desired product **40a** (0.583 g, 1.83 mmol, 53%) was obtained as a light brown oil that solidified upon standing. ^{1}H NMR (400 MHz, DMSO-d_6): δ 10.17 (*br* s, 1H), 8.22 – 8.21 (m, 1H), 8.12 – 8.11 (m, 1H), 7.76 – 7.74 (m, 1H), 7.64 – 7.61 (m, 1H), 7.44 – 7.40 (m, 1H), 7.28 – 7.26 (m, 1H); ESI-MS(-): *m/z* 317.19 $[M - H]^-$.

N-(2-Bromopyridin-4-yl)thiophene-2-sulfonamide (41a)

Following the general method for sulfonamide coupling, from 2-bromopyridin-4-amine (0.750 g, 4.34 mmol) and thiophene-2-sulfonyl chloride (1.19 g, 6.50 mmol), the desired product **41a** (1.37 g, 4.29 mmol, 55%) was obtained as a pale yellow oil that solidified upon standing to a white solid. ^{1}H NMR (400 MHz, DMSO-d_6): δ 11.57 (*br* s, 1H), 8.19 (d, J = 6.0, 1H), 8.01 (dd, J_1 = 4.8, J_2 = 1.2, 1H), 7.79 (dd, J_1 = 3.6, J_2 = 1.2, 1H), 7.24 (d, J = 2.0, 1H), 7.20 – 7.16 (m, 2H); ESI-MS(+): *m/z* 321.13 $[M + H]^+$.

N-(6-Bromopyridin-3-yl)thiophene-2-sulfonamide (42a)

Following the general method for sulfonamide coupling, from 6-bromopyridin-3-amine (0.750 g, 4.34 mmol) and thiophene-2-sulfonyl chloride (1.19 g, 6.50 mmol), the desired product **42a** (1.38 g, 4.29 mmol) was obtained in theoretical yield as a pale yellow solid contaminated with approximately 50% disulfonamide product. The product was used directly in the next step without any additional purification. ^{1}H NMR (400 MHz, DMSO-d_6): δ 10.87 (*br* s, 1H), 8.26 (dd, J_1 = 4.8, J_2 = 1.2, 1H), 8.12 (d, J = 2.8, 1H), 7.95 (dd, J_1 = 5.2, J_2 = 1.2, 1H), 7.79 (dd, J_1 = 4.0, J_2 = 1.6, 1H), 7.62 – 7.57 (m, 2H), 7.30 (t, J = 5.2, 1H); ESI-MS(+): *m/z* 321.15 $[M + H]^+$.

N-(2-Bromopyridin-3-yl)-5-chlorothiophene-2-sulfonamide (43a)

Following the general method for sulfonamide coupling, from 2-bromopyridin-3-amine (3.00 g, 17.3 mmol) and 5-chlorothiophene-2-sulfonyl chloride (1.86 mL, 13.9 mmol), the desired product **43a** (2.27 g, 6.41 mmol, 37%) was obtained as a light tan solid contaminated with approximately 10% disulfonamide product. The product was used directly in the next step without any additional purification. ^{1}H NMR (400 MHz, DMSO-d_6): δ 10.65 (*br* s, 1H), 8.28 (dd, J_1 = 4.4,

J_2 = 1.2, 1H), 7.71 (dd, J_1 = 8.0, J_2 = 1.6, 1H), 7.48 (dd, J_1 = 8.0, J_2 = 4.8, 1H), 7.37 (d, J = 4.0, 1H), 7.25 (d, J = 4.0, 1H); ESI-MS(-): *m/z* 353.09 $[M - H]^-$.

5-Bromo-N-(2-bromopyridin-3-yl)thiophene-2-sulfonamide (44a)

Following the general method for sulfonamide coupling, from 2-bromopyridin-3-amine (1.00 g, 5.78 mmol) and 5-bromothiophene-2-sulfonyl chloride (1.21 g, 4.62 mmol), the desired product **44a** (1.41 g, 3.54 mmol, 61%) was obtained as a pale yellow solid contaminated with approximately 20% disulfonamide product. The product was used directly in the next step without any additional purification. ^{1}H NMR (400 MHz, DMSO-d_6): δ 10.64 (*br* s, 1H), 8.28 (d, J = 4.4, 1H), 7.72 – 7.68 (m, 2H), 7.51 – 7.46 (m, 2H); ESI-MS(-): *m/z* 397.03 $[M - H]^-$.

N-(2-bromopyridin-3-yl)benzo[c][1,2,5]thiadiazole-4-sulfonamide (45a)

Following the general method for sulfonamide coupling, from 2-bromopyridin-3-amine (0.350 g, 2.02 mmol) and benzo[c][1,2,5]thiadiazole-4-sulfonyl chloride (0.380 g, 1.62 mmol), the desired product **45a** (0.382 g, 1.03 mmol, 5l%) was obtained as a cream colored solid. ^{1}H NMR (400 MHz, DMSO-d_6): δ 10.49 (*br* s, 1H), 8.41 (d, J = 8.8, 1H), 8.21 (dd, J_1 = 4.8, J_2 = 1.6, 1H), 8.13 (d, J = 6.8, 1H), 7.84 – 7.76 (m, 2H), 7.43 (dd, J_1 = 8.0, J_2 = 4.8, 1H); ESI-MS(+): *m/z* 373.16 $[M + H]^+$.

N-(2-Chloropyridin-3-yl)-1-((1R,4S)-7,7-dimethyl-2-oxobicyclo[2.2.1]heptan-1-yl)methanesulfonamide (46b)

Following the general method for sulfonamide coupling, from 2-bromopyridin-3-amine (1.08 g, 6.23 mmol) and **46a** (1.24 g, 4.79 mmol), the desired product **46b** (1.13 g, 2.85 mmol, 60%) was obtained as a fluffy bright white solid. ^{1}H NMR (400 MHz, DMSO-d_6): δ 10.53 (*br* s,

1H), 8.28 – 8.26 (m, 1H), 7.75 – 7.70 (m, 3H), 7.56 (d, *J* = 2.4, 1H), 7.48 – 7.39 (m, 5H); ESI-MS(+): *m/z* 393.23 $[M + H]^+$.

N-(2-bromopyridin-3-yl)methanesulfonamide (47a)

Following the general method for sulfonamide coupling, from 2-bromopyridin-3-amine (1.08 g, 6.23 mmol) and methanesulfonyl chloride (645 µL, 8.33 mmol), the desired product **47a** (0.510 g, 2.05 mmol, 25%) was obtained as a pale yellow liquid contaminated with approximately 50% disulfonamide product. The product was used directly in the next step without any additional purification. ^{1}H NMR (400 MHz, DMSO-d_6): δ 9.66 (*br* s, 1H), 8.23 (d, *J* = 8.0, 1H), 7.83 (d, *J* = 7.6, 1H), 7.48 – 7.45 (m, 1H), 3.11 (s, 3H); ESI-MS(-): *m/z* 249 $[M - H]^-$.

Oxidation

General Oxidation Coupling Protocol

Unless otherwise noted, the following protocol was used. To a solution of sulfonamide in 20 mL 1:1 CH_2Cl_2/MeOH, a solution of mCPBA (5 eq.) in 10 mL 1:1 CH_2Cl_2/MeOH was added in one portion. The reaction mixture was then heated at 35 °C for 72 h. Upon completion, the reaction mixture was concentrated under reduced pressure and the resulting crude was purified by column chromatography, running gradient first from 100% hexanes to 100% ethyl acetate, and then from 100% CH_2Cl_2 to 15% MeOH in CH_2Cl_2. The desired products typically eluted in 8 – 10 % MeOH in CH_2Cl_2. Like fractions were combined and concentrated under reduced pressure to obtain the desired oxidized product that was used directly in the subsequent step

2-Bromo-3-(thiophene-2-sulfonamido)pyridine 1-oxide (29b)

Following the general method for oxidation, from **29a** (1.50 g, 4.70 mmol) and mCPBA (6.32 g, 77.0% Wt, 28.2 mmol), at 25 °C for 16 h, the desired product **29b** (0.742 g, 2.21 mmol, 55%) was obtained as a light yellow solid. ^{1}H NMR (400 MHz, DMSO-d_6): δ 10.61 (*br* s, 1H), 8.35 (d, J = 6.8, 1H), 7.99 (d, J = 4.8, 1H), 7.55 (d, J = 3.6, 1H), 7.39 (t, J = 6.8, 1H), 7.21 – 7.16 (m, 2H); ESI-MS(-): *m/z* 333.11 $[M - H]^-$.

3-Benzamido-2-bromopyridine 1-oxide (30b)

Following the general method for oxidation, from **30a** (0.540 g, 1.95 mmol) and mCPBA (2.18 g, 77.0% Wt, 9.74 mmol), at 35 °C for 16 h, the desired product **30b** (0.169 g, 0.577 mmol, 30%) was obtained as an off-white solid. ^{1}H NMR (400 MHz, DMSO-d_6): δ 10.34 (*br* s, 1H), 8.42 (d, J = 6.4, 1H), 7.98 (d, J = 7.2, 1H), 7.64 (t, J = 7.2, 1H), 7.58 – 7.52 (m, 2H), 7.46 (t, J = 6.4, 1H); ESI-MS(+): *m/z* 293.05 $[M + H]^+$.

2-bromo-3-(thiophene-2-carboxamido)pyridine 1-oxide (31b)

Following the general method for oxidation, from **31a** (0.530 g, 1.87 mmol) and mCPBA (2.10 g, 77.0% Wt, 9.36 mmol), at 35 °C for 16 h, the desired product **31b** (0.358 g, 1.20 mmol, 64%) was obtained as a yellow oil that solidified upon standing. ^{1}H NMR (400 MHz, DMSO-d_6): δ 10.38 (*br* s, 1H), 8.42 (dd, J_1 = 6.0, J_2 = 1.6, 1H), 8.01 (dd, J_1 = 2.8, J_2 = 0.8, 1H), 7.92 (dd, J_1 = 4.8, J_2 = 0.8, 1H), 7.51 – 7.46 (m, 2H), 7.25 (dt, J_1 = 3.6, J_2 = 1.2, 1H); ESI-MS(+): *m/z* 299.02 $[M + H]^+$.

2-Bromo-3-((5-methylthiophene)-2-sulfonamido)pyridine 1-oxide (32b)

Following the general method for oxidation, from **32a** (0.380 g, 1.28 mmol) and mCPBA (1.28 g, 77.0% Wt, 5.70 mmol), at 25 °C for 67 h, the desired product **32b** (0.202 g, 0.578 mmol,

51%) was obtained as an off-white solid. ^{1}H NMR (400 MHz, DMSO-d_6): δ 10.52 (*br* s, 1H), 8.35 (d, J = 6.4, 1H), 7.40 – 7.37 (m, 2H), 7.21 (d, J = 8.0, 1H), 6.88 (d, J = 3.2, 1H), 2.48 (s, 3H); ESI-MS(-): *m/z* 347.16 $[M - H]^-$.

2-Bromo-3-((4-methylthiophene)-2-sulfonamido)pyridine 1-oxide (33b)

Following the general method for oxidation, from **33a** (0.560 g, 1.68 mmol) and mCPBA (1.88 g, 77.0% Wt, 8.40 mmol), at 25 °C for 72 h, the desired product **33b** (0.192 g, 0.550 mmol, 33%) was obtained as a yellow solid. ^{1}H NMR (400 MHz, DMSO-d_6): δ 10.56 (*br* s, 1H), 8.35 (d, J = 6.4, 1H), 7.58 (s, 1H), 7.42 (s, 1H), 7.38 (t, J = 6.4, 1H), 7.19 (d, J = 8.4, 1H), 2.20 (s, 3H); ESI-MS(-): *m/z* 349.10 $[M - H]^-$.

2-Bromo-5-methyl-3-(thiophene-2-sulfonamido)pyridine 1-oxide (34b)

Following the general method for oxidation, from **34a** (0.500 g, 1.13 mmol) and mCPBA (1.68 g, 77.0% Wt, 7.50 mmol), at 30 °C for 16 h, the desired product **34b** (0.101 g, 0.289 mmol, 26%) was obtained as a pale yellow solid. ^{1}H NMR (400 MHz, DMSO-d_6): δ 10.53 (*br* s, 1H), 8.29 (s, 1H), 7.98 (d, J = 5.2, 1H), 7.55 (d, J = 4.0, 1H), 7.16 (t, J = 4.0, 1H), 7.01 (s, 1H), 2.20 (s, 3H); ESI-MS(+): *m/z* 349.11 $[M + H]^+$.

2-Bromo-6-methyl-3-(thiophene-2-sulfonamido)pyridine 1-oxide (35b)

Following the general method for oxidation, from **35a** (0.730 g, 1.86 mmol) and mCPBA (5.87 g, 77.0% Wt, 2.45 mmol), at 30 °C for 20 h, the desired product **35b** (0.216 g, 0.289 mmol, 33%) was obtained as a white solid. ^{1}H NMR (400 MHz, DMSO-d_6): δ 10.50 (*br* s, 1H), 7.98 (d, J = 4.8, 1H), 7.52 (d, J = 3.6, 1H), 7.46 (d, J = 8.4, 1H), 7.16 (t, J = 8.8, 1H), 7.11 (d, J = 8.4, 1H), 2.37 (s, 3H); ESI-MS(+): *m/z* 349.14 $[M + H]^+$.

2-Bromo-3-(cyclopropanesulfonamido)pyridine 1-oxide (36b)

Following the general method for oxidation, from **36a** (0.890 g, 3.13 mmol) and mCPBA (3.60 g, 77.0% Wt, 16.1 mmol), at 30 °C for 16 h, the desired product **36b** (0.470 g, 0.160 mmol, 50%) was obtained as a white solid. ^{1}H NMR (400 MHz, DMSO-d_6): δ 9.87 (*br* s, 1H), 8.36 (dd, J_1 = 5.2, J_2 = 2.4, 1H), 7.42 – 7.37 (m, 2H), 2.81 – 2.75 (m, 1H), 1.03 – 0.98 (m, 2H), 0.97 – 0.91 (m, 2H); ESI-MS(+): *m/z* 295.14 $[M + H]^+$.

2-Chloro-3-((((1R,4S)-7,7-dimethyl-2-oxobicyclo[2.2.1]heptan-1-yl)methyl)sulfonamido)pyridine 1-oxide (37b)

Following the general method for oxidation, from **37a** (0.380 g, 1.11 mmol) and mCPBA (1.24 g, 77.0% Wt, 5.54 mmol), at 40 °C for 4 d, the desired product **37b** (0.241 g, 0.672 mmol, 61%) was obtained as a yellow oil that solidified upon standing. ^{1}H NMR (400 MHz, DMSO-d_6): δ 7.98 (d, J = 6.4, 1H), 7.42 (d, J = 8.4, 1H), 7.19 (t, J = 8.0, 1H), 3.37 (d, J = 5.6, 1H), 2.95 (d, J = 14.8, 1H), 2.52 – 2.46 (m, 1H), 2.33 – 2.27 (m, 1H), 2.01 (t, J = 4.0, 1H), 1.90 – 1.86 (m, 2H), 1.53 – 1.46 (m, 1H), 1.39 – 1.33 (m, 1H), 1.00 (s, 3H), 0.76 (s, 3H); ESI-MS(+): *m/z* 357.31 $[M + H]^+$.

2-Bromo-3-((1-methyl-1H-pyrazole)-3-sulfonamido)pyridine 1-oxide (38b)

Following the general method for oxidation, from **38a** (0.350 g, 1.10 mmol) and mCPBA (1.24 g, 77.0% Wt, 5.52 mmol), at 30 °C for 72 h, the desired product **38b** (0.166 g, 0.498 mmol, 45%) was obtained as a yellow solid. ^{1}H NMR (400 MHz, DMSO-d_6): δ 10.40 (*br* s, 1H), 8.33 (d, J = 6.4, 1H), 7.90 (s, 1H), 7.36 (d, J = 1.2, 1H), 7.25 (d, J = 8.4, 1H), 6.61 (s, 1H), 3.91 (s, 3H); ESI-MS(+): *m/z* 333.14 $[M + H]^+$.

2-Bromo-3-((1-methyl-1H-pyrazole)-3-sulfonamido)pyridine 1-oxide (39b)

Following the general method for oxidation, from **39a** (0.600 g, 1.89 mmol) and mCPBA (2.12 g, 77.0% Wt, 9.46 mmol), at 30 °C for 16 h, the desired product **39b** (0.212 g, 0.636 mmol, 34%) was obtained as an off-white solid. ^{1}H NMR (400 MHz, DMSO-d_6): δ 10.18 (*br* s, 1H), 8.31 (dd, J_1 = 6.4, J_2 = 1.2, 1H), 8.28 (s, 1H), 7.74 (s, 1H), 7.36 (t, J = 6.8, 1H), 7.20 (dd, J_1 = 8.4, J_2 = 0.8, 1H), 3.85 (s, 3H); ESI-MS(+): *m/z* 331.17 $[M + H]^+$.

2-Bromo-3-(thiophene-3-sulfonamido)pyridine 1-oxide (40b)

Following the general method for oxidation, from **40a** (0.580 g, 1.82 mmol) and mCPBA (2.04 g, 77.0% Wt, 9.09 mmol), at 25 °C for 67 h, the desired product **40b** (0.256 g, 0.763 mmol, 42%) was obtained as an off-white solid. ^{1}H NMR (400 MHz, DMSO-d_6): δ 10.61 (*br* s, 1H), 8.35 (d, J = 6.8, 1H), 7.99 (d, J = 4.8, 1H), 7.55 (d, J = 3.6, 1H), 7.39 (t, J = 6.8, 1H), 7.21 – 7.16 (m, 2H); ESI-MS(-): *m/z* 333.22 $[M - H]^-$.

2-Bromo-4-(thiophene-2-sulfonamido)pyridine 1-oxide (41b)

Following the general method for oxidation, from **41a** (1.00 g, 3.13 mmol) and mCPBA (2.11 g, 77.0% Wt, 9.40 mmol), at 35 °C for 16 h, the desired product **41b** (0.298 g, 0.889 mmol, 28%) was obtained as a white solid. ^{1}H NMR (400 MHz, DMSO-d_6): δ 11.30 (*br* s, 1H), 8.31 (d, J = 7.2, 1H), 7.98 (d, J = 4.8, 1H), 7.70 (d, J = 3.6, 1H), 7.44 (d, J = 2.8, 1H), 7.19 – 7.14 (m, 2H); ESI-MS(+): *m/z* 335.10 $[M + H]^+$.

2-Bromo-4-(thiophene-2-sulfonamido)pyridine 1-oxide (42b)

Following the general method for oxidation, from **42a** (1.00 g, 3.13 mmol) and mCPBA (2.11 g, 77.0% Wt, 9.40 mmol), at 35 °C for 16 h, the desired product **42b** (0.323 g, 0.964 mmol, 31%) was obtained as a white solid. ^{1}H NMR (400 MHz, DMSO-d_6): δ 11.09 (*br* s, 1H), 8.13 (d, J = 2.0, 1H), 7.99 (dd, J_1 = 4.8, J_2 = 1.6, 1H), 7.81 (d, J = 8.8, 1H), 7.68 (dd, J_1 = 4.0, J_2 = 1.2, 1H), 7.17 (dd, J_1 = 5.2, J_2 = 4.0, 1H), 7.04 (dd, J_1 = 8.8, J_2 = 2.0, 1H); ESI-MS(+): *m/z* 335.08 [M + H]$^+$.

2-Bromo-3-((5-chlorothiophene)-2-sulfonamido)pyridine 1-oxide (43b)

Following the general method for oxidation, from **43a** (1.80 g, 1.86 mmol) and mCPBA (6.84 g, 77.0% Wt, 5.09 mmol), at 35 °C for 48 h, the desired product **43b** (0.876 g, 2.37 mmol, 47%) was obtained as a yellow-tan solid. ^{1}H NMR (400 MHz, DMSO-d_6): δ 10.85 (*br* s, 1H), 8.39 (dd, J_1 = 6.4, J_2 = 0.8, 1H), 7.44 (d, J = 4.0, 1H), 7.40 (t, J = 6.4, 1H), 7.25 (d, J = 4.0, 1H), 7.22 (dd, J_1 = 8.4, J_2 = 0.8, 1H); ESI-MS(-): *m/z* 369.12 [M - H]$^-$.

2-Bromo-3-((5-chlorothiophene)-2-sulfonamido)pyridine 1-oxide (44b)

Following the general method for oxidation, from **44a** (1.40 g, 3.52 mmol) and mCPBA (3.94 g, 77.0% Wt, 17.6 mmol), at 35 °C for 6 d, the desired product **44b** (0.497 g, 1.20 mmol, 34%) was obtained as a tan solid. ^{1}H NMR (400 MHz, DMSO-d_6): δ 10.81 (*br* s, 1H), 8.37 (d, J = 6.4, 1H), 7.42 – 7.39 (m, 2H), 7.34 (d, J = 4.0, 1H), 7.21 (d, J = 8.4, 1H); ESI-MS(-): *m/z* 413.02 [M - H]$^-$.

3-(Benzo[c][1,2,5]thiadiazole-4-sulfonamido)-2-bromopyridine 1-oxide (45b)

Following the general method for oxidation, from **45a** (0.350 g, 0.943 mmol) and mCPBA (1.06 g, 77.0% Wt, 4.71 mmol), at 30 °C for 5 d, the desired product **45b** (0.147 g, 0.380 mmol,

40%) was obtained as a tan solid. ^{1}H NMR (400 MHz, DMSO-d_6): δ 8.26 (d, J = 8.8, 1H), 8.08 (d, J = 7.2, 1H), 7.94 – 7.92 (m, 1H), 7.60 (t, J = 6.8, 1H), 7.17 (d, J = 8.4, 1H), 7.10 – 7.06 (m, 1H); ESI-MS(+): *m/z* 389.11 $[M + H]^+$.

2-Bromo-3-((5-phenylthiophene)-2-sulfonamido)pyridine 1-oxide (46c)

Following the general method for oxidation, from **46b** (1.05 g, 2.66 mmol) and mCPBA (2.98 g, 77.0% Wt, 13.3 mmol), at 35 °C for 16 h, the desired product **46c** (0.590 g, 1.43 mmol, 54%) was obtained as a pale yellow solid. ^{1}H NMR (400 MHz, DMSO-d_6): δ 10.73 (*br* s, 1H), 8.36 (d, J = 6.4, 1H), 7.71 (d, J = 7.6, 2H), 7.57 – 7.54 (m, 2H), 7.47 – 7.39 (m, 4H), 7.25 (d, J = 8.4, 1H); ESI-MS(+): *m/z* 409.17 $[M + H]^+$.

Thionation

General Thionation Protocol

The starting material and 1.5 equivalents of KI were dissolved in 5 mL DI water with a minimal amount of MeOH to dissolve as needed. Then 5 mL of saturated freshly prepared sodium hydrogen sulfide solution (excess) was added to the solution containing the starting material. The reaction mixture was then heated at 50 – 100 °C for 3 – 16 h. Upon reaction completion as indicated by TLC, the reaction mixture was cooled to 0 °C, and slowly quenched with 6 M HCl. CAUTION: The neutralization of NaSH using acid generates H_2S gas, which is both highly flammable and highly toxic by inhalation; only perform neutralization in well-vented fume hood. After waiting ~5 min to allow the resultant H_2S gas to evolve and disperse, the resulting mixture was extracted into organic using 3×15 mL ethyl acetate. The combined organic was washed with aqueous 1 M $Na_2S_2O_3$, until the aqueous went from cloudy to clear. Then the organic was washed with brine,

dried over magnesium sulfate, and the solids were filtered off and discarded. The filtrate was concentrated under reduced pressure, and the remaining residue was then purified by column chromatography, using a gradient of 100% hexanes to 100% CH_2Cl_2, and then to 15% MeOH in CH_2Cl_2. The desired product typically eluted around 80% CH_2Cl_2 in hexanes. When necessary, the collected product was recrystallized from 7:3 IPA to water. The crystals were collected via vacuum filtration and rinsed with a small amount of cold IPA to obtain the desired final products.

N-(1-Hydroxy-2-thioxo-1,2-dihydropyridin-3-yl)thiophene-2-sulfonamide (29)

Following the above general thionation protocol, from **29b** (0.500 g, 1.49 mmol) with KI (0.371 g, 2.24 mmol) in 5 mL saturated NaSH solution (excess) at 100 °C for 8 h, **29** (0.160 g, 0.555 mmol, 37%) was obtained as a pale yellow solid. ^{1}H NMR (400 MHz, DMSO-d_6): δ 9.50 (*br* s, 1H), 8.17 (d, J = 6.8, 1H), 7.98 (d, J = 4.8, 1H), 7.72 (d, J = 4.0, 1H), 7.59 (d, J = 8.0, 1H), 7.14 (t, J = 4.8, 1H), 6.88 (d, J = 7.6, 1H); ^{13}C NMR (500 MHz, DMSO-d_6): δ 164.3, 138.6, 137.3, 135.4, 134.3, 134.0, 128.4, 119.4, 112.8; HRMS (ESI-TOF): *m/z* calcd for $[C_9H_7N_2O_3S_3]^-$: 286.9624 $[M-H]^-$; found: 286.9626.

N-(1-Hydroxy-2-thioxo-1,2-dihydropyridin-3-yl)benzamide (30)

Following the above general thionation protocol, from **30b** (0.160 g, 0.546 mmol) with KI (0.136 g, 0.819 mmol) in 5 mL saturated NaSH solution (excess) at 40 °C for 16 h, **30** (0.065 g, 0.260 mmol, 48%) was obtained as an off white solid. ^{1}H NMR (400 MHz, DMSO-d_6): δ 10.55 (*br* s, 1H), 8.55 (d, J = 7.6, 1H), 8.21 (d, J = 7.2, 1H), 7.96 (d, J = 7.6, 2H), 7.69 – 7.60 (m, 3H), 6.98 (t, J = 7.6, 1H); ^{13}C NMR (500 MHz, DMSO-d_6): δ 165.2, 163.4, 138.7, 134.1, 133.1, 132.6, 129.7, 127.5, 119.1, 113.4; HRMS (ESI-TOF): *m/z* calcd for $[C_{12}H_9N_2O_2S]^-$: 245.0390 $[M-H]^-$; found: 245.0391.

N-(1-Hydroxy-2-thioxo-1,2-dihydropyridin-3-yl)thiophene-2-carboxamide (31)

Following the above general thionation protocol, from **31b** (0.350 g, 1.17 mmol) with KI (0.291 g, 1.76 mmol) in 5 mL saturated NaSH solution (excess) at 40 °C for 16 h, **31** (0.130 g, 0.515 mmol, 44%) was obtained as a grey solid. ^{1}H NMR (400 MHz, DMSO-d_6): δ 10.42 (*br* s, 1H), 8.41 (d, J = 7.6, 1H), 8.21 (d, J = 6.8, 1H), 7.96 (d, J = 4.8, 1H), 7.82 (d, J = 3.2, 1H), 7.27 (t, J = 3.6, 1H), 6.96 (t, J = 6.8, 1H); ^{13}C NMR (500 MHz, DMSO-d_6): δ 163.3, 160.0, 138.7, 138.4, 133.5, 132.6, 130.0, 129.2, 119.3, 113.3; HRMS (ESI-TOF): *m/z* calcd for $[C_{10}H_7N_2O_2S_2]^-$: 250.9954 $[M-H]^-$; found: 250.9957.

N-(1-Hydroxy-2-thioxo-1,2-dihydropyridin-3-yl)-5-methylthiophene-2-sulfonamide (32)

Following the above general thionation protocol, from **32b** (0.200 g, 0.573 mmol) with KI (0.143 g, 0.859 mmol) in 5 mL saturated NaSH solution (excess) at 100 °C for 8 h, **32** (0.058 g, 0.18 mmol, 33%), was obtained as a pale yellow solid. ^{1}H NMR (400 MHz, DMSO-d_6): δ 9.44 (*br* s, 1H), 8.17 (d, J = 6.8, 1H), 7.58 – 7.56 (m, 2H), 6.90 – 6.87 (m, 2H), 2.45 (s, 3H); ^{13}C NMR (500 MHz, DMSO-d_6): δ 164.0, 149.7, 137.4, 135.3, 134.8, 133.9, 127.0, 118.7, 112.9, 15.6; HRMS (ESI-TOF): *m/z* calcd for $[C_{10}H_9N_2O_3S_3]^-$: 300.9781 $[M-H]^-$; found: 300.9780.

N-(1-Hydroxy-2-thioxo-1,2-dihydropyridin-3-yl)-4-methylthiophene-2-sulfonamide (33)

Following the above general thionation protocol, from **33b** (0.190 g, 0.544 mmol) with KI (0.135 g, 0.816 mmol) in 5 mL saturated NaSH solution (excess) at 100 °C for 5 h, **33** (0.070 g, 0.230 mmol, 43%) was obtained as a pale yellow solid. ^{1}H NMR (400 MHz, DMSO-d_6): δ 9.47 (*br* s, 1H), 8.17 (dd, J_1 = 6.8, J_2 = 1.2, 1H), 7.58 – 7.56 (m, 3H), 6.89 (t, J = 8.0, 1H), 2.16 (s, 3H);

^{13}C NMR (500 MHz, DMSO-*d*$_6$): δ 166.5, 153.3, 148.23, 139.3, 138.6, 134.9, 132.7, 129.7, 124.4, 15.5; HRMS (ESI-TOF): *m/z* calcd for $[C_{10}H_9N_2O_3S_3]^-$: 300.9781 $[M-H]^-$; found: 300.9778.

N-(1-Hydroxy-5-methyl-2-thioxo-1,2-dihydropyridin-3-yl)thiophene-2-sulfonamide (34)

Following the above general thionation protocol, from **34b** (0.100 g, 0.286 mmol) with KI (0.071 g, 0.430 mmol) in 3 mL saturated NaSH solution (excess) at 75 °C for 3 h, **34** (0.0057 g, 0.019 mmol, 7%) was obtained as a very pale yellow solid. ^{1}H NMR (400 MHz, Acetone-*d*$_6$): δ 8.65 (*br* s, 1H), 8.17 (s, 1H), 7.92 (d, *J* = 4.8, 1H), 7.77 (d, *J* = 4.0, 1H), 7.63 (s, 1H), 7.16 (t, *J* = 4.0, 1H), 2.34 (s, 3H); HRMS (ESI-TOF): *m/z* calcd for $[C_{10}H_9N_2O_3S_3]^-$: 300.9781 $[M-H]^-$; found: 300.9779.

N-(1-Hydroxy-5-methyl-2-thioxo-1,2-dihydropyridin-3-yl)thiophene-2-sulfonamide (35)

Following the above general thionation protocol, from **35b** (0.210 g, 0.601 mmol) with KI (0.150 g, 0.902 mmol) in 3 mL saturated NaSH solution (excess) at 75 °C for 3 h, **35** (0.011 g, 0.036 mmol, 6%) was obtained as a pale yellow solid. ^{1}H NMR (400 MHz, DMSO-*d*$_6$): δ 12.49 (*br* s, 1H), 9.35 (*br* s, 1H), 7.95 (d, *J* = 4.8, 1H), 7.68 (d, *J* = 4.0, 1H), 7.55 (d, *J* = 8.0, 1H), 7.12 (t, *J* = 4.0, 1H), 6.85 (d, *J* = 8.0, 1H), 2.41 (s, 3H); HRMS (ESI-TOF): *m/z* calcd for $[C_{10}H_9N_2O_3S_3]^-$: 300.9781 $[M-H]^-$; found: 300.9778.

N-(1-Hydroxy-2-thioxo-1,2-dihydropyridin-3-yl)cyclopropanesulfonamide (36)

Following the above general thionation protocol, from **36b** (0.460 g, 0.157 mmol) with KI (0.391 g, 2.35 mmol) in 5 mL saturated NaSH solution (excess) at 100 °C for 8 h, **36** (0.132 g, 0.534 mmol, 34%) was obtained as a pale yellow solid. ^{1}H NMR (400 MHz, DMSO-*d*$_6$): δ 8.94 (*br* s, 1H), 8.22 (dd, J_1 = 6.8, J_2 = 1.2, 1H), 7.58 (dd, J_1 = 7.6, J_2 = 0.8, 1H), 6.90 (t, *J* = 7.6, 1H),

2.87 – 2.81 (m, 1H), 1.05 – 0.95 (m, 4H); ^{13}C NMR (500 MHz, DMSO-*d*$_6$): δ 153.2, 147.9, 135.3, 133.1, 123.9, 30.9, 5.9; HRMS (ESI-TOF): *m/z* calcd for $[C_8H_9N_2O_3S_2]^-$: 245.0060 $[M-H]^-$; found: 245.0061.

1-((1R,4S)-7,7-Dimethyl-2-oxobicyclo[2.2.1]heptan-1-yl)-N-(1-hydroxy-2-thioxo-1,2-dihydropyridin-3-yl)methanesulfonamide (37)

Following the above general thionation protocol, from **37b** (0.240 g, 0.669 mmol) with KI (0.167 g, 1.00 mmol) in 5 mL saturated NaSH solution (excess) at 80 °C for 6 h, **37** (0.011 g, 0.031 mmol, 5%) was obtained as a dark grey solid. ^{1}H NMR (400 MHz, DMSO-*d*$_6$): δ 11.63 (*br* s, 1H), 8.45 (*br* s, 1H), 8.31 (d, *J* = 6.4, 1H), 7.81 (d, *J* = 7.6, 1H), 7.11 (t, *J* = 7.2, 1H), 3.66 (d, *J* = 15.2, 1H), 3.30 (d, *J* = 10.8, 1H), 2.46 – 2.34 (m, 2H), 2.15 – 2.13 (m, 1H), 1.94 (d, *J* = 18.4, 2H), 1.82 – 1.75 (m, 1H), 1.53 – 1.47 (m, 1H), 1.09 (s, 3H), 0.87 (s, 3H); HRMS (ESI-TOF): *m/z* calcd for $[C_{15}H_{19}N_2O_4S_2]^-$: 355.0792 $[M-H]^-$; found: 355.0789.

N-(1-Hydroxy-2-thioxo-1,2-dihydropyridin-3-yl)-1-methyl-1H-pyrazole-3-sulfonamide (38)

Following the above general thionation protocol, from **38b** (0.166 g, 0.498 mmol) with KI (0.124 g, 0.747 mmol) in 5 mL saturated NaSH solution (excess) at 100 °C for 5 h, **38** (0.047 g, 0.17 mmol, 33%) was obtained as a light grey solid. ^{1}H NMR (400 MHz, DMSO-*d*$_6$): δ 9.35 (*br* s, 1H), 8.14 (d, *J* = 6.8, 1H), 7.88 (d, *J* = 1.6, 1H), 7.54 (d, *J* = 7.6, 1H), 6.87 (t, *J* = 7.6, 1H), 6.78 (d, *J* = 1.6, 1H), 3.87 (s, 3H); ^{13}C NMR (500 MHz, DMSO-*d*$_6$): δ 152.7, 149.5, 147.7, 134.2, 133.8, 133.2, 124.2, 107.3, 25.9; HRMS (ESI-TOF): *m/z* calcd for $[C_9H_9N_4O_3S_2]^-$: 285.0122 $[M-H]^-$; found: 285.0122.

N-(1-Hydroxy-2-thioxo-1,2-dihydropyridin-3-yl)-1-methyl-1H-pyrazole-4-sulfonamide (39)

Following the above general thionation protocol, from **39b** (0.210 g, 0.630 mmol) with KI (0.157 g, 0.945 mmol) in 5 mL saturated NaSH solution (excess) at 100 °C for 5 h, **39** (0.057 g, 0.20 mmol, 32%) was obtained as a dark grey solid. ^{1}H NMR (400 MHz, DMSO-*d*$_6$): δ 9.24 (*br* s, 1H), 8.14 (d, *J* = 6.8, 1H), 8.44 (s, 1H), 8.14 (d, *J* = 6.8, 1H), 7.85 (s, 1H), 7.53 (d, *J* = 8.0, 1H), 6.86 (t, *J* = 7.6, 1H), 3.82 (s, 3H); ^{13}C NMR (500 MHz, DMSO-*d*$_6$): δ 163.6, 138.8, 137.7, 133.9, 133.3, 119.9, 117.8, 113.0, 25.9; HRMS (ESI-TOF): *m/z* calcd for $[C_9H_9N_4O_3S_2]^-$: 285.0122 [M-H]$^-$; found: 285.0121.

N-(1-Hydroxy-2-thioxo-1,2-dihydropyridin-3-yl)thiophene-3-sulfonamide (40)

Following the above general thionation protocol, from **40b** (0.250 g, 0.746 mmol) with KI (0.186 g, 1.12 mmol) in 5 mL saturated NaSH solution (excess) at 100 °C for 8 h, **40** (0.053 g, 0.18 mmol, 25%) was obtained as a pale yellow solid. ^{1}H NMR (400 MHz, DMSO-*d*$_6$): δ 9.36 (*br* s, 1H), 8.40 – 8.39 (m, 1H), 8.14 (d, *J* = 6.8, 1H), 7.73 – 7.71 (m, 1H), 7.54 (d, *J* = 8.0, 1H), 7.35 (d, *J* = 5.2, 1H), 6.84 (t, *J* = 8.0, 1H); ^{13}C NMR (500 MHz, DMSO-*d*$_6$): δ 153.2, 148.1, 147.8, 139.2, 132.6, 130.2, 125.6, 124.2, 119.7; HRMS (ESI-TOF): *m/z* calcd for $[C_9H_7N_2O_3S_3]^-$: 286.9624 [M-H]$^-$; found: 286.9623.

N-(1-Hydroxy-2-thioxo-1,2-dihydropyridin-4-yl)thiophene-2-sulfonamide (41)

Following the above general thionation protocol, from **41b** (0.290 g, 0.865 mmol) with KI (0.215 g, 2.30 mmol) in 5 mL saturated NaSH solution (excess) at 100 °C for 8 h, **41** (0.083 g, 0.288 mmol, 33%) was obtained as a very pale yellow solid. ^{1}H NMR (400 MHz, DMSO-*d*$_6$): δ 11.95 (*br* s, 1H), 11.44 (*br* s, 1H), 8.25 (dd, J_1 = 7.2, J_2 = 3.6, 1H), 8.04 – 8.02 (m, 1H), 7.76 – 7.74 (m, 1H), 7.22 – 7.18 (m, 2H), 6.64 – 6.62 (m, 1H); HRMS (ESI-TOF): *m/z* calcd for $[C_9H_7N_2O_3S_3]^-$: 286.9624 [M-H]$^-$; found: 286.9627.

N-(1-Hydroxy-6-thioxo-1,6-dihydropyridin-3-yl)thiophene-2-sulfonamide (42)

Following the above general thionation protocol, from **42b** (0.310 g, 0.925 mmol) with KI (0.230 g, 2.39 mmol) in 5 mL saturated NaSH solution (excess) at 100 °C for 8 h, **42** (0.028 g, 0.097 mmol, 10%) was obtained as a pale yellow solid. ^{1}H NMR (400 MHz, Acetone-d_6): δ 8.31 (dd, J_1 = 2.4, J_2 = 0.4, 1H), 7.93 (dd, J_1 = 4.8, J_2 = 1.2, 1H), 7.64 (dd, J_1 = 3.6, J_2 = 1.2, 1H), 7.58 (dd, J_1 = 9.2, J_2 = 0.4, 1H), 7.33 (dd, J_1 = 9.2, J_2 = 2.4, 1H), 7.19 (dd, J_1 = 5.2, J_2 = 4.0, 1H); ^{13}C NMR (500 MHz, DMSO-d_6): δ 167.0, 139.0, 134.8, 133.7, 133.6, 129.5, 129.4, 128.5, 125.8; HRMS (ESI-TOF): *m/z* calcd for $[C_9H_7N_2O_3S_3]^-$: 286.9624 $[M-H]^-$; found: 286.9626.

5-Chloro-N-(1-hydroxy-2-thioxo-1,2-dihydropyridin-3-yl)thiophene-2-sulfonamide (43)

Following the above general thionation protocol, from **43b** (0.300 g, 0.812 mmol) with KI (0.202 g, 1.22 mmol) in 5 mL saturated NaSH solution (excess) at 65 °C for 16 h, **43** (0.152 g, 0.471 mmol, 58%) was obtained as a pale yellow solid. ^{1}H NMR (400 MHz, DMSO-d_6): δ 9.64 (*br* s, 1H), 8.23 (dd, J_1 = 6.8, J_2 = 0.8, 1H), 7.62 – 7.57 (m, 2H), 7.23 (d, J = 4.0, 1H), 6.89 (t, J = 7.2, 1H); ^{13}C NMR (500 MHz, DMSO-d_6): δ 164.7, 137.2, 136.9, 134.5, 134.2, 128.7, 121.0, 112.8; HRMS (ESI-TOF): *m/z* calcd for $[C_9H_6ClN_2O_3S_3]^-$: 320.9235 $[M-H]^-$; found: 320.9234.

5-Bromo-N-(1-hydroxy-2-thioxo-1,2-dihydropyridin-3-yl)thiophene-2-sulfonamide (44)

Following the above general thionation protocol, from **44b** (0.300 g, 0.724 mmol) with KI (0.180 g, 1.09 mmol) in 5 mL saturated NaSH solution (excess) at 75 °C for 17 h, **44** (0.050 g, 0.14 mmol, 19%) was obtained as a pale yellow solid. ^{1}H NMR (400 MHz, DMSO-d_6): δ 9.62 (*br* s, 1H), 8.22 (d, J = 6.8, 1H), 7.59 – 7.56 (m, 2H), 7.32 (d, J = 3.6, 1H), 6.89 (t, J = 7.2, 1H); ^{13}C

NMR (500 MHz, DMSO-d_6): δ 164.6, 139.7, 137.0, 134.9, 134.4, 132.1, 121.0, 120.8, 112.8; HRMS (ESI-TOF): *m/z* calcd for $[C_9H_6BrN_2O_3S_3]^-$: 364.8729 $[M-H]^-$; found: 364.8728.

N-(1-Hydroxy-2-thioxo-1,2-dihydropyridin-3-yl)benzo[c][1,2,5]thiadiazole-4-sulfonamide (45)

Following the above general thionation protocol, from **45b** (0.150 g, 0.387 mmol) with KI (0.0965 g, 0.581 mmol) in 5 mL saturated NaSH solution (excess) at 75 °C for 17 h, **45** (0.018 g, 0.053 mmol, 14%) was obtained as a deep yellow solid. ^{1}H NMR (400 MHz, DMSO-d_6): δ 9.73 (*br* s, 1H), 8.40 (d, *J* = 8.8, 1H), 8.32 (d, *J* = 7.2, 1H), 8.06 (d, *J* = 6.8, 1H), 7.84 (t, *J* = 6.8, 1H), 7.56 (d, *J* = 8.0, 1H), 6.78 (t, *J* = 6.8, 1H); HRMS (ESI-TOF): *m/z* calcd for $[C_{11}H_7N_4O_3S_3]^-$: 338.9686 $[M-H]^-$; found: 338.9683.

N-(1-Hydroxy-2-thioxo-1,2-dihydropyridin-3-yl)-5-phenylthiophene-2-sulfonamide (46)

Following the above general thionation protocol, from **46c** (0.400 g, 0.973 mmol) with KI (0.242 g, 1.46 mmol) in 5 mL saturated NaSH solution (excess) at 60 °C for 16 h, **46** (0.153 g, 0.420 mmol, 43%) was obtained as a light yellow solid. ^{1}H NMR (400 MHz, DMSO-d_6): δ 9.58 (*br* s, 1H), 8.19 (d, *J* = 7.2, 1H), 7.74 (d, *J* = 3.6, 1H), 7.70 – 7.66 (m, 2H), 7.62 (d, *J* = 8.0, 1H), 7.55 (d, *J* = 4.0, 1H), 7.51 – 7.39 (m, 4H), 6.90 (t, *J* = 7.6, 1H); ^{13}C NMR (500 MHz, DMSO-d_6): δ 150.3, 147.5, 136.1, 133.6, 129.8, 129.7, 129.6, 129.1, 128.5, 128.4, 126.8, 126.5, 125.8, 125.7, 123.9, 113.2.

N-(2-Thioxo-1,2-dihydropyridin-3-yl)methanesulfonamide (47)

To a solution of **47a** (0.500 g, 50% Wt, 0.996 mmol) in 15 mL DMF, thiourea (1.82 g, 23.9 mmol) was added in one portion, and the reaction was placed under argon and heated to reflux at

150 °C for 12 h, after which the reaction mixture had changed color to dark brown. Then the reaction was cooled to 110 °C, and 6 M HCl (15 mL, 90 mmol) was added in one portion; the reaction was heated at 110°C for an additional 2 h. Then the reaction mixture was cooled to 25 °C, diluted with 50 mL brine, and extracted into organic using 3×15 mL ethyl acetate. The combined organic was washed with an additional 15 mL brine, dried over magnesium sulfate, and the solids were filtered off and discarded. The filtrate was concentrated under reduced pressure, and the resulting crude was purified by column chromatography, running gradient from 100% hexanes to 100% ethyl acetate, and then from 100% CH_2Cl_2 to 15% MeOH in CH_2Cl_2. The desired product eluted in 85% ethyl acetate in hexanes. Like fractions of the desired product were combined and concentrated under reduced pressure. The resulting solid was recrystallized from 3:1 ethyl acetate to hexanes, and the solid was collected via vacuum filtration and washed with hexanes to obtain **47** (0.081 g, 0.40 mmol, 40 %) as a pale yellow solid. ^{1}H NMR (400 MHz, DMSO-*d*$_6$): δ 8.71 (*br* s, 1H), 7.61 – 7.58 (m, 2H), 6.90 (t, *J* = 6.8, 1H), 3.16 (s, 3H); HRMS (ESI-TOF): *m/z* calcd for $C_6H_9N_2O_2S_2^+$: 205.0100 $[M+H]^+$; found: 205.0103.

N-(2-Thioxo-1,2-dihydropyridin-3-yl)thiophene-2-sulfonamide (48)

Following the same protocol used in **47**, from **29a** (0.500 g, 1.57 mmol) and thiourea (1.43 g, 18.8 mmol) the desired **48** (0.094 g, 0.35 mmol, 22%) was obtained as a deep yellow solid. ^{1}H NMR (400 MHz, DMSO-*d*$_6$): δ 9.27 (*br* s, 1H), 7.98 (d, *J* = 4.8, 1H), 7.73 (d, *J* = 0.8, 1H), 7.65 (d, *J* = 7.6, 1H), 7.57 (d, *J* = 6.0, 1H), 7.16 – 7.15 (m, 1H), 6.88 (d, *J* = 7.6, 1H); ^{13}C NMR (500 MHz, DMSO-*d*$_6$): δ 168.3, 138.6, 136.4, 135.3, 134.3, 133.8, 128.4, 122.6, 114.2; HRMS (ESI-TOF): *m/z* calcd for $C_9H_7N_2O_2S_3^-$: 270.9675 $[M-H]^-$; found: 270.9675.

Activity Assays

The degradation of Aβ, glucagon, amylin and insulin was quantified by fluorescence polarization-based assays using fluoresceinated and biotinylated peptides, as described (18, 28). For Substrate V, fluorescence dequenching was monitored continuously (λ_{ex} = 385 nm; λ_{em} = 425 nm). Bacterially expressed, recombinant human IDE, generated as described (34) was used in all assays. Reactions were performed in Buffer A (PBS supplemented with 0.05% BSA and 0.5 mM DTT) and, for discontinuous assays, terminated by addition of 10-fold excess avidin (monomer) relative to the substrate concentration and 2 mM 1,10-phenanthroline. A peptidic inhibitor of IDE, **P12-3A** (27) was used as a positive control. All MBP fragments were tested in at least 3 independent experiments, with results normalized to DMSO-only and no-enzyme controls. All activity assays were conducted in 384-well format on a SpectraMAX M5^e multilable plate reader (Molecular Devices). IC_{50} values were obtained from normalized activity data by curve fitting within Prism v8.1 (GraphPad Software Inc.) and converted to K_i values using the Cheng-Prusoff equation and published K_M values for each substrate (18, 28, 90).

Molecular Modelling

The in silico model of **8** bound to the IDE active site was prepared by using the superpose function within the Molecular Operating Environment (MOE) software suite to align the structure of Zn-bound **8** from the structure of [($Tp^{Ph,Me}$)Zn(8)] with the hydroxamic acid of **2** from PDB 4NXO. The atoms of the thione in **8** were aligned with the carbonyl atoms of the hydroxamate group in **2**, and likewise, the hydroxyl atoms of 8 were aligned with the hydroxyl atoms of **2**, resulting in a model of **8** bound to the Zn^{2+} within the IDE active site. Upon modelling **8** in the IDE active site, the image was visually rendered using Pymol.

4.6 Conclusions

In this chapter we have described the development and detailed characterization of novel assays for proteolytic degradation of glucagon by IDE (18), which—together with assays for other substrates—was used to discover cyclic peptide inhibitors of IDE by phage display (27) and to discover and optimize novel zinc-binding IDE inhibitors, some of which exhibit substrate-dependent inhibition.

From an experimental perspective, the long-term objective of these efforts is to develop a collection of substrate-selective inhibitors of IDE (as was done already for insulin (17)), ideally with properties that make them suitable for use in cultured cells and *in vivo*. Inhibitors selective for Aβ, for example, could be used to investigate the role of IDE in AD in a more targeted manner than is achievable by genetic manipulation of the *IDE* gene. Inhibitors selective for amylin would also be of special interest, given that amylin is highly amyloidogenic (121), forming islet amyloid in T2DM (122) and deposits in brain in AD (123). The assays we have developed will facilitate these goals, and the IDE inhibitors we have already discovered using them could represent pharmacophores for future therapeutic development.

From a therapeutic perspective, one goal has been to develop IDE inhibitors suitable for topical use in wound healing and in cosmetic applications such as microneedling (85-87). We succeeded in discovering potent and selective peptidic inhibitors for IDE that have the advantage of being made of all-natural amino acids and being inexpensive to generate (27). However, these bulky peptidic inhibitors are unlikely to penetrate well into the skin, and may be cell impermeant, so there remains a strong need for small-molecule IDE inhibitors more likely to be cell- and skin-penetrant. We have gone part way towards the completion of that goal with the development of very small-molecule IDE inhibitors that target the active-site zinc. The goal of using IDE inhibitors

to treat or manage T2DM would seem to be a plausible strategy, given the work of Maianti and colleagues showing that a potent IDE inhibitor exhibited multiple antidiabetic properties *in vivo* (110). However, emerging evidence suggests that the biology of IDE is likely more complicated than originally believed. For example, IDE has been shown to regulate insulin secretion from the pancreas (124, 125) and appears also to be involved in the machinery mediating insulin uptake (126). Paradoxically, liver-specific *overexpression* of IDE was recently found to reverse diabetes in mice, raising serious questions about the logic of using IDE inhibitors for the same goal (127). Finally, given its role as an AβDP, IDE has been considered a potential target for AD. In this case, the objective would be to increase rather than decrease IDE proteolytic activity. Although this might seem an impossible goal, pharmacological activators of IDE have in fact been discovered already (29), and the assays we have developed could in principle be used to discover activators selective for Aβ.

4.7 Acknowledgements

I would like to acknowledge Shelley Lane and Malcolm A. Leissring for their contributions to the work, experimental design, data analysis, and writing of the publication featured in **4.3**. This work has been previously published in SLAS, an open source journal (18). I would like to acknowledge the hard work and contributions of Sarah J. Nainar, Michael Fazio, Adam G. Kreutzer, Tara Paymozd-Yazdi, Caitlyn L. Topper, Caroline R. Thompson, and Malcolm A. Leissring in the completion of the project and publication featured in **4.4,** which has been previously published in PLoS One, an open source journal (27). I would like to thank and acknowledge Rebecca N. Adamek, Monica K. Brizuela, Malcolm A. Leissring and Seth M. Cohen for their work, contributions and permissions to use the currently unpublished (soon to be submitted) data of section **4.5** in my dissertation.

4.8 References

1. Zhao J, Li L, Leissring MA. Insulin-degrading enzyme is exported via an unconventional protein secretion pathway. Mol Neurodegener. 2009;4:4.

2. McDermott JR, Gibson AM. Degradation of Alzheimer's beta-amyloid protein by human and rat brain peptidases: involvement of insulin-degrading enzyme. Neurochem Res. 1997;22(1):49-56.

3. Chesneau V, Vekrellis K, Rosner MR, Selkoe DJ. Purified recombinant insulin-degrading enzyme degrades amyloid beta-protein but does not promote its oligomerization. Biochem J. 2000;351 Pt 2:509-16.

4. Qiu WQ, Walsh DM, Ye Z, Vekrellis K, Zhang J, Podlisny MB, et al. Insulin-degrading enzyme regulates extracellular levels of amyloid beta-protein by degradation. J Biol Chem. 1998;273(49):32730-8.

5. Betts V, Leissring MA, Dolios G, Wang R, Selkoe DJ, Walsh DM. Aggregation and catabolism of disease-associated intra-Abeta mutations: reduced proteolysis of AbetaA21G by neprilysin. Neurobiol Dis. 2008;31(3):442-50.

6. Abdul-Hay SO, Kang D, McBride M, Li L, Zhao J, Leissring MA. Deletion of insulin-degrading enzyme elicits antipodal, age-dependent effects on glucose and insulin tolerance. PLoS ONE. 2011;6(6):e20818.

7. Mirsky IA. Insulinase, insulinase-inhibitors, and diabetes mellitus. Recent progress in hormone research. 1957;13:429-65; discussion 65-71.

8. Mirsky IA, Perisutti G. Effect of insulinase-inhibitor on hypoglycemic action of insulin. Science. 1955;122(3169):559-60.

9. Simkin B, Broh-Kahn RH, Mirsky IA. The inactivation of insulin by tissue extracts; the effect of force-fed diets on the insulinase activity of rat liver extracts. Archives of biochemistry. 1949;24(2):422-8.

10. Farris W, Mansourian S, Chang Y, Lindsley L, Eckman EA, Frosch MP, et al. Insulin-degrading enzyme regulates the levels of insulin, amyloid beta-protein, and the beta-amyloid precursor protein intracellular domain in vivo. Proc Natl Acad Sci U S A. 2003;100(7):4162-7.

11. Leissring MA, Farris W, Chang AY, Walsh DM, Wu X, Sun X, et al. Enhanced proteolysis of beta-amyloid in APP transgenic mice prevents plaque formation, secondary pathology, and premature death. Neuron. 2003;40(6):1087-93.

12. Abdul-Hay SO, Lane AL, Caulfield TR, Claussin C, Bertrand J, Masson A, et al. Optimization of peptide hydroxamate inhibitors of insulin-degrading enzyme reveals marked substrate-selectivity. J Med Chem. 2013;56(6):2246-55.

13. Charton J, Gauriot M, Guo Q, Hennuyer N, Marechal X, Dumont J, et al. Imidazole-derived 2-[N-carbamoylmethyl-alkylamino]acetic acids, substrate-dependent modulators of insulin-degrading enzyme in amyloid-beta hydrolysis. European journal of medicinal chemistry. 2014;79:184-93.

14. Leissring MA, Malito E, Hedouin S, Reinstatler L, Sahara T, Abdul-Hay SO, et al. Designed inhibitors of insulin-degrading enzyme regulate the catabolism and activity of insulin. PLoS One. 2010;5(5):e10504.

15. Maianti JP, McFedries A, Foda ZH, Kleiner RE, Du XQ, Leissring MA, et al. Anti-diabetic activity of insulin-degrading enzyme inhibitors mediated by multiple hormones. Nature. 2014;511(7507):94-8.

16. Abdul-Hay SO, Bannister TD, Wang H, Cameron MD, Caulfield TR, Masson A, et al. Selective Targeting of Extracellular Insulin-Degrading Enzyme by Quasi-Irreversible Thiol-Modifying Inhibitors. ACS Chem Biol. 2015.

17. Maianti JP, Tan GA, Vetere A, Welsh AJ, Wagner BK, Seeliger MA, et al. Substrate-Selective Inhibitors that Reprogram the Activity of Insulin-Degrading Enzyme. Nat Chem Biol. 2019;15:565-74.

18. Suire CN, Lane S, Leissring MA. Development and Characterization of Quantitative, High-Throughput-Compatible Assays for Proteolytic Degradation of Glucagon. SLAS Discov. 2018;23(10):1060-9.

19. Muller TD, Finan B, Clemmensen C, DiMarchi RD, Tschop MH. The new biology and pharmacology of glucagon. Physiol Rev. 2017;97(2):721-66.

20. Hinke SA, Pospisilik JA, Demuth HU, Mannhart S, Kuhn-Wache K, Hoffmann T, et al. Dipeptidyl peptidase IV (DPIV/CD26) degradation of glucagon. Characterization of glucagon degradation products and DPIV-resistant analogs. J Biol Chem. 2000;275(6):3827-34.

21. Trebbien R, Klarskov L, Olesen M, Holst JJ, Carr RD, Deacon CF. Neutral endopeptidase 24.11 is important for the degradation of both endogenous and exogenous glucagon in anesthetized pigs. Am J Physiol Endocrinol Metab. 2004;287(3):E431-8.

22. Shen Y, Joachimiak A, Rosner MR, Tang WJ. Structures of human insulin-degrading enzyme reveal a new substrate recognition mechanism. Nature. 2006;443(7113):870-4.

23. Evans MR, Wei S, Posner BA, Unger RH, Roth MG. An AlphaScreen Assay for the Discovery of Synthetic Chemical Inhibitors of Glucagon Production. J Biomol Screen. 2016;21(4):325-32.

24. Hall MD, Yasgar A, Peryea T, Braisted JC, Jadhav A, Simeonov A, et al. Fluorescence polarization assays in high-throughput screening and drug discovery: a review. Methods Appl Fluoresc. 2016;4(2):022001.

25. Zhang JH, Chung TD, Oldenburg KR. A simple statistical parameter for use in evaluation and validation of high throughput screening assays. J Biomol Screen. 1999;4(2):67-73.

26. Bannister TD, Wang H, Abdul-Hay SO, Masson A, Madoux F, Ferguson J, et al. ML345: A small-molecule inhibitor of the insulin-degrading enzyme (IDE). Probe Reports from the NIH Molecular Libraries Program. Bethesda (MD)2014.

27. Suire CN, Nainar S, Fazio M, Kreutzer AG, Paymozd-Yazdi T, Topper CL, et al. Peptidic inhibitors of insulin-degrading enzyme with potential for dermatological applications discovered via phage display. PLoS One. 2018;13(2):e0193101.

28. Leissring MA, Lu A, Condron MM, Teplow DB, Stein RL, Farris W, et al. Kinetics of amyloid beta-protein degradation determined by novel fluorescence- and fluorescence polarization-based assays. J Biol Chem. 2003;278(39):37314-20.

29. Cabrol C, Huzarska MA, Dinolfo C, Rodriguez MC, Reinstatler L, Ni J, et al. Small-molecule activators of insulin-degrading enzyme discovered through high-throughput compound screening. PLoS ONE. 2009;4(4):e5274.

30. Shroyer LA, Varandani PT. Purification and characterization of a rat liver cytosol neutral thiol peptidase that degrades glucagon, insulin, and isolated insulin A and B chains. Arch Biochem Biophys. 1985;236(1):205-19.

31. Roth RA. Bacitracin: an inhibitor of the insulin degrading activity of glutathione-insulin transhydrogenase. Biochem Biophys Res Commun. 1981;98(2):431-8.

32. Neant-Fery M, Garcia-Ordonez RD, Logan TP, Selkoe DJ, Li L, Reinstatler L, et al. Molecular basis for the thiol sensitivity of insulin-degrading enzyme. Proc Natl Acad Sci U S A. 2008;105(28):9582-7.

33. Leal MC, Morelli L. Insulysin. In: Rawlings ND, Salvesen G, editors. Handbook of Proteolytic Enzymes. 1. 3rd ed: Academic Press; 2013. p. 1415-20.

34. Farris W, Leissring MA, Hemming ML, Chang AY, Selkoe DJ. Alternative splicing of human insulin-degrading enzyme yields a novel isoform with a decreased ability to degrade insulin and amyloid beta-protein. Biochemistry. 2005;44(17):6513-25.

35. Hersh LB. The insulysin (insulin degrading enzyme) enigma. Cell Mol Life Sci. 2006;63(21):2432-4.

36. Leissring MA, Selkoe DJ. Enzyme target to latch on to. Nature. 2006;443(7113):761-2.

37. Song ES, Hersh LB. Insulysin: an allosteric enzyme as a target for Alzheimer's disease. Journal of molecular neuroscience : MN. 2005;25(3):201-6.

38. Song ES, Juliano MA, Juliano L, Hersh LB. Substrate activation of insulin-degrading enzyme (insulysin). A potential target for drug development. J Biol Chem. 2003;278(50):49789-94.

39. Song ES, Juliano MA, Juliano L, Fried MG, Wagner SL, Hersh LB. ATP effects on insulin-degrading enzyme are mediated primarily through its triphosphate moiety. J Biol Chem. 2004;279(52):54216-20.

40. Im H, Manolopoulou M, Malito E, Shen Y, Zhao J, Neant-Fery M, et al. Structure of substrate-free human insulin-degrading enzyme (IDE) and biophysical analysis of ATP-induced conformational switch of IDE. J Biol Chem. 2007;282(35):25453-63.

41. Delledonne A, Kouri N, Reinstatler L, Sahara T, Li L, Zhao J, et al. Development of monoclonal antibodies and quantitative ELISAs targeting insulin-degrading enzyme. Mol Neurodegener. 2009;4:39.

42. Wilkins MR, Lindskog I, Gasteiger E, Bairoch A, Sanchez JC, Hochstrasser DF, et al. Detailed peptide characterization using PEPTIDEMASS--a World-Wide-Web-accessible tool. Electrophoresis. 1997;18(3-4):403-8.

43. Agrawal A, Johnson SL, Jacobsen JA, Miller MT, Chen LH, Pellecchia M, et al. Chelator fragment libraries for targeting metalloproteinases. ChemMedChem. 2010;5(2):195-9.

44. Puerta DT, Lewis JA, Cohen SM. New beginnings for matrix metalloproteinase inhibitors: identification of high-affinity zinc-binding groups. J Am Chem Soc. 2004;126(27):8388-9.

45. Hrynyk M, Neufeld RJ. Insulin and wound healing. Burns : journal of the International Society for Burn Injuries. 2014;40(8):1433-46.

46. Aaronson SA, Rubin JS, Finch PW, Wong J, Marchese C, Falco J, et al. Growth factor-regulated pathways in epithelial cell proliferation. The American review of respiratory disease. 1990;142(6 Pt 2):S7-10.

47. Monaco S, Illario M, Rusciano MR, Gragnaniello G, Di Spigna G, Leggiero E, et al. Insulin stimulates fibroblast proliferation through calcium-calmodulin-dependent kinase II. Cell cycle. 2009;8(13):2024-30.

48. Wertheimer E, Trebicz M, Eldar T, Gartsbein M, Nofeh-Moses S, Tennenbaum T. Differential roles of insulin receptor and insulin-like growth factor-1 receptor in differentiation of murine skin keratinocytes. The Journal of investigative dermatology. 2000;115(1):24-9.

49. Benoliel AM, Kahn-Perles B, Imbert J, Verrando P. Insulin stimulates haptotactic migration of human epidermal keratinocytes through activation of NF-kappa B transcription factor. J Cell Sci. 1997;110 (Pt 17):2089-97.

50. Liu Y, Petreaca M, Yao M, Martins-Green M. Cell and molecular mechanisms of keratinocyte function stimulated by insulin during wound healing. BMC cell biology. 2009;10:1.

51. Villee DB, Powers ML. Effect of glucose and insulin on collagen secretion by human skin fibroblasts in vitro. Nature. 1977;268(5616):156-8.

52. Kjellstrom T, Malmquist J. Insulin effects on collagen and protein production in cultured human skin fibroblasts from diabetic and non-diabetic subjects. Hormone and metabolic research = Hormon- und Stoffwechselforschung = Hormones et metabolisme. 1984;16(4):168-71.

53. Goldstein RH, Poliks CF, Pilch PF, Smith BD, Fine A. Stimulation of collagen formation by insulin and insulin-like growth factor I in cultures of human lung fibroblasts. Endocrinology. 1989;124(2):964-70.

54. Krupsky M, Fine A, Kuang PP, Berk JL, Goldstein RH. Regulation of type I collagen production by insulin and transforming growth factor-beta in human lung fibroblasts. Connective tissue research. 1996;34(1):53-62.

55. Trevisan R, Yip J, Sarika L, Li LK, Viberti G. Enhanced collagen synthesis in cultured skin fibroblasts from insulin-dependent diabetic patients with nephropathy. Journal of the American Society of Nephrology : JASN. 1997;8(7):1133-9.

56. Gore-Hyer E, Pannu J, Smith EA, Grotendorst G, Trojanowska M. Selective stimulation of collagen synthesis in the presence of costimulatory insulin signaling by connective tissue growth factor in scleroderma fibroblasts. Arthritis and rheumatism. 2003;48(3):798-806.

57. Musselmann K, Kane B, Alexandrou B, Hassell JR. Stimulation of collagen synthesis by insulin and proteoglycan accumulation by ascorbate in bovine keratocytes in vitro. Investigative ophthalmology & visual science. 2006;47(12):5260-6.

58. Wertheimer E, Spravchikov N, Trebicz M, Gartsbein M, Accili D, Avinoah I, et al. The regulation of skin proliferation and differentiation in the IR null mouse: implications for skin complications of diabetes. Endocrinology. 2001;142(3):1234-41.

59. Baltzis D, Eleftheriadou I, Veves A. Pathogenesis and treatment of impaired wound healing in diabetes mellitus: new insights. Advances in therapy. 2014;31(8):817-36.

60. Hanam SR, Singleton CE, Rudek W. The effect of topical insulin on infected cutaneous ulcerations in diabetic and nondiabetic mice. The Journal of foot surgery. 1983;22(4):298-301.

61. Belfield WO, Golinsky S, Compton MD. The use of insulin in open-wound healing. Veterinary medicine, small animal clinician : VM, SAC. 1970;65(5):455-60.

62. Weringer EJ, Kelso JM, Tamai IY, Arquilla ER. Effects of insulin on wound healing in diabetic mice. Acta endocrinologica. 1982;99(1):101-8.

63. Madibally SV, Solomon V, Mitchell RN, Van De Water L, Yarmush ML, Toner M. Influence of insulin therapy on burn wound healing in rats. The Journal of surgical research. 2003;109(2):92-100.

64. Apikoglu-Rabus S, Izzettin FV, Turan P, Ercan F. Effect of topical insulin on cutaneous wound healing in rats with or without acute diabetes. Clinical and experimental dermatology. 2010;35(2):180-5.

65. Wilson JM, Baines R, Babu ED, Kelley CJ. A role for topical insulin in the management problematic surgical wounds. Annals of the Royal College of Surgeons of England. 2008;90(2):160.

66. Lima MH, Caricilli AM, de Abreu LL, Araujo EP, Pelegrinelli FF, Thirone AC, et al. Topical insulin accelerates wound healing in diabetes by enhancing the AKT and ERK pathways: a double-blind placebo-controlled clinical trial. PLoS One. 2012;7(5):e36974.

67. Greenway SE, Filler LE, Greenway FL. Topical insulin in wound healing: a randomised, double-blind, placebo-controlled trial. Journal of wound care. 1999;8(10):526-8.

68. Rezvani O, Shabbak E, Aslani A, Bidar R, Jafari M, Safarnezhad S. A randomized, double-blind, placebo-controlled trial to determine the effects of topical insulin on wound healing. Ostomy/wound management. 2009;55(8):22-8.

69. Coid DR. Hypoglycaemia during treatment of decubitus ulcer with topical insulin. British medical journal. 1977;2(6094):1063-4.

70. Tang WJ. Targeting Insulin-Degrading Enzyme to Treat Type 2 Diabetes Mellitus. Trends Endocrinol Metab. 2016;27(1):24-34.

71. Mirsky IA, Perisutti G, Diengott D. Effect of insulinase-inhibitor on destruction of insulin by intact mouse. Proc Soc Exp Biol Med. 1955;88(1):76-8.

72. Miller BC, Eckman EA, Sambamurti K, Dobbs N, Chow KM, Eckman CB, et al. Amyloid-beta peptide levels in brain are inversely correlated with insulysin activity levels in vivo. Proc Natl Acad Sci U S A. 2003;100(10):6221-6.

73. Kuo WL, Montag AG, Rosner MR. Insulin-degrading enzyme is differentially expressed and developmentally regulated in various rat tissues. Endocrinology. 1993;132(2):604-11.

74. Shearer JD, Coulter CF, Engeland WC, Roth RA, Caldwell MD. Insulin is degraded extracellularly in wounds by insulin-degrading enzyme (EC 3.4.24.56). The American journal of physiology. 1997;273(4 Pt 1):E657-64.

75. Duckworth WC, Fawcett J, Reddy S, Page JC. Insulin-degrading activity in wound fluid. The Journal of clinical endocrinology and metabolism. 2004;89(2):847-51.

76. Durham TB, Toth JL, Klimkowski VJ, Cao JX, Siesky AM, Alexander-Chacko J, et al. Dual Exosite-binding Inhibitors of Insulin-degrading Enzyme Challenge Its Role as the Primary Mediator of Insulin Clearance in Vivo. J Biol Chem. 2015;290(33):20044-59.

77. Charton J, Gauriot M, Totobenazara J, Hennuyer N, Dumont J, Bosc D, et al. Structure-activity relationships of imidazole-derived 2-[N-carbamoylmethyl-alkylamino]acetic acids, dual binders of human insulin-degrading enzyme. European journal of medicinal chemistry. 2015;90:547-67.

78. Abdul-Hay SO, Bannister TD, Wang H, Cameron MD, Caulfield TR, Masson A, et al. Selective targeting of extracellular insulin-degrading enzyme by quasi-irreversible thiol-modifying inhibitors. ACS Chem Biol. 2015;10(12):2716-24.

79. Smith GP. Filamentous fusion phage: novel expression vectors that display cloned antigens on the virion surface. Science. 1985;228(4705):1315-7.

80. Cabrol C, Huzarska MA, Dinolfo C, Rodriguez MC, Reinstatler L, Ni J, et al. Small-molecule activators of insulin-degrading enzyme discovered through high-throughput compound screening. PLoS One. 2009;4(4):e5274.

81. Cheng Y, Prusoff WH. Relationship between the inhibition constant (K1) and the concentration of inhibitor which causes 50 per cent inhibition (I50) of an enzymatic reaction. Biochem Pharmacol. 1973;22(23):3099-108.

82. Gordon MK, Hahn RA. Collagens. Cell and tissue research. 2010;339(1):247-57.

83. Bannister TD, Wang H, Abdul-Hay SO, Masson A, Madoux F, Ferguson J, et al. ML345, A Small-Molecule Inhibitor of the Insulin-Degrading Enzyme (IDE). Probe Reports from the NIH Molecular Libraries Program. Bethesda (MD)2010.

84. Leissring MA, Selkoe DJ. Structural biology: enzyme target to latch on to. Nature. 2006;443(7113):761-2.

85. Singh A, Yadav S. Microneedling: Advances and widening horizons. Indian dermatology online journal. 2016;7(4):244-54.

86. Aust MC, Fernandes D, Kolokythas P, Kaplan HM, Vogt PM. Percutaneous collagen induction therapy: an alternative treatment for scars, wrinkles, and skin laxity. Plastic and reconstructive surgery. 2008;121(4):1421-9.

87. Fernandes D. Minimally invasive percutaneous collagen induction. Oral and maxillofacial surgery clinics of North America. 2005;17(1):51-63, vi.

88. Liang CC, Park AY, Guan JL. In vitro scratch assay: a convenient and inexpensive method for analysis of cell migration in vitro. Nature protocols. 2007;2(2):329-33.

89. Roth RA. In: Handbook of Proteolytic Enzymes. Barrett AJ, Rawlings, N.D., Woessner, J.F., editor. London: Elsevier; 2004.

90. Shen Y, Joachimiak A, Rosner MR, Tang WJ. Structures of Human Insulin-Degrading Enzyme Reveal a New Substrate Recognition Mechanism. Nature. 2006;443:870-4.

91. Manolopoulou M, Guo Q, Malito E, Schilling AB, Tang WJ. Molecular Basis of Catalytic Chamber-Assisted Unfolding and Cleavage of Human Insulin by Human Insulin-Degrading Enzyme. J Biol Chem. 2009;284:14177-88.

92. McCord LA, Liang WG, Dowdell E, Kalas V, Hoey RJ, Koide A, et al. Conformational States and Recognition of Amyloidogenic Peptides of Human Insulin-Degrading Enzyme. Proc Natl Acad Sci U S A. 2013;110:13827-32.

93. Tang WJ. Targeting Insulin-Degrading Enzyme to Treat Type 2 Diabetes Mellitus. Trends Endocrinol Metab. 2016;27:24-34.

94. Hersh LB. The Insulysin (Insulin Degrading Enzyme) Enigma. Cell Mol Life Sci. 2006;63:2432-4.

95. Tundo GR, Sbardella D, Ciaccio C, Grasso G, Gioia M, Coletta A, et al. Multiple Functions of Insulin-Degrading Enzyme: A Metabolic Crosslight? Crit Rev Biochem Mol Biol. 2017;52:554-82.

96. Duckworth WC, Kitabchi AE. Insulin and Glucagon Degradation by the Same Enzyme. Diabetes. 1974;23:536-43.

97. Farris W, Mansourian S, Chang Y, Lindsley L, Eckman EA, Frosch MP, et al. Insulin-Degrading Enzyme Regulates the Levels of Insulin, Amyloid Beta-Protein, and the Beta-Amyloid Precursor Protein Intracellular Domain in Vivo. Proc Natl Acad Sci U S A. 2003;100:4162-7.

98. Hayes MR, Mietlicki-Baase EG, Kanoski SE, De Jonghe BC. Incretins and Amylin: Neuroendocrine Communication between the Gut, Pancreas, and Brain in Control of Food Intake and Blood Glucose. Annu Rev Nutr. 2014;34:237-60.

99. Jiang G, Zhang BB. Glucagon and Regulation of Glucose Metabolism. Am J Physiol Endocrinol Metab. 2003;284:E671-8.

100. Kurochkin IV, Guarnera E, Berezovsky IN. Insulin-Degrading Enzyme in the Fight against Alzheimer's Disease. Trends Pharmacol Sci. 2018;39:49-58.

101. Malito E, Hulse RE, Tang WJ. Amyloid Beta-Degrading Cryptidases: Insulin Degrading Enzyme, Presequence Peptidase, and Peprilysin. Cell Mol Life Sci. 2008;65:2574-85.

102. Duckworth WC, Bennett RG, Hamel FG. Insulin Degradation: Progress and Potential. Endocr Rev. 1998;19:608-24.

103. Costes S, Butler PC. Insulin-Degrading Enzyme Inhibition, a Novel Therapy for Type 2 Diabetes? Cell Metab. 2014;20:201-3.

104. Deprez-Poulain R, Hennuyer N, Bosc D, Liang WG, Enee E, Marechal X, et al. Catalytic Site Inhibition of Insulin-Degrading Enzyme by a Small Molecule Induces Glucose Intolerance in Mice. Nat Commun. 2015;6:8250.

105. Leissring MA, Malito E, Hedouin S, Reinstatler L, Sahara T, Abdul-Hay SO, et al. Designed Inhibitors of Insulin-Degrading Enzyme Regulate the Catabolism and Activity of Insulin. PLoS One. 2010;5:e10504.

106. Cohen SM. A Bioinorganic Approach to Fragment-Based Drug Discovery Targeting Metalloenzymes. Acc Chem Res. 2017;50:2007-16.

107. Durham TB, Toth JL, Klimkowski VJ, Cao JX, Siesky AM, Alexander-Chacko J, et al. Dual Exosite-binding Inhibitors of Insulin-degrading Enzyme Challenge Its Role as the Primary Mediator of Insulin Clearance in Vivo. J Biol Chem. 2015;290:20044-59.

108. Charton J, Gauriot M, Totobenazara J, Hennuyer N, Dumont J, Bosc D, et al. Structure-Activity Relationships of Imidazole-Derived 2-[N-carbamoylmethyl-alkylamino]acetic acids, Dual Binders of Human Insulin-Degrading Enzyme. Eur J Med Chem. 2015;90:547-67.

109. Abdul-Hay SO, Bannister TD, Wang H, Cameron MD, Caulfield TR, Masson A, et al. Selective Targeting of Extracellular Insulin-Degrading Enzyme by Quasi-Irreversible Thiol-Modifying Inhibitors. ACS Chem Biol. 2015;10(12):2716-24.

110. Maianti JP, McFedries A, Foda ZH, Kleiner RE, Du XQ, Leissring MA, et al. Anti-Diabetic Activity of Insulin-Degrading Enzyme Inhibitors Mediated by Multiple Hormones. Nature. 2014;511:94-8.

111. Roth RA. Bacitracin: An Inhibitor of the Insulin Degrading Activity of Glutathione-Insulin Transhydrogenase. Biochem Biophys Res Commun. 1981;98:431-8.

112. Neant-Fery M, Garcia-Ordonez RD, Logan TP, Selkoe DJ, Li L, Reinstatler L, et al. Molecular Basis for the Thiol Sensitivity of Insulin-Degrading Enzyme. Proc Natl Acad Sci U S A. 2008;105:9582-7.

113. Agrawal A, Johnson SL, Jacobsen JA, Miller MT, Chen LH, Pellecchia M, et al. Chelator Fragment Libraries for Targeting Metalloproteinases. Chemmedchem. 2010;5:195-9.

114. Jacobsen JA, Fullagar JL, Miller MT, Cohen SM. Identifying Chelators for Metalloprotein Inhibitors Using a Fragment-Based Approach. J Med Chem. 2011;54:591-602.

115. Liu Z, Zhu H, Fang GG, Walsh K, Mwamburi M, Wolozin B, et al. Characterization of Insulin Degrading Enzyme and Other Amyloid-Beta Degrading Proteases in Human Serum: A Role in Alzheimer's Disease? J Alzheimers Dis. 2012;29:329-40.

116. Pearson RG. Hard and Soft Acids and Bases. J Am Chem Soc. 1963;85:3533-9.

117. Pearson RG. Hard and Soft Acids and Bases HSAB.1. Fundamental Principles. J Chem Educ. 1968;45(9):581-7.

118. Jones RA, Katritzky AR. N-Oxides and Related Compounds .17. The Tautomerism of Mercapto-Pyridine and Acylamino-Pyridine 1-Oxides. J Chem Soc. 1960(Jul):2937-42.

119. Adamek RN, Credille CV, Dick BL, Cohen SM. Isosteres of Hydroxypyridinethione as Drug-like Pharmacophores for Metalloenzyme Inhibition. J Biol Inorg Chem. 2018;23:1129-38.

120. Vilar S, Cozza G, Moro S. Medicinal chemistry and the molecular operating environment (MOE): application of QSAR and molecular docking to drug discovery. Curr Top Med Chem. 2008;8(18):1555-72.

121. Hay DL, Chen S, Lutz TA, Parkes DG, Roth JD. Amylin: Pharmacology, Physiology, and Clinical Potential. Pharmacol Rev. 2015;67(3):564-600.

122. Bishoyi AK, Roham PH, Rachineni K, Save S, Hazari MA, Sharma S, et al. Human islet amyloid polypeptide (hIAPP) - a curse in type II diabetes mellitus: insights from structure and toxicity studies. Biol Chem. 2020.

123. Raimundo AF, Ferreira S, Martins IC, Menezes R. Islet Amyloid Polypeptide: A Partner in Crime With Abeta in the Pathology of Alzheimer's Disease. Front Mol Neurosci. 2020;13:35.

124. Fernandez-Diaz CM, Merino B, Lopez-Acosta JF, Cidad P, de la Fuente MA, Lobaton CD, et al. Pancreatic beta-cell-specific deletion of insulin-degrading enzyme leads to dysregulated insulin secretion and beta-cell functional immaturity. Am J Physiol Endocrinol Metab. 2019;317(5):E805-E19.

125. Steneberg P, Bernardo L, Edfalk S, Lundberg L, Backlund F, Ostenson CG, et al. The type 2 diabetes-associated gene ide is required for insulin secretion and suppression of alpha-synuclein levels in beta-cells. Diabetes. 2013;62(6):2004-14.

126. Villa-Perez P, Merino B, Fernandez-Diaz CM, Cidad P, Lobaton CD, Moreno A, et al. Liver-specific ablation of insulin-degrading enzyme causes hepatic insulin resistance and glucose intolerance, without affecting insulin clearance in mice. Metabolism. 2018;88:1-11.

127. Merino B, Fernandez-Diaz CM, Parrado-Fernandez C, Gonzalez-Casimiro CM, Postigo-Casado T, Lobaton CD, et al. Hepatic insulin-degrading enzyme regulates glucose and insulin homeostasis in diet-induced obese mice. Metabolism. 2020;113:154352.

CHAPTER 5

CONCLUSIONS

5.1 Concluding remarks

Alzheimer disease (AD) is an incredibly complex disease that currently affects over 30 million people worldwide (1, 2), and there is a vital need for advancements in biomarker development, diagnostics, and therapeutics, as well as in our basic understanding of the cause(s) of late-onset AD (LOAD) in particular. The work in this dissertation has focused on key regulators of amyloid β-protein (Aβ)—Aβ-degrading proteases (AβDPs)—both as possible candidates for LOAD risk and also as tools for addressing specific mechanistic hypotheses about the disease. Although therapeutics targeting Aβ have so far proven unsuccessful in clinical tests of patients already showing symptoms, there remains incontrovertible evidence implicating a causal role in the etiology the disease. Given that Aβ can accumulate >20 years before cognitive changes are identified (3), it is becoming increasingly urgent to explore what changes are mediated by Aβ at earlier time frames in the course of the disease. Understanding how non-genetic risk-factors for AD, such as head injury, affect Aβ proteostasis promises to yield fresh insights into the molecular pathogenesis of LOAD, and could lead to new prophylactic uses for existing Aβ-lowering therapeutics.

The work in this dissertation focused on AβDPs, a relatively poorly understood aspect of AD pathogenesis. This is evidenced most strikingly by our discovery of CatD as a major AβDP, which has emerged a full 20 years after *in vivo* validation of the first AβDP, neprilysin (4). By several measures, CatD is the most impactful regulator of cerebral Aβ levels yet identified, and yet this key role had gone unrecognized for decades. CatD's role in Aβ proteostasis is not only significant from a sheer quantitative perspective, but also more qualitatively; our finding that CatD

can regulate Aβ42/40 ratios reveals a novel and wholly unexpected mechanism by which this critical parameter can be regulated. In addition, the finding that CatD regulates lysosomal pools of Aβ holds significance because it demonstrates that a significant portion of newly synthesized Aβ is trafficked to lysosomes; heretofore Aβ was widely considered as primarily a secreted protein, so this finding truly advances our basic understanding of the fundamental biology of Aβ proteostasis.

The work in this dissertation also highlights the value of utilizing AβDPs as powerful tools for investigating AD pathogenesis. First, in Aim 1 inhibition of AβDPs was used as tool to reversibly increase cerebral Aβ levels and, thereby, investigate the specific mechanistic hypothesis that acute increases in Aβ can trigger LOAD in the context of aging (and in the absence of EOAD mutations). Second, our discovery in Aim 2 of CatD as a major intracellular AβDP can also be construed as the development of a new tool. Because CatD's effect was limited so exclusively to lysosomal Aβ, it becomes possible to selectively manipulate this pool by targeting CatD; this, in turn, makes it feasible for the first time to experimentally address key questions about the relative importance of this pool of Aβ. Finally, the value of AβDPs as experimental tools is frequently dependent on reagents that can manipulate them, and Aim 3 was focused on developing substrate-selective IDE modulators. IDE degrades both Aβ and insulin and consequently is implicated in the pathogenesis of both AD and diabetes. To properly assess IDE's role in AD, tools that can selectively alter its ability to degrade Aβ are needed, and the assays we developed, as well as the novel IDE inhibitors we discovered with them, help advance this long-term objective.

5.2 Future directions

Several aspects of this body of work warrant further investigation. From Aim 1, we learned that the hAβ-KI mouse line successfully models what occurs following brain injury in humans—namely a transient elevation of cerebral Aβ. This finding augurs well for the use of this model and other APP-KI models similar to it, to uncover the molecular mechanisms underlying various AD risk factors. On the other hand, this model failed to develop Aβ plaques up to 22 months of age, despite the induction of large elevations in cerebral Aβ lasting 4 weeks. Problematically, it is difficult to disentangle whether the failure to develop plaques was the fault of the treatment or the model itself. With respect to the treatment, it is notable that phosphoramidon treatment resulted in larger effects on shorter, less amyloidogenic Aβ species, than on more amyloidogenic Aβ42 peptide, resulting in reductions, for example, in the Aβ42/40 ratio (whereas the opposite was seen with head injury in the same model). It is conceivable that elevations in Aβ per se might not be sufficient to trigger amyloidogenesis, requiring instead appreciable increases in the Aβ42/40 ratio. On the other hand, the hAβ-KI line might not be sufficiently aggressive to trigger amyloid deposition. In this regard, it is notable that a very similar APP knock-in model featuring the Swedish double mutation (NL) that increases Aβ production 2-fold also fails to develop amyloid deposits(5). On the other hand, adding the Iberian (F) mutations to the Swedish mutation, which increases the Aβ42/40 ratio, leads to reliable amyloidogenesis when two copies are present (6). We propose that to faithfully model LOAD, a balance must be struck between models that are insufficiently aggressive and those that develop plaques inexorably. In this regard, it is notable that mice with just one copy of the NL-F APP knock-in allele develop diffuse plaques by 24 months of age, then go on to develop only modest amounts of dense-core plaques by 30 months of age.

This temporal sequence resembles what occurs in normal human aging, and so might be an ideal model for testing factors that trigger or modulate the risk for LOAD.

From our second Aim, we conclusively demonstrated that CatD is a major AβDP, with a knock-out mouse line accumulating drastic levels of Aβ in a very short time frame. Unfortunately, global deletion of CatD also causes premature lethality. Consequently, we advise further experimentation using conditional—and preferably reversible—approaches, which could be done either with genetic methods or via the development of selective CatD inhibitors. With regards to our third Aim, we strongly encourage continuing the efforts to develop substrate-selective IDE modulators. These research directions are incredibly promising; elucidating how early Aβ accumulation affects AD risk hold great promise both for advancing our fundamental understanding of AD pathogenesis and also for developing effective therapies targeting this devastating disease of brain and mind.

5.3 References

1. Alzheimer's A. 2012 Alzheimer's disease facts and figures. Alzheimers Dement. 2012;8(2):131-68.

2. Hebert LE, Scherr PA, Bienias JL, Bennett DA, Evans DA. Alzheimer Disease in the US Population Prevalence Estimates Using the 2000 Census. Arch Neurol. 2003;60(8):1119-22.

3. Sperling RA, Aisen PS, Beckett LA, Bennett DA, Craft S, Fagan AM, et al. Toward defining the preclinical stages of Alzheimer's disease: recommendations from the National Institute on Aging-Alzheimer's Association workgroups on diagnostic guidelines for Alzheimer's disease. Alzheimers Dement. 2011;7(3):280-92.

4. Iwata N, Tsubuki S, Takaki Y, Watanabe K, Sekiguchi M, Hosoki E, et al. Identification of the major Abeta1-42-degrading catabolic pathway in brain parenchyma: suppression leads to biochemical and pathological deposition. Nat Med. 2000;6(2):143-50.

5. Tambini MD, Yao W, D'Adamio L. Facilitation of glutamate, but not GABA, release in Familial Alzheimer's APP mutant Knock-in rats with increased beta-cleavage of APP. Aging Cell. 2019;18(6):e13033.

6. Saito T, Matsuba Y, Mihira N, Takano J, Nilsson P, Itohara S, et al. Single App knock-in mouse models of Alzheimer's disease. Nat Neurosci. 2014;17(5):661-3.

APPENDICES

LIST OF SUPPLEMENTAL FIGURES

LIST OF SUPPLEMENTAL TABLES

APPENDIX A

CHAPTER 2 SUPPLEMENTAL FIGURES

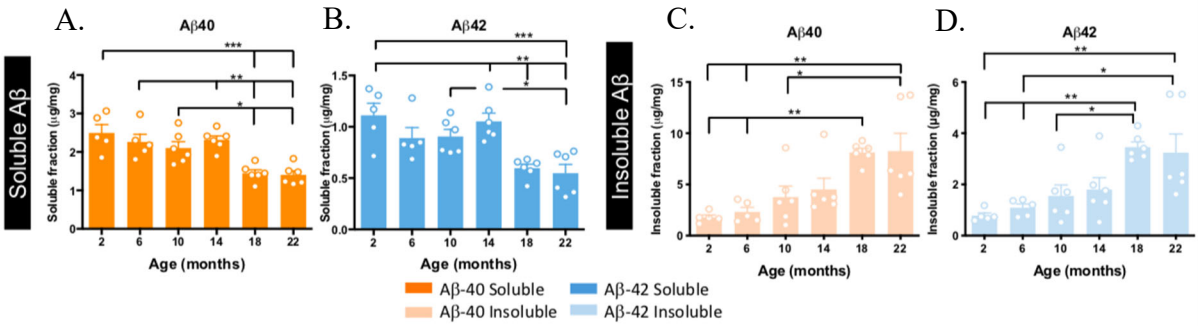

Figure S2.1. Changes in Aβ levels as a function of age in the hAβ-KI mouse line. ***A-B***, Levels of soluble Aβ40 (***A***) and Aβ42 (***B***) across age. ***C-D***, Levels of insoluble Aβ40 (***C***) and Aβ42 (***D***) across age. Note the significant decrease in soluble Aβ and increase in insoluble Aβ emerging at 18 months of age. **P*<0.05; ***P* <0.01; ****P* <0.001.

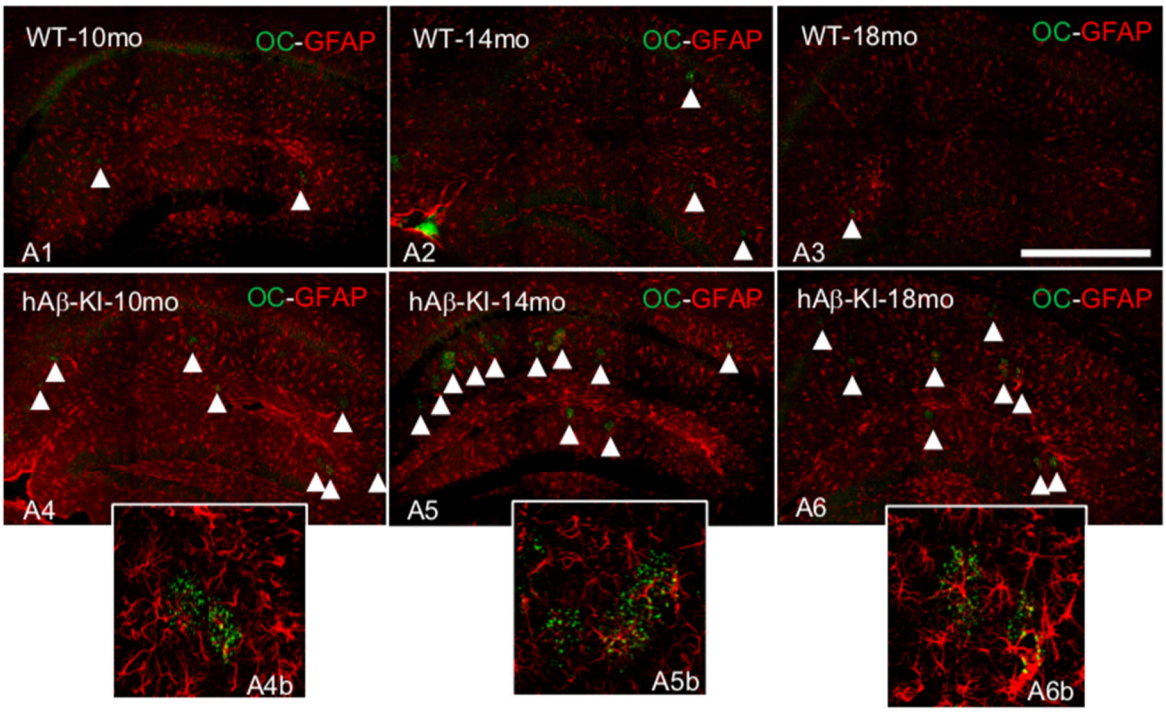

Figure S2.2. Association of Aβ fibrils with GFAP-labeled astrocytes. ***A1-A3***, Staining for Aβ fibrils with the OC antibody (green) and astrocytes with a GFAP antibody (red) in brain sections from 10- (***A1***), 14- (***A2***) and 18- (***A3***) month-old wildtype (WT) mice. Note the minimal Aβ fibril staining present (arrow heads). ***A4-A6***, Similar staining for Aβ fibrils in 10- (***A4***), 14- (***A5***) and 18- (***A6***) month-old hAβ-KI mice. Note the increased Aβ fibril staining present (arrow heads). ***A4b-A6b***, Higher magnification images of the association of OC fibrils with GFAP-labelled astrocytes in 10- (***A4b***), 14- (***A5b***) and 18- (***A6b***) month-old hAβ-KI mice.

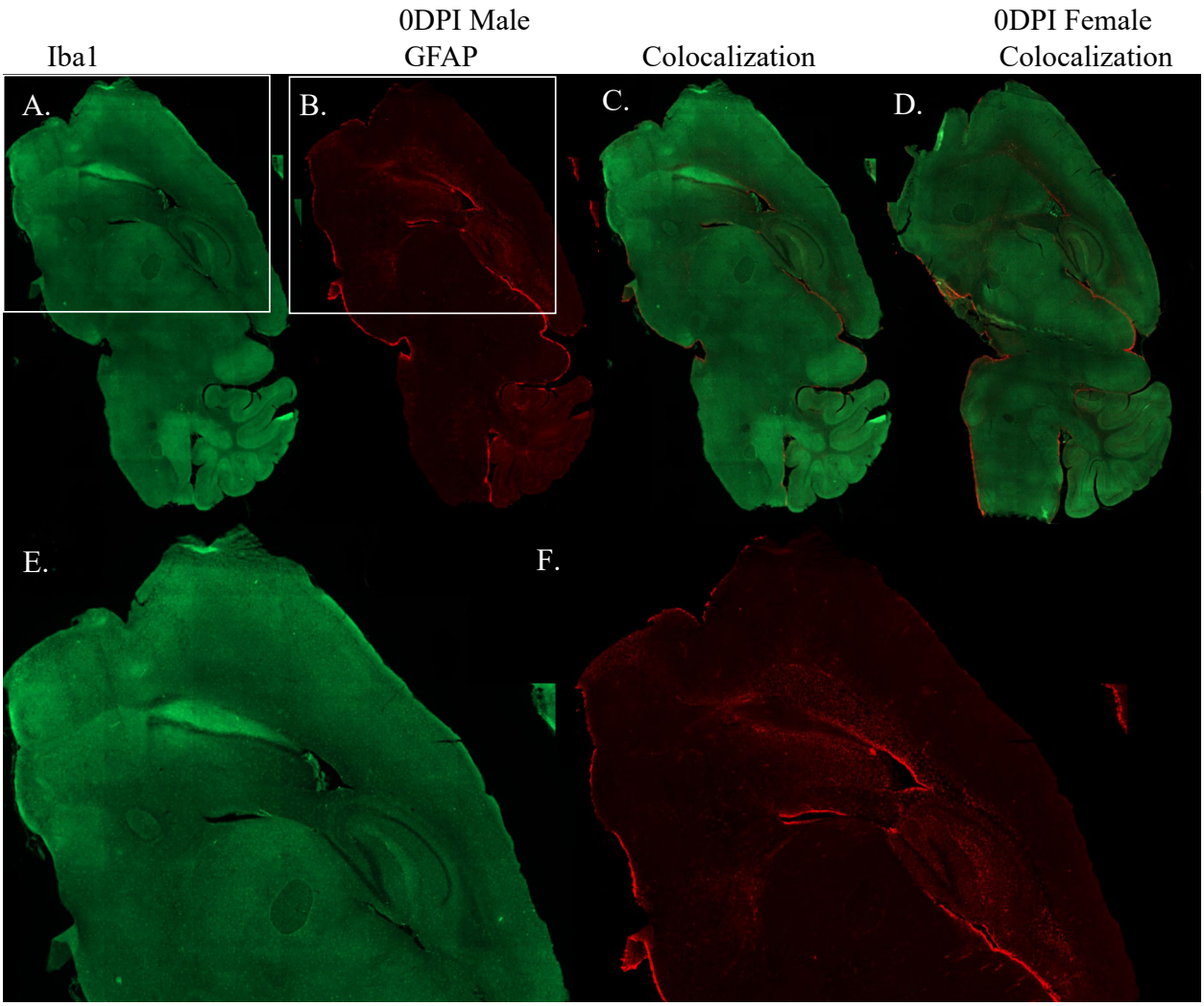

Figure S2.3. Microglia and astrocytes in uninjured hAβ-KI 6-month mice. ***A***, Microglia stained with Iba1 antibody (green) in uninjured male animals. ***B***, Astrocytes stained with GFAP antibody (red) in the same animal. ***C***, Merged image of ***A*** and ***B***. ***D***, Similar merged image in female uninjured animals. ***E,F***, Higher magnification view of Iba1 staining and GFAP (***F***) staining.

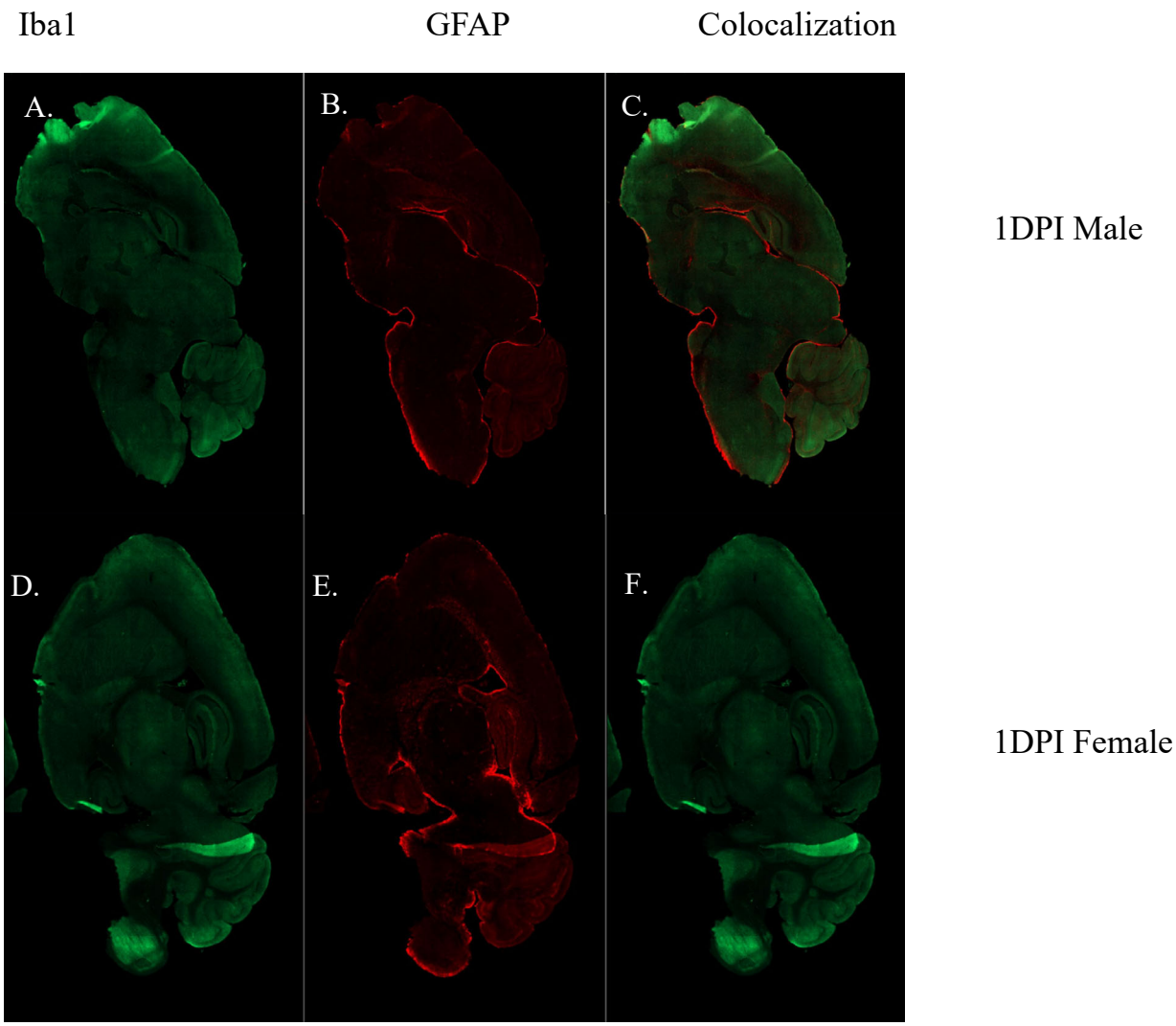

Figure S2.4. Microglia and astrocytes following sCHI in hAβ-KI 6-month mice 1DPI. ***A-C***, Sagittal sections of brains from a male 6-month old hAβ-KI mouse stained for microglia (***A***, green), astrocytes (***B***, red) or both (***C)***. ***D-F***, Similar images for a female hAβ-KI mouse brain.

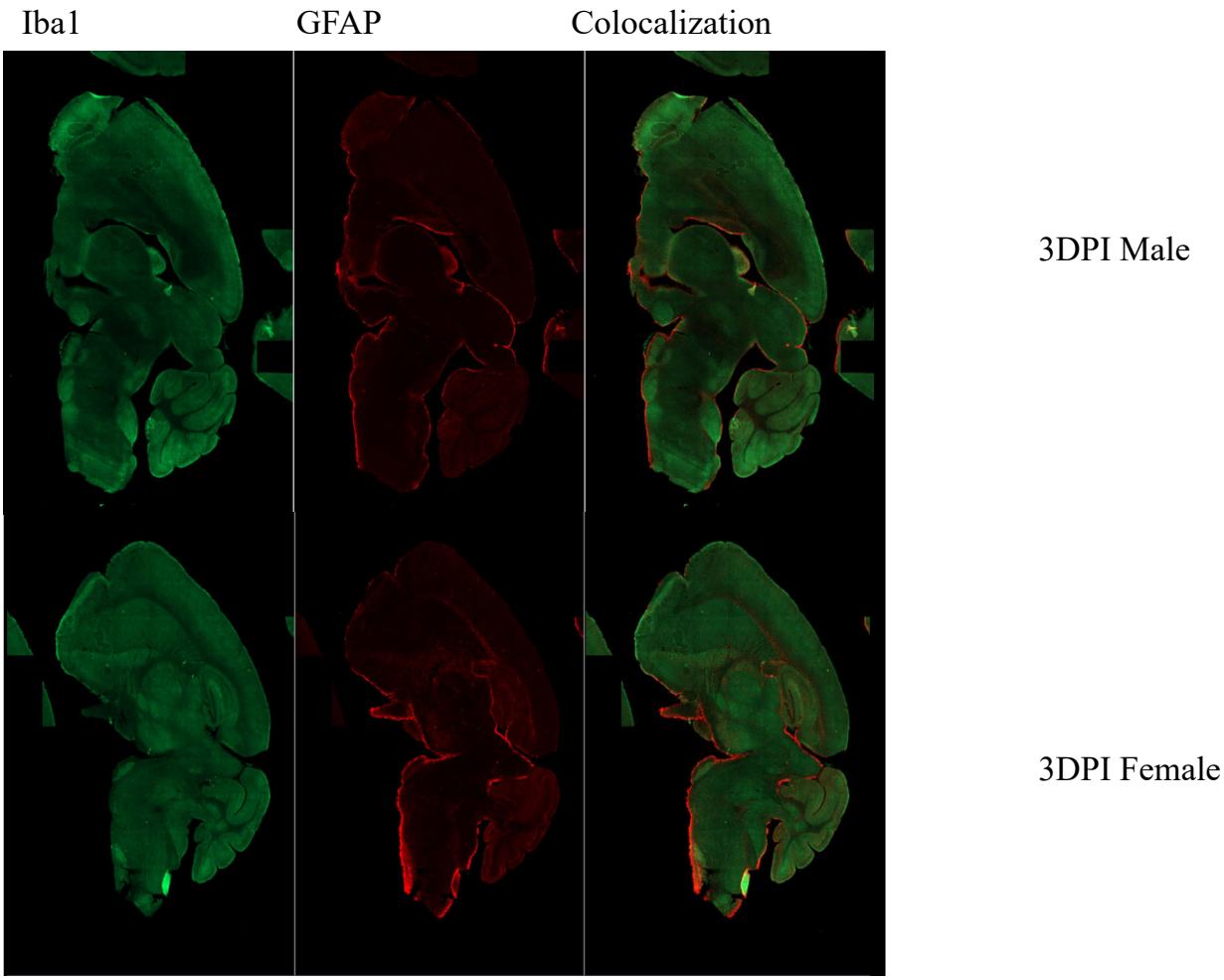

Figure S2.5. Microglia and astrocytes following sCHI in hAβ-KI 6-month mice 3DPI. ***A-C***, Sagittal sections of brains from a male 6-month old hAβ-KI mouse stained for microglia (***A***, green), astrocytes (***B***, red) or both (***C)***. ***D-F***, Similar images for a female hAβ-KI mouse brain.

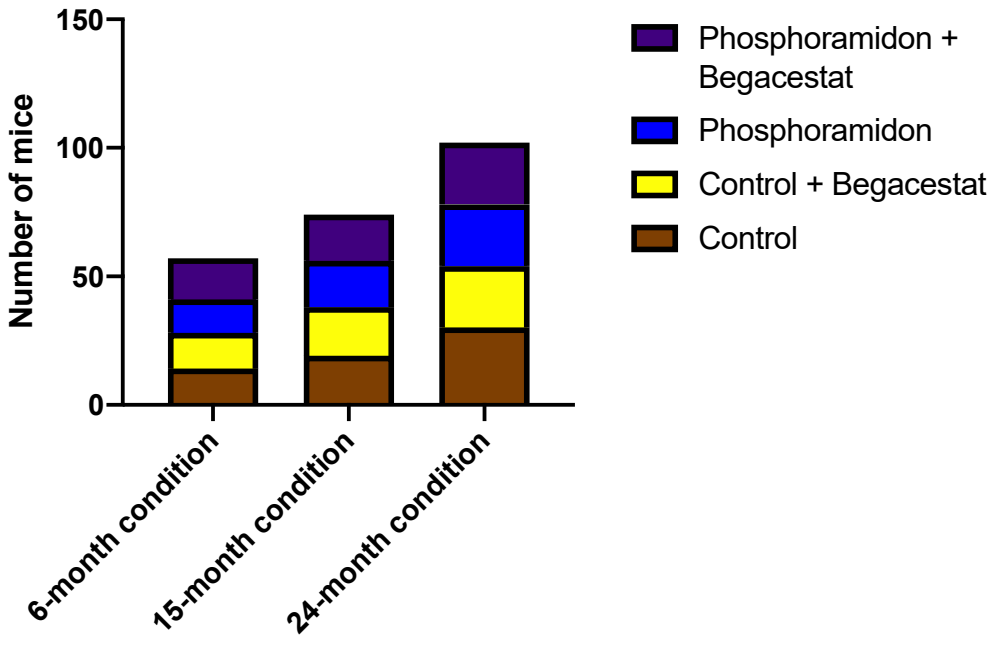

Figure S2.6. Number of mice in each treatment condition and time point of tissue collection.

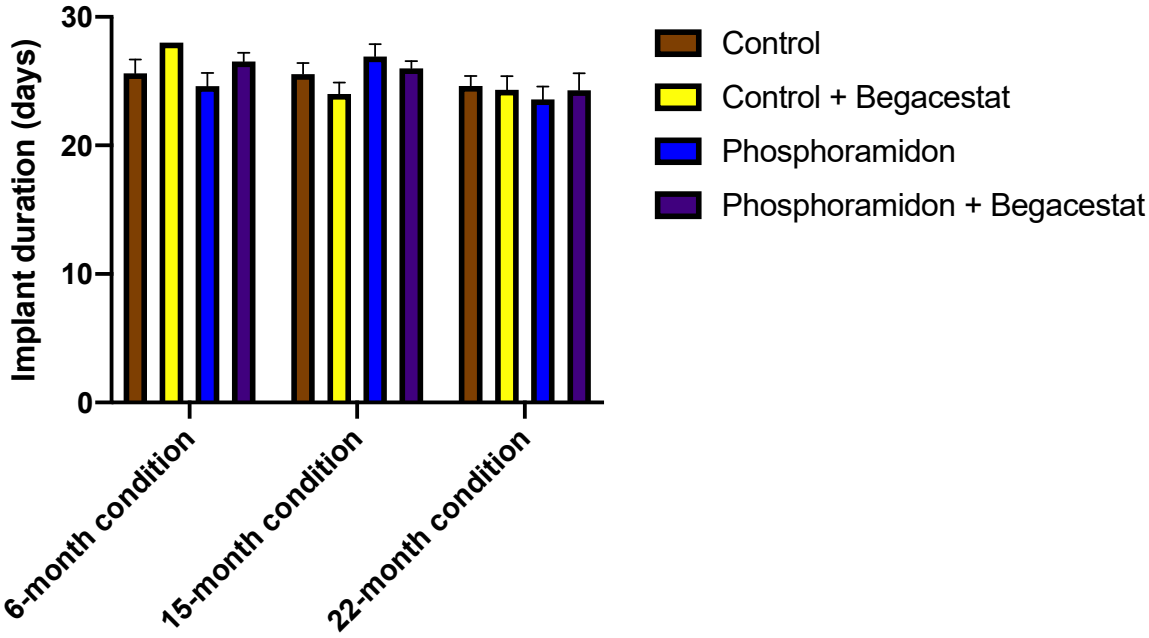

Figure S2.7. Average duration of implantation of mini-osmotic pump in brain. No significant differences are found between the treatment durations of ages or conditions.

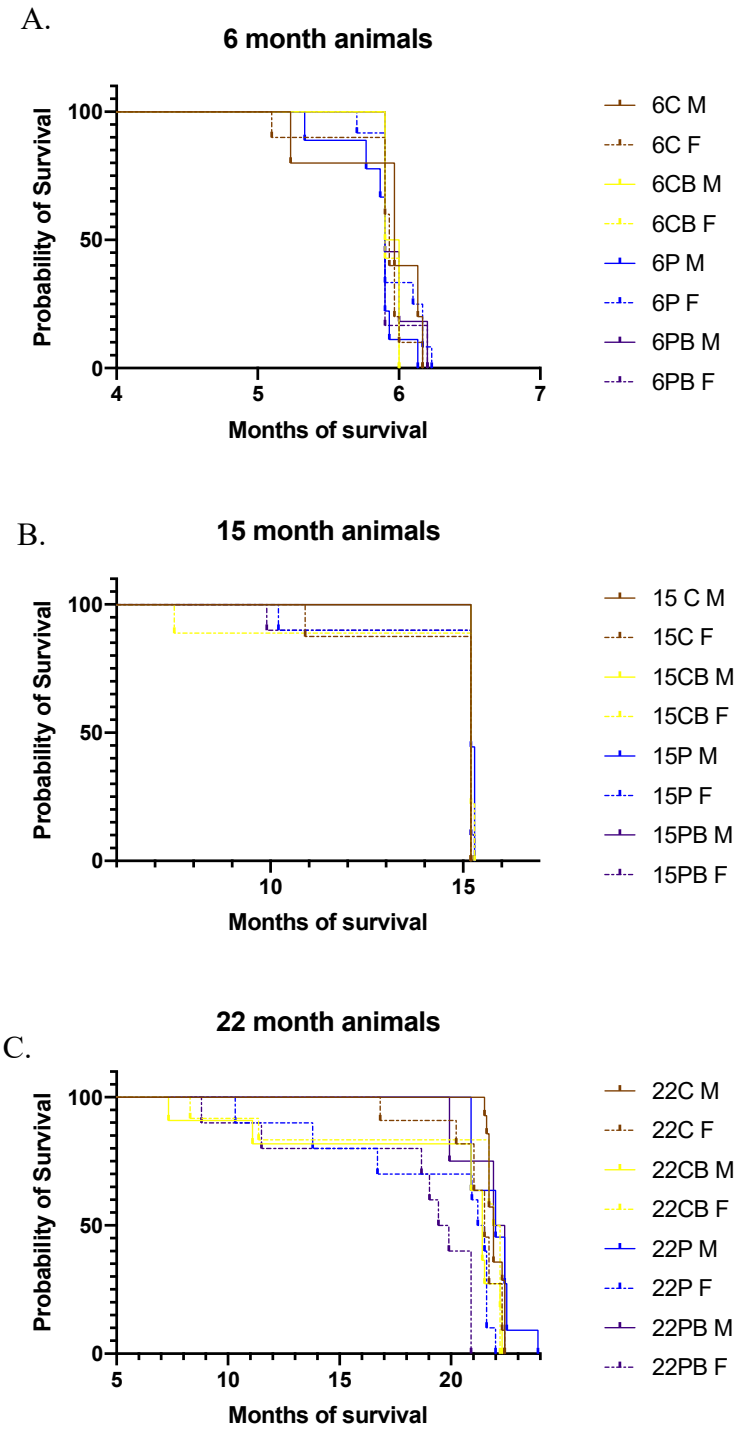

Figure S2.8. Survival graphs of treated hAβ-KI mice from Aim 1B. ***A-C***, Kaplan-Meier plots of survival in male vs. female mice in different treatment groups and in the 6- (***A***), 15- (***B***), and 22- (***C***) month collection time points. Note that all animals were administered compounds (or vehicle) for 4-weeks beginning at 5 months of age. Significant differences were observed between groups in the 22- (but not the 6- or 15-) month collection time, with females dying at a faster rate than males regardless of treatment condition. C =vehicle only (control); CB = begacestat only; P = phosphoramidon only; PB = phosphoramidon plus begacestat.

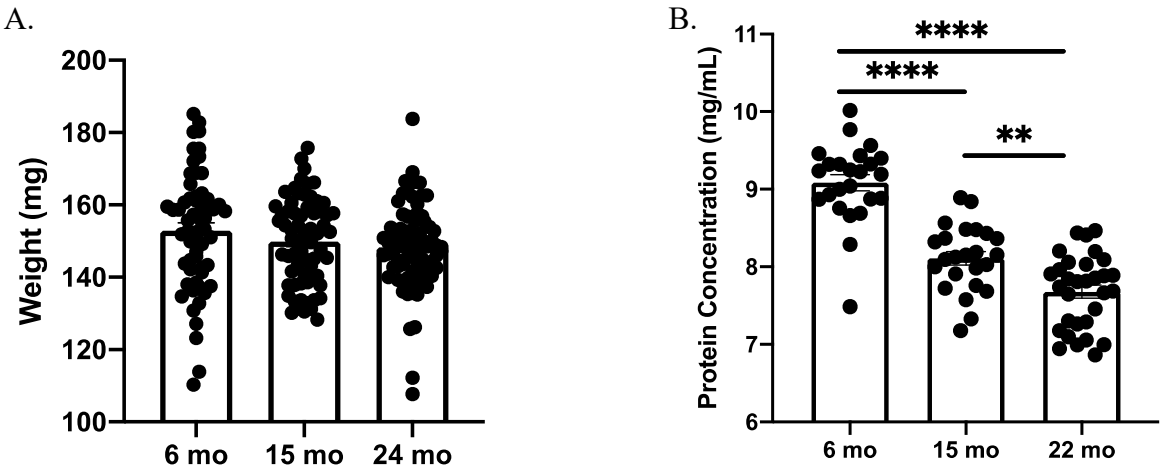

Figure S2.9. Brain weights per hemisphere and soluble protein levels in treated hAβ-KI mice from Aim 1B. ***A***, Weights of flash-frozen brain hemispheres from treated mice collected at the indicated ages. No significant differences were observed.; ***B***, Protein levels (determined by nanodrop) in soluble fractions after extraction for biochemical analysis from treated mice collected at the indicated ages. **P*<0.05; ***P* <0.01; ****P* <0.001; *****P* <0.0001.

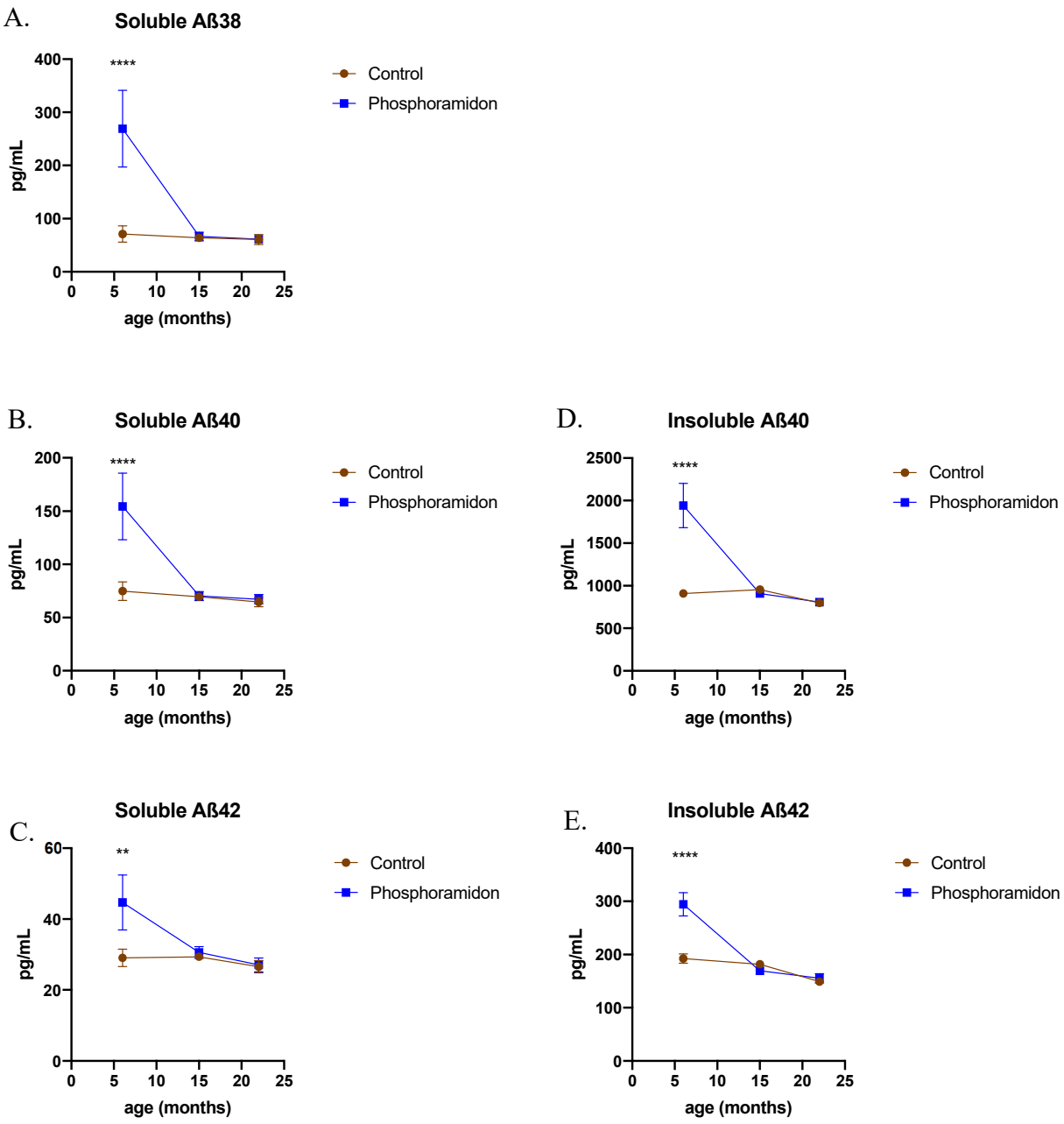

Figure S2.10. Effects of phosphoramidon treatment on individual Aβ species as a function of age. ***A-C***, Levels of soluble Aβ38 (***A***), Aβ40 (***B***), and Aβ42 (***C***) in phosphoramidon- vs. vehicle-treated (Control) hAβ-KI mice. Note that significant increases in soluble Aβ species were present in phosphoramidon-treated mice only at immediately after the treatment (6-month collection time). with no significant changes at later ages; ***D-E***, Levels of insoluble Aβ40 (***D***) and€42 (***E***) in phosphoramidon-treated hAβ-KI mice vs. controls. Again, there was a significant elevation in insoluble Aβ40 and Aβ42 in phosphoramidon-treated mice at 6 months, with no significant differences at 15 or 22 months. *$P< 0.05$; ** $P< 0.01$; *** $P< 0.001$; ****$P< 0.0001$.

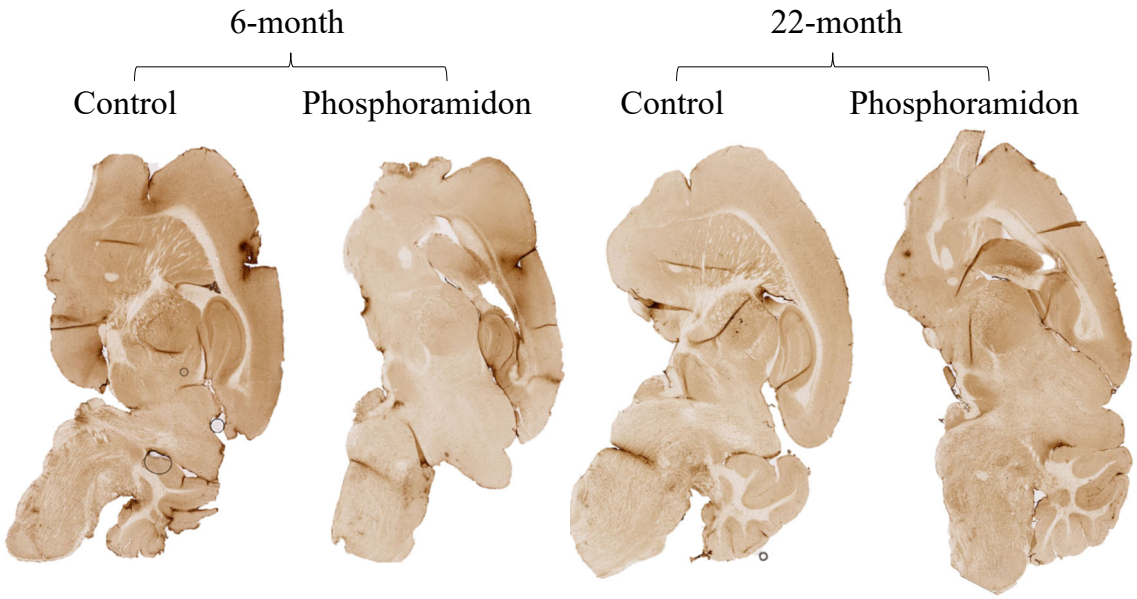

Figure S2.11. Aβ/APP staining in 6- and 22-month-old phosphoramidon-treated hAβ-KI mice and age-matched controls. Sagittal sections of hAβ-KI brains stained with the 6E10 antibody that recognizes human Aβ, holo-APP and Aβ-containing fragments of APP. Note the lack of diffuse or neuritic plaques.

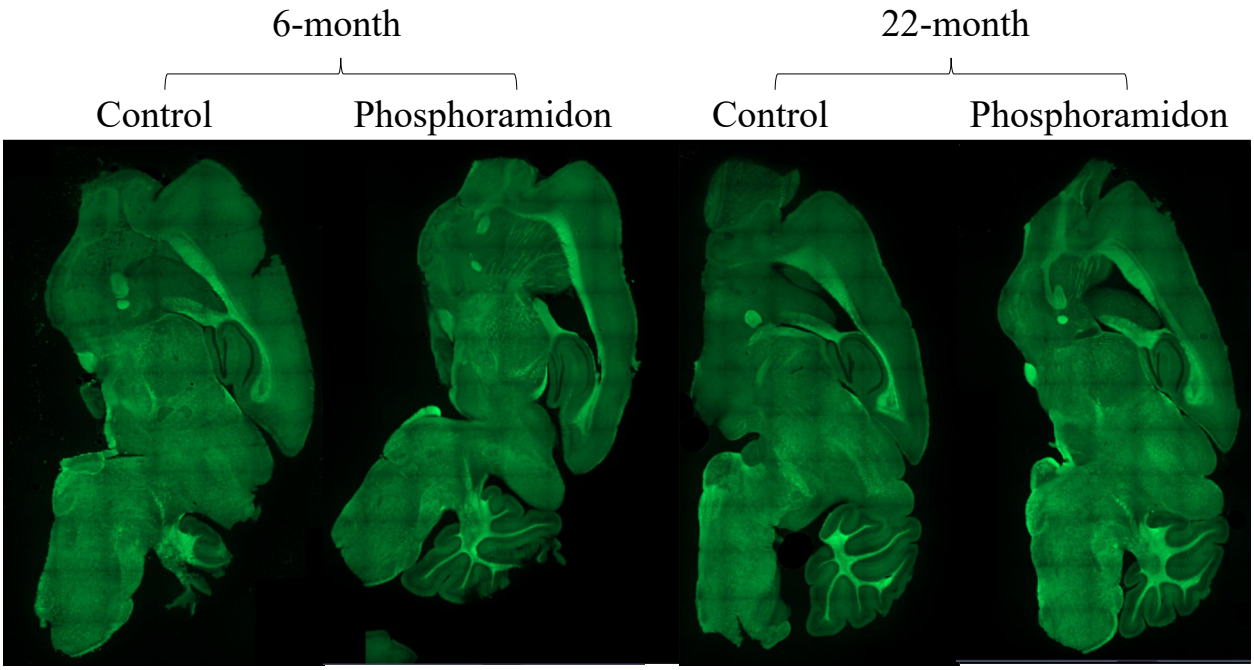

Figure S2.12. Amyloid staining by thioflavin S in 6- and 22-month-old phosphoramidon-treated hAβ-KI mice and age-matched controls. Sagittal sections of hAβ-KI brains stained with Thio S, a histological stain for beta-pleated sheets such as that found in dense-core plaques and other mature amyloid deposits. Note the absence of amyloid plaques.

APPENDIX B

CHAPTER 3 SUPPLEMENTAL FIGURES

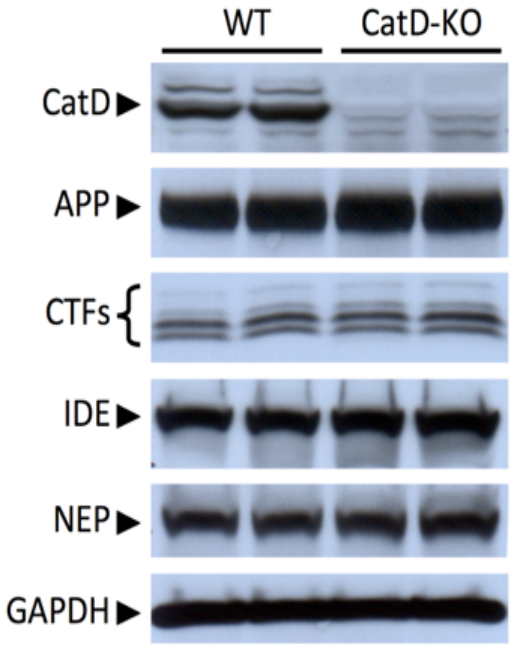

Figure S3.1. The mechanism by which CatD regulates Aβ levels does not involve effects on APP, Aβ production or known Aβ-degrading proteases. Figure shows relative levels of CatD, the amyloid precursor protein (APP), C-terminal fragments of the latter (CTFs) that include the immediate precursors to Aβ, insulin-degrading enzyme (IDE), neprilysin (NEP) and, as a loading control, GAPDH.

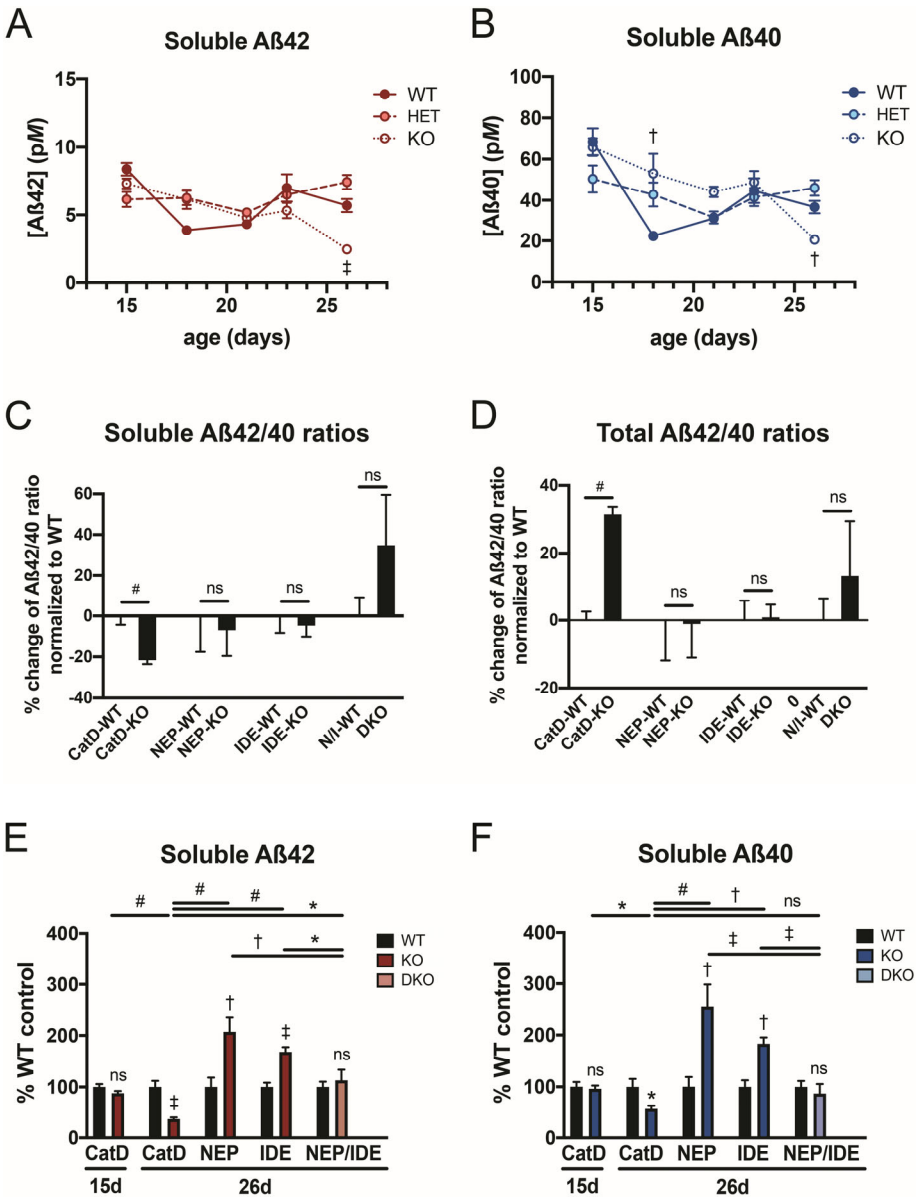

Figure S3.2. Soluble Aβ42 and Aβ40 levels in CatD-KO, -HET and -WT brains. ***A***,***B***, Levels of soluble, endogenous brain Aβ42 (***A***) and Aβ40 (***B***) in CatD-KO, -HET and -WT mice as a function of age. Data are mean ± SEM for 4-6 replicates per group. $^{\dagger}P<0.01$; $^{\ddagger}P<0.001$. ***C***,***D***, Soluble Aβ42/40 ratios (***C***) are significantly decreased in CatD-KO mice relative to WT controls, whereas total (combined soluble and insoluble Aβ) Aβ42/40 ratios are increased (***D***). Note that both soluble and total Aβ42/40 ratios are not significantly changed in NEP-KO, IDE-KO or NEP/IDE-DKO mice relative to their line-specific WT controls. Data are mean ± SEM for 28-30 replicates per group for CatD-KO and -WT mice and 5-11 replicates per group for the other genotypes. $^{\#}P<0.0001$. ***E***,***F***, Levels of soluble, endogenous brain Aβ42 (***E***) and Aβ40 (***F***) in 15- and 26-d-old CatD-KO mice as compared to 26-d-old NEP-KO IDE-KO and NEP/IDE-DKO mice and their respective controls. Data are mean ± SEM for 4-6 replicates per group. $^{*}P<0.05$; $^{\dagger}P<0.01$; $^{\ddagger}P<0.001$; $^{\#}P<0.0001$.

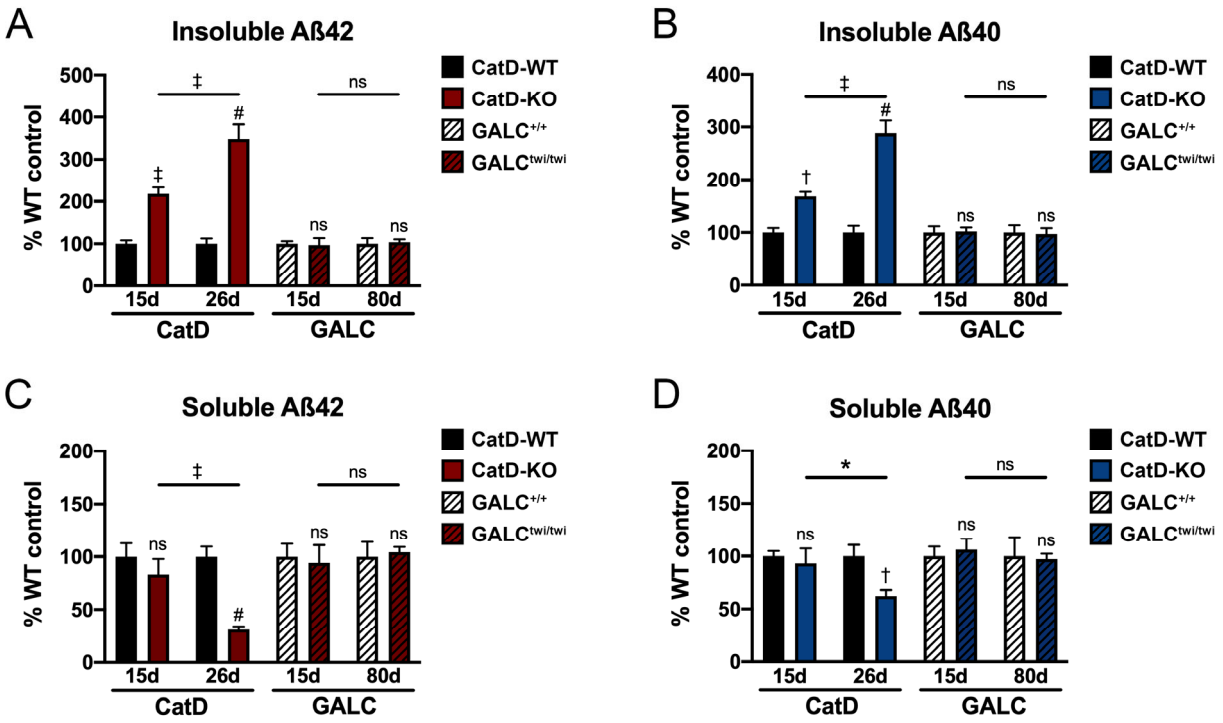

Figure S3.3. Cerebral Aβ levels are unchanged in another mouse model featuring profound lysosomal dysfunction and premature lethality. ***A***,***D,*** Levels of endogenous insoluble Aβ42 (***A***) and Aβ40 (***B***) as well as soluble Aβ42 (***C***) and Aβ40 (***D***) in CatD-KO and GALC$^{twi/twi}$ (*Twitcher* mouse) brains relative to strain-specific WT littermate controls at different ages. Note that GALC$^{twi/twi}$ mice at 80 d of age are at a similar state of moribundity as CatD-KO mice at 26 d of age. Data are mean ± SEM for 6 replicates per group. *P<0.05; $^{\dagger}P$<0.01; $^{\ddagger}P$<0.001; $^{\#}P$<0.0001.

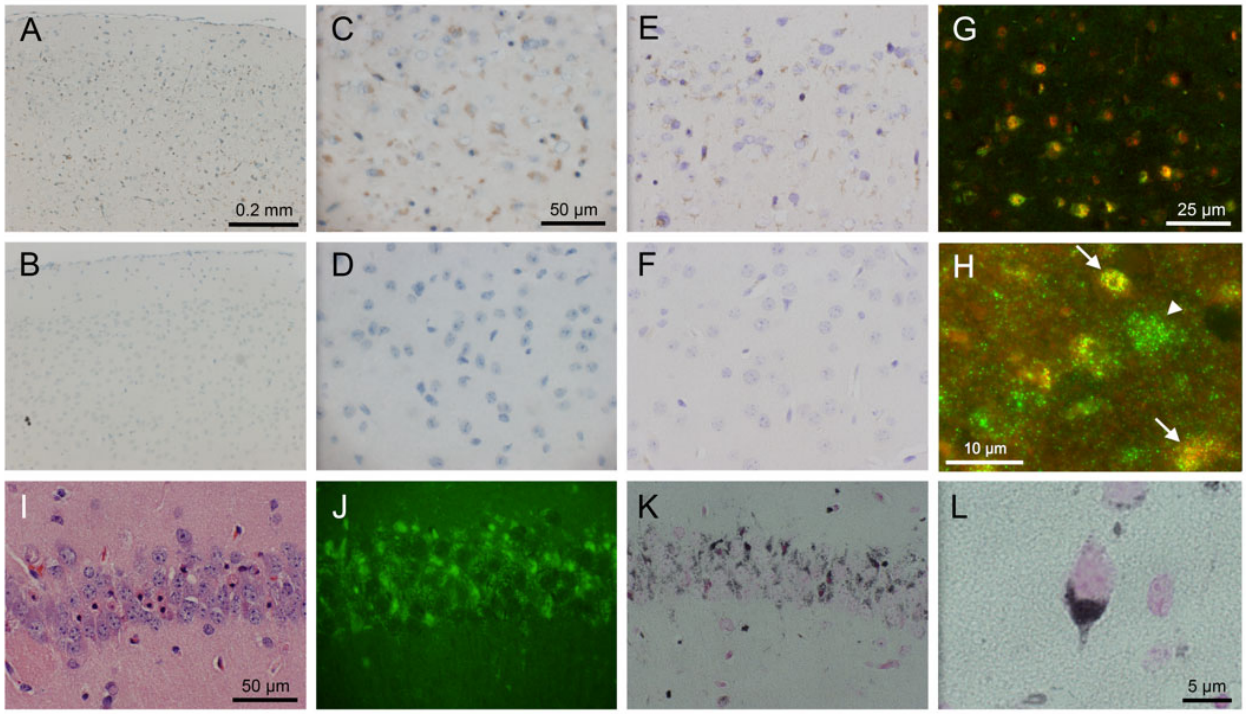

Figure S3.4. Immunohistochemical analysis shows selective accumulation of Aβ42 in lysosomes and other intracellular compartments of CatD-KO mice by 3 weeks of age. ***A*-*F***, Intracellular accumulation of Aβ42 detected in brains of CatD-KO (***A***, ***C***, ***E***) but not WT (***B***, ***D***, ***F***) mice using well-characterized end-specific antibodies from Wako (***A*-*D***) and Mayo Clinic (***E***,***F***). ***G***,***H***, Colocalization of Aβ42 (*red*) and the lysosomal marker Lamp2 (*green*) in cortical layers III – V of CatD-KO brain. ***H***, Higher resolution image showing that the overlap between Aβ42 and Lamp2 in some cells (*arrows*); notably, a subset of cells show no deposition of Aβ42 (*arrowhead*). ***I*-*L***, Hippocampal CA1 pyramidal layer in a 3-week-old CatD-KO mouse stained with hematoxylin and eosin (***I***), thioflavin S (***J***), and Gallyas silver stain (***K***,***L***). Note the presence of pyknotic cells with condensed nuclei (***I***) and the accumulation of thioflavin- (***J***) and Gallyus- (***K***,***L***) positive staining in perinuclear regions of pyramidal neurons.

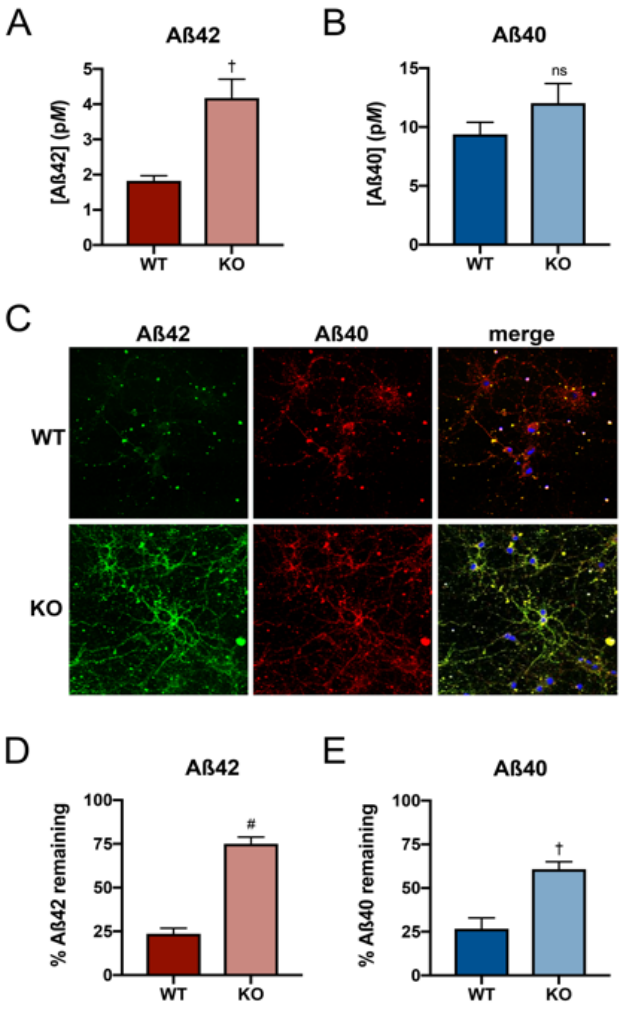

Figure S3.5. Studies in primary embryonic cultured neurons. ***A***,***B***, Aβ42 (***A***) and Aβ40 (***B***) levels in the conditioned medium of cultured neurons from CatD knockout (KO) mice and wildtype (WT) controls. Note that KO neurons secrete significantly more Aβ42 than WT controls (***A***) and, although a trend towards higher Aβ40 levels is evident, it does not achieve statistical significance. Data are mean ± SEM for 4 replicates. $^{\dagger}P<0.01$. ***C***, Representative images of exogenously applied, fluorescently tagged Aβ42 (*green*) or Aβ40 (*red*) remaining in WT and KO cultured neurons after loading and subsequent 2-h incubation (see *Supplemental Methods* for details). ***D***,***E***, Percent Aβ42 (***D***) and Aβ40 (***E***) remaining after 2-h incubation, relative to freshly loaded neurons immediately after washing. Data are mean ± SEM for 6 replicates. $^{\#}P<0.0001$; $^{\dagger}P<0.01$.

A

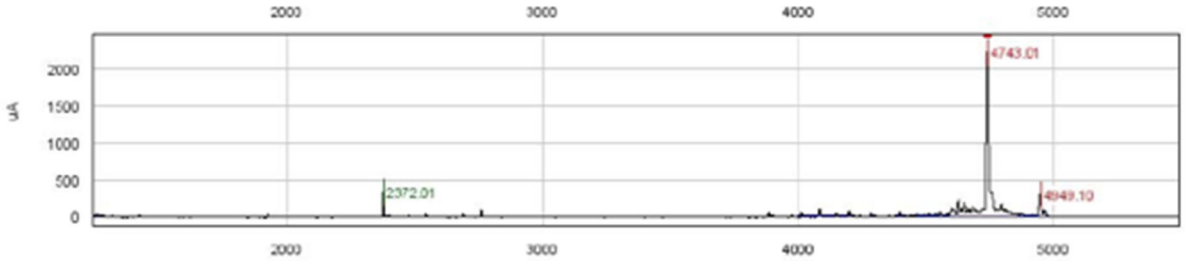

B

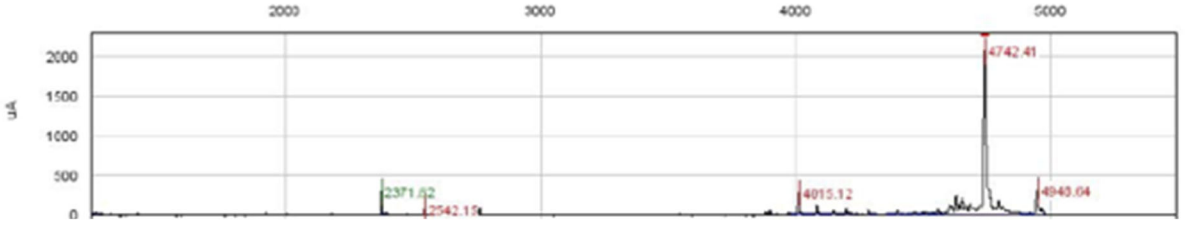

C

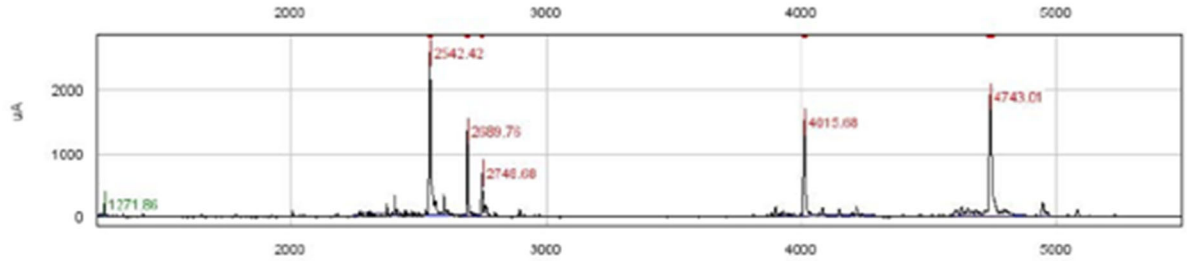

Figure S3.6. Mass spectra of Aβ42 degradation by CatD. ***A-C***, SELDI spectra of biotinylated Aβ42 at t=0 (***A***) or after incubation with recombinant human CatD for 10 min (***B***) or 2 h (***C***). Numbers in *red* and *green* reflect m/z values corresponding to charge states $[M+H]^{+}$ and $[M+2H]^{2+}$, respectively.

A

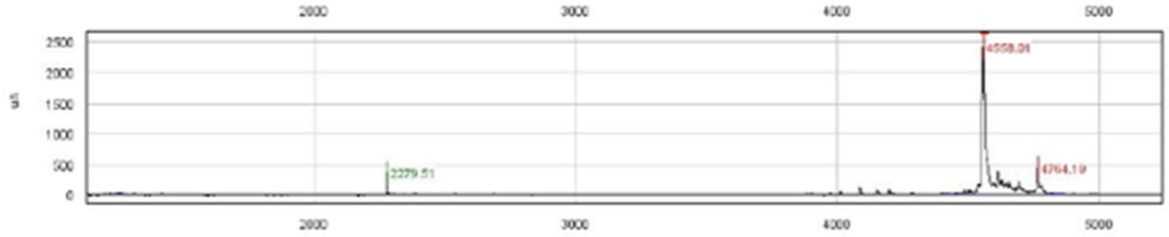

B

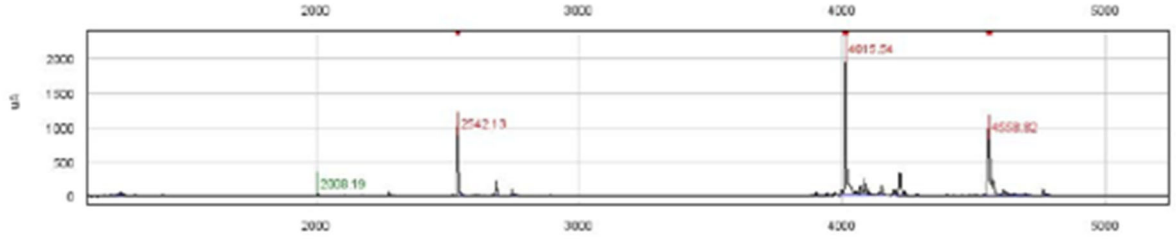

C

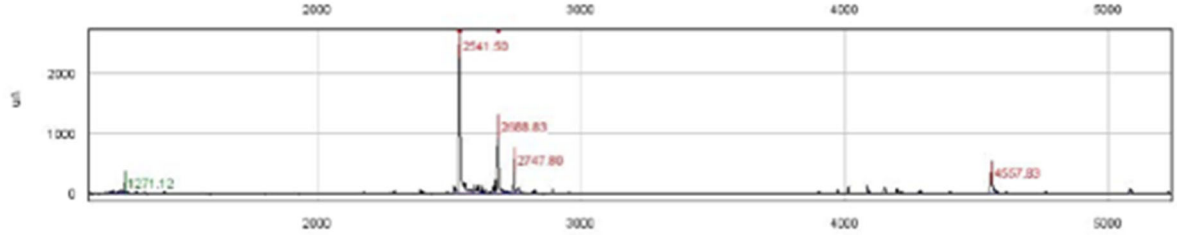

Figure S3.7. Mass spectra of Aβ40 degradation by CatD. ***A*****-*****C***, SELDI spectra of biotinylated Aβ40 at t=0 (***A***) or after incubation with recombinant human CatD for 10 min (***B***) or 2 h (***C***). Numbers in *red* and *green* reflect m/z values corresponding to charge states $[M+H]^{+}$ and $[M+2H]^{2+}$, respectively.

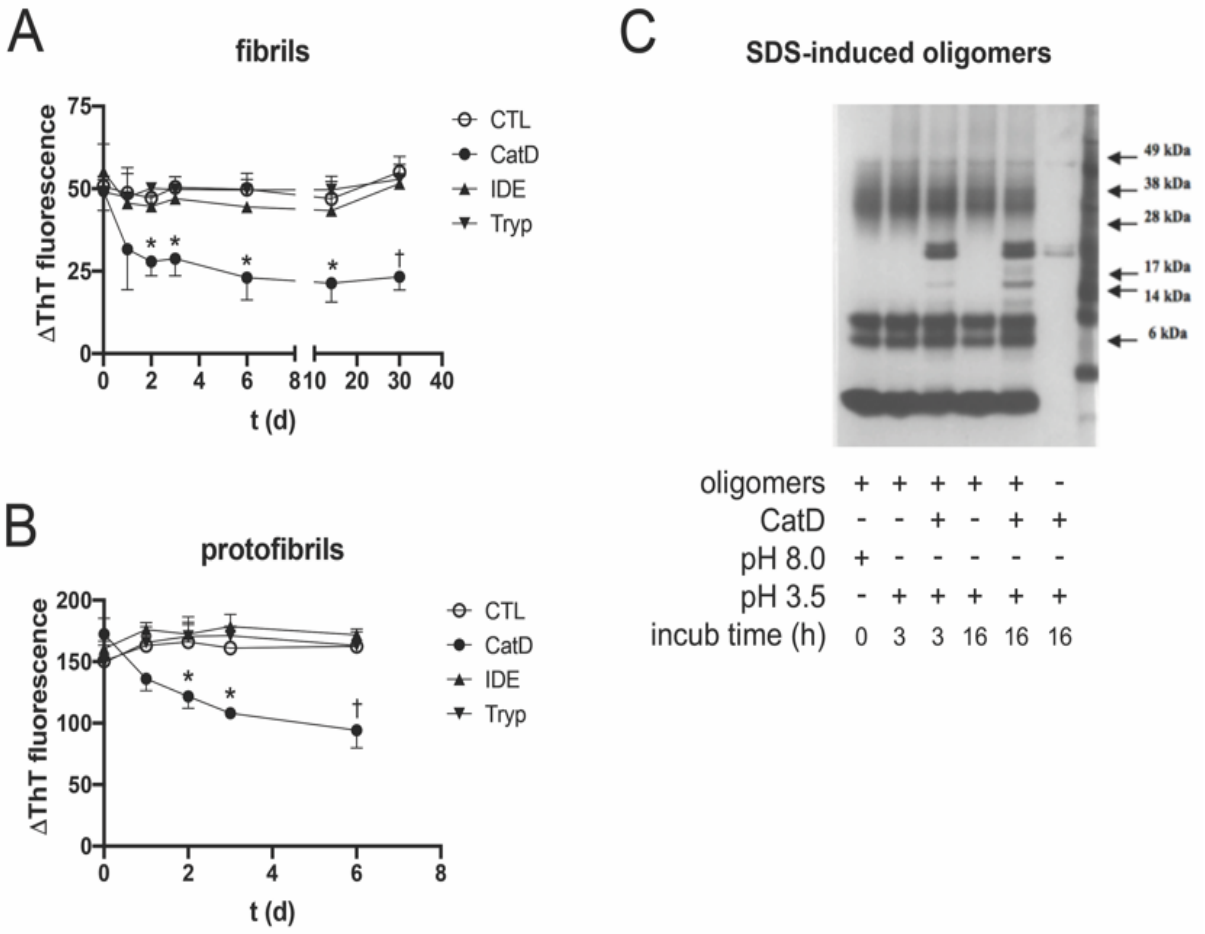

Figure S3.8. Activity of CatD against aggregated Aβ species. ***A***,***B***, Aβ fibrils (***A***) and protofibrils (***B***) are degraded by CatD at pH 4.0 as assessed by thioflavin T (ThT) fluorescence, albeit on a time-scale of days. As controls, we also tested trypsin (tryp) at pH 4.0 and IDE at pH 7.4. The protease-free control (CTL) shown is for pH 4.0; another control for pH 7.4 showed similar results, but has been omitted for clarity. See *Supplemental Methods* for details. Data are mean ± SEM for 4 independent replications. **P*<0.05; †*P*<0.01. ***C***, CatD shows no effect on SDS-induced Aβ oligomers, at least after 16-h incubation. See *Supplemental Methods* for details.

A

B

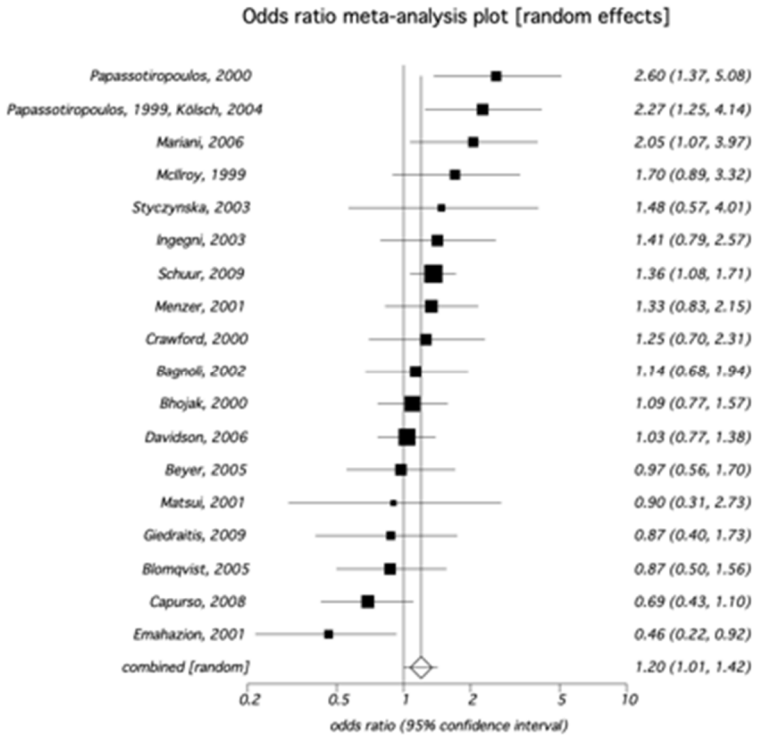

Figure S3.9. Evidence for a statistically significant genetic association between a functional polymorphism in *CTSD* and risk for LOAD. ***A***, Cartoon showing the location of the C224→T/A58V polymorphism in relation to other relevant features of the CatD molecule including the active-site aspartyl residues. SP = signal peptide. ***B***, Forest plot showing odds ratios (*black squares*), 95% confidence limits (*lines*), and the summary measure (*diamond*) for the association between C→224T and LOAD in 18 published Caucasian series from AlzGene (1) composed of 4,154 ADs and 9,302 controls, excluding series with Hardy-Weinberg disequilibrium in controls at P<0.01 . To perform a meta-analysis of all published, Caucasian series, allelic counts were calculated using the reported allelic frequency and sample size information from the AlzGene website (1). Test statistics are reported for each series and pooled test statistics are reported using the random effects model (DerSimonian-Laird). Note that meta-analysis of the combined 18 series reveals a statistically significant association ($P<0.05$), with the loss-of-function SNP conferring increased risk for LOAD.

Table S3.1 CatD-mediated cleavage sites within Aβ. Determination of CatD-mediated cleavage sites within Aβ42 and Aβ40 via mass spectrometry.

DAEFRHDSGYEVHHQKLVFFAEDVGSNKGAIIGLMVGGVVIA

Aß42					Observed		
Fragment	Sequence	Charge state	Expected (avg. mass)	0 min	10 min	120 min	Exp-Obs (avg.)
Aß(1-42)	biot-DAEFRHDSGYEVHHQKLVFFAEDVGSNKGAIIGLMVGGVVIA	$[M+H]^+$	4741.7025	4743.01	4742.41	4743.01	-1.1075
Aß(1-42)	biot-DAEFRHDSGYEVHHQKLVFFAEDVGSNKGAIIGLMVGGVVIA	$[M+2H]^{2+}$	2371.4299	2372.01	2371.62		-0.3851
Aß(1-34)	biot-DAEFRHDSGYEVHHQKLVFFAEDVGSNKGAIIGL	$[M+H]^+$	4014.7701		4015.12	4015.68	-0.6299
Aß(1-20)	biot-DAEFRHDSGYEVHHQKLVFF	$[M+H]^+$	2689.2858			2689.76	-0.4742
Aß(1-19)	biot-DAEFRHDSGYEVHHQKLVF	$[M+H]^+$	2542.1092		2542.15	2542.42	-0.1758

DAEFRHDSGYEVHHQKLVFFAEDVGSNKGAIIGLMVGGVV

Aß40					Observed		
Fragment	Sequence	Charge state	Expected (avg. mass)	0 min	10 min	120 min	Exp-Obs (avg.)
Aß(1-40)	biot-DAEFRHDSGYEVHHQKLVFFAEDVGSNKGAIIGLMVGGVV	$[M+H]^+$	4557.4643	4558.01	4558.82	4557.83	-0.7557
Aß(1-40)	biot-DAEFRHDSGYEVHHQKLVFFAEDVGSNKGAIIGLMVGGVV	$[M+2H]^{2+}$	2279.3108	2279.51			-0.1992
Aß(1-34)	biot-DAEFRHDSGYEVHHQKLVFFAEDVGSNKGAIIGL	$[M+H]^+$	4014.7701		4015.54		-0.7699
Aß(1-34)	biot-DAEFRHDSGYEVHHQKLVFFAEDVGSNKGAIIGL	$[M+2H]^{2+}$	2007.9637		2008.19		-0.2263
Aß(1-20)	biot-DAEFRHDSGYEVHHQKLVFF	$[M+H]^+$	2689.2858			2688.83	0.4558
Aß(1-19)	biot-DAEFRHDSGYEVHHQKLVF	$[M+H]^+$	2542.1092		2542.13	2541.5	0.2942
Aß(1-19)	biot-DAEFRHDSGYEVHHQKLVF	$[M+2H]^{2+}$	1271.6333			1271.12	0.5133

Table S3.2. Kinetics of Aβ42 vs Aβ40 degradation at pH 4.0 quantified by several independent methods.

Aβ42 catabolism	ELISA	^{125}I-Aβ42	silent substrate	HTRF
K_M (nM)	27.7 ± 6.0	7.34 ± 1.64	3.17 ± 0.62	24.1 ± 4.6
k_{cat} (min^{-1})	0.219 ± 0.011	0.401 ± 0.087	0.55 ± 0.097	1.13 ± 0.10
k_{cat}/K_M (M^{-1} min^{-1})	1.38 x 10^7	1.24 x 10^7	3.18 x 10^7	6.34 x 10^7

Aβ40 catabolism	ELISA	^{125}I-Aβ40	silent substrate	HTRF
K_M (nM)	1510 ± 260	1240 ± 180	1880 ± 330	1490 ± 230
k_{cat} (min^{-1})	20.8 ± 1.1	15.4 ± 3.6	59.8 ± 7.9	94.8 ± 13
k_{cat}/K_M (M^{-1} min^{-1})	0.79 x 10^7	5.46 x 10^7	1.74 x 10^7	4.58 x 10^7

CHAPTER 3 SUPPLEMENTAL METHODS

Western Blotting

Western blots were performed as described (2), using the following antibodies: αCatD (Santa Cruz Biotechnology, Inc.), IDE-1 (3) (generous gift of D. Selkoe), C20 (reactive with the carboxy terminus of APP; generous gift of D. Selkoe), αNEP antibody 56C6 (Santa Cruz Biotechnology, Inc.), and αGAPDH (Alpha Diagnostic Intl.).

Immunohistochemistry

Brains were collected following transcardial perfusion with PBS, fixed in 10% formalin solution, then embedded in paraffin. Parasagittal sections (5 μm) were deparaffinized in a graded alcohol series, and endogenous peroxidase activity was quenched by treatment with 3% H_2O_2 for 5 min prior to staining. Primary antibodies used (and their sources and dilutions) were: 2.1.3.35.86 (Mayo; 1:1000); 13.1.1 (Mayo; 1:1000); BC05 (Wako; 1:1000); BA27 (Wako; 1:1000); Lamp2 (1:2000; AbCam). For immunohistochemical staining, the primary antibodies were detected using appropriate HRP-conjugated secondary antibodies (Novus Biologicals; 1:5000). For immunofluorescence studies, endogenous fluorescence was quenched using 1% Sudan Black-B (SPI Supplies), and primary antibodies were detected with Alexa Fluor™-tagged secondary antibodies (Invitrogen; 1:5000). Staining with hematoxylin/eosin, thioflavin S, and Gallyus silver stain were conducted as described (4).

Live cell imaging and Aβ quantification

Hippocampus-enriched neurons were cultured as described (5) from individual E18 embryos derived from a cross between CatD-HET mice, and plated (10^6 cells/cm^2) on 35-mm poly-D-lysine-coated glass bottom culture dishes (MatTek Corp.). After maintenance for 7 to 10

days in Neurobasal medium containing the growth supplement B27 (Invitrogen). For quantification of secreted Aβ, cells were washed twice, then incubated in the latter medium overnight, and the conditioned medium was collected, supplemented with Complete Protease Inhibitor Cocktail (Roche) and analyzed without further extraction using in-house ELISA systems based on antibody pairs 33.1.1/13.1.1 and 2.1.3.35.86/33.1.1. Aβ uptake and catabolism was assessed by washing neurons twice, then incubated in the growth medium containing a mixture of Aβ42 and Aβ40 (500 nM each) labeled N-terminally with HiLyte Fluor^{TM} 488 or HiLyte Fluor^{TM} 555, respectively (Anaspec). Following incubation at 37 ºC/5% CO_2 for 2 h, cells were washed 3 times, imaged by confocal microscopy (see below), returned to 37 ºC/5% CO_2 for 2 h, stained with Hoescht 33258 (Invitrogen), washed and imaged again. Images were obtained using the 488-nm and 543-nm laser lines on a Zeiss LCM 510 confocal microscope the intensities of which were calibrated and maintained constant for all imaging. A computer-operated stage (Zeiss) was used to record the position of imaged cells and to facilitate their subsequent location, which was verified by manual inspection prior to the capture of the second image. Images were processed and analyzed using MetaMorph software according to manufacturer's recommendations (Molecular Devices).

Mass Spectrometry

The cleavage sites within Aβ40 and Aβ42 hydrolyzed by CatD were determined essentially as described (6) with minor modifications. Briefly, biotinylated Aβ peptides were incubated for various lengths of time with purified CatD. The reaction was stopped by addition of PepA (1 μM) and pH adjustment. Aβ fragments were precipitated by magnetic beads coated with streptavidin (for biotinylated Aβ). Beads were washed with 10 mM NH4CO3, pH 8.0, and peptide fragments were eluted using 0.5% trifluoroacetic acid in 75% acetonitrile in water,

followed by the addition of an equal volume of a saturated sinapic acid solution dissolved in 0.5% trifluoroacetic acid in 50% acetonitrile and water. Digested products were spotted onto gold chip and analyzed using a Ciphergen ProteinChip SELDI time-of-flight system (Bio-Rad). Mass spectra were acquired automatically in a linear positive mode at 1350 shots per spectrum.

Enzymological studies

For experiments based on radiolabeled Aβ peptides, ^{125}I-Aβ42 and ^{125}I-Aβ40 prepared as described (7) (generous gift of R. Deane and B. Zlokovic) were mixed in a 1:10 ratio with the corresponding unlabeled Aβ peptides, and degradation was quantified by trichloroacetic acid precipitation, as described (8). Kinetic parameters obtained from "silent substrate" experiments with the fluorogenic substrate were carried out and calculated from the resulting data as described (9). Homogeneous time-resolved fluorescence (HTRF)-based kinetic experiments were carried out using end-specific anti-Aβ42 and -Aβ40 antibodies (Wako) labeled with europium cryptate and N-terminal antibodies labeled with XL665 prepared and quantified according to manufacturer's recommendations on a SpectraMax® M5^{e} multilabel plate reader (Molecular Devices). Fibrils, protofibrils and SDS-induced oligomers of Aβ42 were prepared and quantified as described (10).

APPENDIX C

CHAPTER 4 SUPPLEMENTAL FIGURES

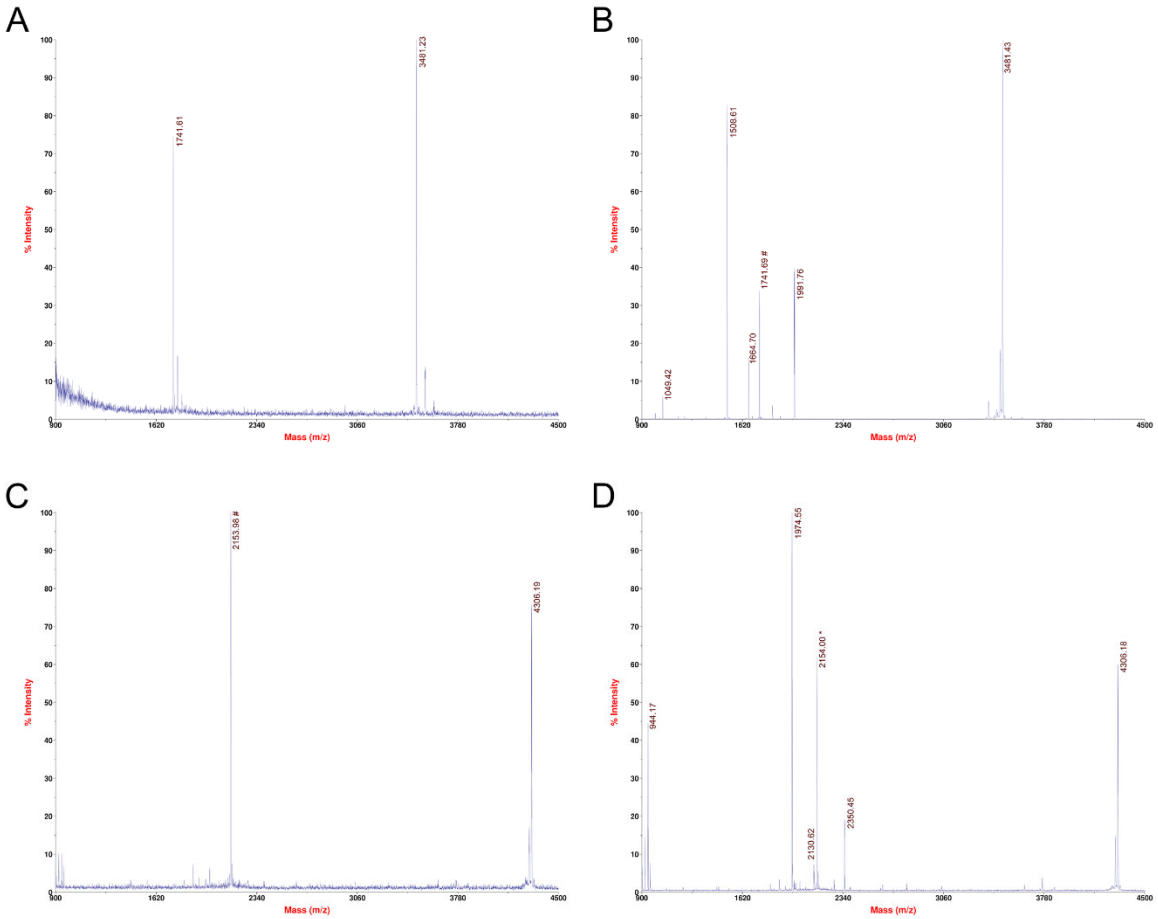

Figure S4.1. Mass spectra of intact and partially cleaved glucagon and FBG. ***A***,***B***, Mass spectra of intact (***A***) and hydrolyzed (***B***) human glucagon. ***C***,***D***, Mass spectra of intact (***C***) and hydrolyzed (***D***) FBG. # = $[M+2H]^{2+}$; * = $[M+Na]^{+}$.

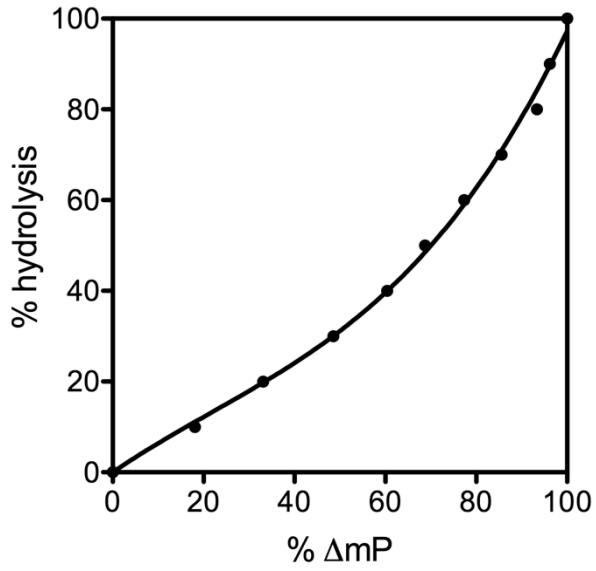

Figure S4.2. Derivation of equation for conversion of percent mP change to percent hydrolysis of FBG for FP-based assay. Equation 1 was derived by fitting a 3rd order curve to these data.

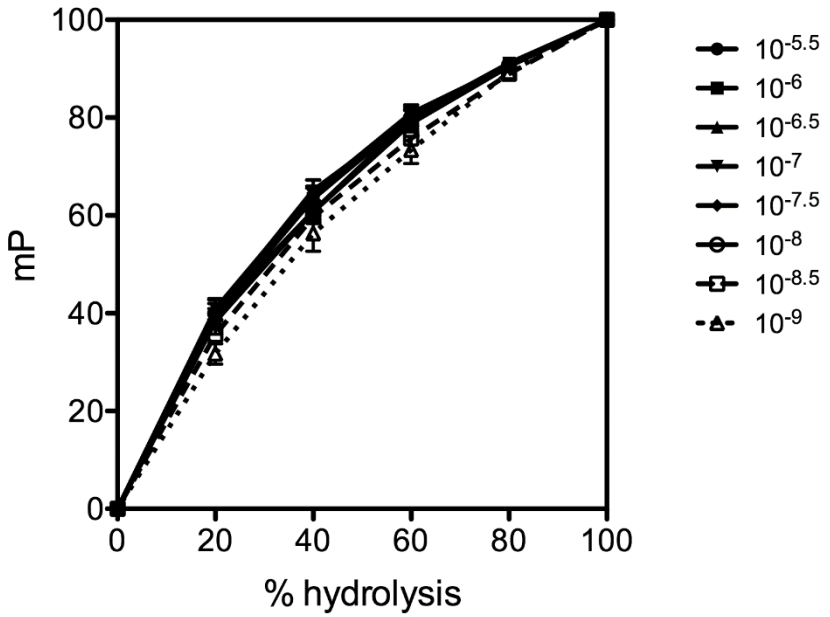

Figure S4.3. Percent mP change as a function of percent hydrolysis for FBG at different concentrations. Note that the relationship is similar for all concentrations except the very lowest two (1 and 3 nM; *dotted* and *dashed lines*, respectively). Concentrations are labeled in units of molarity.

Sample: P7293-1
Method: C:\32Karat\Projects\Default\Methods\ANAPEP2.met
File Name: C:\32Karat\Projects\Default\Data\P7293-1T
Solvent: A: 0.05 % TFA in H2O; B: 0.05 % TFA in ACN
Colomn: Onyx Monolithic C18, 100x 3.00mm 3u Flow Rate: 1.0ml min.
Run Time: 1/18/2018 4:33:06 PM
HPLC ID # CD-159/EQ-066

Project: KM101624.1 MW:4307.68
[Fluo(5FAM)]HSQGTFTSDYSKYLDSRRAQDFVQWL
MNT-Lys(Ahx-Biotin)[Amide]
ID:Peptide 1
P7293-1 5 mg
Thermo SCIENTIFIC
800-874-3723 or 815-968-0747 • FOR RESEARCH USE ONLY
3747 N. Meridian Rd., Rockford, IL 61101 U.S.A.
www.thermoscientific.com/pierce

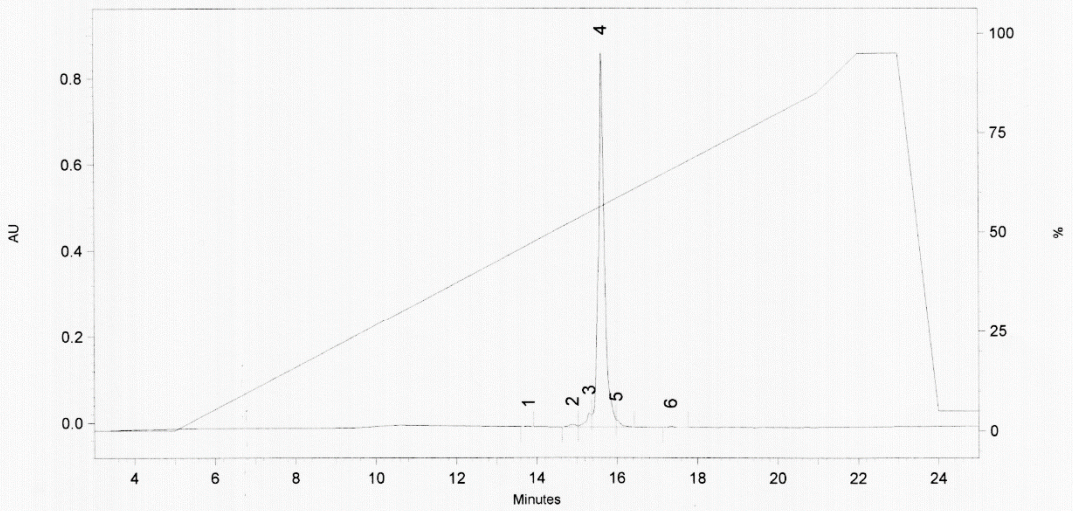

Det 166 Results

Pk #	Time	Area	Area %
1	13.792	10909	0.12
2	14.892	69717	0.74
3	15.308	287363	3.04
4	15.625	8954528	94.58
5	15.975	122902	1.30
6	17.333	21768	0.23
Totals		9467187	100.00

Figure S4.4. HPLC trace confirming purity of FBG.

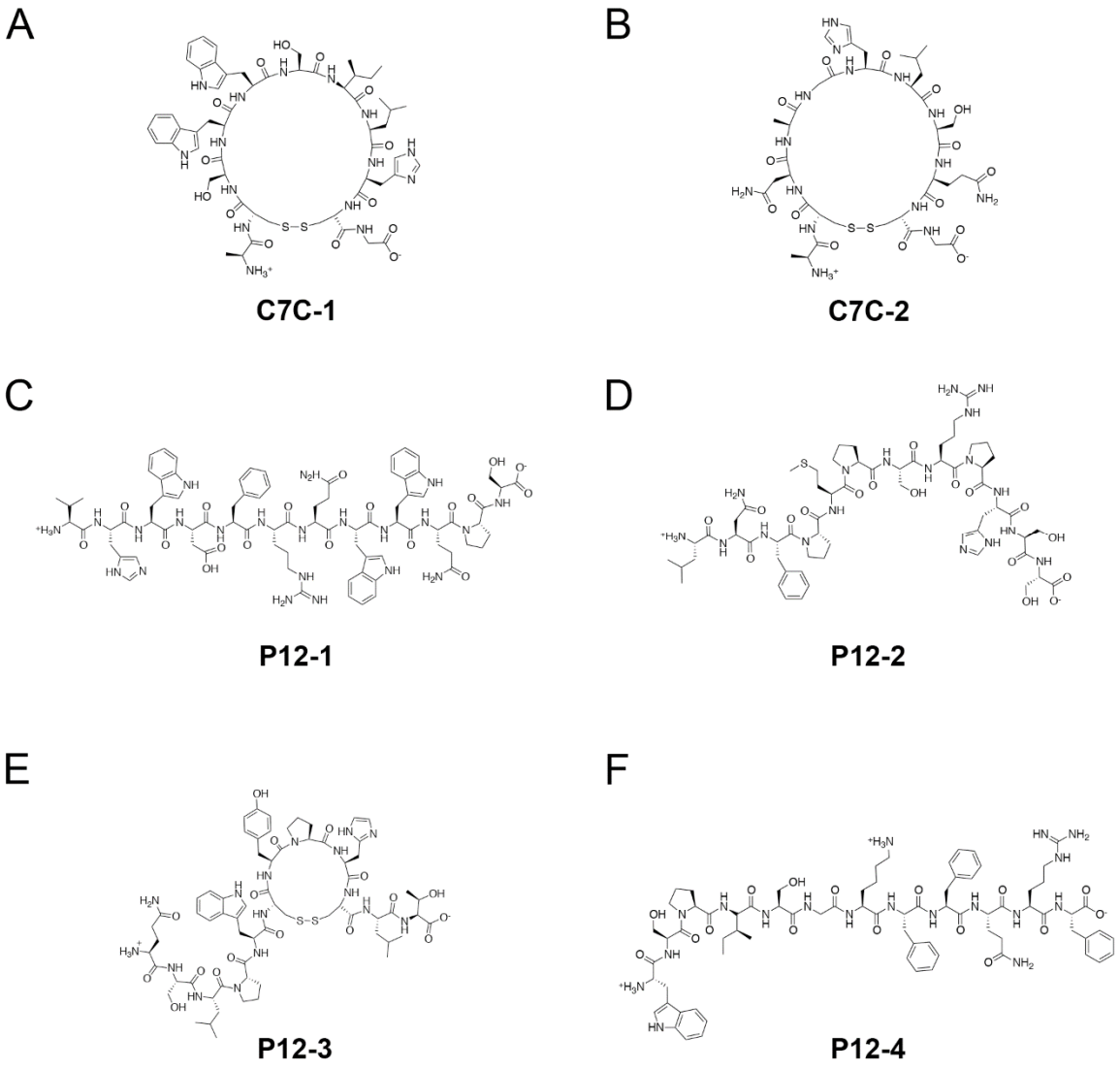

Figure S4.5. Structures of parent peptides discovered by phage display. Note that P12-3, although derived from a library of primarily linear peptides, is predicted to be a cyclic peptide.

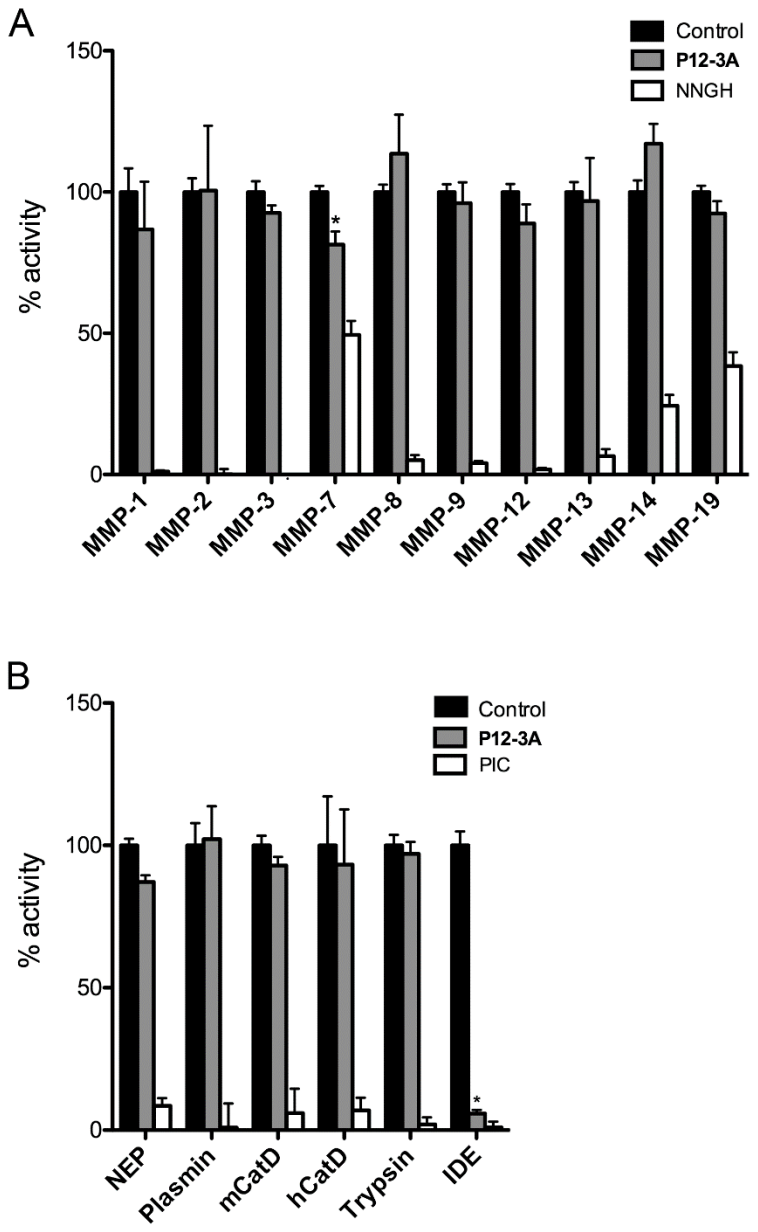

Figure S4.6. Selectivity of P12-3A for IDE vis-à-vis other proteases. Activity of P12-3A (100 μM) against (***A***) multiple matrix-metalloproteases (MMPs) and (***B***) multiple peptidases of different protease classes. Note that significant inhibition was observed exclusively for IDE, with modest inhibition (~18%) observed for just one of 15 other proteases tested (MMP-7). Data are mean ± SEM, n = 8-16 per group. $P<0.05$ by 2-tailed Student's t-test. Note that all positive controls (NNGH or protease inhibitor cocktail (PIC)) exhibited significant inhibition ($P< 0.01$) (not shown for clarity). See *Experimental Procedures* for details. NEP, neprilysin; mCatD, murine cathepsin D; hCatD, human cathepsin D.

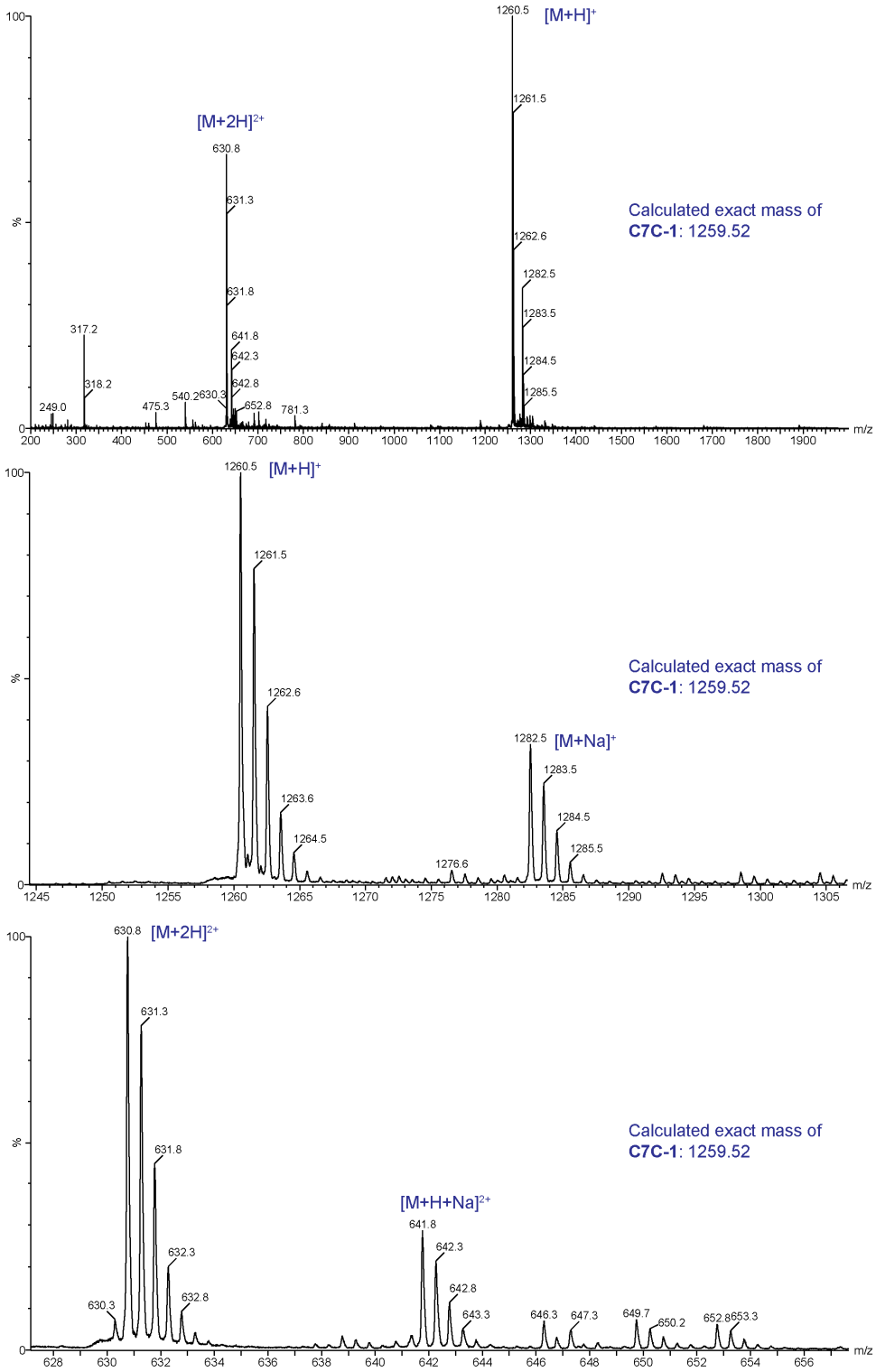

Figure S4.7. Confirmation of mass of C7C-1 by ESI-MS. The entire spectrum as well as expanded regions are shown.

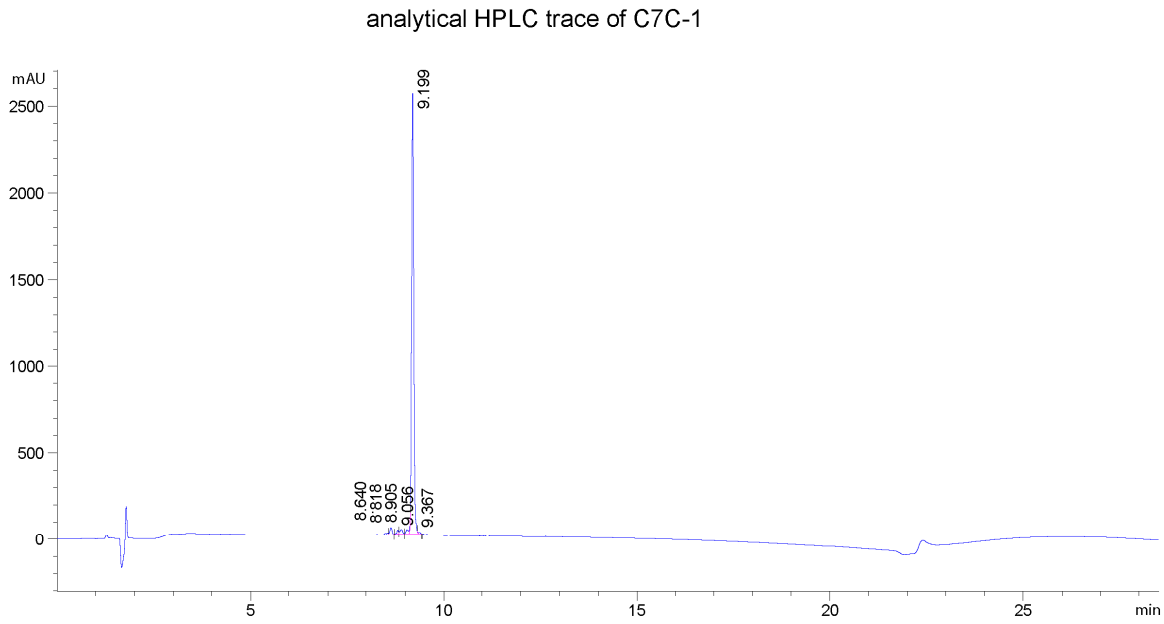

Peak #	RetTime [min]	Type	Width [min]	Area [mAU*s]	Height [mAU]	Area %
1	8.640	VB	0.0637	160.10162	40.83241	1.5189
2	8.818	BV	0.0526	87.10760	25.00230	0.8264
3	8.905	VB	0.0775	128.50171	27.02070	1.2191
4	9.056	BV E	0.0892	151.47963	23.50020	1.4371
5	9.199	VV R	0.0638	9978.79395	2544.24048	94.6678
6	9.367	VB E	0.0611	34.86900	8.28348	0.3308

Figure S4.8. Analysis of purity of C7C-1 by HPLC. Note that the purity is ~95%.

CHAPTER 4 SUPPLEMENTAL TABLES

Table S4.1. Kinetic parameters of FBG degradation by IDE. Quantitative kinetic parameters calculated from the data shown in Figure 3 using the AP and FP methods. For the FP method, raw percent changes in mP values were first converted to percent hydrolysis using Eq. 1. Note that k_{cat} determinations take into account different IDE concentrations used with the different methods. Data are mean ± SEM of 4 independent replications.

	AP	FP
K_M^{app} (nM)	800 ± 110	380 ± 72
v_{max}^{app} (nM s^{-1})	2.81 ± 0.30	3.70 ± 0.35
k_{cat} (s^{-1})	1.76 ± 0.19	1.16 ± 0.11
k_{cat}/K_M (M^{-1} s^{-1})	2.25 ± 0.12 x 10^6	3.26 ± 0.59 x 10^6

Table S4.2. Effects of two different inhibitors of IDE on the kinetics of FBG degradation. Kinetic parameters calculated from the data shown in Figure 4C, D. Note that **P12-3A** results in increased K_M^{app} values, consistent with reversible inhibition, while **ML345** results in reduced v_{max}^{app} values, consistent with irreversible inhibition, in agreement with the established mechanisms of inhibition of the two inhibitors. Data are mean ± SD of 3 independent runs calculated from hyperbolic curves drawn through the raw S vs. v_o data (not from double reciprocal plots).

	DMSO	ML345
K_M^{app} (nM)	331 ± 71	392 ± 73
v_{max}^{app} (nM s^{-1})	3.37 ± 0.26	0.827 ± 0.032

References

1. Bertram L, McQueen MB, Mullin K, Blacker D, Tanzi RE. Systematic meta-analyses of Alzheimer disease genetic association studies: the AlzGene database. Nat Genet. 2007;39(1):17-23.

2. Leissring MA, Farris W, Chang AY, Walsh DM, Wu X, Sun X, et al. Enhanced proteolysis of beta-amyloid in APP transgenic mice prevents plaque formation, secondary pathology, and premature death. Neuron. 2003;40(6):1087-93.

3. Vekrellis K, Ye Z, Qiu WQ, Walsh D, Hartley D, Chesneau V, et al. Neurons regulate extracellular levels of amyloid beta-protein via proteolysis by insulin-degrading enzyme. J Neurosci. 2000;20(5):1657-65.

4. Dickson DW, Bergeron C, Chin SS, Duyckaerts C, Horoupian D, Ikeda K, et al. Office of Rare Diseases neuropathologic criteria for corticobasal degeneration. J Neuropathol Exp Neurol. 2002;61(11):935-46.

5. Farris W, Mansourian S, Leissring MA, Eckman EA, Bertram L, Eckman CB, et al. Partial loss-of-function mutations in insulin-degrading enzyme that induce diabetes also impair degradation of amyloid beta-protein. Am J Pathol. 2004;164(4):1425-34.

6. Abdul-Hay SO, Sahara T, McBride M, Kang D, Leissring MA. Identification of BACE2 as an avid β-amyloid-degrading protease. Mol Neurodegener. 2012;7(1):46.

7. LaRue B, Hogg E, Sagare A, Jovanovic S, Maness L, Maurer C, et al. Method for measurement of the blood-brain barrier permeability in the perfused mouse brain: application to amyloid-beta peptide in wild type and Alzheimer's Tg2576 mice. J Neurosci Methods. 2004;138(1-2):233-42.

8. Leissring MA, Lu A, Condron MM, Teplow DB, Stein RL, Farris W, et al. Kinetics of amyloid beta-protein degradation determined by novel fluorescence- and fluorescence polarization-based assays. J Biol Chem. 2003;278(39):37314-20.

9. Case A, Huskey WP, Stein RL. Enzymatic reaction of silent substrates: kinetic theory and application to the serine protease chymotrypsin. Biochemistry. 2003;42(16):4727-32.

10. Rangachari V, Moore BD, Reed DK, Sonoda LK, Bridges AW, Conboy E, et al. Amyloid-beta(1-42) rapidly forms protofibrils and oligomers by distinct pathways in low concentrations of sodium dodecylsulfate. Biochemistry. 2007;46(43):12451-62.